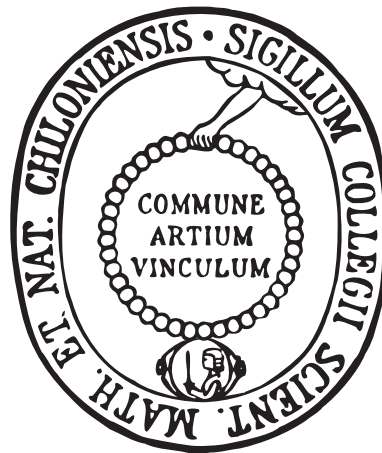


---

# Melting Processes and Laser Manipulation of Strongly Coupled Yukawa Systems

Hauke Thomsen

---



Christian-Albrechts-Universität zu Kiel



---

# **Melting Processes and Laser Manipulation of Strongly Coupled Yukawa Systems**

**Hauke Thomsen**

---

Dissertation  
zur Erlangung des Doktorgrades der  
Mathematisch-Naturwissenschaftlichen Fakultät  
der Christian-Albrechts-Universität zu Kiel

vorgelegt von  
Hauke Thomsen,  
geb. am 23.IV.1985 in Kiel

Kiel, April 2015

This work was typeset in  $\LaTeX$ .

The figures were created with Gnuplot—a command-line driven graphing utility, POV-Ray—the Persistence of Vision Raytracer, and TikZ—a Graphic system for  $\TeX$ .

Erstgutachter: Prof. Dr. Dr. h.c. M. Bonitz

Zweitgutachter: Prof. Dr. H. Kersten

Tag der mündlichen Prüfung: 12.Juni 2015

# Contents

<b>1</b>	<b>Motivation and Outline</b>	<b>1</b>
<b>2</b>	<b>Introduction</b>	<b>5</b>
2.1	Strongly Coupled Systems . . . . .	5
2.2	Coupling Parameter . . . . .	6
2.3	Spherical Dust Clusters . . . . .	8
2.3.1	Experimental Realization . . . . .	8
2.3.2	Coupling Parameter in Finite Dust Clusters . . . . .	11
2.4	Experiments with Laser-Heated Clusters . . . . .	12
2.5	Melting as Loss of Order . . . . .	12
2.6	Motivation for new Melting Parameters . . . . .	13
<b>3</b>	<b>Model System and Simulation Methods</b>	<b>17</b>
3.1	Model for Charged Dust Grains . . . . .	17
3.1.1	Finite 2D Dust Clusters . . . . .	19
3.1.2	Extended 2D Dust Clusters . . . . .	19
3.1.3	Spherical Dust Balls . . . . .	20
3.1.4	Dimensionless System of Units . . . . .	20
3.2	Metropolis Monte Carlo . . . . .	21
3.2.1	Metropolis Monte Carlo for Spherical Shells . . . . .	24
3.2.2	Parallel Tempering in Monte Carlo Simulations . . . . .	25
3.2.3	Ergodicity of the Monte Carlo Algorithm . . . . .	26
3.3	Molecular Dynamics Simulations . . . . .	27
3.3.1	Microcanonical Molecular Dynamics Simulations . . . . .	27
3.3.2	Langevin Molecular Dynamics Simulations . . . . .	28
<b>4</b>	<b>Melting Parameters for Dusty Plasmas</b>	<b>31</b>
4.1	Voronoi analysis . . . . .	31
4.1.1	Stereographic Projection . . . . .	33
4.1.2	Validity of the Delaunay Triangulation . . . . .	36
4.1.3	The Euler-Poincaré Characteristic . . . . .	37
4.2	Bond Order Parameter . . . . .	38
4.3	$n$ -Particle Distributions in Generalized Coordinates . . . . .	40

4.3.1	Pair Distribution Function . . . . .	43
4.3.2	Center-Two-Particle Distribution Function . . . . .	44
4.3.3	Triple-Correlation Function in Macroscopic Systems . . . . .	46
4.3.4	Triple-Correlation Function in Spherical Shells . . . . .	49
4.4	Reduced Entropy and Heat Capacity . . . . .	52
<b>5</b>	<b>Melting in Finite Dust Clusters</b>	<b>55</b>
5.1	Finite 2D Dust Clusters . . . . .	60
5.2	Spherical 3D Dust Clusters . . . . .	67
5.2.1	Classification of the Intra-Shell Order by the Means of Voronoi Diagrams	67
5.2.2	Small “Magic” Cluster . . . . .	69
5.2.3	Melting Processes in Further Coulomb Balls . . . . .	77
5.3	Particles on a Unit Sphere . . . . .	84
<b>6</b>	<b>Laser Excitation of 2D Dust Clusters</b>	<b>89</b>
6.1	Laser Heating Method . . . . .	90
6.1.1	Including Heating Lasers in the Model System . . . . .	92
6.1.2	The Effect of Different Heating Methods on Structure and Dynamics of a Dust Cluster . . . . .	94
6.1.3	Analytical Model of the Laser Heating Process . . . . .	96
6.2	Inhomogeneous Excitation and Heat Transport . . . . .	106
6.2.1	Analytical Model for the Temperature Profile . . . . .	110
6.2.2	Influence of the Background Temperature $T_0$ and the Heating Power $F_L$ . . . . .	113
6.2.3	Discussion of the Results . . . . .	115
6.2.4	Heat Transport in a Magnetized Cluster . . . . .	117
<b>7</b>	<b>Conclusion</b>	<b>121</b>
	<b>Appendix</b>	<b>123</b>
<b>A</b>	<b>Distribution Functions in Generalized Coordinates and Reduced Entropy</b>	<b>123</b>
<b>B</b>	<b>Analytical Model of the Laser Heating: Calculations &amp; Tables</b>	<b>141</b>
<b>C</b>	<b>Used Abbreviations and Symbols</b>	<b>149</b>
	<b>Bibliography</b>	<b>161</b>
	<b>Danksagung</b>	<b>163</b>
	<b>Selbstständigkeitserklärung</b>	<b>165</b>

# Abstract

The thesis at hand is devoted to the melting processes in spherical dust crystals and mechanisms for the selective heating of the dust particles. The observed dust crystals are composed of micrometer-sized plastic spheres, which become negatively charged inside an rf-plasma, and are therefore subject to strong (screened) Coulomb interactions. In a three-dimensional harmonic confinement potential, so-called Coulomb or Yukawa balls are formed. These “artificial atoms” consist of nested spherical shells even at room temperature. In addition to the radial order, the melting process of these three-dimensional shell structures involves the loss of the relative orientation of the shells to each other and the specific arrangement of the dust particles within a shell. For the investigation of the multi-stage melting process of Yukawa balls, classical Monte Carlo simulations are applied. In order to cover a broad temperature range, the so-called parallel tempering method has been implemented which allows exchanges between system replicas at different temperatures.

The first topical part of this work is the development of appropriate melting criteria for finite dust clusters that make it possible to resolve different melting processes. For this purpose, the center-two-particle distribution function and the triple-correlation function are introduced. These quantities describe the distributions of particle pairs and triples, respectively, in generalized coordinates. The coordinates are adjusted to the spherical symmetry of the confined Yukawa systems. As a measure of the degree of order in such a distribution, a reduced entropy  $S^{(n)}$  is introduced, which generalizes the concept of the thermodynamic Boltzmann entropy to pair and three-particle distributions. The application of this quantity allows a systematic analysis of the multi-level structural transitions in the studied dust crystals. In particular the intra-shell order within the spherical shells are proved to be highly stable.

The second main topic of this thesis deals with the selective heating of two-dimensional, planar dust crystals by means of moving laser spots. In order to characterize the properties of the considered heating method, Langevin molecular dynamics (LMD) simulations are performed, in which the radiation pressure of the laser is used as an additional, time-dependent force acting on the dust particles. In addition to the laser power, other parameters such as the spot size or the speed at which the spots are moved through the cluster have a significant influence on the heating power. A simple analytical model is presented, which allows for an estimation of the resulting dust temperature in dependence on the parameters of the laser heating.

In the final part of the thesis at hand, a realistic experimental setup is considered in which the central part of the dust cluster is selectively heated. The particular temperature profiles obtained in the LMD simulations allow for conclusions about the radial thermal conductivity.

The presented quantities are well suited for experimental applications since they are based only on the positions and velocities of the particles which are accessible in experiments. The thermal conductivity does not show any dependency on the dust temperature over wide ranges. At the same time, already a relatively weak perpendicular magnetic field is found to reduce the thermal conductivity.



# Zusammenfassung

Die vorliegende Dissertation behandelt Schmelzprozesse in sphärischen Staubkristallen sowie Mechanismen zur Staubheizung. Die betrachteten Staubkristalle setzen sich aus mikrometergroßen Plastik Kügelchen zusammen, die sich in einem rf-Plasma negativ aufladen und daher einer starken (abgeschirmten) Coulomb-Wechselwirkung unterliegen. In dreidimensionalen harmonischen Fallenpotentialen formen sich sogenannte Coulomb- oder Yukawa-Balls. Diese "künstlichen Atome" bestehen bei Raumtemperatur aus ineinander geschichteten Kugelschalen. Bei der Analyse der Schmelzübergänge wird zwischen der radialen Ordnung, der relativen Orientierung der Schalen zueinander, sowie der Anordnung der Staubteilchen innerhalb einer Schale unterschieden. Zur Untersuchung des mehrstufigen Schmelzprozesses der Staubkristalle werden klassische Monte Carlo Simulationsverfahren implementiert. Um weite Temperaturbereiche berücksichtigen zu können, wird die sogenannte Parallel-Tempering-Methode verwendet, die einen Austausch zwischen den Teilchenkonfigurationen bei verschiedenen Temperaturen ermöglicht.

Den ersten Schwerpunkt dieser Arbeit stellt die Entwicklung geeigneter Schmelzkriterien für finite Staubcluster dar, die es ermöglichen, die verschiedenen Schmelzprozesse detailliert aufzulösen und zu analysieren. Zu diesem Zweck werden die "Center-Two-Particle" Verteilungsfunktion und die "Triple-Correlation Function" eingeführt. Diese eingeführten Größen beschreiben die Verteilungen von Teilchenpaaren und -tripeln in generalisierten Koordinaten, welche an die sphärische Symmetrie der finiten Cluster angepasst sind. Als ein Maß für den Grad der Ordnung in einer solchen Verteilung wird eine reduzierte Entropie  $S^{(n)}$  eingeführt, die in ihrer Form der thermodynamischen Boltzmann-Entropie sehr ähnlich ist. Mit ihrer Hilfe können mehrstufige Strukturübergänge in den untersuchten Staubkristallen systematisch analysiert werden. Dabei stellt sich insbesondere die Ordnung innerhalb der Schalen als außerordentlich stabil heraus.

Der zweite Themenkomplex dieser Arbeit ist der gezielten Heizung von zweidimensionalen, ebenen Staubkristallen mit Hilfe von bewegten Laserspots gewidmet. Um die Eigenschaften der einzelnen Heizmethoden zu charakterisieren, werden Langevin Molekulardynamik Simulationen durchgeführt, in denen der Strahlungsdruck der Laser als zusätzliche, zeitabhängige Kraft auf die Staubteilchen berücksichtigt wurde. Umfangreiche Parameterscans zeigen, dass neben der Leistung des Lasers auch Parameter wie die Spotgröße oder die Geschwindigkeit, mit der die Spots durch den Cluster bewegt werden, erheblichen Einfluss auf die Heizleistung haben. Des Weiteren wird ein einfaches analytisches Modell vorgestellt, das es erlaubt, die resultierende Staubtemperatur in Abhängigkeit von den Parametern der Laserheizung abzuschätzen.

Im abschließenden Teil dieser Arbeit wird eine konkrete Versuchsanordnung betrachtet, in der selektiv der zentrale Bereich des Staubclusters geheizt wird. Das in den Simulationen bestimmte Temperaturprofil läßt Rückschlüsse auf die radiale Wärmeleitfähigkeit zu. Die verwendeten Methoden beruhen ausschließlich auf den Positionen und Geschwindigkeiten der Teilchen, die auch in Experimenten zugänglich sind. Während die Wärmeleitfähigkeit über weite Bereiche keine Abhängigkeit von der Staubtemperatur erkennen läßt, ist bereits ein relativ schwaches, senkrecht zur Clusterebene angelegtes Magnetfeld geeignet, die Wärmeleitfähigkeit zu reduzieren.

# Chapter 1

## Motivation and Outline

**S**elf-organization and structure formation are among the most fascinating and fundamental processes in physics. Dusty plasmas provide a unique possibility of studying these phenomena on a single-particle level. Experimentally, dusty plasmas are studied, for example, in Kiel and in Greifswald laboratories by adding micrometer-sized plastic particles into a capacitively coupled radio frequency (rf) discharge [1, 2]. Inside the plasma, these particles collect up to several thousand elementary charges. While electrons and ions are—by definition—weakly coupled in the plasma state, the heavy micro-particles are subject to strong (screened) Coulomb interaction forces due to their large charges. For this reason, the dust particles can form highly correlated structures within the plasma even at room temperature, so-called dust crystals or dust clusters. Both planar 2D and spherical 3D dust clusters are the main subject of this thesis which is grouped into two topical complexes.

The first topical complex is concerned with the equilibrium properties of the crystalline dust structures. Especially, their melting transitions are subject of this part with the focus being on *finite* 3D clusters. The melting behavior of these clusters is qualitatively different from extended systems, because of their spherical confinement that results in a structure which consisting of nested shells in three-dimensional traps. For example, the *radial* order of particles can even persist when the *intra-shell* order is already lost. It is therefore a central concern of the thesis at hand to develop melting parameters which are suitable for a systematic analysis of the different structural disordering processes. At this point, a high level of universality is required: The melting parameters are developed with the goal to be based on quantities that are (i) accessible in experiments, (ii) completely compatible with equilibrium Monte Carlo simulation methods, and (iii) applicable for quantum systems as well. Finite systems are known to exhibit broad melting regions rather than sharp transitions temperatures [3]. On this account, this work aims to elucidate the melting processes in detail and to specify characteristic temperature ranges for certain types of transitions.

The second topical complex of this thesis is devoted to a laser heating method for confined 2D dust systems. Studying the melting process requires the selective control of the kinetic temperature of the dust particles experimentally. The considered laser manipulation method provides this control through the momentum transfer to the dust particles by moving laser beams

of moderate intensities [4–6]. While the kinetic temperature of the dust component is increased, the other plasma parameters like pressure, electron density etc. remain unaffected. The features and optimal parameter settings of the laser heating method acting as a thermostat for the dust systems are addressed by Langevin molecular dynamics (LMD) simulations. Specific attention is paid to the pattern that is scanned by the laser spots. The laser heating can be restricted to a certain spatial region, and it grants the possibility to investigate transport phenomena. At this point, a particular goal of this thesis is to provide predictions about the thermal conductivity in 2D dust systems.

## Outline of the Thesis

- Chapter 2 introduces the physics of strongly coupled plasmas with the particular focus being on dusty plasmas. The experimental realization of harmonically confined dust clusters is discussed. At the end of the chapter, a motivation is given for the development of an improved melting parameters which are suitable for spherically confined systems.
- Chapter 3 addresses the model for harmonically confined dust clusters in 2D and in 3D as the particular systems of interest. In addition to the model Hamiltonian, the system of dimensionless units is introduced which will be used throughout this work. The Metropolis Monte Carlo method is applied in order to sample the  $N$ -particle phase space distribution of a dust system in equilibrium efficiently. It is, therefore, briefly presented including the parallel tempering enhancement which allows exchanges between system replicas at different temperatures. As a second important numerical method, Langevin molecular dynamics (LMD) simulations are subject to this chapter. The LMD method will be used for the non-equilibrium simulation of a laser heated 2D cluster in chapter 6.
- Chapter 4 is devoted to the development of improved melting parameters for 3D confined dusty plasmas. It starts with a review of the Voronoi diagram as a topological scheme for identifying lattice structures and nearest neighbor particles. In 3D confined systems, the stereographic projection enables the calculation of these diagrams within a spherical shell. In the second part of the chapter, the center-two-particle (C2P) distribution function and the triple-correlation function (TCF) are introduced as structural parameters for spherically confined dust clusters. These two quantities are deduced from a universal concept of spatial  $n$ -particle distributions which are expressed in general coordinates. In order to identify a structural transition from the multi-dimensional distribution functions, the reduced entropy  $S^{(n)}$  is extracted as a measure of disorder.
- Chapter 5 presents the detailed results for the specific melting transitions in confined 3D dusty plasmas, using the parameters derived in Chap. 4. At the beginning, an extended 2D system is considered as a reference system for the TCF and the corresponding reduced entropy is computed as a novel melting parameter. Thereafter, structural transitions of circular 2D dust clusters are studied by the means of the C2P. The focus is on the inter-shell angular order and its stability against the twist of adjacent shells.

In the main part of this chapter, the different disordering processes in spherically confined dust balls are subject of interest. Monte Carlo simulations are applied in order to obtain their equilibrium properties over a temperature range that covers four orders of magnitude. Compared to planar 2D clusters, the particle configuration within a shell exhibits an additional degree of freedom giving rise to a more complex structure. This intra-shell structure is studied with the focus on disordering processes. This chapter closes with the investigation of the melting process in a system of charged particles on a Thomson sphere. Such a system represents the idealization of a spherical cluster shell with infinitesimal width, and suppressing the interaction with other shells.

- Chapter 6 is devoted to the laser excitation of 2D dust clusters with circular shape. This non-equilibrium experiment is modeled by Langevin molecular dynamics simulations. Different concepts of laser heating are compared with respect to the self-organized structure of the cluster and the dynamics of the excited dust grains. For the most elaborated heating method, an analytic estimation is derived for the equilibrium temperature of the dust. The second part of this chapter is concerned with a laser excitation scenario where the power input is restricted to the central region of the cluster. Fitting the radial temperature profile from the simulation by the analytics solution of a fluid model for the heat transport allows one to determine the thermal conductivity. Furthermore, also the influence of a magnetic field on the thermal conductivity is subject to the final part of the chapter.
- Chapter 7 summarizes the main results of this work.
- The appendix contains supplementary mathematic details. Moreover, the analytic estimation of the equilibrium dust temperature is compared to the numerical results in tables. Abbreviations used in this thesis are compiled in the final part of the appendix.



---

## Chapter 2

### Introduction



Within the broad field of plasma physics, this thesis focuses on complex structures in dusty plasmas. At the beginning of this chapter, strongly coupled systems are reviewed, and the Coulomb coupling parameter is introduced since it allows for quantifying the inter-particle interaction strength. The discussion of crystals formed by charged dust particles inside a plasma as the key subject of this thesis is followed by a review of the melting process interpreted as a loss of order. This disordering can be induced by different excitation mechanisms. The chapter closes with a motivation for new melting parameters in the context of finite dust clusters.

#### 2.1 Strongly Coupled Systems

A lot of physical phenomena can be described in theories, where the pair interaction of single particles is not modeled exactly. Such theories are typically very successful in describing fluids, e.g. Refs. [7–9], conventional plasmas, e.g. Refs. [10, 11], or the electron gas inside a metal, e.g. Refs. [12, 13]. A comprehensive presentation of fluid mechanics is for example given in Ref. [7].

However, strongly coupled systems are characterized by interaction energies which are large compared to the typical thermal energies. Since the strong coupling of individual particles dominates the behavior of the systems, the fluid approach fails to describe their physics accurately. A typical phenomenon of a strongly coupled system is a self-organization that leads to the formation of highly-ordered structures [14].

In conventional solid matter, as for example a salt crystal or iron, with lattice constants of a few ångström, the strong coupling is caused by the small inter-particle distances. The dynamical processes as, e.g., the oscillations of single atoms take place on very short timescales in the femtosecond regime. Small time and length scales make it very difficult to achieve spatiotemporally resolved measurements [11, 15].

Indeed, such time-resolved measurements on a single-particle level are possible in *dusty* or *complex* plasmas, where the high particle charge causes strong correlations. In addition to electrons, ions and neutral gas atoms, a dusty or complex plasma contains micrometer-sized

particles which are often referred to as dust. The plasma which surrounds the dust particles is commonly generated in a capacitively coupled radio frequency (rf) discharge. Argon and neon are typically used as inert operating gases at pressures between 0.5 Pa and 150 Pa. The radio frequency  $f_{\text{rf}} = 13.56$  MHz is widely used, and the input power ranges from a few up to several hundred watts, e.g. Refs. [16–20]. If the inert operating gas is mixed with a reactive gas such as acetylene, dust particles can be grown inside the plasma, e.g. Ref. [21].

The radio frequency is chosen way above the plasma frequency of the heavy ions but way below the plasma frequency of the light electrons, which is expressed by the ordering  $f_{\text{pi}} \ll f_{\text{rf}} \ll f_{\text{pe}}$ . This means that the response time of electrons is small compared to the rf period, and they can follow the electric field quasi-instantaneously. In contrast, the ions can be considered to be at rest during one rf period. The electron cloud is, in this picture, moved back and forth through the steady ion background. This mechanism results in electron temperatures of a few eV and significantly lower ion temperatures. A detailed description of this plasma heating process is for example given in Refs. [10, 22].

When immersed into such a plasma environment, the dust particles accumulate high negative charges due to the electron and ion impact. It is the high charge that causes the strong coupling at inter-particle distances on the order of micrometers at room temperature. The strongly coupled dust particles confined in a trap can form highly ordered structures which are referred to as *dust crystals*. A crystal formed of only a few up to several thousand particles is called (*finite*) *dust cluster*. These can be realized as planar 2D clusters with circular shape or as spherical 3D *dust balls*. Taking into account the pair-interaction potential of the dust grains, these clusters are also called *Coulomb balls* or *Yukawa balls*. Due to the relatively low specific charge (i.e., the charge per mass ratio) of the heavy dust grains compared to the electrons and the ions, their dynamics takes place on time-scales on the order of seconds.

Three properties render dusty plasmas ideal as model systems for studying strong coupling effects on a single-particle level: First, the comparatively large inter-particle distances and, second, the comparatively slow dynamics make it technically feasible to resolve single-particle trajectories [23]. The third convenient property is the low optical opacity of the dust clouds caused by the large inter-particle distances compared to the particle diameter. Thus, single particles can be resolved even for 3D dust clouds that contain millions of particles [24]. Elaborated imaging diagnostics in dusty plasmas are briefly discussed in Sec. 2.3.1.

## 2.2 Coupling Parameter

In order to characterize the coupling strength of a system, it is common practice to use the dimensionless *Coulomb coupling parameter*  $\Gamma$ . This parameter relates the typical Coulomb interaction energy of two adjacent particles to the thermal energy as

$$\Gamma = \frac{q^2}{4\pi\epsilon_0 a_{\text{WS}} k_{\text{B}}T}, \quad (2.1)$$

where  $a_{\text{WS}}$  denotes the Wigner-Seitz radius and  $q, T$  denote the charge and the temperature of a certain particle species. In a dusty plasma, these species are electrons, ions and dust particles.



For an extended system, the Wigner-Seitz radius is related to the density as

$$\pi a_{\text{WS}}^2 = n^{-1} \quad (2\text{D}) \quad \text{and} \quad \frac{4\pi}{3} a_{\text{WS}}^3 = n^{-1} \quad (3\text{D}), \quad (2.2)$$

where  $n$  describes the particle number density. It can be interpreted as the radius of the sphere (or circle in 2D) which is occupied by one particle. A system with a low coupling parameter  $\Gamma \ll 1$  is called *ideal* or *weakly non-ideal* while for  $\Gamma \approx 1$ , the system is called *non-ideal*. When the coupling parameter exceeds a value of roughly 100, the system is referred to as *strongly coupled* [11].

The same coupling parameter is capable to describe systems at very different conditions. In experiments, high coupling can be realized in different ways by controlling the three parameters temperature, density and charge. One possibility is to realize a low temperature as it is done in experiments with ultra-cold ions [25, 26]. Another realization of a strongly coupled system is represented by ionic systems at extremely high densities as, for example, the inside of white dwarfs [27]. Finally, in complex plasmas, the high coupling parameter of the dust component results from the high charges  $Q_d$  of the dust grains. These can be on the order of several (ten) thousand elementary charges and enter quadratically into  $\Gamma$ . At the same time, electrons and ions are commonly weakly coupled in a laboratory plasma. Besides their charges, also the temperatures of electrons, ions, neutrals and dust particles may differ because of the rf-heating mechanism.

For the dust grains, one can consider at least two different temperatures. On the one hand, their “kinetic” temperature  $T_d$  is assigned to their center-of-mass motion. In this thesis, the temperature of interest is always the kinetic temperature of the dust grains and the coupling parameter  $\Gamma$  refers to the ratio of the dust particles’ interaction energy and the thermal energy of their center-of-mass motion. A high coupling parameter  $\Gamma \gg 1$  is necessary for observing ordered dust crystals. On the other hand, every dust particle consists of approximately  $10^{12}$  melamine molecules. As such a solid body, the dust grains have a bulk temperature  $T_{\text{bulk}}$ , which is not subject to this work.

In a plasma, electric fields are generally screened by mobile charge carriers, i.e., electrons and ions. For this reason, the interaction of the dust grains is described by a Yukawa potential with a finite screening parameter  $\kappa$  rather than by the pure Coulomb potential. Equation (2.1) which defines the Coulomb coupling parameter then does not employ the correct interaction energy. The simplest approach towards a modified Yukawa coupling parameter  $\Gamma_Y$  is to multiply  $\Gamma$  by the exponential factor  $\exp(-\kappa)$ . However, different systems at the same modified coupling  $\Gamma_Y$  do not necessarily show similar behavior in general but can behave liquid-like or solid-like depending on the screening parameter  $\kappa$  [28–30].

VAULINA and KHRAPAK argued that the melting point of a crystal rather depends on the curvature of the energy landscape at the equilibrium positions of the dust particles than on the potential energy at these positions [29]. Hence, they considered a one-dimensional model in which one particle is caged in the middle between two other particles. For both, Coulomb and Yukawa interaction, they expanded the potential energy as a function of the position of the central particle up to the second order. The condition of equal local oscillation frequencies in

the potential minimum for both types of interaction allowed them to define

$$\Gamma_V \equiv \Gamma \cdot e^{-\kappa} \cdot \left(1 + \kappa + \frac{\kappa^2}{2}\right), \quad (2.3)$$

as a modified coupling parameter for Yukawa systems [29, 31]. While the melting curve of 3D systems is consistent with a constant value  $\Gamma_V$  for  $\kappa \leq 5$ , deviations are observed for 2D systems.

For this reason, various empiric scaling functions  $f(\Gamma, \kappa)$  have been applied by different authors in order to define a universal coupling parameter

$$\Gamma^* = f(\Gamma, \kappa) \cdot \Gamma \quad (2.4)$$

which is constant along the lines in  $(\Gamma, \kappa)$  parameter space with constant height of the pair distribution function's first peak [28, 30, 32–35].

For most of the dust clusters which are considered in the thesis at hand, the particles interact via a bare Coulomb potential. Moreover, the focus is not on the precise value of  $\Gamma$  but on its critical order of magnitude since the melting processes of finite clusters are characterized rather by broad melting regions than by sharp transition points. For this reason, the Coulomb coupling parameter  $\Gamma$  is used in the following to characterize the coupling strength in Yukawa systems as well. The  $\kappa$  dependence of the melting line is accepted for the benefit of a simple, unique definition of the coupling parameter.

## 2.3 Spherical Dust Clusters

As discussed in Sec. 2.1, the highly charged dust grains in a complex plasma can form well ordered structures. In extended dust clouds the particles typically arrange themselves in a Bravais lattice. A hexagonal lattice is formed in 2D [36], while both base centered cubic (bcc) and face centered cubic (fcc) lattices occur in 3D systems depending on the system parameters [37, 38].

Except for experiments with reactive plasmas where the dust particles are grown in situ, one can control the exact particle number  $N$  by adding single dust particles. The so prepared dust clusters with particle numbers ranging from a very few up to several hundred allow one to study finite size effects. Since all dust particles are negatively charged, their interaction is purely repulsive in general. It is therefore indispensable to set up an external potential in order to confine a finite dust cluster. For certain parameters, the ion focus causes an attractive inter-particle force.

### 2.3.1 Experimental Realization

In most cases, the ambipolar electric field in the plasma bulk is not strong enough to compensate the downward force of a dust grain with a diameter of several micrometers in the gravitational field of the earth. The dust grain will sink to the bottom of the plasma, where it is trapped by the strong electric field in the plasma sheath [10]. At the equilibrium position, the strong vertical confining potential results from the balance of gravitational force and upward

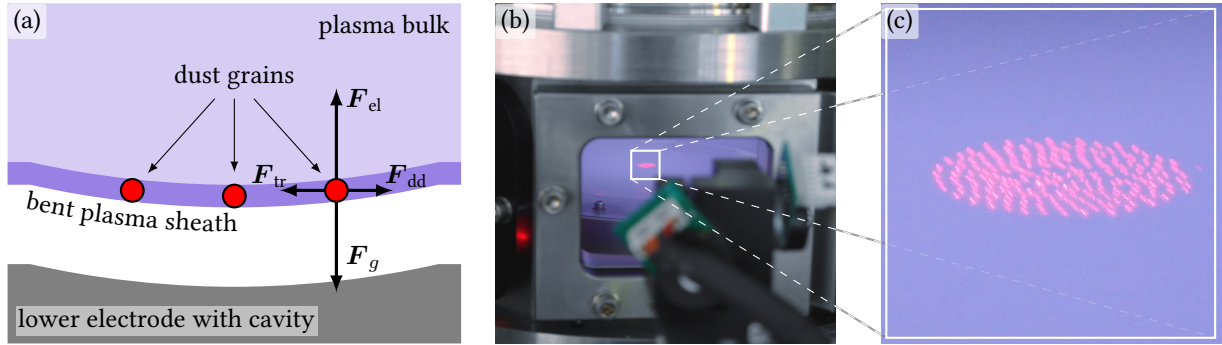


**Figure 2.1:** Finite 2D dust clusters. (a) The gravitational force  $F_g$  is compensated by the electric force  $F_{el}$  in the plasma sheath which is bent due to the cavity in the lower electrode. The particles are levitated in this “bowl” and subject to a trapping force  $F_{tr}$  that balances the dust interaction force  $F_{dd}$  within the plane. (b) View into the plasma chamber. The cluster is levitated above the lower electrode and illuminated by a red laser fan. (c) Closer view of the 2D dust cluster in the experiment. Photographic images kindly provided by J. Schablinski.

directed electric force. In order to create a finite 2D cluster, the remaining task is to set up a horizontal confinement. This can be achieved by the application of a lower electrode that has a cylindrical or spherical depression [39, 40]. The plasma sheath gets bent to a “bowl” in which the dust grains are confined. Since a small depth of the bowl is sufficient, the resulting particle arrangement can be treated as a finite, flat 2D cluster. An illustration of confining forces and photos of the experimental setup are shown in Fig. 2.1.

These 2D systems have been studied in great detail in several experiments and numerical simulations, e.g. Refs. [40–49]. For extended 2D dust crystals, a hexagonal particle order is found at high coupling. In contrast, small clusters with  $N \lesssim 100$  particles consist of several concentric rings (“shells”). The exact occupation numbers may have crucial impact on the stability of the cluster with respect to certain excitations such as, for example, inter-shell rotations [45, 50]. Confined clusters with larger particle numbers show a hexagonal structure in the central region, while the outer particles form shells reproducing the symmetry of the trap [41].

Additional effort is required in order to form a spherical dust ball in the plasma bulk, since gravitational force has to be eliminated or compensated. Dusty plasmas under microgravity were studied on parabolic flights and on the International Space Station (ISS) where 3D dust clouds with dust-free regions (voids) in the center could be observed [24, 51]. These voids are attributed to the outflow of ions from the plasma center, which exerts a drag force on the dust particles [1, 24, 52].

ARP *et al.* were the first to create a void-free spherical dust cluster in 2004 [1]. As in previous works [53, 54], ARP *et al.* applied a thermophoretic force to levitate the dust cluster within the plasma bulk. For this purpose, the lower electrode is heated and the resulting temperature gradient in the plasma causes an upward force on the dust grains. The dust cluster is formed within an open glass box or tube which is placed on the lower electrode. Much like the dust grains, the glass box becomes negatively charged and, hence, causes an inward electric force on the dust particles. The inward facing ion drag force in horizontal direction and electric force due to the charged glass box in combination with the thermophoretic and gravitational forces in vertical

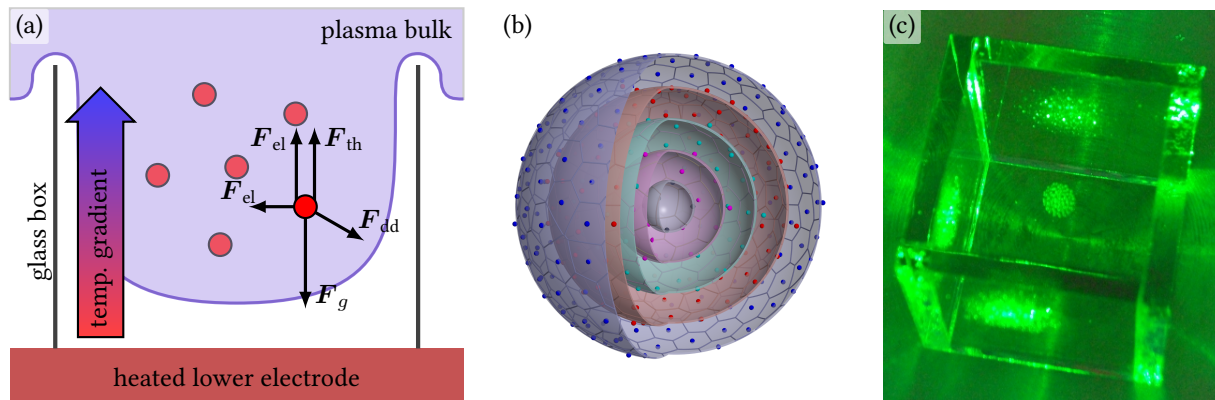


**Figure 2.2:** Spherical 3D dust clusters. (a) The lower electrode is heated in order to set up a vertical temperature gradient. Moreover, the plasma sheath is bent by a glass box which is placed on the electrode and becomes negatively charged. The gravitational force  $F_g$  is compensated by the combination of thermophoretic force  $F_{th}$  and an electric force  $F_{el}$  through the bent plasma sheath. An inward horizontal force  $F_{el}$  is mainly caused by the charged walls of the glass box. The highlighted particle is subject to an outward force  $F_{dd}$  due to the interaction with the other dust particles. After Ref. [19]. (b) Illustration of a 3D dust cluster with five nested spherical shells from a numerical simulation. A section of this Coulomb ball is masked for a better view. The particles are colored according to their shell affiliation and the intra-shell Voronoi grids are shown in gray. (c) Picture of a 3D dust cluster inside the cubic glass box from the experiment in Greifswald. Photographic image kindly provided by A. Schella.

direction allow one to realize an isotropic harmonic confinement potential [1, 19, 55, 56]. A sketch of the forces which act on the dust particles and illustrations of a dust cluster from simulation and experiment are shown in Fig. 2.2.

The clusters, which are trapped in this potential, exhibit an onion-like structure of nested shells [1, 57–60]. For certain parameters, one observes the formation of vertical particle strings. These strings are attributed to the ion focus that causes a non-reciprocal particle interaction [61, 62]. When two dust particles are aligned in a streaming plasma, the down-stream particle experiences an attractive force by the ion wake of the up-stream particle, while its own wake has minor influence on the up-stream particle [63]. The non-reciprocal interaction can result in unstable oscillations of the dust particle. This mechanism can transfer energy from the plasma environment into the dust subsystem [64, 65], and is called *Schweigert instability*. However, this thesis is concerned with systems in which the ion focus can be neglected.

Measuring the full 3D coordinates of all particles requires elaborated camera setups. An overview of the different methods is given by BLOCK and MELZER in Ref. [11]. The experimentally used techniques include scanning video microscopes [1, 66], the color gradient method [67, 68], stereoscopy setups with multiple optical axis [60, 69–73] as well as the digital holography [71, 74–76] and methods that combine the latter two [77, 78].

During the last decade, the ground and metastable states of spherical dust clusters as well as their dynamical properties were investigated in various experiments [60, 70, 79, 80], in computer simulations and analytical theories [57, 59, 79, 81–87]. Structural transitions and melting processes in these clusters are of particular interest [26, 81, 88].

Further experiments focused on the influence of an anisotropic confinement [50] as well as of wake effects of the streaming ions on the cluster configuration and on the dynamic properties [20, 61]. In recent MD simulations, APOLINARIO *et al.* investigated spherically confined binary dust Coulomb clusters with particles of two different species regarding their charges. Varying the charge ratio, they found a first order transition when the radial configuration changes from magic to non-magic due to minor charged particles which move from outer to inner shell [89]. In this connection, a cluster configuration is named *magic* when the shell-occupation numbers allow for a highly symmetric particle arrangement within the shells, cf. Sec. 5.2.2.

### 2.3.2 Coupling Parameter in Finite Dust Clusters

In the previous section, the Coulomb coupling parameter  $\Gamma$  was discussed as a measure of the interaction energy of adjacent particles in relation to the thermal energy. The Wigner-Seitz radius enters the definition of  $\Gamma$  as the typical inter-particle distance. However, the Wigner-Seitz radius is strictly defined only for extended systems with a homogeneous number density  $n$ .

While the density is constant for 3D Coulomb balls, harmonically trapped 2D clusters as well as 3D Yukawa balls have an inhomogeneous density in general [59]. One possibility to define  $\Gamma$  is to use the average density  $\bar{n} = 3N/(4\pi R_C^3)$  in 3D ( $\bar{n} = N/(\pi R_C^2)$  in 2D), where  $R_C$  describes the radius of the cluster. However, this approach involves the definition of a meaningful radius of the cluster which can be difficult, especially for small clusters. To name two possible definitions, the position of the last peak in the radial density can be used as  $R_C$ , or one half of the radial inter-shell spacing can be added. Depending on its definition,  $R_C$  may also depend on the temperature itself since the radial density is smeared out when the temperature grows. A coupling parameter defined this way is unsuited as an input parameter for numerical simulations. Since the trap frequency  $\omega_0$ , the dust charge  $Q_d$  and the dust mass  $m_d$  fix the typical pair distance in a cluster, one can deduce a characteristic length  $r_0 = \sqrt[3]{Q_d^2/(4\pi\epsilon_0 m_d\omega_0)}$  from these three parameters. This length follows from the equilibrium position of two Coulomb interacting particles in the harmonic trap. Moreover, this definition becomes equivalent with the Wigner-Seitz radius for large 3D Coulomb balls [59].

As discussed below in Sec. 3.2.1, one can also define an intra-shell Wigner-Seitz radius by dividing the surface of a spherical shell into  $N_s$  spherical caps, where  $N_s$  is the number of particles on the shell. The deviation between this length scale for the inter-particle spacing and  $r_0$  is typically below 10 % for Coulomb balls.<sup>1</sup> As the occupation number  $N_s$  of a certain shell and its radius  $R_s$  are *a priori* unknown, the intra-shell coupling parameter is not suitable as an input parameter for the coupling strength in numerical simulations of spherical dust clusters.

In this thesis, the length  $r_0$  is applied to define the coupling parameter  $\Gamma$  for Coulomb and Yukawa clusters in 3D as well as in 2D. The conversion of  $\Gamma$  to definitions which involve a different length scale is readily executed via multiplication by a factor which is of the order of unity.

<sup>1</sup>Considering the Coulomb ball with  $N = 80$  particles at strong coupling  $\Gamma = 1000$  as an example, the outer shell has a radius  $R_s = 3.588 r_0$  and is occupied by  $\langle N_s \rangle = 59.22$  particles on average. The intra-shell Wigner-Seitz radius is calculated as  $a_{\text{WS}}^{\text{is}} = 0.935 r_0$ , cf. Eq. (3.10) on page 24.

## 2.4 Experiments with Laser-Heated Clusters

In a typical laboratory dusty plasma experiment, the coupling parameter of the dust particles is very high,  $\Gamma \gtrsim 500$ . On the one hand, this is a key feature of these systems allowing one to examine strong correlation effects without cooling effort. The study of melting and structural transitions, on the other hand, requires a possibility to reduce the coupling parameter in a controlled manner. In first experiments, the plasma crystal was melted by changing the plasma parameters, namely rf-power [90] and neutral gas pressure [17, 91]. The heating effect is mainly based on the Schweigert instability [64, 65]. This method has the disadvantage that the parameter changes can have a sophisticated impact on all dust properties like the dust charge, the neutral gas friction, the mean particle distance and the confining electric forces as well as on the particle interaction potential.

Studying the temperature dependence of either static or dynamic properties of a dust cluster makes it preferable to alter the kinetic temperature, which is associated with the random motion of the dust particle as a whole, keeping all other plasma parameters constant. The concept of transferring momentum from a laser beam to the dust particles has already been used in early dusty plasma experiments [92–96]. In early experiments, the most that could be done to the laser beams was the interruption by an optical chopper. In modern experiments, galvanometer mirrors are used to move the laser spot across the cluster [4, 5, 97].

The momentum is transferred from the laser light to a mesoscopic dust particle due to the radiation pressure. Laser powers of a few hundred milliwatts are sufficient to induce a significant heating effect and powers up to a few watts are used in elaborate setups [40]. The modest laser power is too low to have significant influence on the surrounding plasma and on the neutral gas allowing to manipulate the dust particles selectively.

## 2.5 Melting as Loss of Order

Melting processes are always closely linked to the loss of a certain spatial order [98, 99]. During the phase transition from the crystalline state to the liquid-like state of an extended dust cluster, the long-range spatial order is lost. Below a critical temperature, the dust grains of the 2D system arrange themselves in a highly-ordered crystalline structure forming a hexagonal lattice. At higher temperatures, this lattice is destroyed and a disordered arrangement is observed.

The Voronoi diagrams shown in Fig. 2.3 illustrate the loss of spatial order during the melting process in a 2D extended dust crystal. These diagrams are appropriate for identifying the nearest neighbors, cf. Sec. 4.1. Deep in the solid phase, every particle has six nearest neighbors as indicated by the hexagonal Voronoi cells colored in blue, Fig. 2.3(a). A particle is referred to as a defect when it has more or less than six neighbors. When in the solid phase, these defects appear as pairs with equal number of pentagonal and heptagonal Voronoi cells, Fig. 2.3(b). Due to this pairing, the global bond order persists. Finally, threads of defects pervade the entire system in the liquid phase, Fig. 2.3(c,d) and it becomes impossible to state a crystal direction. The global bond order is lost and, since all Voronoi cells are clearly deformed, the local bond order is also lost.

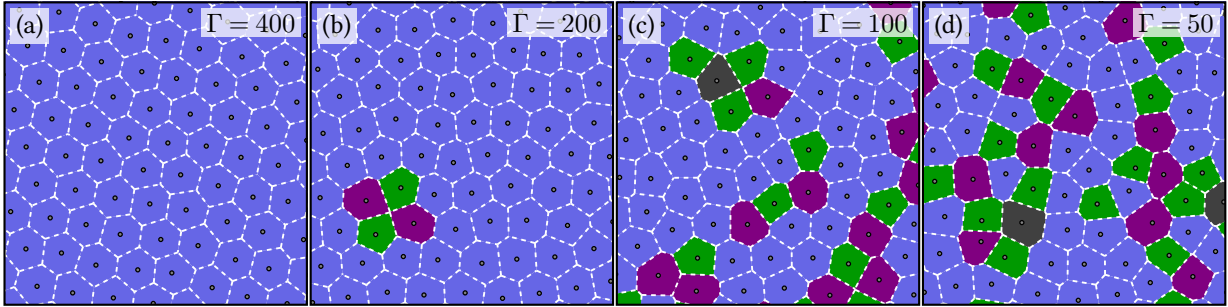


**Figure 2.3:** Cropped Voronoi diagrams of an extended 2D Yukawa ( $\kappa = 1$ ) crystal at different temperatures. The particle positions (circles) were obtained in a Monte Carlo simulation with parallel tempering enhancement and periodic boundary conditions, cf. Sec. 3.2. As the temperature increases from left to right, the phase transition takes place between panel (b) and (c) at  $\Gamma_m = 187$ . The color of a Voronoi cell corresponds to the coordination number  $n$  of the particle, i.e. the number of neighboring particles: green for  $n = 5$ , blue for  $n = 6$ , violet for  $n = 7$  and dark gray for  $n = 8$ . The dashed white lines show the border of the Voronoi cells.

Without going into the details of the melting process, this example showed how the melting process can be understood as a loss of order. Although one can easily identify solid, (a,b), and fluid phase, (c,d), in Fig. 2.3, the quantitative analysis of the melting process demands a more rigid melting criterion.

## 2.6 Motivation for new Melting Parameters

While the order of an extend 2D system is well described by a hexagonal lattice in the solid phase, and the melting process is characterized by emerging defects in this lattice, the melting process of spherical dust balls is more complex. The ground state of such a cluster consists of several nested onion-like shells [1, 57–60] which are almost spherical. Within these shells, the particle arrangement with the lowest energy is closely linked to the Thomson problem [100]. While for a large number of particles on a shell, the intra-shell structure is dominated by hexagonal Voronoi cells [1, 55, 101], a finite number of particles must have a lower coordination number due to the curvature of the sphere. For this reason, the particles with five nearest neighbors cannot be treated as lattice defects in general. At least four transition mechanisms are important for these spherical clusters [56, 89, 102–104]:

- The **radial melting** takes place at a coupling strength on the order of  $\Gamma_{RM} = \mathcal{O}(100)$ . During this process, the radial structure with distinct shells is lost. Although a radial modulation of the density persists, the occupation number of a shell is no longer strictly defined in the radially molten phase due to the overlapping shells. While the radial density between two shells is virtually zero in the solid phase, a significant density is found for all radii in the molten phase.
- Depending on the total particle number  $N$ , **inter-shell transitions** may occur at significantly higher coupling strength  $\Gamma_{RT} > \Gamma_{RM}$ . During this process one particle moves

from one shell to another. This results in changed shell occupation numbers and therefore a different *radial isomer* is realized. Since the particle transitions are rare events, they have virtually no impact on the radial density between the shells. For example for the 3D Coulomb cluster with  $N = 60$ , only the (48-12-0) radial isomer is found at high coupling  $\Gamma \gtrsim 500$ . This radial isomer is characterized by 48 particles on the outer shell, twelve particles on the inner shell and no particle in the center. When lowering the coupling strength, the (47-12-1) isomer dominates while the radial density is still separated in narrow shells.

- The particle arrangement within one spherical shell is subject to **intra-shell structural transitions**. In the ground state of a 3D cluster, typically twelve particles<sup>2</sup> have pentagonal intra-shell Voronoi cells while the remaining particles have hexagonal Voronoi cells. This is a result of the curvature of the sphere, and hence the pentagonal cells are not treated as lattice defects. *Intra-shell isomers* can differ by the arrangement of pentagonal, hexagonal and higher order Voronoi cells as well as by the numbers of those cells. While the transition between ordered and totally disordered intra-shell structure typically takes place at a coupling strength that is similar to the critical value for radial melting, transitions between different intra-shell isomers can occur at significantly higher coupling strengths. On the one hand, an inter-shell transition causes necessarily a change of the intra-shell order of the involved shells. On the other hand, at transition between two intra-shell isomers can occur without effecting the radial configuration.
- The **inter-shell angular disordering** process is well known from circular 2D clusters where the shells are rings. When the occupation number of a shell matches the occupation number of an adjacent shell, the relative angle of the two shells is locked at high coupling. Below a critical coupling strength  $\Gamma_{IS}$ , the thermal energy is sufficient to twist the two shells relative to each other. The critical coupling strength for this kind of transition is heavily influenced by the exact occupation numbers of the shells. For example for the 2D Coulomb cluster with  $N = 19$  particles in total, the ground state configuration is (12-6-1) [43]. The inner shell with six particles can perfectly interlock the outer shell with twelve particles which causes a very high stability against the inter-shell angular disordering.

Even though the particle arrangement on spherical shells is much more complex compared to rings, an interlock of adjacent shells may occur for certain particle numbers. Since the two shells can be twisted along a path in the two dimensional plane of the twist angles  $\vartheta$  and  $\varphi$ , the critical coupling strength for such a transition is expected to be very high.

The compilation of these disordering processes can be interpreted as a road map for choosing an appropriate melting parameter. Such a parameter should include the ability to distinguish the different processes. Commonly used parameter such as the specific heat capacity [105], the radial pair distribution function (PDF) [28, 34, 35] and Lindemann-like parameters [106–108]

<sup>2</sup>The number of pentagonal Voronoi cells in the ground state may deviate from twelve when there are particles with less than five or more than six neighbors, cf. Eq. (4.12) in Sec. 4.1



exhibit weaknesses in this context. In particular, the radial PDF cannot distinguish between particle pairs within the same shell and those with particles from different shells [6].



---

## Chapter 3

# Model System and Simulation Methods

**I**n this chapter, the model system for dust clouds in complex plasmas is considered as well as simulation techniques for these systems. The first section reviews the one-component model for the dust grains. In this model, the light species in the plasma are included statistically by their overall effect while the heavy dust particles are described by their Hamilton function. Finite spherically confined dust clusters in 3D as well as harmonically confined 2D dust clusters are of special interest in this thesis. Therefore, these two systems are presented in detail and the assumptions for the computer simulations are discussed. Prior to discussing the computational method, a system of dimensionless units suited for harmonically trapped clusters and the representation of the Hamiltonian in these units are reviewed. Since different sets of dimensionless units are widely used in the dusty cluster community, three important systems of units are listed.

The latter part of this chapter is concerned with Metropolis Monte Carlo (MC) and molecular dynamics (MD) simulations as two very important computational methods. For MC simulations, the adaptation for infinitesimally thin spherical shell as well as the parallel tempering enhancement are discussed. The description of a pure MD integration scheme is followed by a short review of Langevin molecular dynamics (LMD) simulations which allow for including the interaction with the background gas statistically.

### 3.1 Model for Charged Dust Grains

Dusty plasmas are distinguished from conventional plasmas by the presence of micrometer-sized particles. These particles are referred to as dust grains. Neutral gas atoms, electrons and ions are all much lighter than these mesoscopic dust grains and their dynamics take place on time scales which are several orders of magnitude below the time scale of the dust system. Due to this great difference in the time scales, an exact simulation of all plasma constituents is still beyond reach.

In the following, the structure and the dynamics of the dust sub-system are considered. Both kinds of free charges in the plasma, electrons and ions, screen electric fields. Under typical laboratory plasma condition, an initially neutral dust particle gets negatively charged up to a

charge  $Q_d$ . The charge  $Q_d$  ranges from a few hundred up to several (ten) thousand elementary charges and depends on the particle radius  $r_d$  among other parameters. Inside the plasma, the electron density around this particle is locally decreased while the ion density is increased. This screening effect can be taken into account in the *Debye screening model* [10, 109], where the interaction of two equally charged grains separated by  $\mathbf{r}_{(ij)} = \mathbf{r}_{(j)} - \mathbf{r}_{(i)}$ <sup>1</sup> is described by

$$\Phi_Y(\mathbf{r}_{(i)}, \mathbf{r}_{(j)}) = \frac{Q_d^2}{4\pi\epsilon_0 |\mathbf{r}_{(ij)}|} \cdot e^{-\kappa|\mathbf{r}_{(ij)}|}. \quad (3.1)$$

While this so-called *Yukawa* [110] or *Debye-Hückel* potential is isotropic, streaming plasmas can lead to highly anisotropic potentials with oscillatory wake structures [61, 111, 112]. However, these streaming plasmas are not subject of the thesis at hand, and an isotropic, monotonic pair potential is considered in the following. In contrast to the bare Coulomb interaction potential, Eq. (3.1) contains a length scale via the screening parameter  $\kappa$ . This length scale is the Debye length  $\lambda_D$  and consists of contributions from electrons and ions as

$$\lambda_D = \frac{1}{\kappa} = \left( \frac{\bar{n}_e e^2}{\epsilon_0 k_B T_e} + \frac{\bar{n}_i Z_i^2 e^2}{\epsilon_0 k_B T_i} \right)^{-1/2}, \quad (3.2)$$

where  $\bar{n}_e$  ( $\bar{n}_i$ ) is the unperturbed electron (ion) density and  $T_e$  and  $T_i$  are the temperatures of electrons and ions, respectively. Both temperatures coincide in thermodynamic equilibrium. However, the radio-frequency (rf) heating mechanism causes a plasma state in which the electrons are hotter than the ions. While the light electrons follow the rf field, the heavier ions stay at rest since their plasma frequency  $\omega_i$  is below the rf frequency [10, 22]. The ions are only heated indirectly by collisions with the fast electrons. Therefore, different temperatures for the electrons and the ions have to be considered. In Eq. (3.2), only one single species of ions with charge number  $Z_i$  is taken into account, but the expression can easily be extended to several ion species by replacing the second summand by a sum over all these species.

Throughout this work,  $\kappa$  is used as an input parameter for the simulations, and its detailed dependence on the plasma parameters is not subject to the used model. One can readily verify that the Yukawa potential, Eq. (3.1), includes the Coulomb potential as special case with zero screening parameter,  $\kappa = 0$ . This case corresponds either to dilute plasmas with low charge carrier densities or plasmas with high electron and ion temperatures.

Since the interaction of the dust particles is purely repulsive, an external confinement is necessary in order to realize a finite dust cluster. This confinement is commonly provided as a harmonic trap with trap frequency  $\omega_0$ .

The Hamiltonian of a harmonically confined finite cluster with  $N$  equally charged, monodisperse dust particles then reads as

$$\mathcal{H} = \frac{1}{2m_d} \sum_{i=1}^N \mathbf{p}_{(i)}^2 + \frac{m_d \omega_0^2}{2} \sum_{i=1}^N \mathbf{r}_{(i)}^2 + \frac{Q_d^2}{4\pi\epsilon_0} \sum_{i=1}^{N-1} \sum_{j=i+1}^N \frac{1}{|\mathbf{r}_{(ij)}|} e^{-\kappa|\mathbf{r}_{(ij)}|}. \quad (3.3)$$

<sup>1</sup>Notation: In order to distinguish particle indices from the coordinate indices in higher-order distribution functions, the single-particle indices are written in parentheses.

The interaction with the background gas via frequent collisions or with manipulations lasers via radiation pressure is not included in this “unperturbed” Hamiltonian. While the former is modeled by a friction term and a random force in Langevin molecular dynamics (LMD) simulations or by the temperature in Monte Carlo (MC) simulations, the latter one is handled as an additional time and space-dependent force in LMD, see Chap. 6.

### 3.1.1 Finite 2D Dust Clusters

Among finite crystals, the 2D dust clusters have been investigated first, starting in the late 1990s [41–46]. As the heavy dust particles typically fall through the plasma bulk and sediment in the lower sheath where strong electric fields compensate the gravitational force, these particles can form a monolayer crystal. In order to realize an isotropic trap in two dimensions, a lower electrode with a parabolic depression is widely used, e.g [40, 45, 113]. The plasma sheath in which the dust grains are confined follows the shape of the lower electrode and the dust grains are horizontally trapped in this “bowl”. Another possibility to shape a horizontal confinement is to use a lower electrode with a cylindrical depression as for example in Ref. [39] or to place an metallic barrier on top of the electrode that bends the equipotentials [10].

Since already a shallow bowl allows for a sufficiently strong confinement in horizontal direction [10], the depth of depression is neglected in the model. Moreover, the vertical confinement is very strong compared to one in the horizontal direction. For this reason, both the vertical width of the cluster and the vertical motion are disregarded in the following. The combination of the low bend and the very small width the cluster justifies considering a strictly flat cluster which is described in 2D coordinates. In the vector notation, the Hamiltonian (3.3) has the same form as for spherical clusters, but all vectors are 2D, here.

### 3.1.2 Extended 2D Dust Clusters

Throughout this thesis, extended 2D systems are considered in order to test novel melting parameters in a system where the melting behavior is well understood. This system is described by the Hamiltonian (3.3) without the harmonic confinement potential ( $\omega_0 = 0$ ).

Since these systems are only considered marginally, a very simple Monte Carlo code is used for the simulations. A rectangular simulation cell with periodic boundary conditions is utilized. Every particle interacts with all neighbors in the original simulation cell as well as with the imaged particles in the periodically repeated cells. Whenever a particle leaves the simulation box at one side, it enters it at the opposite side. Since only the Yukawa case with a finite screening parameter  $\kappa > 0$  is treated, the interaction potential decays fast and a cutoff radius  $d_{\max}$  is introduced. The interaction energy is only calculated for particle pairs with a distance up to  $d_{\max}$ . The fast decay of the interaction potential allows to renounce more complex simulation techniques as for example the Ewald summation [114].

### 3.1.3 Spherical Dust Balls

As described in the introduction, realizing an isotropic 3D confinement is more complex. Here, the dust grains can be horizontally trapped by placing a glass box on the lower electrode. The walls of the box become negatively charged and provide a repelling electric field. A thermophoretic force is utilized to realize a harmonic confinement in vertical direction.

In general, the confinement strength is isotropic due to the different mechanism for the vertical and the horizontal trapping. This can be model by specifying three different trap frequencies  $\omega_x$ ,  $\omega_y$  and  $\omega_z$  for the three spatial directions. Choosing the vertical confinement frequency  $\omega_z$  lower or higher than the horizontal frequencies results in vertically elongated or vertically compressed clusters, respectively [61].

However, a careful adjustment of the thermophoretic force allows for tailoring an isotropic harmonic confinement. In this thesis, this ideal case is considered, and the confinement potential is therefore modeled by one scalar trap frequency  $\omega_0$  in the Hamiltonian (3.3).

### 3.1.4 Dimensionless System of Units

It is due to universal scaling laws in the Hamiltonian (3.3) that different systems behave equally when scaling the energy, the length and the time. Hence, the system can be described by only three parameters, namely the particle number  $N$ , the screening parameter  $\kappa$  and the coupling parameter  $\Gamma$  as a measure for the ratio of the thermal energy and the typical interaction energy.

At least three different systems of units are widely used in the dusty plasma community for the dimensionless description of lengths, energies, times and deduced qualities like forces or pressures in clusters of harmonically confined dust particles interacting via a Yukawa potential or a Coulomb potential as a special case [11, 31, 88, 103]. These three systems of units are presented in Tab. 3.1. All three systems of units have in common that the Hamiltonian  $\mathcal{H}$ , Eq. (3.3), of the dust systems gets a very handy form.

Throughout this thesis, the  $\sim$ -system of units is used for all calculations. Besides the “natural” appearance of the Hamiltonian with the factors  $\frac{1}{2}$  in front of the quadratic terms which describe the harmonic confinement and the kinetic energy, this system has the advantage that the unit of length  $\tilde{r}_0$  is equivalent to the Wigner-Seitz radius for large Coulomb balls, as shown by HENNING *et al.* [59]. Therefore, the inverse temperature in these units is a well suited representative of the Coulomb coupling parameter for finite systems.

Provided that there is no likelihood of a confusion, the  $\sim$  is dropped in the following for a better readability. The conversion of a certain quantity like energy or length between different systems of units involves the multiplication by a factor which is of the order of unity. Since these factors depend on source and target system of units as well as on the quantity, a conversion table is given in Tab. 3.2.

	$\sim$ -units	*-units	$\dagger$ -units
length $r_0$	$\tilde{r}_0 = \left( \frac{Q_d^2}{4\pi\epsilon_0 m_d \omega_0^2} \right)^{1/3}$	$r_0^* = \left( \frac{2 \cdot Q_d^2}{4\pi\epsilon_0 m_d \omega_0^2} \right)^{1/3}$	$r_0^\dagger = \left( \frac{2 \cdot Q_d^2}{4\pi\epsilon_0 m_d \omega_0^2} \right)^{1/3}$
energy $E_0$	$\tilde{E}_0 = \left( \frac{m_d \omega_0^2 Q_d^4}{(4\pi\epsilon_0)^2} \right)^{1/3}$	$E_0^* = \left( \frac{m_d \omega_0^2 Q_d^4}{2 \cdot (4\pi\epsilon_0)^2} \right)^{1/3}$	$E_0^\dagger = \left( \frac{m_d \omega_0^2 Q_d^4}{2 \cdot (4\pi\epsilon_0)^2} \right)^{1/3}$
time $t_0$	$\tilde{t}_0 = \omega_0^{-1}$	$t^* = \sqrt{2} \cdot \omega_0^{-1}$	$t^\dagger = \omega_0^{-1}$
Hamilt. $\mathcal{H}$	$\mathcal{H} = \frac{1}{2} \sum_i \mathbf{p}_{(i)}^2 + \frac{1}{2} \sum_i \mathbf{r}_{(i)}^2$ $+ \sum_{i<j} \frac{1}{ \mathbf{r}_{(ij)} } e^{-\kappa \mathbf{r}_{(ij)} }$	$\mathcal{H} = \frac{1}{2} \sum_i \mathbf{p}_{(i)}^2 + \sum_i \mathbf{r}_{(i)}^2$ $+ \sum_{i<j} \frac{1}{ \mathbf{r}_{(ij)} } e^{-\kappa \mathbf{r}_{(ij)} }$	$\mathcal{H} = \sum_i \mathbf{p}_{(i)}^2 + \sum_i \mathbf{r}_{(i)}^2$ $+ \sum_{i<j} \frac{1}{ \mathbf{r}_{(ij)} } e^{-\kappa \mathbf{r}_{(ij)} }$

**Table 3.1:** Common systems of units. Note that the only differences in the Hamiltonian are the factors  $\frac{1}{2}$  in front of the harmonic confinement term  $\mathbf{r}_{(i)}^2$  and in front of the term  $\mathbf{p}_{(i)}^2$  for the kinetic energy. The unit of mass is always the mass of one dust grain  $m_d$ . The units for other quantities such as force can be derived from these units.

## 3.2 Metropolis Monte Carlo

This section gives a brief introduction to the Metropolis Monte Carlo (MC) method used in this thesis. The thermodynamic state of a system with contact to a heat bath is described by three variables: the number of particles in the system  $N$ , the volume  $V$  and the temperature  $T$ . For harmonically confined clusters, the role of the volume  $V$  is taken by the trap frequency  $\omega_0$ . The microstates of such a system are represented by the *canonical ensemble*  $(N, \omega_0, \Gamma)$  where the temperature is described by the coupling parameter  $\Gamma$ , cf. Sec. 2.3.2. The central quantity in statistical mechanics is the *canonical partition function*  $Z$ . For a classical system with non-degenerate microstates  $s$ , the partition function is defined as the sum of possible microstates weighted by the *Boltzmann factor* which decays exponentially with the energy of the state  $E_s$  in units of the thermal energy,

$$Z = \sum_s e^{-\frac{E_s}{k_B T}} = \frac{1}{N!(2\pi\hbar)^{3N}} \int d^{3N} \mathbf{P} \int d^{3N} \mathbf{R} e^{-\frac{\mathcal{H}(\mathbf{P}, \mathbf{R})}{k_B T}}. \quad (3.4)$$

While the first equality in this equation is valid for any kind of microstates, the second equality presumes a *classical system with  $N$  identical particles*. The configuration sum is replaced by a configuration integral over the momenta  $\mathbf{P}$  and positions  $\mathbf{R}$  of all particles. This replacement requires the division by  $(2\pi\hbar)^{3N}$  as the *phase space volume* of a single microstate. The *Gibbs factor*  $1/N!$  compensates the multi counting of identical states because of the indistinguishability of the particles.

**Table 3.2:** Conversion table between different systems of units. A quantity in the source system of units has to be multiplied or divided by the factor given in this table in order to obtain the value of this quantity in the target system of units. The conversion factor for other deduced units is obtained by multiplication of the single conversion factors.

		source system of units		
		$\sim$	*	†
target system of units	$\sim$	$l$	$\times \sqrt[3]{2}$	$\times \sqrt[3]{2}$
		$E$	$\div \sqrt[3]{2}$	$\div \sqrt[3]{2}$
		$t$	$\times \sqrt{2}$	$\times 1$
	*	$l$	$\div \sqrt[3]{2}$	$\times 1$
		$E$	$\times \sqrt[3]{2}$	$\times 1$
		$t$	$\div \sqrt{2}$	$\div \sqrt{2}$
	†	$l$	$\div \sqrt[3]{2}$	$\times 1$
		$E$	$\times \sqrt[3]{2}$	$\times 1$
		$t$	$\times 1$	$\times \sqrt{2}$

The equilibrium properties such as internal energy  $U$ , Boltzmann entropy  $S$  or heat capacity  $C_V$  are accessible through  $Z$  which is connected to the discrete probability distribution of microstates as

$$\mathcal{P}(s) = \frac{1}{Z} e^{-\frac{E_s}{k_B T}}, \quad \text{or as} \quad \mathcal{P}(\mathbf{P}, \mathbf{R}) = \frac{1}{N!} \frac{1}{Z} e^{-\frac{\mathcal{H}(\mathbf{P}, \mathbf{R})}{k_B T}}, \quad (3.5)$$

for the continuous phase space distribution. The momentum part of the partition function is readily solved analytically by factorization for the classical Hamiltonian (3.3) since it does not contain any velocity-dependent interactions. In contrast, the spatial part of  $Z$  cannot be solved analytically in general as the factorization into one-dimensional integrals is impossible due to the interaction terms.

A Metropolis MC algorithm provides a possibility to generate a sequence of microstates  $\{\mathbf{R}_1, \mathbf{R}_2, \dots\}$  distributed according to Eq. (3.5) without explicit knowledge of the partition function  $Z$ . Except for the sequence of random numbers and the acceptance probability of the updates, the generation of a new state  $\mathbf{R}_j$  is based on no further information than on the knowledge of the previous state  $\mathbf{R}_i$ . Such a sequence is called a *Markov chain* of states. The algorithm works as follows [115]:

- (1) Start with randomly chosen initial positions  $\mathbf{R}_0$ .
- (2) Choose a particle  $i$  randomly and propose a random displacement  $\Delta \mathbf{r}$  (MC move).
- (3) Accept the MC move with probability  $\mathcal{P}_{\text{acc}}$ .
- (4) Repeat (2) and (3) about as often as there are particles in the system (MC step).
- (5) Perform a measurement.
- (6) Start the next MC step at (2).



The proposed displacement  $\Delta\mathbf{r}$  does not depend on the initial state and moreover the inverse displacement  $-\Delta\mathbf{r}$  is proposed with the same probability. Therefore, the correct distribution of the generated states is guaranteed for this algorithm by an acceptance probability between two states,  $P_{\text{acc}}$ , that fulfills the *detailed balance condition*

$$\mathcal{P}(\mathbf{R}_i) \cdot \mathcal{P}_{\text{acc}}(\mathbf{R}_i \rightarrow \mathbf{R}_j) = \mathcal{P}(\mathbf{R}_j) \cdot \mathcal{P}_{\text{acc}}(\mathbf{R}_j \rightarrow \mathbf{R}_i), \quad (3.6)$$

where  $\mathcal{P}_{\text{acc}}(\mathbf{R}_i \rightarrow \mathbf{R}_j)$  describes the probability to accept the move from a microstate  $\mathbf{R}_i$  towards a microstate  $\mathbf{R}_j$ . The probability  $\mathcal{P}(\mathbf{R})$  from Eq. (3.5) is inserted. When forming the ratio of the two acceptance probabilities, the partition function cancels and the expression

$$\frac{\mathcal{P}_{\text{acc}}(\mathbf{R}_i \rightarrow \mathbf{R}_j)}{\mathcal{P}_{\text{acc}}(\mathbf{R}_j \rightarrow \mathbf{R}_i)} = \frac{e^{-\frac{\mathcal{H}_R(\mathbf{R}_j)}{k_B T}}}{e^{-\frac{\mathcal{H}_R(\mathbf{R}_i)}{k_B T}}} = e^{-\frac{\Delta E_{ij}}{k_B T}} \quad (3.7)$$

remains as a condition for a valid acceptance probability. An appropriate acceptance probability,

$$\mathcal{P}_{\text{acc}}(\mathbf{R}_i \rightarrow \mathbf{R}_j) = \begin{cases} 1 & : \Delta E_{ij} \leq 0 \\ e^{-\frac{\Delta E_{ij}}{k_B T}} & : \Delta E_{ij} > 0 \end{cases}, \quad (3.8)$$

was proposed by METROPOLIS *et al.* in 1953 [115]. This choice was used for all MC results presented in this thesis. An MC move which decreases the total energy of the system is always accepted while a move that increases the total energy is only accepted with a certain probability  $\mathcal{P}_{\text{acc}} < 1$  that depends on the temperature. It is essential for the simulation in the canonical ensemble to accept a certain fraction of the latter moves. If all these moves would be rejected, the total energy could only decrease and the simulation would be trapped in a local energy minimum after a short sequence of MC steps.

Every MC step involves up to  $5N$  random numbers for the choice of a particle, the proposal of a 3D displacement and the decision of whether the move is accepted or not. The MC simulation of a cluster with  $N = 100$  particles at  $N_T = 81$  different temperatures in parallel, see Sec. 3.2.2, and  $M_{\text{step}} = 50 \times 10^6$  MC steps per temperature value involves approximately  $N_{\text{ran}} = 2 \times 10^{12}$  random numbers in total. Since the period of the (*pseudo*) random number generator (RNG) has to be large compared to the number of used random numbers  $N_{\text{ran}}$ , simple linear congruential RNGs are not suitable. Moreover, these RNGs have poor statistical properties. For these reasons, the Mersenne Twister [116] of the GNU Scientific Library (GSL)<sup>2</sup> is used for the simulations in this thesis. The Mersenne Twister has a period of  $N_{\text{MT19937}} = 2^{19937} - 1 \approx 10^{6000}$  and good statistical properties as it passed the DIEHARD statistical tests [116]. In order to combine the demand of reproducibility of the MC simulations with the comfort of an automatically generated seed, the seed for the RNG can either be given in the input file or it is quasi-randomly chosen utilizing the exact value of the system clock. The used seed is then stored together with the output data to provide the possibility to run the simulation again with exactly the same random numbers.

<sup>2</sup><http://www.gnu.org/software/gsl>

### 3.2.1 Metropolis Monte Carlo for Spherical Shells

The MC sampling algorithm is suited for adaptation to different geometries. In this paragraph the adaptation for an infinitesimally thin spherical shell is presented. Such a system is of interest in order to resolve pure intra-shell correlations without any effects that result from the interaction with other shells or from the finite shell width in spherical clusters.

The spherical system is presented by  $N_s$  particle positions on the unit sphere. This is always equivalent to a spherical system with radius  $R_s$  when rescaling the length and the energy. Except for the finite temperature, this setup describes the generalized Thomson problem [100], i.e., finding the ground state of  $N_s$  particles with a repulsive pair interaction and with the holonomic constraint  $|\mathbf{r}_{(k)}| = k$  for all particles  $k$ .

The MC algorithm is modified in the following way: After addition of a three-dimensional random displacement  $\Delta\mathbf{r}$ , the new particle position is in general not within the spherical surface. Therefore, it is projected back onto the sphere by normalization of the new position vector, before the energy difference  $\Delta E_{ij}$  between the new and the old configuration is calculated in order to decide whether the MC move is accepted or rejected. Since the MC algorithm involves only the potential energy, which is calculated from the particle positions, the projection onto the sphere in every move is unproblematic.

In order to ensure that the detailed balance condition is not violated, the displacement  $\mathbf{r}_i \mapsto \mathbf{r}_j$  within the spherical surface is to be proposed with the same probability as the inverse displacement. When the three-dimensional displacements  $\Delta\mathbf{r}$ —prior to the projection of the position back onto the sphere—are equally distributed within a cube with edge length  $2d_{\max}$  centered around zero, the on-sphere displacements towards the intersections of the sphere with the coordinate planes are preferred. As shown in the simplified sketch in Fig. 3.1, that problem is circumvented by choosing displacements which are equally distributed within a sphere with radius  $d_{\max}$  centered around zero. In practice, the effect becomes relevant only for very large values  $d_{\max} \gtrsim 0.5$  of the maximum displacements.

The temperature of the particles on the Thomson sphere is again characterized by the Coulomb coupling parameter  $\Gamma$ . Defining this parameter requires a meaningful equivalent for the Wigner-Seitz radius as the typical inter-particle distance. For this purpose, the surface of the shell is divided into  $N_s$  spherical caps. As the sphere with Wigner-Seitz radius represents the volume which is occupied by one particle in 3D, every spherical cap represents the area which is occupied by one particle. The area of such a cap is given by

$$A_{\text{cap}} = 2\pi R_s h = 2\pi R_s^2 \cos \vartheta, \quad (3.9)$$

where  $\vartheta$  is half the central angle. This angle is related to the particle number  $N_s$  as

$$\vartheta = \cos^{-1} \left( 1 - \frac{2}{N_s} \right). \quad (3.10)$$

The arc length  $R_s \vartheta$  represents the radius of the spherical cap and is therefore used as an equivalent of the Wigner-Seitz radius in the definition of the coupling parameter  $\Gamma$  for a Thomson sphere.

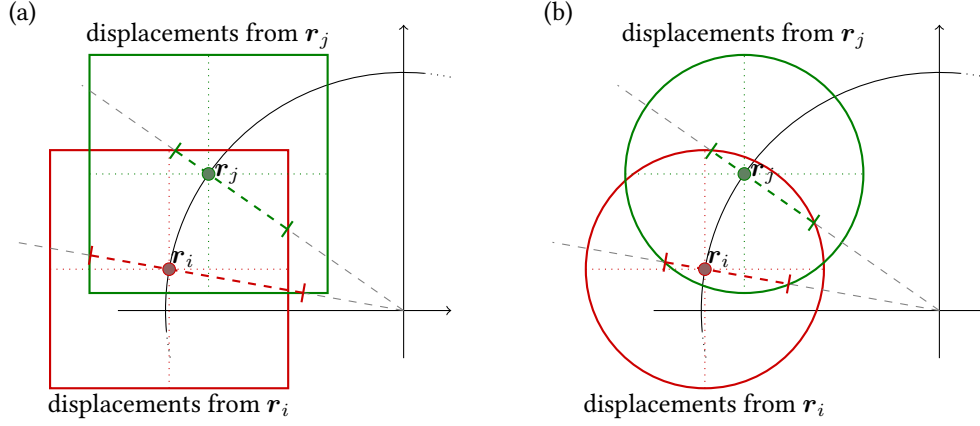


**Figure 3.1:** Particle displacements on a sphere. (a) All proposed displacements starting at point  $r_i$  ( $r_j$ ) are indicated by the red (green) square. Points which are then projected onto the other point  $r_j$  ( $r_i$ ) are marked by the dashed green (red) line. The on-sphere displacement towards  $r_i$  closer to a coordinate axis is more likely than the opposite displacement as the red line is longer than the green one. (b) The squares of proposed displacements are replaced by circles. Since both dashed lines have equal length, both on-sphere displacements  $r_i \mapsto r_j$  and  $r_j \mapsto r_i$  are proposed with the same probability, here.

### 3.2.2 Parallel Tempering in Monte Carlo Simulations

The *parallel tempering* extension is used during all MC simulation regardless of the geometry of the studied system. This system can be a flat extended dust crystal, a harmonically confined cluster in 2D and in 3D, or a composition of charges on a spherical shell. Since the sequence of configurations during the MC propagation is not limited to the true particle trajectories, it is possible to simulate several replicas of the system in parallel and swap the configuration between those. The replicas can have different temperatures as long as the energy histograms of adjacent temperature have a significant overlap. This means that a configuration with energy  $E_a$  which is found at temperature  $T_a$  will also occur at temperature  $T_{a+1}$  with a finite probability. For simulations of dust clusters, a finite overlap is achieved by using about ten to twenty points per order of magnitude on a logarithmic temperature. Swaps are proposed with equal probability for all pairs of adjacent temperatures and the acceptance probability is chosen as

$$\mathcal{P}_{\text{acc}}^{\text{swap}} = \begin{cases} 1 & : E_a \geq E_{a+1} \\ e^{(E_a - E_{a+1}) \cdot \left( \frac{1}{k_B T_a} - \frac{1}{k_B T_{a+1}} \right)} & : E_a < E_{a+1} \end{cases}, \quad (3.11)$$

in order to comply with the detailed balance condition. A move that swaps a configuration with lower energy from the “hot” to the “cold” system is always accepted, while the reverse swap is accepted with a finite probability only. When phase transitions are investigated, the temperature is a scanning parameter and simulations are run for a sequence of temperatures. Therefore, the additional computational effort for parallel tempering is very low.

The advantage of the swapping moves is that energy barriers can be overcome more efficiently. While transitions between different metastable configurations are very unlikely at low temperatures, and the simulation would virtually get stuck in one configuration, these

transitions occur frequently at higher temperatures. With the parallel tempering technique, the transitions between different metastable states at a low temperature are possible via the swapping of the configuration with a cluster at a higher temperature. For details of this method, see Refs. [31, 117–119].

In order to allow the individual MC processing of the system replicas in parallel between the swapping moves, every replica uses a separate RNG. One additional RNG is used for the swapping moves. These Mersenne Twister RNGs are seeded with random numbers which are generated by a different RNG. Using a different type of RNG for seeding the different Mersenne Twisters reduces statistical dependence. The poor statistical properties of the seeding generator have no relevance in this case.

### 3.2.3 Ergodicity of the Monte Carlo Algorithm

From the theoretical point of view, it is readily proven that the canonical ensemble  $(N, \omega_0, \Gamma)$  is ergodic for a finite dust cluster. Since the particles are considered as point charges, any configuration  $\mathbf{R}$  can be transferred into any other  $\mathbf{R}'$  along a path in configuration space. Every configuration along this path has a finite energy and is therefore realized with a finite probability. Hence, the accessible phase space volume is continuous, although different regions, i.e., different cluster isomers, are separated by energy barriers of finite height.

From the technical point of view, the simulation algorithm can get stuck in one energy valley for a very long time at low temperature, i.e., only one isomer is realized. This behavior may reflect the correct thermodynamic distribution of states, when all other isomers have significantly higher energies. However, it cannot be ruled out from the outset that no other isomer has equal or lower energy than the one found. The parallel tempering enhancement is used to ensure the ergodic sampling of the entire accessible phase space within a reasonable simulation time also at low temperatures by allowing the exchange with ensembles at higher temperature.

The ergodicity of the algorithm is checked by analyzing the order of the different isomers in the output sequence of configurations. A good indicator for an ergodic sampling algorithm is the occurrence of frequent changes between different sections of the configuration space. When different isomers are found, these should be widely distributed over the output sequence. If, for example, only one single particle transition between two shells occurs during the entire simulation at a certain value of  $\Gamma$ , the first isomer is found before the transition only. After the transition, the second isomer is found in every simulation step. Such a separation of the output sequence of states into only two blocks indicates a low validity of results, since the ratio of the two isomers is strongly affected by the “time” of the transition and also by the total number of MC steps in the simulation.

The wide distribution of different isomers was checked at random tests for the MC simulations of this thesis. Good results were found for both radial isomers, i.e., occupations numbers of the shells, and intra-shell isomers, i.e., the arrangement of pentagonal and hexagonal Voronoi cells within a shell.

Another measure for the sampling efficiency is the *auto-correlation* “time”  $\tau_{\text{corr}}$ .<sup>3</sup> This time scale describes the decay of the auto-correlation function of important system properties as for example the potential energy  $E$ . When  $\tau_{\text{corr}}$  is larger than the number of MC steps between two samples, the effective number of samples is reduced by a factor proportional to  $\tau_{\text{corr}}$  since the samples are not statistically independent [117, 120]. Frequent exchanges of configurations between the replicas in the parallel tempering method can reduce the auto-correlation time.

### 3.3 Molecular Dynamics Simulations

A method that allows for studying the dynamics of the dust system is given by *molecular dynamics* (MD) simulations. In the first part of this section, the pure microcanonical MD scheme is briefly described and the second part is concerned with the *Langevin molecular dynamics* (LMD) extension that includes the interaction of the dust with a background medium statistically. The microcanonical MD and the LMD simulation method allow for the inclusion of time-dependent external forces such as the momentum transfer from manipulation lasers.

#### 3.3.1 Microcanonical Molecular Dynamics Simulations

Microcanonical MD simulations aim to calculate the particle trajectories via the numerical integration of the equations of motion which are given by Newton’s second law. These represent a system of coupled differential equations for the positions and the velocities of all dust particles. While the velocity,  $\mathbf{v}_{(i)} = \dot{\mathbf{r}}_{(i)}$ , of a particle  $i$  is given by the time derivative of its position, the acceleration,  $\mathbf{a}_{(i)} = \ddot{\mathbf{r}}_{(i)}$ , involves the interaction forces with all other particles and the force by an external potential  $V$ ,

$$m_d \ddot{\mathbf{r}}_{(i)} = \mathbf{F}_{(i)} = -\nabla_{(i)} V(\mathbf{r}_i) - \sum_{j \neq i} \nabla_{(i)} W(\mathbf{r}_{(i)}, \mathbf{r}_{(j)}), \quad (3.12)$$

where  $W$  is a pair-interaction potential. The nabla operator  $\nabla_{(i)}$  describes the gradient with respect to the coordinates  $\mathbf{r}_{(i)}$ . Since the total energy  $E$  of the system is conserved in Newton’s equations, Eq. (3.12) describes the microcanonical ensemble  $\Omega(N, V, E)$ . As discussed above, the role of the volume  $V$  is taken over by the trap frequency  $\omega_0$  for harmonically confined clusters.

An efficient integration scheme is the “Leapfrog” method which is obtained from the Taylor expansion of the equation of motion. In the following, the particle index is suppressed for the benefit of a better readability. The expansion is carried out for each position  $\mathbf{r}_{(i)}(t)$  around

<sup>3</sup>In the context of MC simulations, the term “time” is to be understood as the number of MC steps.

$t - \frac{\Delta t}{2}$  and truncated after the second order term,

$$\begin{aligned} \mathbf{r} \left( t + \frac{\Delta t}{2} \right) &\approx \mathbf{r} \left( t - \frac{\Delta t}{2} \right) + \mathbf{v} \left( t - \frac{\Delta t}{2} \right) \Delta t + \frac{1}{2} \mathbf{a} \left( t - \frac{\Delta t}{2} \right) \Delta t^2 \\ &= \mathbf{r} \left( t - \frac{\Delta t}{2} \right) + \left[ \mathbf{v} \left( t - \frac{\Delta t}{2} \right) + \mathbf{a} \left( t - \frac{\Delta t}{2} \right) \frac{\Delta t}{2} \right] \Delta t \end{aligned} \quad (3.13)$$

$$\text{with} \quad \mathbf{v} \left( t + \frac{\Delta t}{2} \right) \approx \mathbf{v} (t) + \mathbf{a} \left( t + \frac{\Delta t}{2} \right) \frac{\Delta t}{2} \quad (3.14)$$

$$\text{and} \quad \mathbf{v} (t + \Delta t) \approx \mathbf{v} \left( t + \frac{\Delta t}{2} \right) + \mathbf{a} \left( t + \frac{\Delta t}{2} \right) \frac{\Delta t}{2}, \quad (3.15)$$

where the square bracket in Eq. (3.13) is identified as  $\mathbf{v}(t)$ . The last two steps, Eqs. (3.14) and (3.15), are combined into one step,

$$\mathbf{r} \left( t + \frac{\Delta t}{2} \right) \approx \mathbf{r} \left( t - \frac{\Delta t}{2} \right) + \mathbf{v} (t) \Delta t \quad (3.16)$$

$$\mathbf{v} (t + \Delta t) \approx \mathbf{v} (t) + \mathbf{a} \left( t + \frac{\Delta t}{2} \right) \Delta t. \quad (3.17)$$

In this integration scheme, the particle velocities are evaluated at the full time steps and the positions are evaluated at the half time steps between them. The interleaved time points for the velocity and the position “leapfrog” each other.

Since, both the positions and the velocities, have to be evaluated at the same time point in order to calculate the total energy for example, the position update is split into two half time steps in the computer simulation. Starting with positions and velocities at time  $t$ , all particle positions are first updated by half a time step. Then, all accelerations are calculated at the intermediate positions and the velocities are updated by a full time step. Finally, the positions are propagated by a second half time step from  $t + \frac{\Delta t}{2}$  to  $t + \Delta t$  using the new velocities. While the computational effort for the time propagation of the positions scales linearly with the particle number, the effort for the accelerations scales quadratic with the particle number due to the number of pair interactions. Therefore, it is important that the accelerations are calculated only once per time step.

### 3.3.2 Langevin Molecular Dynamics Simulations

As discussed above, the dust particles in a complex plasma are interacting with the surrounding plasma and with the neutral gas. The primary effects of the plasma are the charging of the dust grains by electron and ion impact on the one hand, and the screening the Coulomb interaction on the other hand. Neutral gas atoms collide frequently with the dust particles. Due to the large difference of several orders of magnitude in the time scales of light neutral gas atoms and heavy dust particles, the exact treatment of these collisions is beyond reach. In *Langevin dynamics*, the dust-neutral collisions are included statistically in a combination of the friction

force,  $-m_d\gamma\mathbf{v}$ , and the random force,  $\boldsymbol{\xi}(t)$  [121]. Complementing the equation of motion for particle  $i$ , Eq. (3.12), by these two terms results in the *Langevin equation*,

$$m_d\dot{\mathbf{r}}_{(i)} = -\mathbf{F}_{(i)} - m_d\gamma\mathbf{v}_{(i)} + \boldsymbol{\xi}_{(i)}(t), \quad (3.18)$$

where the *friction coefficient*  $\gamma$  characterizes the coupling between the dust particles and the neutral gas. Often, the product of the particle mass and the friction coefficient is referred to as the *damping parameter*  $\lambda = m_d\gamma$ . Since  $m_d$  is used as the mass unit in this thesis, both the friction coefficient  $\gamma$  and the damping parameter  $\lambda$  are equivalent in the dimensionless units. The details of the neutral gas collision process are not subject to this work, but  $\gamma$  is used as an input parameter for the simulations.

In this model, the dust system can exchange energy with a heat bath and its total energy  $E$  is therefore no longer fixed. The system adopts the temperature  $T$  of the heat bath at thermal equilibrium and is described by the canonical ensemble  $Z(N, V, T)$ . Hence, LMD simulations approximate the canonical ensemble, where the friction and the stochastic force simulate the heat bath.

The stochastic force  $\boldsymbol{\xi}$  can be modeled by a Gaussian probability distribution (Gaussian white noise) with zero average and with an amplitude that grows with the temperature. In order to model the stochastic interactions with a heat bath at temperature  $T$ , the correlation function of the stochastic force has to obey the property

$$\langle \boldsymbol{\xi}_{(i),\alpha}(t)\boldsymbol{\xi}_{(j),\beta}(t') \rangle = 2m\gamma k_B T \delta_{i,j} \delta_{\alpha,\beta} \delta(t-t'), \quad (3.19)$$

where the Greek indices  $\alpha, \beta = x, y, z$  denote the spatial direction. The random force is uncorrelated for different particles  $i \neq j$ , and it has no memory because of the delta function  $\delta(t-t')$ . The friction and the random forces are included in the “leapfrog” integration scheme as described by MANNELLA in Ref. [122]. While the position update, Eq. (3.16), is not changed, the velocity update, Eq. (3.17), for Langevin molecular dynamics simulations reads

$$\mathbf{v}(t + \Delta t) = c_2 \left[ c_1 \mathbf{v}(t) + \mathbf{a} \left( t + \frac{\Delta t}{2} \right) \Delta t + d_1 \boldsymbol{\eta} \right], \quad (3.20)$$

where  $\boldsymbol{\eta}$  is a vector of Gaussian distributed random variables with standard deviation  $\sigma = 1$  and zero average  $\mu = 0$ . The constants are given by

$$c_1 = 1 - \frac{\gamma\Delta t}{2}, \quad c_2 = \frac{1}{1 + \frac{\gamma\Delta t}{2}}, \quad \text{and} \quad d_1 = \sqrt{\frac{2k_B T \gamma \Delta t}{m}}, \quad (3.21)$$

as shown in the reference [122].





## Chapter 4

# Melting Parameters for Dusty Plasmas

**S**uitable melting parameters are of central importance for the study of disordering processes. As described in the introduction, the melting process of finite dust clusters is qualitatively different from bulk materials. The focus lies on the spatial arrangement of the dust grains and on structural transitions. For this reason, the desired parameters have to be sensitive to the spatial structure. The first section 4.1 is concerned with the Voronoi analysis as a technique which allows for the identification of the underlying lattice of a particle arrangement. Moreover, the necessary adaption for a spherical shell instead of planar system are described. In section 4.3, as the first step, spatial pair and three-particle distribution functions are reviewed in general. As the second step, generalized coordinates are introduced which take into account the symmetry of harmonically confined dust clusters. Finally, section 4.4 discusses the reduced entropy as a measure of disorder in the clusters.

### 4.1 Voronoi analysis

This section gives a short introduction to the Voronoi analysis as a tool for the identification of nearest neighbor particles. While the classification of neighbors in a colloquial sense is usually possible by a quick look at a configuration of particles, the automatic calculation of bond order parameters or the identification of lattice defects as particles with an abnormal number of neighbors require an exact definition of the term *neighbor*. One possibility was to introduce a maximum pair distance  $d_{\min}$  and define neighbors as particle pairs with a distance not larger than  $d_{\min}$ . However, this approach causes an unwanted arbitrariness by introducing that length.

The *Voronoi diagram* allows for an unambiguous classification of neighbors and for the identification of patterns. Different intra-shell isomers can be distinguished by the arrangement of pentagonal and hexagonal Voronoi cells [63, 85]. A detailed overview of the properties and the importance of Voronoi diagrams in various fields is given in Ref. [123]. Such a diagram is constructed from a set of points  $P$  which are called *seeds*. The *Voronoi cell* of a seed  $P$  is defined by all points which are not closer to any other seed than to  $P$ . This definition is very intuitive and would probably be among the first ideas for defining cells from given seeds  $P$  in a plane or in three-dimensional space. Voronoi diagrams are inherently constructed in various situations

in nature. As just one example, consider a petri dish seeded with different species of bacteria. The bacteria start to grow—all with the same rate—and populate the free space in the petri dish. If a population reaches the border of the area already populated by another species, the growth stops. After a while, every point in the plane will be occupied by the first bacteria to reach it which is the one starting at the closed seed point. The bacteria have constructed the Voronoi diagram [124]. In the following, the structure of extended and, especially, spherical dust clusters are being analyzed. Therefore, the seeds of the Voronoi are given by the particle positions in a snapshot of the cluster.

An example for a Voronoi diagram in a 2D plane and the Delaunay triangulation as its dual graph is shown in Fig. 4.1. Before adapting the Voronoi diagrams to spherical cluster shells, a few important properties of these diagrams are reviewed:

- The points along the perpendicular bisector between two seeds  $P_1$  and  $P_2$  are equally distant from the two seeds and can belong to both Voronoi cells. Hence, segments of the perpendicular bisectors form the *edges* of the Voronoi diagram. Two seed points are called “neighbors” if and only if their Voronoi cells have a common edge.
- The Voronoi diagram is closely related to the *Delaunay triangulation* which represents its dual graph. Each Delaunay *edge* connects two Voronoi seeds which are the so called *vertices*. Since these vertices are fixed by the particle positions, we use the two terms “vertex” and “particle” synonymously in the following.
- The Voronoi edges are perpendicular bisectors of the Delaunay edges.<sup>1</sup>
- The statement that two particles are neighbors is equivalent to the statement that the corresponding vertices are connected by one Delaunay edge.
- The Delaunay edges form a mesh of triangles. These triangles are called *faces*.

These properties can specify a projection between the surface of a sphere and a flat 2D plane which then allows to construct the Voronoi diagram for seeds on sphere.

During the investigating of disordering processes in spherical clusters, the *intra-shell* order within spherical shells is of central interest. Therefore, the Voronoi diagram has to be constructed within the shell in order to identify neighboring particles within that shell. As discussed in the previous paragraph, this task is equivalently completed by construction of the Delaunay triangulation within the shell. In the following, this problem is reduced to the calculation of several Delaunay triangulations in a 2D plane by decomposing the spherical shell into several spherical caps and projecting the particle positions into a plane by a *stereographic projection*.

---

<sup>1</sup>Note that the intersection of a Voronoi edge and the corresponding Delaunay edge may be outside the shown Voronoi edge.

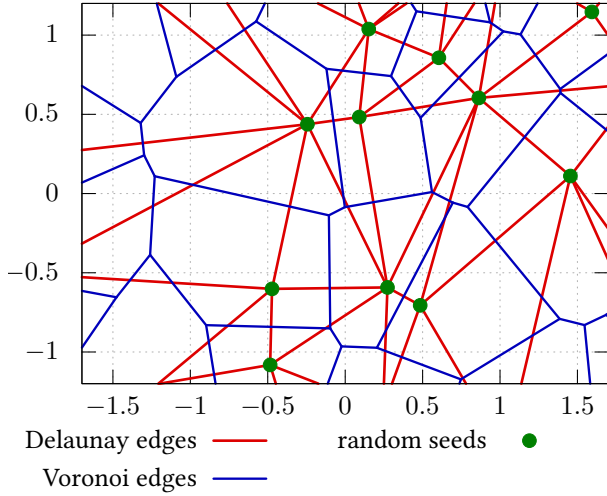


**Figure 4.1:** Example for a Voronoi diagram. A few points (green) are placed randomly in the plane as seeds for the triangulation. The Delaunay edges are shown in red and form a mesh of triangles. The Voronoi edges (blue) are perpendicular bisectors to the Delaunay edges and the number of edges in the Voronoi cells represent the *coordination number*, i.e., the number of nearest neighbors, of its seed.

### 4.1.1 Stereographic Projection

For the analysis of the structure inside one shell  $S$ , all particles  $i$  on this shell are assumed to have the same radial coordinate  $|r_i| = R_S$ . The particle coordinates are then projected onto a unit sphere by normalization. The remaining problem is to project the surface of the sphere, or, more precisely, a region of this surface, into a plane in order to apply the Delaunay triangulation algorithm. The Delaunay triangulation constructs a mesh of triangles from a given set of seed points  $\mathbf{P}$  with the property that the circumcircle of the triangle with the edge points  $A, B, C \in \mathbf{P}$  contains no other point  $D \in \mathbf{P}$ . Hence, it is essential that circles are preserved under the projection, so that the triangulation in the projection plane is valid on the sphere surface as well.

The stereographic projection (SP) has this property. For a chosen point  $P_C$  on the sphere as projection center, it maps the sphere surface without the projection center  $\mathbb{S}^2 \setminus P_C$  onto the plane  $\mathbb{E}$ . The point  $P_0$  located opposite of the projection center  $P_C$  is mapped onto the origin of the projection plane. The image  $A' \in \mathbb{E}$  of a point  $A \in \mathbb{S}^2 \setminus P_C$  is constructed as the intersection of the straight line through  $A$  and  $P_C$  with the plane  $\mathbb{E}$  perpendicular to  $\overrightarrow{OP_C}$  through the center of the sphere, see illustration in Fig. 4.2. Since this plane contains the equator of the sphere, the projection is referred to as *equatorial stereographic projection* (ESP). A very simple mathematical description of the projection is achieved by choosing the south pole  $P_C = (0, 0, -1)$  as projection center. The image of  $P = (x, y, z)$  is then calculated as

$$(x, y, z) \xrightarrow{\text{SP}} \left( \frac{x}{1+z}, \frac{y}{1+z} \right), \quad (4.1)$$

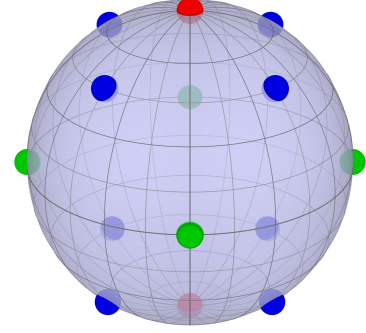
and the inverse stereographic projection (ISP) is given by

$$(x', y') \xrightarrow{\text{ISP}} \left( \frac{2x'}{\xi}, \frac{2y'}{\xi}, \frac{2-\xi}{\xi} \right), \quad \text{with } \xi = x'^2 + y'^2 + 1. \quad (4.2)$$

The SP is in this case an injective mapping from  $\mathbb{S}^2 \setminus P_C$  to  $\mathbb{R}^2$ . Some authors instead define the image  $P'$  of a point  $P$  as the intersection of the straight line through  $P_C$  and  $P$  with the

**Table 4.1:** Tangential points  $P_0$ : Points 1 and 2 only are used for large particle numbers on the shell, points 1 to 6 for medium numbers and all points are used for small particle numbers.

#	$\theta$	$\phi$	#	$\theta$	$\phi$
1	0°	0°	8	45°	135°
2	180°	0°	9	45°	225°
3	90°	0°	10	45°	315°
4	90°	90°	11	135°	45°
5	90°	180°	12	135°	135°
6	90°	270°	13	45°	225°
7	45°	45°	14	45°	315°



tangential plane at  $P_0$ . The projection is referred to as *tangential stereographic projection* (TSP) in that case. In view of the above, the point  $P_0$  is called tangential point and this term is used for the equatorial stereographic projection as well in the following. Both definitions are equivalent except for a factor of two in the tangential projection with  $(x', y')_{\text{TSP}} = 2(x', y')_{\text{ESP}}$  and it therefore does not matter which definition is used for the purpose of constructing the intra-shell Voronoi diagram.

Since the projection of the full sphere (without the projection center) requires an infinite 2D plane, a finite region around the projection center  $P_C$  is excluded. For this purpose, only those points  $P$  with a  $z$  coordinate  $P_z \geq -z_{\text{max}}$  are selected. The images of these points are within a circle with finite radius

$$R_{\text{max}} = \frac{\sqrt{1 - z_{\text{max}}^2}}{1 - z_{\text{max}}} = \sqrt{\frac{1 + z_{\text{max}}}{1 - z_{\text{max}}}}. \quad (4.3)$$

For example, the radius of the projection is  $R_{\text{max}} = \sqrt{1 + 0.9/(1 - 0.9)} = \sqrt{19} \approx 4.359$  for a choice of  $z_{\text{max}} = 0.9$ .

However, the Delaunay triangulation is required on the entire sphere and the validity has to be guaranteed for every point. In order to achieve this demand, several projections are performed, each for a different projection center. Then, the Delaunay triangulation is calculated for each of them individually. Every projection contains the points from a different spherical cap. Since the validity of the triangulation cannot be guaranteed for the points at the edge of a cap, see Sec. 4.1.2 below, a significant overlap of the spherical caps is essential. When the particle number on the shell is large ( $100 \lesssim N_s$ ), two projections with tangential points at the poles of the sphere are sufficient since enough particles are located in the overlap. When the particle number is lower ( $30 \lesssim N_s \lesssim 100$ ), the angular pair distances are larger and therefore larger overlap is required. For this reason, four additional projections are used with tangential points on the equator of the sphere, see Tab 4.1. For even lower particle numbers  $N_s \lesssim 30$ , another eight projections with tangential points between the former ones are added, see Tab. 4.1. Of course, all fourteen tangential points can be used for large particle numbers as well, but this causes unnecessary computational effort compared to calculating the Voronoi diagrams for two tangential points only.

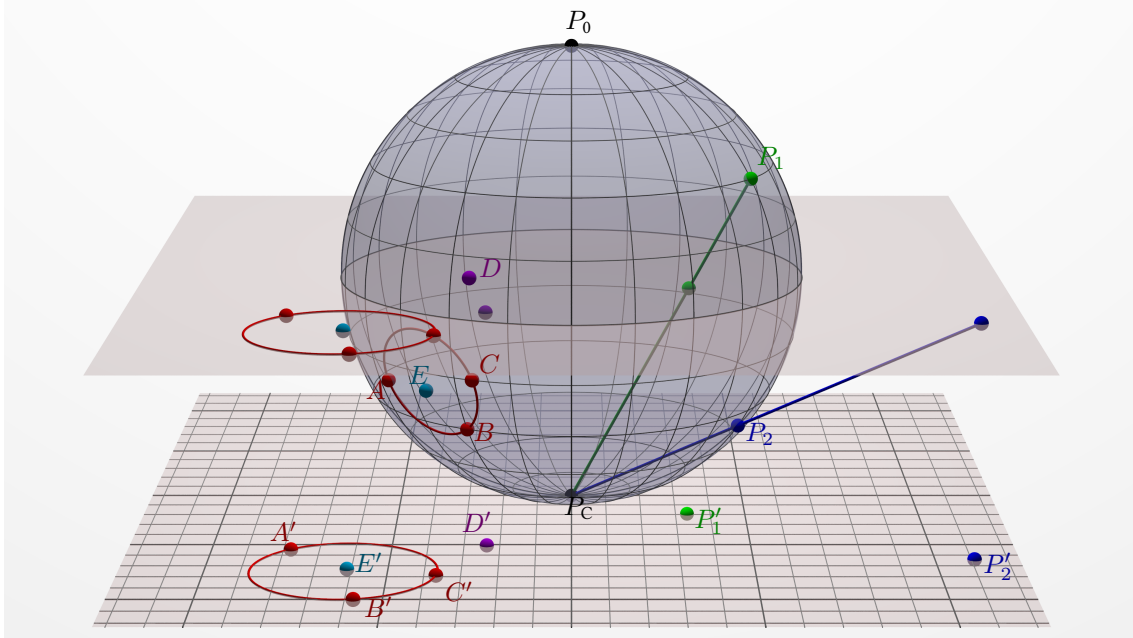


**Figure 4.2:** Illustration of the stereographic projection with the south pole as projection center  $P_C$ . The image plane is repeated below the sphere for a better view. The image  $P'$  of a point  $P$  is constructed as the intersection of the straight line that connects  $P$  with  $P_C$  and the plane through the origin, as illustrated for  $P_1$  and  $P_2$ . As the point  $D$  ( $E$ ) is outside (inside) the circumscribed circle of the points  $A, B$  and  $C$ , the image point  $D'$  ( $E'$ ) is outside (inside) the circumscribed circle of the images  $A', B'$  and  $C'$ .

**Rotation.** In order to use formula (4.1) and (4.2) for an arbitrary point  $P_C$  on the sphere surface as projection center, the entire surface first has to be rotated as the first step. In the following, the tangential point  $P_0$  is specified instead of the projection center  $P_C$ . This is more practical, since the tangential point  $P_0$  is mapped onto the origin by the SP. Indeed, the conversion between tangential point and projection center by  $P_0 = -P_C$  is very simple. Any point on the unit sphere surface can be expressed by

$$P_0 = -P_C = \begin{pmatrix} \sin \theta \cos \phi \\ \sin \theta \sin \phi \\ \cos \theta \end{pmatrix}, \quad (4.4)$$

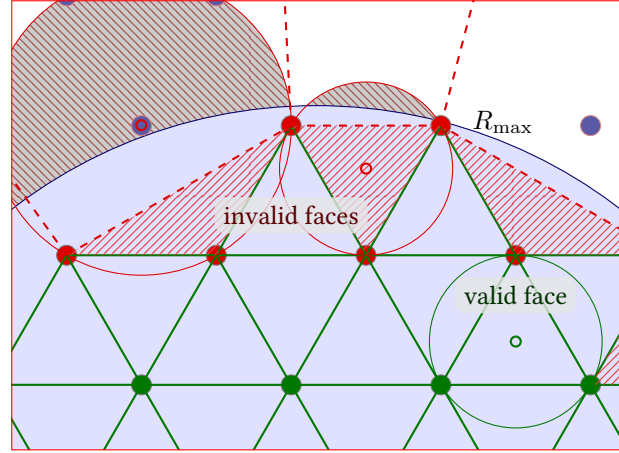
in spherical polar coordinates  $\theta$  and  $\phi$ . Using the rotation matrix

$$\mathbf{R} = \begin{pmatrix} \cos \theta \cos \phi & \cos \theta \sin \phi & -\sin \theta \\ -\sin \phi & \cos \phi & 0 \\ \sin \theta \cos \phi & \sin \theta \sin \phi & \cos \theta \end{pmatrix}, \quad (4.5)$$

the tangential point is transformed to  $\mathbf{R}P_0 = (0, 0, 1)$  and the projection center is transformed to  $\mathbf{R}P_C = (0, 0, -1)$ . The transformed coordinates are given by the set

$$\bar{\mathbf{P}} = \{\mathbf{R}A \mid A \in \mathbf{P}\}. \quad (4.6)$$

**Figure 4.3: Valid (green) and invalid (red) vertices of the triangulation:** A vertex is treated as invalid when it has at least one adjacent face for which the validity is not guaranteed. The circumscribed circles are shown for three example faces. One circumcircle is completely inside the selected region and hence the validity of this face is guaranteed. While the left red face remains invalid if the selected array is enlarged due to the outer vertex (blue), the central red face will become valid since no outer vertex is inside its circumcircle.



After this rotation, the points  $P$  with a  $z$  coordinate  $P_z \geq -z_{\max}$  are then selected as the set  $\bar{P}^{\text{sl}}$ . Equation (4.1) is then applied in order to project these points into a plane and their Delaunay triangulation is calculated.

### 4.1.2 Validity of the Delaunay Triangulation

The Delaunay triangulation itself is calculated by the 2D triangulation algorithm `Delaunay_triangulation_2` of the CGAL<sup>2</sup> library. Since there are typically points on the sphere which are outside the selected spherical cap, the triangulation may be invalid for some points at the border of this spherical cap. Before the different triangulations can be fit together, it has to be checked for which of its points the validity can be guaranteed.

Each triangular face  $ABC$  with  $A, B, C \in \bar{P}^{\text{sl}}$  is constructed by the condition that no other point  $D \in \bar{P}^{\text{sl}}$  is inside the triangle's circumscribed circle with center  $M_{cc}$  and radius  $r_{cc}$ . Indeed, there may exist a point  $E \in \bar{P} \setminus \bar{P}^{\text{sl}}$  among the remaining points with  $|\overrightarrow{EM_{cc}}| < r_{cc}$  that makes the triangle  $ABC$  invalid. The existence of such a point  $E$  is excluded when the circumscribed circle center is fully contained by the selected region, i.e. it is not near the border, so that the relation

$$|\overrightarrow{OM_{cc}}| + r_{cc} \leq R_{\max} \quad (4.7)$$

is fulfilled. Since all infinite faces have infinite radius, all points which have at least one infinite face are invalid. Because of the closed surface of the sphere, there cannot exist any infinite faces in the valid triangulation. An example for valid and invalid faces is show in Fig. 4.3. In that example, a circular region from a regular hexagonal lattice is selected. Note that an intra-shell configuration of a Yukawa cluster looks different in the stereographic projection (inter alia since the SP does not conserve lengths), but the problem that outer points may be inside some circumscribed circles is illuminated by this example.

<sup>2</sup>Computational Geometry Algorithms Library (Open Source Project), <http://www.cgal.org>

When quantities (like fraction of sixfold particles, bond order parameters etc.) are sampled, the validity of the Delaunay triangulation has to be checked for each vertex. Therefore, the condition (4.7) is checked for all incident faces of the vertex. If the validity cannot be guaranteed for at least one incident face, the vertex has to be treated as invalid. That means that this projection is not sufficient for the determination of the neighbors of the particle or its coordination number. The neighbors then have to be identified in another projection where the particle is closer to the tangential point  $P_0$  and therefore the circumscribed circles of all incident faces are totally contained by the selected area of that second projection.

It turns out that for large shells with  $N_s \gtrsim 100$  particles, the validity can be ensured for all particles on a shell, when two SPs are performed: One projection for the upper hemisphere and one for the lower hemisphere. In each projection, the selected region is chosen larger than the actual hemisphere ( $z_{\max} \approx 0.8$ ). But for the further calculation, every point is taken from the projection according to its correct hemisphere. This scheme can be extended to more than two regions. In that case, every point is taken from the projection with the closest tangential point. While the condition to have at least one valid triangulation for every point representing the position of one particle is fulfilled even by two projections and a small overlap for large clusters, a larger overlap or more projections are required for small clusters, see Sec. 4.1.1 above.

### 4.1.3 The Euler-Poincaré Characteristic

An indicator for the validity of the entire triangulation is derived from the *Euler-Poincaré Characteristic*  $\chi$  defined as:

$$\chi = V - E + F, \quad (4.8)$$

where  $V$  is the number of vertices,  $E$  the number of edges and  $F$  the number of faces of a polyhedron. The *characteristic number* of a convex space like a sphere is  $\chi = 2$ . The number of vertices  $V$  is determined by the number of particles on the investigated sphere. The Delaunay triangulation constructs a polyhedron with triangular faces. Since every edge belongs to exactly two faces, the face number  $F$  and the edge number  $E$  are connected through the relation

$$2E = 3F. \quad (4.9)$$

When this result, Eq. (4.9), is insert into the Euler-Poincaré Characteristic for a convex space, Eq. 4.8, the relation

$$3V - E = 6, \quad (4.10)$$

is obtained. This relation connects the number of vertices  $V$  with the number of edges  $E$ .

While this equation can already be used as a checksum for the plausibility of the Delaunay triangulation, it contains also a descriptive relation for coordination numbers of the particles as discussed in the following. The intra-shell coordination number  $n$  of a particle is defined as its number of nearest neighbors, where two vertices are called “nearest neighbors” when they have one edge in common. The lowest considerable coordination number is  $n_{\min} = 3$  and the

maximum is  $n_{\max} = V - 1$  for the (very unlike) case that at least one vertex has common edges with all other vertices. The numbers  $N_n$  with  $n \in \{3, \dots, V - 1\}$  are defined as the number of vertices with coordination number  $n$ . This definition can be extended to larger coordination numbers, where the occupation numbers are zero for all the additional coordination numbers. Since every edge connects exactly two vertices, this leads to the expressions

$$2E = \sum_{n=3}^{\infty} n \cdot N_n, \quad V = \sum_{n=3}^{\infty} N_n, \quad (4.11)$$

for number of edges and the number of vertices, respectively. These two expressions are inserted into (4.10) in order to obtain

$$3 \cdot \sum_{n=3}^{\infty} N_n - \frac{1}{2} \cdot \sum_{n=3}^{\infty} n \cdot N_n = 6 \quad \Leftrightarrow \quad \sum_{n=3}^{\infty} (6 - n) \cdot N_n = 12, \quad (4.12)$$

as a constraint for the coordination numbers.

In the following, some important implication of Eq. (4.12) are discussed. The first important implication of this equation is the well-known fact that it is unfeasible to cover a singly closed surface with a perfect hexagonal lattice where every particle has six nearest neighbors. For such a lattice, the sum on the left hand side vanishes and violates the equation.

Equation (4.12) can also be read as follows: Particles with six neighbors do not contribute to the sum and every particle with five nearest neighbors contributes to the sum by one. Every particle with four neighbors contributes to the sum with plus two, every particle with seven neighbors contributes to the sum with minus one, and so on. Hence, a possible particle arrangement of the sphere consists of twelve pentagons and an arbitrary number of hexagons.<sup>3</sup> Every additional pentagon has to be compensated by a Voronoi cell with at least seven adjacent cells.

Two prominent examples for such an arrangement are the icosahedron of twelve particles, where each particle has a pentagonal Voronoi cell, and the “football” configuration of 32 particles. The latter configuration consists of twelve pentagonal and 20 hexagonal Voronoi cells in a very symmetric arrangement where every pentagon is fully surrounded by hexagons. This intra-shell configuration is for example realized by the 32 particles on the outer shell for the “magic number” Coulomb cluster with  $N = 38$  particles in total, cf. Fig. 5.11.

## 4.2 Bond Order Parameter

Bond Order Parameters are quantities that measure the angular symmetry of a given structure with respect to the angles between bonds [125–127]. For dusty plasmas, these bonds are the edges of the Delaunay triangulation. Each bond connects two particles which are then called

<sup>3</sup>Here, the terms “pentagon” and “hexagon” are used for particles with five and six neighbors, respectively, corresponding to the Voronoi diagram. The deformation of the Voronoi cell is not taking into account for this classification.



neighbors. In two dimensional systems, the quantity  $\Psi_k$  is defined as

$$\Psi_k(l) = \sum_{m=1}^{N_{\text{nn}}(l)} e^{ik\varphi_{lm}}, \quad (4.13)$$

for each particle  $l$ . The number of nearest neighbors of this particle  $l$  is denoted by  $N_{\text{nn}}(l)$  and  $\varphi_{lm}$  is the angle of the bond between this particle  $l$  and its  $m$ -th neighbor with respect to a fixed reference direction  $e_d$ . While the absolute  $|\Psi_k|$  is independent of the reference direction, the phase  $\Psi_k$  depends on it.

While defining this direction  $e_d$  is trivial for a flat system, fixing a meaningful reference direction on the entire spherical surface is impossible as a consequence of the *hairy ball theorem* [128]. At a chosen point  $P_0$  on the sphere, one can define nevertheless a tangential vector  $e_d$  with  $|e_d| = 1$ . In order to calculate the phase of  $\Psi_k$  for a particle at an arbitrary point  $P$ , a continuous mapping is required that defines the reference direction at this point  $e_d(P)$ . This would mean defining a continuous non-vanishing field of tangential vectors that covers the entire sphere. Indeed, the hairy ball theorem states that such a vector field cannot exist for the two-dimensional surface of a sphere in  $\mathbb{R}^3$ .

The symmetry number  $k$  should be chosen in accordance to the expected symmetry, e.g.  $k = 6$  in the case of a hexagonal structure. Since the angles are not conserved under the SP for every triangle, the bond order parameter must not be calculated in the projection plane. The ISP back from plane to sphere surface is applied before calculating the bond order parameter.

**Local Bond Order Parameter** The *local bond order* is defined as the average of absolute value  $|\Psi_k|$  over all particles with the correct number of neighbors, i.e.

$$\langle |\Psi_6| \rangle = \frac{1}{N_6} \sum_l^N |\Psi_6(l)| \delta_{6, N_{\text{nn}}(l)}, \quad (4.14)$$

for the hexagonal parameter. Here,  $N_6$  is the total number of particles with six neighbors and the Kronecker delta selects only these particles. The choice of the reference direction has no influence on this parameter since the absolute value is formed *before* averaging over all particles. It does not even change when choosing different reference directions for individual particles. Hence, this parameter can easily be applied to particles in a curved space. Within a spherical surface, it is necessary to decide which angles to measure. Several problems arise when using the angles between the chords,  $\varphi^{\text{ch}}$ :

- The angles are not additive, i.e. the difference angle  $\varphi_{lm}^{\text{ch}}$  between two bonds is not given by the difference of  $\varphi_m^{\text{ch}}$  and  $\varphi_l^{\text{ch}}$  which are the angles between the individual bonds and the reference direction.
- The parameter  $|\Psi_k|$  would be smaller than unity even for a perfectly symmetric arrangement of particles. This is due to the fact that the bond angular sum at a lattice point is smaller than  $2\pi$  in a space with positive Gaussian curvature.

For this reason, a different method is chosen to measure the bond angles. The bond angle  $\varphi$  is measured in the tangential plane  $E_t$  at the position of the considered central particle  $l$ . These angles can be calculating by projecting the bond vectors  $\mathbf{r}_{lm} = \mathbf{r}_{(m)} - \mathbf{r}_{(l)}$  into the tangential plane at point  $\mathbf{r}_{(l)}$ . This projections are performed for each center particle's position  $\mathbf{r}_{(l)}$  separately. The normal direction on the sphere surface at point  $\mathbf{r}_{(l)}$  is given by

$$\mathbf{e}_l = \frac{1}{|\mathbf{r}_{(l)}|} \cdot \mathbf{r}_{(l)}. \quad (4.15)$$

The projected bond vectors are thus calculated as,<sup>4</sup>

$$\tilde{\mathbf{r}}_{lm} = \mathbf{r}_{lm} - \langle \mathbf{r}_{lm}, \mathbf{e}_l \rangle \mathbf{e}_l, \quad (4.16)$$

which together with an reference direction in the plane  $\mathbf{e}_d$  (with  $|\mathbf{e}_d| = 1$ ) allow for the calculation of the bond angles  $\varphi_m$ . Calculating the bond order parameter requires knowledge of the “full” angles  $\varphi_m \in [0, 2\pi)$  which is obtained from the two relations

$$\cos \varphi_m = \frac{\langle \tilde{\mathbf{r}}_{lm}, \mathbf{e}_d \rangle}{|\tilde{\mathbf{r}}_{lm}|} \quad \text{and} \quad \sin \varphi_m = \frac{\langle \mathbf{e}_d \times \tilde{\mathbf{r}}_{lm}, \mathbf{e}_l \rangle}{|\tilde{\mathbf{r}}_{lm}|}. \quad (4.17)$$

### 4.3 $n$ -Particle Distributions in Generalized Coordinates

This section is concerned with a whole class of parameters which allow one to describe prominent features of the structure as well as disordering processes.

A melting parameter suited for both dusty plasma experiments and also for computer simulations—especially Monte Carlo simulations—has to meet several demands:

- The parameter should not require precise knowledge of the internal energy or its fluctuations. It is calculated from the particle positions. This is important for experiments since these positions can be measured with high accuracy, while measuring the internal energy of the dust sub-system is challenging due to the energy exchange with the surrounding plasma and with the neutral gas.
- The parameter should not require knowledge of the true particle trajectories. It is calculated from snapshots of the configuration and is invariant when changing the order of these snapshots. Moreover, it does not require labeled particles, but instead is invariant when two uniform particles are exchanged. This demand is essential for the application of the melting parameter to results from MC simulations without any concern about how to map the MC dynamics onto a true time dynamics.
- The parameter should take into account the symmetry of the Hamiltonian. When, for example, the Hamiltonian is invariant under rotation, the parameter is invariant under rotation of the entire system as well.

---

<sup>4</sup> $\langle \mathbf{a}, \mathbf{b} \rangle$  denotes the scalar product of the vectors  $\mathbf{a}$  and  $\mathbf{b}$ .

A well known quantity which fulfills all these criteria is the spatial  $N$ -particle density  $\rho_N(\mathbf{r}_1, \dots, \mathbf{r}_N) = \rho_N(\mathbf{R})$ , i.e. the spatial part of the canonical phase-space distribution of the ensemble. A detailed introduction to distribution functions in statistical mechanics is for example given in Ref. [129]. The relation between spatial density and canonical phase-space distribution is briefly sketched in the following.

The Hamiltonian of a classical  $N$ -particle system without velocity dependent forces, Eq. (3.3), can be separated into a sum of a spatial part and a momentum part. For this reason, the full phase-space distribution can be factorized as

$$\begin{aligned} \mathcal{P}_N(\mathbf{P}, \mathbf{R}) &= \frac{1}{N!} \frac{1}{Z} e^{-\frac{\mathcal{H}(\mathbf{P}, \mathbf{R})}{k_B T}} \\ &= \underbrace{\frac{1}{N!} \frac{1}{Z_R} e^{-\frac{\mathcal{H}_R(\mathbf{R})}{k_B T}}}_{=\rho_N(\mathbf{R})} \cdot \underbrace{\frac{1}{(2\pi m k_B T)^{3N/2}} \exp\left\{-\sum_{i=1}^N \frac{\mathbf{p}_i^2}{2m k_B T}\right\}}_{=f_N(\mathbf{P})}, \end{aligned} \quad (4.18)$$

where the spatial part of the partition function is defined as

$$Z_R = \frac{1}{N!} \int d^{3N} \mathbf{R} e^{-\frac{\mathcal{H}_R(\mathbf{R})}{k_B T}}, \quad (4.19)$$

which has the dimension of a  $3N$  dimensional volume. It is readily shown that the momentum part is normalized and the spatial part is normalized to the number of  $N$ -particle pairs,

$$1 = \int d^{3N} \mathbf{P} f_N(\mathbf{P}) \quad \text{and} \quad N! = \int d^{3N} \mathbf{R} \rho_N(\mathbf{R}). \quad (4.20)$$

The *canonical partition function* can be written as

$$Z = \frac{1}{h^{3N}} Z_R (2\pi m k_B T)^{3N/2} = \frac{Z_R}{\lambda_{\text{DB}}^{3N}} \quad \text{with} \quad \lambda_{\text{DB}} = \left( \frac{2\pi \hbar^2}{m k_B T} \right)^{1/2} = \frac{h}{\sqrt{2\pi m k_B T}} \quad (4.21)$$

denoting the *thermal de Broglie wavelength*. Since the momentum part of the partition function was readily solved analytically and has a simple temperature dependence, only the spatial part is analyzed in the following.

On the one hand, the spatial  $N$ -particle density  $\rho_N(\mathbf{R})$  contains all information about the dust structure—including its temperature dependence. On the other hand, sampling this quantity in computer simulations or in experiments is beyond reach due to its high dimensionality. It is appropriate to introduce reduced densities  $\rho_n(\mathbf{r}_1, \dots, \mathbf{r}_n)$  which depend on the coordinates of  $n \leq N$  particles only. Formally, they are obtained from  $\rho_N$  by integration over the remaining  $N - n$  coordinates as

$$\rho_n(\mathbf{r}_1, \dots, \mathbf{r}_n) = \frac{1}{(N - n)!} \int d^3 \mathbf{r}_{n+1} \dots \int d^3 \mathbf{r}_N \rho_N(\mathbf{R}). \quad (4.22)$$

For identical particles,  $\rho_N$  is invariant under particle permutation and so  $\rho_n$  is invariant under permutation of the  $n$  positions. Moreover, it is not important which positions are fixed and

which ones are integrated over in Eq. (4.22). The normalization of  $\rho_n$  is  $N!/(N-n)!$  which is the number of  $n$ -particle pairs, e.g. the normalization of the spatial density  $\rho_1$  is  $N$  and the normalization of the pair density  $\rho_2$  is  $N(N-1)$ .

In practical applications,  $\rho_N$  is usually unknown but different snapshots of the many particle configuration serve as input data. The subjects of this thesis are classical systems with discrete particle positions. These positions are denoted by  $(\mathbf{r}_{(1)}, \dots, \mathbf{r}_{(N)})$ , where the index in brackets refers to the index of the particle. The reduced densities in this case are given as the ensemble average over a sum of products of  $\delta$ -functions,

$$\rho_n(\mathbf{r}_1, \dots, \mathbf{r}_n) = \left\langle \underbrace{\sum_{i=1}^N \sum_{j=1}^{N'} \dots \sum_{z=1}^{N'}}_{n \text{ sums}} \underbrace{\delta(\mathbf{r}_1 - \mathbf{r}_{(i)}) \delta(\mathbf{r}_2 - \mathbf{r}_{(j)}) \dots \delta(\mathbf{r}_n - \mathbf{r}_{(z)})}_{\text{product of } n \text{ } \delta\text{-functions}} \right\rangle. \quad (4.23)$$

Since all  $n$  indices have to be different, summands with at least one pair of identical indices are excluded which is indicated by the prime at the sum symbol. For example, the pair density of discrete particles is given by

$$\rho_2(\mathbf{r}_1, \mathbf{r}_2) = \left\langle \sum_{i=1}^N \sum_{j=1}^{N'} \delta(\mathbf{r}_1 - \mathbf{r}_{(i)}) \delta(\mathbf{r}_2 - \mathbf{r}_{(j)}) \right\rangle. \quad (4.24)$$

The next step is to simplify  $\rho_n$  further making use of the known symmetries. Symmetries of the Hamiltonian are also found in the densities  $\rho_N$  and  $\rho_n$ . When the Hamiltonian is for example invariant under translation, the average density is also invariant under translation.<sup>5</sup>

Against this background, a new set of coordinates is introduced,  $(Q, B)$  with  $\dim Q = \alpha$ ,  $\dim B = \beta$  and  $\alpha + \beta = 3n$ . At this point, it should be noted that  $Q$  and  $B$  are  $n$ -particle coordinates in general while  $\mathbf{r}_1, \dots, \mathbf{r}_n$  are one-particle coordinates. For an appropriate choice of these coordinates,  $\rho_n$  is independent of all components of  $B$ , as a consequence of symmetries of the Hamiltonian. In this case, the density in the new variables  $\rho_n \rightarrow \tilde{\rho}_n$  is only a function of  $\alpha$  arguments. The pair density of a homogeneous system for example only depends on the distance of the two positions.

The coordinate transformation for the new coordinates is defined by  $(\mathbf{r}_1, \dots, \mathbf{r}_n) = \Phi(Q, B)$ , and  $|\mathcal{J}\Phi(Q, B)|$  denotes the Jacobi determinant. The  $n$ -particle distribution function in the new variables is formally defined as

$$\tilde{\rho}_n(Q) = \underbrace{\int d^\beta B}_{V_n(Q)} \underbrace{|\mathcal{J}\Phi(Q, B)| \rho_n[\Phi(Q, B)]}_{\text{independent of } B} = V_n(Q) \cdot \rho_n[\Phi(Q, B)]. \quad (4.25)$$

While the spatial coordinates depend on both  $Q$  and  $B$ , the density does not depend on  $B$  and, therefore, the above equation is valid for any choice of the irrelevant coordinates  $B$ .

<sup>5</sup>Every single realization of discrete particle positions is of course not invariant under a general translation, but the ensemble average as thermodynamic observable has to be invariant.

For practical purposes, the generalized density is again calculated as the ensemble average

$$\tilde{\rho}_n(Q) = \left\langle \underbrace{\sum_{i=1}^N \sum_{j=1}^{N'} \dots \sum_{z=1}^{N'}}_{n \text{ sums}} \delta [Q - \Phi^{-1}(\mathbf{r}_{(i)}, \dots, \mathbf{r}_{(z)})] \right\rangle, \quad (4.26)$$

where  $\Phi^{-1}$  is the inverse coordinate transformation and the  $\alpha$ -dimensional  $\delta$ -function compares all components of  $Q$ .

Note that the definition of the distribution in generalized coordinates, Eq. (4.25), includes the volume element. The normalization of the new density is

$$\int d^\alpha Q \tilde{\rho}_n(Q) = \frac{N!}{(N-n)!}, \quad (4.27)$$

without an additional volume element. When plotting the distribution, it is most feasible to eliminate the volume element by considering the ratio  $\tilde{\rho}_n/V_n$  which has the dimension *particles per volume to the power of  $n$* . As discussed below, it is often possible to divide by the *ideal  $n$ -particle density*  $\tilde{\rho}_n^{\text{id}} \propto V_n$  in order to obtain a dimensionless quantity  $g_n = \tilde{\rho}_n/\tilde{\rho}_n^{\text{id}}$  that approaches unity for uncorrelated systems.

The concept of  $n$ -particle distribution in generalized coordinates is in the following carried out for *pairs* and *triples* of particles in both extended systems as well as in spherical systems. For isotropic homogeneous system, this leads to the well-known radial *pair distribution function*  $g(r)$ .

### 4.3.1 Pair Distribution Function

The first test system for the  $n = 2$  particle distribution function is an extended system of  $N$  classical particles in a volume  $V$ , where the thermodynamic limit  $N \rightarrow \infty$  and  $V \rightarrow \infty$  with constant density  $N/V = \rho_0$  is considered. Two properties have to be met:

- **Homogeneity:** There is no external potential. The Hamiltonian and consequently the pair density are invariant under translation, i.e. the position of the pair does not matter.
- **Isotropy:** The pair-wise interaction potential depends only on the modulus of the pair distance.<sup>6</sup> The Hamiltonian and consequently the pair density is invariant under rotation, i.e. the orientation of the pair does not matter.

The appropriate coordinate system to describe  $\rho_2$  uses Cartesian coordinates  $\mathbf{R}$  for the first position<sup>7</sup> and spherical polar coordinates  $(r, \vartheta, \varphi)$  for the second position relative to the first one. In these coordinates,  $r$  is the radial pair distance. Due to the translation invariance,  $\rho_2$

<sup>6</sup>In principle, the following argumentation does not rely on pair-wise interaction potentials but is valid also for higher order potentials as long as they are invariant under rotation. However, most of the interaction potentials of interest are pair potentials.

<sup>7</sup>Often,  $\mathbf{R}$  is defined as the center-of-mass coordinate, but it is more useful for the following derivations to define it as the position of the first particle.

does not depend on  $\mathbf{R}$  and it does not depend on  $\vartheta$  and  $\varphi$  due to the isotropy. Following the notation above, the relevant coordinate is  $Q = \{r\}$  with  $\alpha = 1$  and the irrelevant coordinates are  $B = \{\mathbf{R}, \vartheta, \varphi\}$  with  $\beta = 5$ . The functional determinant of the coordinate transformation is given by  $|\mathcal{J}\Phi(Q, B)| = r^2 \sin \vartheta$  and the volume element is

$$V_2(r) = \int d^3 \mathbf{r} \int_0^\pi d\vartheta \int_0^{2\pi} d\varphi r^2 \sin \vartheta = V \cdot 4\pi r^2. \quad (4.28)$$

The knowledge of the coordinate transformation  $\Phi$  itself is less important at this point. It is sufficient to know how  $r = |\mathbf{r}_1 - \mathbf{r}_2|$  is calculated from the two Cartesian positions in order to sample  $\tilde{\rho}_2$  as an ensemble average,

$$\tilde{\rho}_2(r) = \left\langle \sum_{i=1}^N \sum_{j=1}^N \delta [r - |\mathbf{r}_{(j)} - \mathbf{r}_{(i)}|] \right\rangle. \quad (4.29)$$

In an ideal system with the same overall density  $\rho_0$ , the pair density is simply given by  $\rho_2(\mathbf{r}_1, \mathbf{r}_2) = \rho_0^2$ . The ideal pair density in generalized coordinates  $\tilde{\rho}_2^{\text{id}}$  is obtained by application of Eq. (4.25) as

$$\tilde{\rho}_2^{\text{id}}(r) = \int d^3 \mathbf{R} \int_0^\pi d\vartheta \int_0^{2\pi} d\varphi \rho_0^2 = \rho_0^2 \cdot V \cdot 4\pi r^2 = N \cdot \rho_0 \cdot 4\pi r^2, \quad (4.30)$$

and

$$g_2(r) = \frac{1}{N} \frac{\tilde{\rho}_2(r)}{4\pi r^2 \rho_0} \quad (4.31)$$

is the well-known radial *pair distribution function* (PDF). This function approaches unity for large  $r$  at low coupling as shown in Fig. 5.1 (p. 56).

### 4.3.2 Center-Two-Particle Distribution Function

While the radial pair distribution function is well suited for the investigation of the structure in homogeneous systems, several issues surface for the spherical confined clusters. On the one hand, the distribution of pairs may depend on the position within the cluster and, on the other hand, a function that depends on the modulus of the pair distance only cannot distinguish between intra-shell and inter-shell pairs.

The unfitness of the radial pair distribution for spherical clusters can be understood when reconsidering the assumptions made when deriving this quantity in Sec. 4.3.1. The first assumption there was that the system is homogeneous and this is apparently violated for a spherically confined cluster. The considered cluster of  $N$  particles still meets one of the properties discussed above:

- **Isotropy:** The pair-wise interaction potential depends only on the modulus of the pair distance and the confinement potential only on the modulus of the distance from center of the trap. The Hamiltonian, Eq. (3.3), and consequently the pair density is invariant under rotation with respect to the center of the trap.

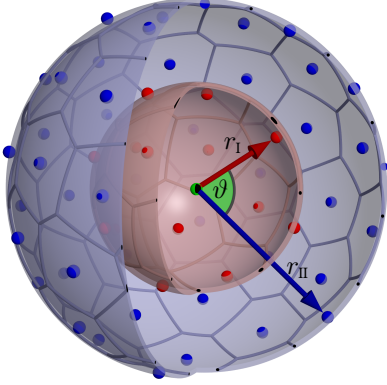


**Figure 4.4:** Coordinate system  $Q = (r_I, r_{II}, \vartheta)$  of the center-two-particle distribution. The radial coordinates of the two positions are denoted by  $r_I$  and  $r_{II}$  and  $\vartheta$  is the angular pair distance with respect to the trap center marked by a black dot. For better visibility, the particles are colored corresponding to their shell affiliation, where the very inner shell consists of one particle only in the center. In addition, the intra-shell Voronoi diagrams are sketched in gray.

The appropriate coordinate system to describe  $\rho_2$  consists of spherical polar coordinate  $(r_I, \vartheta_1, \varphi_1)$  for the first position and spherical polar coordinates  $(r_{II}, \vartheta, \varphi_2)$  for the second position. The  $z$ -axis of the second coordinate system is chosen along  $\mathbf{r}_I$  so that  $\vartheta$  describes the *angular pair distance* with respect to the trap center, see Fig. 4.4. Due to the rotational invariance,  $\tilde{\rho}_2$  can only depend on the two radial coordinates and on the angular pair distance [56, 130, 131]. The relevant coordinates here are  $Q = \{r_I, r_{II}, \vartheta\}$  with  $\alpha = 3$  and the irrelevant coordinates are  $B = \{\vartheta_1, \varphi_1, \varphi_2\}$  with  $\beta = 3$ . REHMUS *et al.* also used these coordinates in order to visualize electron correlations in hydrogen anions and in helium atoms [132, 133].

The functional determinant of the coordinate transformation is given by  $|\mathcal{J}\Phi(Q, B)| = r_I^2 r_{II}^2 \sin \vartheta_1 \sin \vartheta$  and the volume element is

$$V_2(r_I, r_{II}, \vartheta) = \int_0^\pi d\vartheta_1 \int_0^{2\pi} d\varphi_1 \int_0^{2\pi} d\varphi_2 r_I^2 r_{II}^2 \sin \vartheta_1 \sin \vartheta = 8\pi^2 r_I^2 r_{II}^2 \sin \vartheta. \quad (4.32)$$

While the explicit form of the coordinate transformation  $\Phi$  is of minor interest, it is again sufficient to know how to calculate  $Q$  from two given positions. The pair density  $\tilde{\rho}_2$  is sampled as the ensemble average,

$$\tilde{\rho}_2(r_I, r_{II}, \vartheta) = \left\langle \sum_{i=1}^N \sum_{j=1}^N \delta [r_I - |\mathbf{r}_{(i)}|] \cdot \delta [r_{II} - |\mathbf{r}_{(j)}|] \cdot \delta \left[ \vartheta - \cos^{-1} \left( \frac{\mathbf{r}_{(i)} \cdot \mathbf{r}_{(j)}}{|\mathbf{r}_{(i)}| \cdot |\mathbf{r}_{(j)}|} \right) \right] \right\rangle, \quad (4.33)$$

which is called *center-two-particle* (C2P) distribution referring to the chosen coordinate system.

The external confining potential imprints an inhomogeneous structure to the system. It is therefore not sensible to calculate  $\tilde{\rho}_2$  for a homogeneous density. The pseudo-ideal system considered at this point consists of homogeneously filled spherical shells. Hence, the density has a radial dependence only. This dependence is captured by the radial density which is defined as

$$\rho_1(\mathbf{r}) = \rho_1(r) = \frac{\tilde{\rho}_1(r)}{V_1(r)} = \frac{1}{4\pi r^2} \left\langle \sum_{i=1}^N \delta [r - |\mathbf{r}_{(i)}|] \right\rangle, \quad (4.34)$$

which has the dimension “*particles per volume*” due to the pre-factor. The only difference between the two functions  $\rho_1$  and  $\tilde{\rho}_1$  is the division by the volume element. The former density  $\rho_1(r)$  is defined as “particles per unit volume” at distance  $r$  from the trap center and is constant for a homogeneous system. The latter density  $\tilde{\rho}_1(r)$  in contrast is defined as “particles per shell with unit width” at radius  $r$  around the trap center. For a homogeneous system, this density grows with  $r^2$  as the volume of the shell grows.

The pair density of the pseudo-ideal system is considered as a product of one-particle densities and is written as

$$\rho_2^{\text{id}}(\mathbf{r}_1, \mathbf{r}_2) = \rho_1(\mathbf{r}_1) \cdot \rho_1(\mathbf{r}_2) = \rho_1(r_1) \cdot \rho_1(r_2). \quad (4.35)$$

The ideal pair density in generalized coordinates  $\tilde{\rho}_2^{\text{id}}(r_I, r_{\text{II}}, \vartheta)$  is obtained by application of Eq. (4.25) as

$$\begin{aligned} \tilde{\rho}_2^{\text{id}}(r_I, r_{\text{II}}, \vartheta) &= \int_0^\pi d\vartheta_1 \int_0^{2\pi} d\varphi_1 \int_0^{2\pi} d\varphi r_I^2 r_{\text{II}}^2 \sin \vartheta_1 \sin \vartheta \rho_1(r_I) \rho_1(r_{\text{II}}) \\ &= 8\pi^2 r_I^2 r_{\text{II}}^2 \sin \vartheta \rho_1(r_I) \rho_1(r_{\text{II}}) \end{aligned} \quad (4.36)$$

$$= \frac{1}{2} \sin \vartheta \tilde{\rho}_1(r_I) \tilde{\rho}_1(r_{\text{II}}). \quad (4.37)$$

The *center-two-particle correlation function* is defined as the ratio of two-particle density and pseudo-ideal two-particle density in generalized coordinates

$$g_2(r_I, r_{\text{II}}, \vartheta) = \frac{2}{\sin \vartheta} \frac{\tilde{\rho}_2(r_I, r_{\text{II}}, \vartheta)}{\tilde{\rho}_1(r_I) \cdot \tilde{\rho}_1(r_{\text{II}})}. \quad (4.38)$$

This function is well suited to visualize angular correlation within shells (for  $r_I$  and  $r_{\text{II}}$  chosen from the same shell) and between different shells (for  $r_I$  and  $r_{\text{II}}$  chosen from different shells). When  $r_I$  and  $r_{\text{II}}$  are chosen from different shells, the C2P correlation function, Eq. (4.38), is unity for a system without inter-shell correlations. The correlation function is also defined as  $g_2 = 1$  for those radii where the density is exactly zero and where consequently the ratio in Eq. (4.37) is undefined.

### 4.3.3 Triple-Correlation Function in Macroscopic Systems

The following sections are dedicated to the correlations of three particles. The motivation for investigation of triples is the sensitivity to the bond order. Considering a perfect 2D hexagonal lattice, nearest neighbor triples are found with multiples of  $60^\circ$  as bond angles and these angles are distinguished also for distant neighbors. While the *global bond order parameter* [125–127] is an excellent tool to resolve the bond order in planar systems, it lacks in an appropriate global reference direction in spherical shells. Hence, the *triple-correlation function* (TCF) is introduced for spherical systems. However, this quantity is first present for planar 2D systems here, since these systems will serve as a test case. As done for the PDF in Sec. 4.3.1, a macroscopic system of



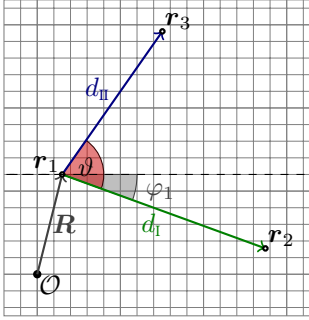


**Figure 4.5:** Coordinate system of the triple-correlation function in planar 2D systems. The two pair distances  $r_1$  and  $r_{II}$  together with the bond angle  $\vartheta$  represent the relevant coordinates  $Q$ . The first position  $\mathbf{R}$  and the angle  $\varphi_1$  are irrelevant coordinates  $B$  in a homogeneous isotropic system. For completeness, the Cartesian coordinates  $\mathbf{r}_1$ ,  $\mathbf{r}_2$  and  $\mathbf{r}_3$  of the three positions are also labeled.  $\mathcal{O}$  is the origin.

$N$  classical particles in a volume  $V$ , where the thermodynamic limit  $N \rightarrow \infty$  and  $V \rightarrow \infty$  with constant density  $N/V = \rho_0$  is considered.<sup>8</sup> Two properties shall be met as previously mentioned in the introduction of the PDF:

- **Homogeneity:** There is no external potential. The Hamiltonian and consequently the pair density is invariant under translation, i.e. the position of the pair does not matter.
- **Isotropy:** The pair-wise interaction potential depends only on the modulus of the pair distance. The Hamiltonian and consequently the pair density is invariant under rotation, i.e. the orientation of the pair does not matter.

One appropriate coordinate system to describe  $\rho_3$  uses Cartesian coordinates  $\mathbf{R}$  for the first position, polar coordinates  $(d_1, \varphi_1)$  for the second position relative to the first one, and a second set of polar coordinates  $(d_{II}, \vartheta)$  for the third position relative to the first one. The  $x$ -axis of the third coordinates is chosen along  $\mathbf{r}_{12} = \mathbf{r}_2 - \mathbf{r}_1$ , so that  $\vartheta$  describes the *bond angle* between the two pair distances, see Fig. 4.5.

The density  $\rho_3$  cannot depend on the position  $\mathbf{R}$  of the triple due to the homogeneity of the system and it cannot depend on the orientation  $\varphi_1$  of the triple due to the isotropy. The relevant coordinates in this case are  $Q = \{d_1, d_{II}, \vartheta\}$  with  $\alpha = 3$  and the irrelevant coordinates are  $B = \{\mathbf{R}, \varphi_1\}$  with  $\beta = 3$  due to the two components of  $\mathbf{R}$ . The functional determinant of the coordinate transformation is given by  $|\mathcal{J}\Phi(Q, B)| = d_1 d_{II}$  and the volume element is calculated as

$$V_3(d_1, d_{II}, \vartheta) = 2 \cdot \int d^2 \mathbf{R} \int_0^{2\pi} d\varphi_1 d_1 d_{II} = V \cdot 4\pi d_1 d_{II}, \quad (4.39)$$

where the factor 2 in front the integral has to be included, since the orientation of the bond angle is not resolved. Bond angles above  $\vartheta' > \pi$  are mapped to the interval  $[0 : \pi]$  by  $\vartheta' \mapsto 2\pi - \vartheta'$ .

The important aspect of the coordinate transformation  $\Phi$  is as before the calculation of the relevant coordinates  $Q$  from three given positions. The three-particle density  $\tilde{\rho}_3$  is sampled as

<sup>8</sup>Despite the dimensionality of two, the symbols  $V$  and  $\rho$  are used for the 2D volume and the areal density.

the ensemble average

$$\tilde{\rho}_3(d_1, d_{\parallel}, \vartheta) = \left\langle \sum_{i=1}^N \sum_{j=1}^N \sum_{k=1}^N \delta [r_1 - |\mathbf{r}_{(j)} - \mathbf{r}_{(i)}|] \cdot \delta [r_{\parallel} - |\mathbf{r}_{(k)} - \mathbf{r}_{(i)}|] \cdot \delta \left[ \vartheta - \cos^{-1} \left( \frac{(\mathbf{r}_{(j)} - \mathbf{r}_{(i)}) \cdot (\mathbf{r}_{(k)} - \mathbf{r}_{(i)})}{|\mathbf{r}_{(j)} - \mathbf{r}_{(i)}| \cdot |\mathbf{r}_{(k)} - \mathbf{r}_{(i)}|} \right) \right] \right\rangle. \quad (4.40)$$

In an ideal system with the same overall density  $\rho_0$ , the three-particle density is simply given by  $\rho_3(\mathbf{r}_1, \mathbf{r}_2, \mathbf{r}_3) = \rho_0^3$ . The ideal three-particle density in generalized coordinates  $\tilde{\rho}_3^{\text{id}}$  is obtained by application of Eq. (4.25) as

$$\tilde{\rho}_3^{\text{id}}(d_1, d_{\parallel}, \vartheta) = 2 \cdot \int d^2 \mathbf{R} \int_0^{2\pi} d\varphi_1 d_1 d_{\parallel} \cdot \rho_0^3 = \rho_0^3 \cdot V \cdot 4\pi d_1 d_{\parallel} = N \cdot \rho_0^2 \cdot 4\pi d_1 d_{\parallel}, \quad (4.41)$$

and the ratio of sampled density and this ideal density,

$$g_3(d_1, d_{\parallel}, \vartheta) = \frac{1}{N} \frac{\tilde{\rho}_3(d_1, d_{\parallel}, \vartheta)}{4\pi d_1 d_{\parallel} \rho_0^2} \quad (4.42)$$

is the *triple-correlation function*. This dimensionless function can be understood as the relative probability of finding a triple of particles forming a triangle with edge lengths  $d_1$ ,  $d_{\parallel}$  and with an enclosed angle of  $\vartheta$ .

The choice of the coordinate system is, in a way, ambiguous. The triangle which is formed by three particles is described by two side lengths and the enclosed angle. A complete description is also possible by three side lengths or by one length and two angles. However, the Jacobi determinant becomes unwieldy for the latter two coordinate systems. In the last coordinate system, the valid range of third length  $d_{\parallel}$  would depend on the first two lengths.

Moreover, that coordinate system is not appropriate for a description three particles along one line, since it requires an extremely high resolution of all three lengths to resolve the bond angles in that configuration. Consider three particles aligned along the  $x$ -axis at  $x_1 = -d$ ,  $x_2 = 0$  and  $x_3 = d$ . When displacing the left particle in  $y$ -direction by  $\Delta y$ , the changes of the bond lengths  $d_{12}$  and  $d_{13}$  are both on the order of  $\Delta y^2$ . This means that the considered particle displacement is poorly resolved by a coordinate system that consists of the three length of the triangle formed by three particles. As this configuration of three is often realized in dust clusters, e.g. for a hexagonal lattice, the coordinate system is inappropriate for practical applications.

The TCF can also be calculated for 3D homogeneous isotropic systems and the derivation is analogous. Instead of plane polar coordinates, spherical polar coordinates have to be used to describe the second and the third position. The first two angles ( $\vartheta_1, \varphi_1$ ) as well as the second azimuth angle  $\varphi_2$  are irrelevant due to the symmetries. With the functional determinant  $|\mathcal{J}\Phi^{3D}| = d_1^2 d_{\parallel}^2 \sin \varphi_1 \sin \vartheta$ , the ideal density is obtained as

$$(3D) \quad \tilde{\rho}_3^{\text{id}}(d_1, d_{\parallel}, \vartheta) = \int d^3 \mathbf{R} \int_0^{\pi} d\vartheta_1 \int_0^{2\pi} d\varphi_1 \int_0^{2\pi} d\varphi_2 d_1^2 d_{\parallel}^2 \sin \vartheta_1 \sin \vartheta \cdot \rho_0^3 \\ = \rho_0^3 \cdot V \cdot 8\pi^2 d_1^2 d_{\parallel}^2 \sin \vartheta = N \cdot \rho_0^2 \cdot 8\pi^2 d_1^2 d_{\parallel}^2 \sin \vartheta. \quad (4.43)$$

The TCF for extended 3D systems is given here for completeness without showing examples.

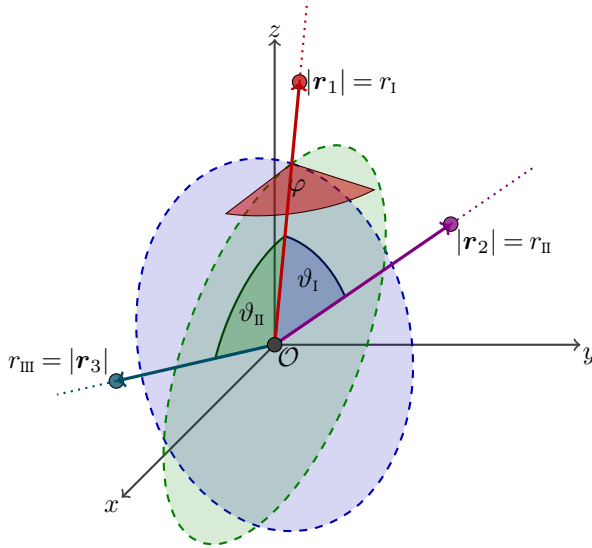


**Figure 4.6:** Coordinate system for describing the three-particle density in spherical clusters. The radial coordinates of the three positions are denoted by  $r_I$ ,  $r_{II}$  and  $r_{III}$ . The angular pair distance between first and second (third) particle is denoted by  $\vartheta_I$  ( $\vartheta_{II}$ ) and  $\varphi$  describes the “bond angle” of the two pair connections. For the sake of clarity, the coordinates  $B = \{\vartheta_0, \varphi_0, \varphi_1\}$  are omitted in this sketch.

#### 4.3.4 Triple-Correlation Function in Spherical Shells

The intra-shell structure of spherical clusters is one of the main aspects of this thesis. While the shells in 2D clusters are simple rings without a sophisticated intra-shell structure, the particle arrangement within the spherical shells shows interesting phenomena. There are for example “magic numbers” of particles which allow for a highly symmetric configuration on the shell [57, 89, 134] and for large clusters, the intra-shell structure shows features similar to an extended 2D lattice. In this section, a modification of the *triple-correlation function* for spherical clusters in 3D is introduced. The goal is to obtain a parameter which is sensitive to the bond order within a spherical shell and which also allows to resolve structural transitions.

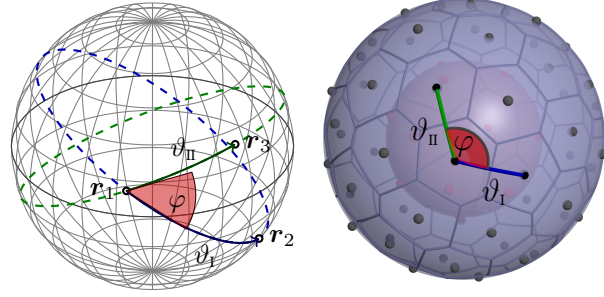
A spherically confined Coulomb or Yukawa cluster with  $N$  particles meets one symmetry property as previously mentioned in the introduction of the center-two-particle function:

- **Isotropy:** The pair-wise interaction potential depends only on the modulus of the pair distance and the confinement potential only on the modulus of the distance from the center of the trap. The Hamiltonian, Eq. (3.3), and consequently the pair density is invariant under rotation with respect to the center of the trap.

The appropriate coordinate system to describe  $\rho_3$  consists of spherical polar coordinates  $(r_I, \vartheta_0, \varphi_0)$  for the first position, spherical polar coordinates  $(r_{II}, \vartheta_I, \varphi_1)$  for the second position and a third set of spherical polar coordinates  $(r_{III}, \vartheta_{II}, \varphi)$  describing the last position. The  $z$ -axis of the second coordinate system is chosen along  $\mathbf{r}_I$  so that  $\vartheta_I$  describes the first *angular pair distance* with respect to the trap center, see Fig. 4.6. The  $z$ -axis of the third coordinate system is also chosen along  $\mathbf{r}_I$  so that  $\vartheta_{II}$  describes the second *angular pair distance*. The  $y$ -axis of the latter is chosen along  $\mathbf{r}_I \times \mathbf{r}_{II}$  and  $\varphi$  is interpreted as “bond angle” for particles within one shell.

Because of the invariance of the Hamiltonian under rotation, the three-particle density  $\rho_3$  cannot depend on the coordinates  $B = \{\vartheta_0, \varphi_0, \varphi_1\}$  with the dimension  $\beta = 3$ . Unfortunately, the remaining relevant coordinates  $Q = \{r_I, r_{II}, r_{III}, \vartheta_I, \vartheta_{II}, \varphi\}$  still have a dimension of  $\alpha = 6$ . One histogram with 100 bins in for each coordinate and with two-byte numbers as counters would

**Figure 4.7:** Left: Coordinate system for describing the *intra-shell* three-particle density in spherical clusters. The angular pair distance between first and second (third) particle is denoted by  $\vartheta_1$  ( $\vartheta_{\text{II}}$ ) and  $\varphi$  describes the “bond angle” of the two pair connections.  $\varphi$  is the angle of intersection of the two great circles each connecting one particle pair. Right: The three coordinates of the TCF are illustrated for three particles from the outer shell of a cluster from a MC simulation.



require  $2 \times 10^{12}$  B=2 TB of storage. Fortunately, the key interest is the intra-shell structure, since radial structure and inter-shell correlation are well resolved by the C2P function. When one thin shell  $s$  is investigated by the TCF, the selected particles all have approximately the same radial coordinate  $r_1 \approx r_{\text{II}} \approx r_{\text{III}} \approx R_s$ —namely the radius of that shell. Hence, the particle position are projected onto the sphere with radius  $R_s$  and the investigated density  $\rho_3$  is of the dimension “particle pairs per area to the power of three”. The relevant coordinates that describe this density are  $Q = \{\vartheta_1, \vartheta_{\text{II}}, \varphi\}$  with  $\alpha = 3$  and the irrelevant coordinates remain  $B = \{\vartheta_0, \varphi_0, \varphi_1\}$  with  $\beta = 3$ . These coordinates are illustrated in Fig. 4.7.

The functional determinant of the spherical TCF coordinate transformation is given by  $|\mathcal{J}\Phi(Q, B)| = R_s^3 \sin \vartheta_0 \sin \vartheta_1 \sin \vartheta_{\text{II}}$  and the volume element is calculated as

$$V_3(\vartheta_1, \vartheta_{\text{II}}, \varphi) = 2 \cdot \int_0^\pi d\vartheta_0 \int_0^{2\pi} d\varphi_0 \int_0^{2\pi} d\varphi_1 R_s^6 \sin \vartheta_0 \sin \vartheta_1 \sin \vartheta_{\text{II}} = 16\pi^2 R_s^6 \sin \vartheta_1 \sin \vartheta_{\text{II}}, \quad (4.44)$$

where again the factor 2 in front the integral has to be included since the orientation of the bond angle is not resolved. Reflex bond angles  $\vartheta' > \pi$  are mapped to the interval  $[0 : \pi]$  by  $\vartheta' \mapsto 2\pi - \vartheta'$ .

The sampled three-particle density  $\tilde{\rho}_3$  is compared to the density of a suitable ideal system. An appropriate ideal reference system is a spherical shell with the same radius  $R_s$  and the same number of particles  $N_s$ . The areal particle density of this homogeneously filled shell is  $\rho_0 = N_s/4\pi R_s^2$  and the ideal three particle density is simple given by this density cubed. The ideal three-particle density in spherical TCF coordinates  $\tilde{\rho}_3^{\text{id}}$  is obtained by application of Eq. (4.25) as

$$\begin{aligned} \tilde{\rho}_3^{\text{id}}(\vartheta_1, \vartheta_{\text{II}}, \varphi) &= 2 \cdot \int_0^\pi d\vartheta_0 \int_0^{2\pi} d\varphi_0 \int_0^{2\pi} d\varphi_1 R_s^6 \sin \vartheta_0 \sin \vartheta_1 \sin \vartheta_{\text{II}} \cdot \rho_0^3 \\ &= \rho_0^3 \cdot 16\pi^2 R_s^6 \sin \vartheta_1 \sin \vartheta_{\text{II}} \\ &= \frac{N_s^3}{4\pi} \sin \vartheta_1 \sin \vartheta_{\text{II}}. \end{aligned} \quad (4.45)$$

When plotting and discussing the *triple-correlation function*, this term refers to the ratio of sampled and ideal densities

$$g_3(\vartheta_1, \vartheta_{\text{II}}, \varphi) = \frac{\tilde{\rho}_3(\vartheta_1, \vartheta_{\text{II}}, \varphi)}{\tilde{\rho}_3^{\text{id}}(\vartheta_1, \vartheta_{\text{II}}, \varphi)}. \quad (4.46)$$

---

In order to obtain a meaningful function of two coordinates, both  $\tilde{\rho}_3$  and  $\tilde{\rho}_3^{\text{id}}$  are integrated over an  $r_1$  range which corresponds to nearest neighbors. This means that one pair of nearest neighbors is chosen by the procedure and the positions of the other particles relative to this bond is resolved.

## 4.4 Reduced Entropy and Heat Capacity

In this section, an expression for the reduced entropy  $S^{(n)}$  is introduced. The idea to calculate a reduced entropy from  $n$ -particle distributions has been widely used for extended systems [135–137], especially in the context of glass-transitions [138, 139]. That entropy is calculated from the  $n$ -particle density in analogy with the full thermodynamic entropy  $S$ . It is shown how  $S^{(n)}$  can be computed from the reduced density in generalized coordinates  $\tilde{\rho}_n$ . The second step is to define a reduced the heat capacity  $c^{(n)}$  as a derivative of  $S^{(n)}$  with respect to the temperature.

The introduction of  $S^{(n)}$  is motivated by the importance of the thermodynamic entropy with respect to phase transitions on the one hand and its inaccessibility in most dusty plasma experiments on the other hand. A phase transition usually manifests itself already in the few-particle distribution, for example as a drop of the first peak height of the pair distribution function [28]. Therefore, the reduced entropy  $S^{(n)}$  is expected to resolve those transitions. In contrast to the analysis of the first peak height, the entire PDF including its long-range tail enters in  $S^{(2)}$ .

As shown in Sec. A.2 in the appendix, the entropy in the canonic ensemble can be expressed as a expectation value of the logarithm of the  $n$ -particle density. Moreover, the entropy can be split into a spatial contribution

$$S_R = -\frac{k_B}{N!} \int d^{3N} \mathbf{R} \log \{ \Delta l^{3N} \cdot \rho_N(\mathbf{R}) \} \cdot \rho_N(\mathbf{R}) \quad (4.47)$$

and a momentum contribution  $S_P$  for classical Hamiltonians without velocity dependent forces, see Sec. A.3. The length  $\Delta l$  had to be introduced to make the argument of the logarithm dimensionless. This length can be thought of as the spatial extension of a phase space cell. The only ambiguity caused by the actual choice of  $\Delta l$  is a constant offset in  $S_R$  which does not affect the temperature dependence as a key feature of  $S_R$ .

With the definitions of the spatial entropy, Eq. 4.47, and of the  $n$ -particle spatial distribution  $\rho_n(\mathbf{r}_1, \dots, \mathbf{r}_n)$ , Eq. 4.22, a *reduced  $n$ -particle entropy*  $S^{(n)}$  is introduced as

$$S^{(n)} = -k_B \frac{(N-n)!}{N!} \int d^3 \mathbf{r}_1 \dots \int d^3 \mathbf{r}_n \rho_n(\mathbf{r}_1, \dots, \mathbf{r}_n) \log \{ \Delta l^{3n} \rho_n(\mathbf{r}_1, \dots, \mathbf{r}_n) \} . \quad (4.48)$$

This definition is the perfect analogy of the thermodynamic entropy—more precisely, of its spatial part  $S_R$ —for the  $n$ -particle distribution and becomes equivalent for  $n = N$ . Formally, the logarithm is not defined for points of zero density. Because of the limit

$$\lim_{x \rightarrow 0} x \log(x) = 0 , \quad (4.49)$$

the above integral is well defined. When the entropy is calculated from histogram bins in applications, empty bins make no contribution.

As discussed above, the  $n$ -particle density often obeys certain symmetries and is described in appropriate coordinates  $(Q, B)$ . The integration over possible  $n$ -particle configurations is

performed in these new coordinates, where Eq. (4.25) is inverted to obtain  $\rho_n$  in Cartesian coordinates from  $\tilde{\rho}_n$  in the generalized coordinates,

$$\begin{aligned} S^{(n)} &= -k_B \frac{(N-n)!}{N!} \int d^\alpha Q \underbrace{\int d^\beta B |\mathcal{J}\Phi(Q, B)|}_{=V_n(Q)} \underbrace{\frac{\tilde{\rho}_n(Q)}{V_n(Q)} \log \left\{ \Delta l^{3N} \frac{\tilde{\rho}_n(Q)}{V_n(Q)} \right\}}_{\text{independent of } B} \\ &= -k_B \frac{(N-n)!}{N!} \int d^\alpha Q \tilde{\rho}_n(Q) \log \left\{ \Delta l^{3n} \frac{\tilde{\rho}_n(Q)}{V_n(Q)} \right\}. \end{aligned} \quad (4.50)$$

It should be noted at this point, that Eq. (4.50) is exact if the Hamiltonian and therefore the  $n$ -particle density is independent of  $B$ . The great advantage of Eq. (4.50) compared to Eq. (4.48) is that underlying distribution  $\tilde{\rho}_n$  is a function of  $\alpha$  variables instead of  $3n$  ( $2n$  for 2D systems) variables. The reduced  $n = 2$  particle entropy in homogeneous systems  $S^{(2)}$  for example is this way obtained from the PDF  $\tilde{\rho}_2(r)$  as a function with one argument.

The reduced entropies  $S^{(2)}$  and  $S^{(3)}$  are calculated for the radial pair distribution function, the center-two-particle distribution function and the triple-correlation function by applying Eq. (4.50). Since the choice of  $\Delta l$  has no qualitative influence on the further results, it is chosen equal to the unit of length,  $\Delta l = r_0$ . When the density  $\rho_n$  is expressed in units of  $r_0$ , the  $\Delta l$ -factor is unity and it is hence omitted in the following. A special case is represented by the spherical TCF, see Sec. 4.3.4, where  $\Delta l = R_s$  is chosen equal the average radius of the analyzed shell in order to cancel the factor  $R_s^6$  in the denominator which results from the volume element.

In practical applications,  $\tilde{\rho}_n(Q)$  is typically sampled as an  $\alpha$ -dimensional histogram. Section A.4 of the appendix describes how the entropy  $S^{(n)}$  is obtained from such a histogram. The comparability of entropies  $S^{(n)}$  with different degrees  $n$  is simplified by using an  $n$ -particle density which is normalized to unity in place of the number of pairs. Formally, this procedure represents the subtraction of the contribution for the number of pairs  $-\log(N!/(N-n)!)$ . However, this contribution is constant for any canonic ensemble due to the fixed particle number and the derived reduced heat capacity is not influenced by it.

The *heat capacity at constant volume*  $C_V$  in the canonic ensemble can be expressed as logarithmic temperature derivative of the entropy

$$\begin{aligned} C_V &= \frac{\partial U}{\partial T} = \frac{\partial}{\partial T} \left( \frac{k_B T^2}{Z} \frac{\partial Z}{\partial T} \right) \\ &= \frac{\partial}{\partial \log T} \underbrace{\frac{\partial}{\partial T} (k_B T \log Z)}_{=S} = \frac{\partial S}{\partial \log T}, \end{aligned} \quad (4.51)$$

where for spherical clusters, the fixed trap frequency  $\omega_0$  takes the place of the volume  $V$ . Therefore, the heat capacity at constant trap frequency is denoted by  $C_\omega$  in that case. In agreement with Eq. (4.51) the *reduced heat capacity*  $c^{(n)}$  is introduced for  $S^{(n)}$ , Eq. (4.48), as

$$c_V^{(n)} = \frac{\partial S^{(n)}}{\partial \log T} = -\frac{\partial S^{(n)}}{\partial \Gamma}. \quad (4.52)$$

The coupling parameter  $\Gamma$  and temperature  $T$  are inversely proportional at constant volume or constant trap frequency, respectively. Thus, the heat capacity is expressed as the entropy derivative with respect to the dimensionless coupling parameter. In practice, the reduced heat capacity is calculated as the derivative of the cubic spline that interpolates the measurements of  $S^{(n)}$  as a function of coupling parameter's logarithm  $\log \Gamma$ .

The full heat capacity per particle  $c_V$  and the reduced heat capacity  $c_V^{(n)}$  are similar quantities with respect to their definition as a temperature derivative of an entropy. One qualitative difference between these two quantities is how they are calculated. In a computer simulation,  $c_V$  is obtained from the fluctuation of the internal energy, while the particle positions are recorded in order to obtain the  $n$ -particle distribution  $\tilde{\rho}_n$ , the corresponding entropy  $S^{(n)}$  and finally the reduced heat capacity  $c_V^{(n)}$ . The former requires precise knowledge of the energy and the latter requires precise knowledge of the particle positions. For this reason,  $c_V^{(n)}$  is a promising candidate as a melting parameter for dust plasmas as well as for colloids. While the positions of the dust particles are accessible with high resolution [40, 48, 72, 140], measuring the energy of the dust (colloid) system is challenging due to the energy exchange with the surrounding plasma (fluid).



## Chapter 5

# Melting in Finite Dust Clusters

**S**tructural transitions in harmonically confined Yukawa and Coulomb clusters are the focus of this chapter. These clusters are qualitatively different from extended systems. While an extended 2D dust system has a hexagonal configuration in the solid phase, the circular shape of the harmonic confinement imprints a different structure to finite clusters. For this reason, small clusters are characterized by concentric rings. For larger particle numbers, the outer particles form rings reflecting the circular trap, while the inner particles arrange themselves in a hexagonal structure. Two different structural transition processes can be considered for small clusters. On the one hand, the *inter-shell melting* describes the loss of the relative orientation of different shells. On the other hand, the *radial melting* is the loss of radial order, where the shell structure vanishes.

An extended 3D Yukawa crystal can exist as a bcc-lattice or as an fcc-lattice depending on screening parameter  $\kappa$  and coupling strength  $\Gamma$  [38]. In contrast, the characteristic feature of a spherically confined cluster is a structure with spherical shells. Here, at least three transition processes can be considered. In addition to radial and inter-shell melting, the *intra-shell melting* is connected to the order within the shells. Listing three types of transitions shall not hide the fact, that the interplay between the processes is sophisticated.

In this chapter, the structural transitions in finite dust clusters are investigated. The center-two-particle and the triple-correlation function are applied as two new quantities in the context of these systems.

Before two and three-particle distribution functions in general coordinates and the corresponding entropies are calculated for finite dust clusters, this concept is tested in an extended 2D system. For a screening parameter  $\kappa = 1$ , such a system undergoes an phase transition at  $\Gamma = 187$  [28]. This phase transition is visible as a peak in the specific heat and it also causes a step-like decrease in the first peak height of the pair distribution function. In top part of Fig. 5.1, the PDF  $g(r)$  of this system is shown for a sequence of increasing coupling strengths, equally distributed on a logarithmic scale. Starting at low coupling, the peak heights increase gradually with  $\Gamma$  until a step-like increase is visible at the phase transitions. When  $\Gamma$  is further increased, the peak heights increase gradually again. Moreover a splitting of the second peak in  $g(r)$  sets in at the phase transition. The lower part of Fig. 5.1 shows the corresponding entropy  $S^{(2)}$

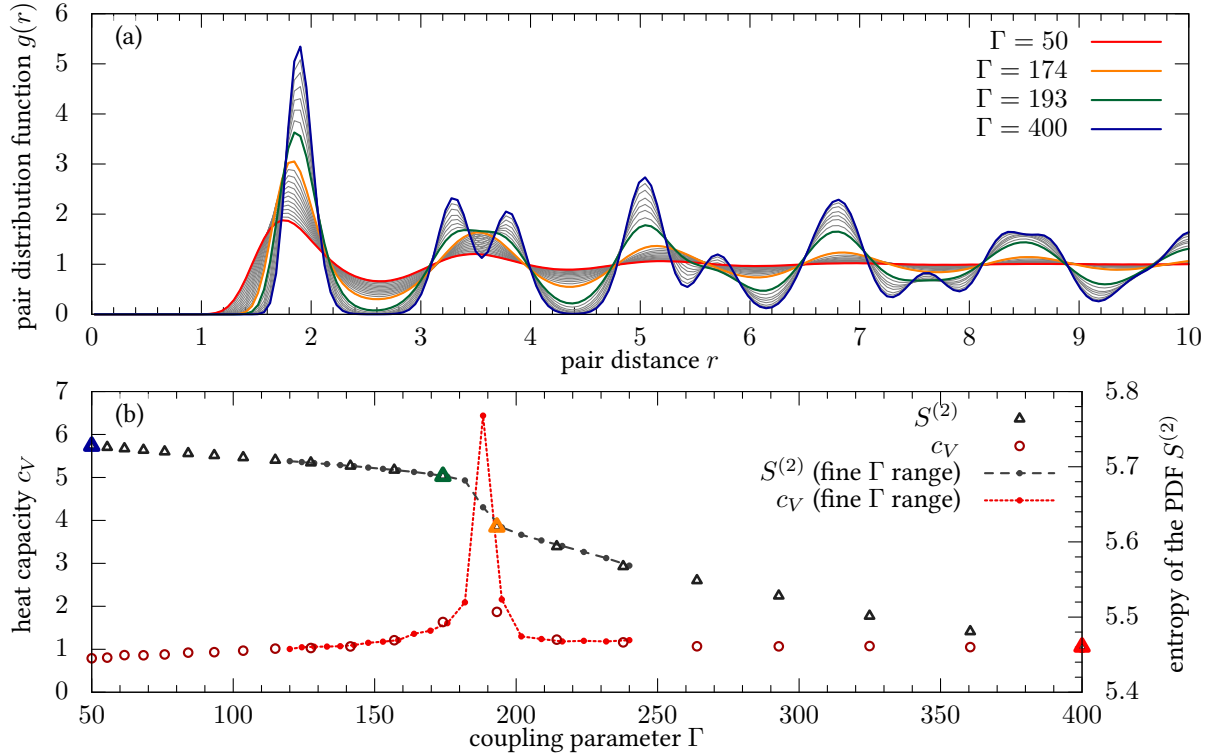


**Figure 5.1:** (a) Radial pair distribution function (PDF) in an extended 2D system for different coupling strengths. (b) The reduced entropy  $S^{(2)}$  of the PDF shows a step-like decrease around  $\Gamma = 187$ . This drop is found at the same coupling strengths as the peak in the specific heat capacity  $c_V$ . The plot is complemented by the data from a second simulation with a narrow  $\Gamma$  range around the phase transition. In both parts, four  $\Gamma$ -points in the solid phase (blue), at both sides of the transition (green, orange) and in the fluid phase (red) are highlighted. Data are from an MC simulation with periodic boundary conditions,  $N = 2000$  particles and a screening parameter  $\kappa = 1$ .

which can be interpreted as a measure of the disorder in  $g(r)$ . This quantity reflects the phase transition as a step-like decrease. The system undergoes an abrupt transition from a state of low order to a state of high order. In contrast to the first peak height, the long-range tail of  $g(r)$  enters  $S^{(2)}$ , since the latter is calculated from the full PDF.

Even though the reduced entropy from the PDF was sufficient for the identification of the phase transition, the TCF of this system is regarded in the following. For the later investigation of spherical cluster shells, it is important to know the characteristic features of the TCF for ordered and disordered structures. The extended 2D system is ideally suited for this purpose. In Fig. 5.2, the triple-correlation function of such a system is shown for two values of the coupling strength in the liquid and two in the solid phase. The choice of the  $d_1$ -integration range selects the first particle pair as nearest neighbors.<sup>1</sup> The virtual connection between these two particles is termed “bond”. Other particle positions are then described with respect to this bond by the second pair distance  $r_{II}$  and the “bond angle”  $\varphi$ . The term “bond angle” is most applicable when

<sup>1</sup>The definition of nearest “nearest neighbors” at this point is less strict as it is during the Voronoi analysis since only the pair distance is taken into account.

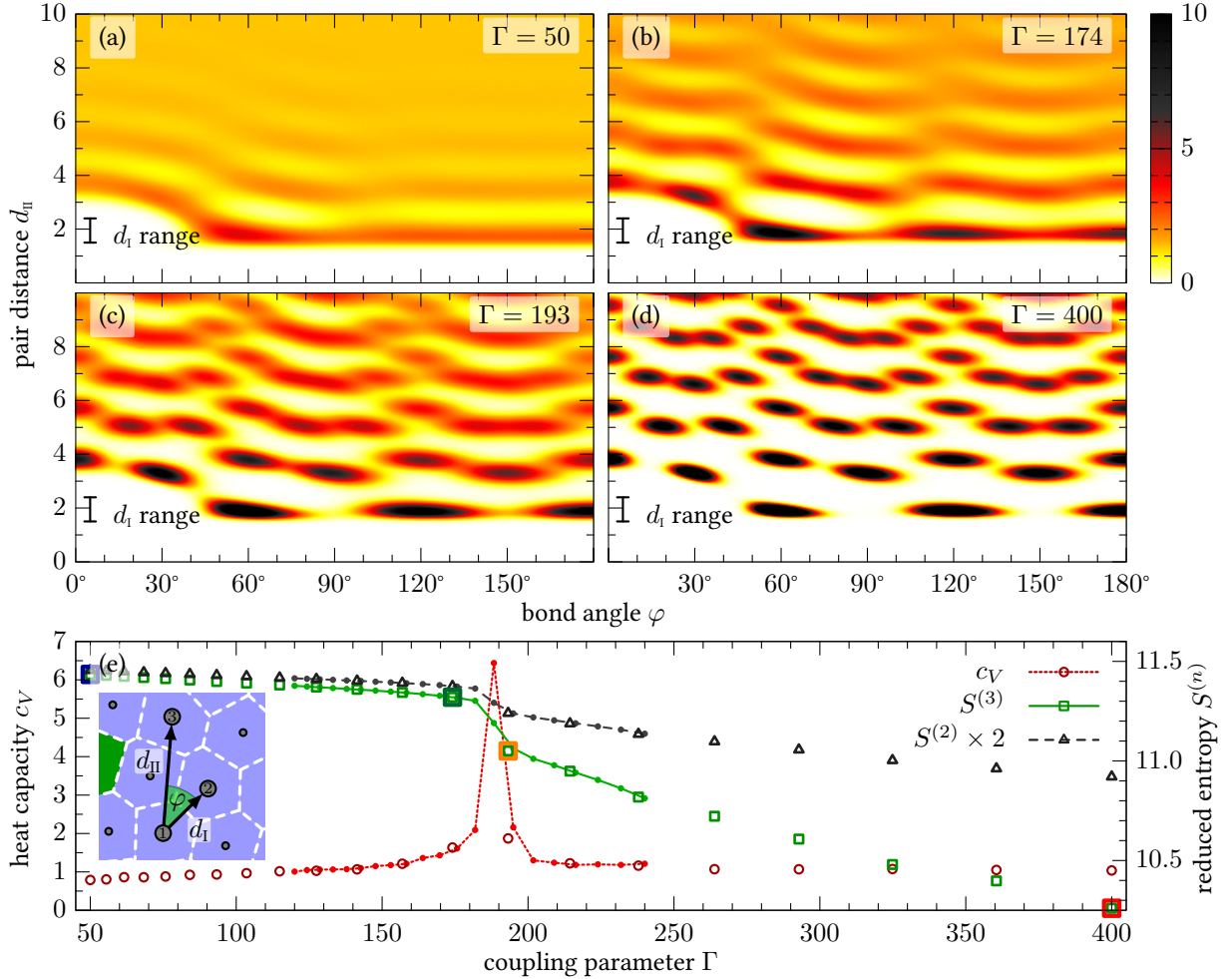


**Figure 5.2:** (a)-(d) Triple-correlation function of the extended system from Fig. 5.1 for the same four  $\Gamma$ -points. The first particle pair is chosen as nearest neighbors by the  $d_I$ -integration range, compare inset in (e). For the plot, both  $\tilde{\rho}_3(d_I, d_{II}, \varphi)$  and  $V_3(d_I, d_{II}, \varphi)$  are integrated over this range individually. (e) The reduced entropy  $S^{(3)}$  from the TCF shows a sharp drop around the same  $\Gamma = 187$  as the entropy  $S^{(2)}$  of the PDF and where the specific heat capacity  $c_V$  has a peak. In the liquid regime,  $S^{(3)}$  is well approximated by two times  $S^{(2)}$ . A maximum distance  $d_{\max} = 10$  was used for the entropy calculation. The theoretical maximum for an ideal system is then  $S_{\max}^{(3)} = 2 \cdot S_{\max}^{(2)} = 2 \cdot \log(\pi 10^2) \approx 11.5$ . The three particles are enumerated in the inset in order to facilitate the discussion of the TCF.

$d_{ii}$  is in the same range as  $d_i$ . In this case, the second and the third particle are nearest neighbors to the first one. However, the term “bond” is in the following used in a more general sense for any pair of two particles.

For all temperatures, Fig. 5.2, one finds zero density for distances  $d_{ii} \lesssim 1.5$  and a correlation hole in the TCF as a void around  $d_{ii} = d_i$  and  $\varphi = 0^\circ$ . Finding a particle triple with the coordinates  $d_i \approx d_{ii} \approx d_{nn}$  and  $\varphi \approx 0^\circ$  would mean that particle two and three of this triple are very close. Due to the repulsive interaction potential, this is impossible even in the liquid regime. At moderate coupling strength  $\Gamma = 50$ , Fig. 5.2(a), one finds only a slight modulation of the TCF in radial direction besides the correlation hole.

Part (b) of the figure shows the TCF at the brink of the phase transition. When particle three is a nearest neighbor of the first particle, this arrangements corresponds to the horizontal strip at  $d_{ii} \approx 2$ . As peaks are found at natural multiplies of  $60^\circ$ , these bond angles are preferred indicating a hexagonal arrangement. However, the peaks are not clearly separated in bond angular direction, which is a sign of a deformed hexagonal lattice including defects, i.e. particles with more or less than six nearest neighbors. A fairly pronounced peak at  $d_{ii} = 3.5$ ,  $\varphi = 30^\circ$  corresponds to second neighbors of particle one under an angle of  $30^\circ$  with respect to a nearest neighbor bond. Such a particle triple is drawn in the inset. Interestingly, this peak has a smaller width in bond angular direction than the peaks for two nearest neighbor pairs discussed before.

The TCF of the solid crystal close to the phase transition is shown in Fig. 5.2(c). The short-range structure has changed only slightly compared to the previous temperature as the peaks for  $d_{ii} \approx 2$  are pronounced more clearly but they are not yet completely separated. The qualitative differences between fluid (b) and solid (c) regime show up a larger distances  $d_{ii}$ . For the latter, clear peaks are found even at distances that correspond to fifth neighbors suggesting a long-range angular order.

Finally, Fig. 5.2(d) shows the long-range bond angular order in the solid phase at  $\Gamma = 400$ . The TCF shows a pattern of distinct peaks with hardly any overlap. Three directions are distinguished along  $\varphi = 0^\circ$ ,  $60^\circ$  and  $120^\circ$  with respect to the first particle pair even at large pair distances  $d_{ii}$ . This long-range order persists although the arrangement of the six nearest neighbors of a particle may be deformed as indicated by the relatively large extension in bond angular direction of the peaks around  $d_{ii} = 2$ .

Even particles with five or seven nearest neighbors, so called defects, are in agreement with the above pattern of the TCF. When one particle with five and one with seven neighbors are grouped, the hexagonal symmetry of the lattice is preserved. This finding is in excellent agreement with the Voronoi diagram of the solid crystal in Fig. 5.3. Deformed hexagonal cells as well as two pairs of defects are found, but these have only local impact on the hexagonal lattice structure. Moreover, the three distinct directions of the crystal are visible in the diagram.

The horizontal sequence around  $d_{ii} = 3.5$  can be grouped into two kinds of second neighbors, those with integer multiplies of  $60^\circ$  as bond angles and those with half integer multiples. The peaks of the latter ones are found at slightly smaller distances  $d_i$  than the former. This observation can be explained by comparing to the hexagonal lattice, where each particle—referred to as the central particle—has six nearest and twelve second neighbors. Six of the latter are aligned with the six inner neighbors and the other six occupy the gaps in between which results in a reduced distance towards the central particle in this picture.

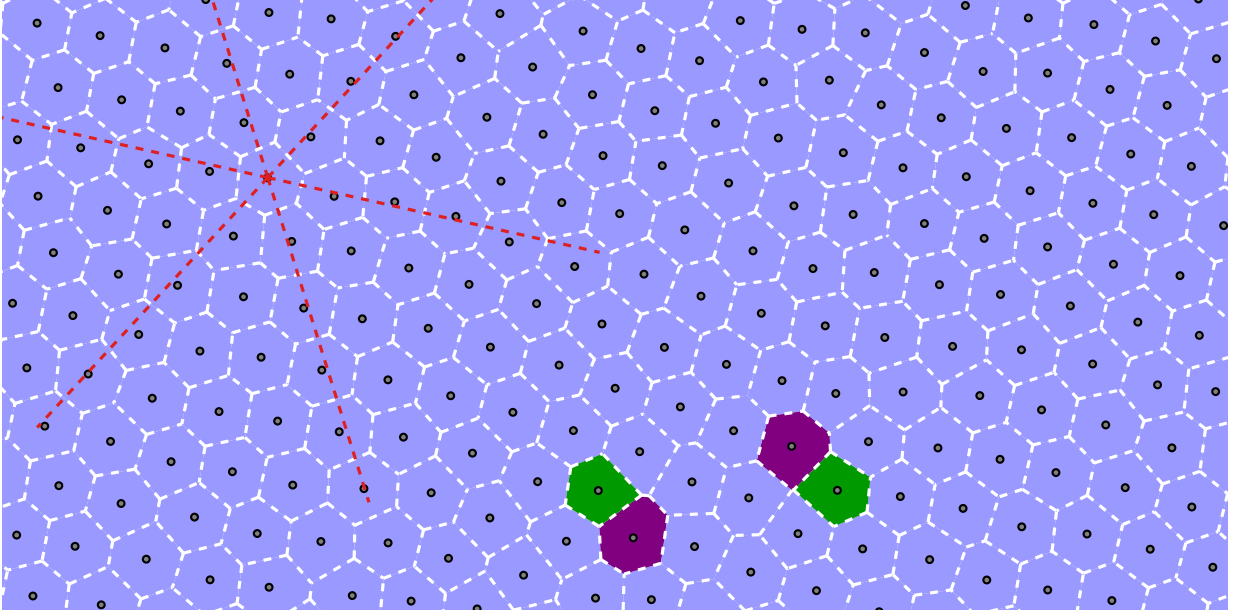


**Figure 5.3:** Voronoi diagram for a snapshot of the 2D Yukawa crystal in the solid phase at  $\Gamma = 400$ . The Voronoi cells with six neighbors are colored in blue as regular cells and cells with five (seven) neighbors are colored in green (purple) as defects. The hexagonal lattice is only disturbed locally by the pairs of defects. As a guide to the eye, the three distinct directions of the crystal are sketched in red.

While the plots of the TCF allowed deep insight to the structure and its temperature dependence, it is challenging to pinpoint a melting point. For this purpose, the entropy  $S^{(3)}$  is a more suitable quantity, as it is a measure for the disorder in the triple-correlation function. In Fig. 5.2(e), this quantity shows a step-like decrease at the phase transition.

Interestingly, the reduced entropy from the TCF is approximately twice the reduced entropy of the PDF in the fluid phase, whereas  $S^{(3)}$  is significantly smaller in the solid phase. This can be explained in the context of joint probabilities since  $\tilde{\rho}_3(d_1, d_{\text{II}}, \varphi)$  is connected to the probability of finding a particle pair with distance  $d_1$  and a third particle with distance  $d_{\text{II}}$  of the first particle under an bond angle  $\varphi$ . The pair density  $\tilde{\rho}_2(d_1)$  is connected to the probability of finding a pair with distance  $d_1$ . A joint entropy which is twice the single entropy associated with the pair distribution implies that the joint probability for finding certain particle triples is given by

$$\tilde{\rho}_3(d_1, d_{\text{II}}, \varphi) \propto \tilde{\rho}_2(d_1) \cdot \tilde{\rho}_2(d_{\text{II}}), \quad (5.1)$$

as a product of two individual probabilities. This means that the knowledge of the first pair distance  $d_1$  does not reduce the uncertainty about the position of a third particle. The relation between entropy and joint probabilities is illustrated for a simple example in Sec. A.4.1 in the appendix.

It should be noted that the  $d_1$  integration was done for the visualization only, while the entropy  $S^{(3)}$  is calculated from  $\tilde{\rho}_3(d_1, d_{\text{II}}, \varphi)$  as a function of three coordinates. However, a finite cut-off range of  $d_{\text{max}} = 10$  had to be introduced for the practical calculation due to the finite size of the simulation box. Apart from the cut-off range, the definition of  $S^{(3)}$  is unique which is important for a reliable melting parameter.

The explicit expression for the entropy from the TCF follows from Eq. (4.50) by insertion of the coordinates  $Q = \{d_I, d_{II}, \varphi\}$  as

$$S^{(3)} = -k_B \frac{(N-3)!}{N!} \int_0^{d_{\max}} dd_I \int_0^{d_{\max}} dd_{II} \int_0^\pi d\varphi \tilde{\rho}_3(d_I, d_{II}, \varphi) \log \left\{ \frac{\tilde{\rho}_3(d_I, d_{II}, \varphi)}{V \cdot 4\pi d_I d_{II}} \right\}, \quad (5.2)$$

where the  $\Delta l$  factor was omitted in dimensionless units. The constant contribution  $\log(V)$  is subtracted in the following to provide a better comparability of  $S^{(3)}$  and  $S^{(2)}$ . Concretely, the contribution  $\log(V)$  corresponds to the number of possible positions the first particle of the triple can have and is temperature independent for a homogeneous system at constant volume.

Here and in the further thesis, the contribution for the number of pairs is subtracted which in practice is implemented by using an  $n$ -particle density normalized to unity, as described in Sec. 4.4.

Although the above example did not deliver considerable new knowledge about the melting of extended 2D dust crystal, it proved that reduced entropies are well suited in order to obtain a critical coupling parameter. These reduced entropies are calculated from the well-known pair distribution function as well as from the triple-correlation function. The structure of the triple-correlation function was discussed in detail for the established crystal at this point since the understanding of its structure is essential for the later application of this quantity to spherical shells.

## 5.1 Finite 2D Dust Clusters

*Inter-shell melting* describes the loss of the angular correlations between the particle configurations on different shells. This process exhibits qualitative differences between 2D and 3D systems. The shells of a 2D dust cluster are concentric rings and there is only one possibility to twist two shells, along a single angle  $\vartheta$ . In contrast, the shells of a 3D dust ball are concentric spherical shells. Since the relative orientation of two shells is described by two angles  $\vartheta$  and  $\varphi$ , the twisting of the shells takes places along a two-dimensional path in the  $\vartheta, \varphi$ -plane.

For example, two spherical shells can be twisted without a particle on the outer shell ever being at the same angular position  $(\vartheta, \varphi)$  as a particle on the inner shell. The outer particle can pass along a “gap” between two inner particles, see Fig. 5.13 (p. 76) which, in contrast, is impossible for 2D rings. For this reason, the inter-shell melting is discussed for a 2D system first. A solid inter-shell order in a 2D cluster means that the angular arrangement of the particles on a shell  $A$  are dependent on the angular positions of the particles on another shell  $B$ .

The *magic number* Coulomb cluster with  $N = 19$  particles may serve as an example for pronounced inter-shell correlations, see Fig. 5.4. The particles arrange themselves on three shells with one particle in the center, six particles on the inner shell, and twelve particles on the outer shell. The number of particles on the outer shell is exactly twice the number of particles on the inner shell. It is due to this commensurable occupation numbers that the two shells can perfectly interlock and one can expect a high critical temperature for this inter-shell melting process. This melting process is inspected by the means of the center-two-particle distribution function  $\tilde{\rho}_2(r_I, r_{II}, \vartheta)$ .

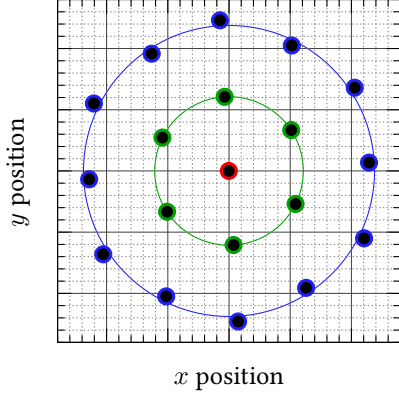


**Figure 5.4:** Ground state of a 2D Coulomb cluster with  $N = 19$  particles. The particles are colored according to their shell affiliation and the average radius of the inner (outer) shell is indicated by the green (blue) circle. The outer particles alternately fall in line with an inner particle and with a gap between to inner particle.

The center-two-particle as ratio  $\tilde{\rho}_2(r_1, r_{\text{II}}, \vartheta)$  and the volume  $V_2(r_1, r_{\text{II}}, \vartheta)$  is plotted in parts (a)-(d) of Figs. 5.5 and 5.6 where the first radial coordinate  $r_1$  is integrated over a radial range that corresponds to the inner shell. In other words, a reference particle is chosen from the inner shell for the upper two plots. While the first simulation was performed for Coulomb interacting particles, a screened interaction potential with  $\kappa = 1$  was used in the second simulation. In order to accent the angular correlation, the effect of the radial density was removed by plotting the correlation function  $g_2(r_{\text{II}}, \vartheta)$  as discussed in Sec. 4.3.2 in parts (e)-(h) of the figures. For that procedure,  $\tilde{\rho}_2(r_1, r_{\text{II}}, \vartheta)$  is related to the pseudo-ideal density  $\tilde{\rho}_2^{\text{id}}(r_1, r_{\text{II}}, \vartheta)$  which one would find in a system with the same radial structure but without any structure within the shells.

First, the Coulomb case, Fig. 5.5, is discussed and later compared with the Yukawa case. For the strongest coupling, the inner and outer shells are occupied by six and twelve particles, respectively. The intra-shell correlations are visible as three distinct peaks at radius  $r_{\text{II}} = 1.2$  and pair angles  $\vartheta$  at multiples of  $60^\circ$ . Moreover, sharp peaks are found at a second radius  $r_{\text{II}} \approx 2.2$  corresponding to pairs with one first particle on the inner and one on the outer shell. These peaks located at those pair-angles  $\vartheta$  that are multiples of  $30^\circ$ . The fact that no pair-angles in between appear implies that the orientation of the outer shell is fixed with respect to inner one. When the outer particle is aligned with an inner one, it is pushed outward. The outer particles in the gaps are found at slightly smaller radii. This causes a split peak in the radial density for the outer shell. A statement about angular correlations is impossible for radii between the shells because of the vanishing particle density.

Parts (b) and (f) of the figure show the cluster in the transition region between fixed angular order and rotating shells. The peaks at  $\vartheta = 51^\circ, 103^\circ$  and  $154^\circ$  indicate that configurations with  $N_1 = 7$  particles on the inner shell form a significant fraction of the canonic ensemble. For such radial configurations, the shells can rotate freely and, hence, a finite density is found at the outer shell radius even for angles between the peaks.

It may seem odd that two different radial configurations are contribute to the ensemble around  $\Gamma = 300$  although the radial density is found to be zero between the shells. A transition between the configurations requires one particle to move from the outer to the inner shell. The absence of these transitions in the shown density can have two reasons. On the one hand, the configuration is not sampled in every MC step and, on the other hand, such a transition can take place via a cluster at lower temperature in the parallel tempering algorithm. Since the energy

barrier for the transition is high compared to the thermal energy at  $\Gamma = 300$  but yet finite, these transition happen very rarely. Therefore extremely long simulation times were required without the parallel tempering extension.

At the coupling strength  $\Gamma = 79$  shown in parts (c) and (g), inter-shell transitions are still rare but can be resolved in the C2P function. While the transitions are hardly visible as a finite density between the shells in (c), the transitions paths are displayed in the correlation function in (g). The radial shell structure is lost for the lowest coupling strength  $\Gamma = 20$  shown in parts (d) and (h). A weak modulation of only the radial density is preserved. Moreover, slight angular correlations with neighbor particles from the same radial range as the first particle persist.

Both the thermodynamic heat capacity  $c_\omega$  and the reduced heat capacity  $c_\omega^{(2)}$  have peaks in the transition region at  $\Gamma_{\text{IM}} \approx 280$ . While the former is obtained from the energy fluctuations in the simulation, the latter is calculated as the temperature derivative of the entropy of C2P. At  $\Gamma_{\text{IM}}$ , the (11-7-1) configuration start to contribute to the canonic ensemble. Since inner and outer shell are not locked for that configuration, the inter-shell correlations are affected. A second peak in  $c_\omega$  is found at  $\Gamma_{\text{r}} \approx 45$ . This peak is weakly pronounced in  $c_\omega^{(2)}$  but appears more clearly in  $c_\omega^{(1)}$ . The latter capacity is associated with the entropy of the radial density. Even though the radial information is included in the C2P, the radial melting only has a minor impact on the entropy due to the overlap with angular effects.

In conclusion, the two-step melting process of the cluster can be described as follows. At very strong coupling, the cluster is in the highly symmetric (12-6-1) configuration, where inner and outer shell have a fixed orientation. The first melting step sets in at  $\Gamma_{\text{IM}}$ , where (11-7-1) configurations occur. These configurations allow for an inter-shell rotation. The angular order is lost in the second transition which takes place at an approximately ten times lower coupling strength.

The reduced entropy  $S^{(2)}$ , which is shown in part (i) of Figs. 5.5 and 5.6, is calculated from the full three-dimensional histogram of  $\tilde{\rho}_2(r_{\text{I}}, r_{\text{II}}, \vartheta)$  without averaging any coordinate over a specific range prior to the calculation. Moreover, the sampled two-particle density is related to the “ideal” two-particle density of a system with no intra-shell structure only for the plots but not for the calculation of the entropy. Hence, the reduced entropy  $S^{(2)}$  is influenced by both radial structure—radial width and occupation number of the shells—and the angular order—intra-shell and inter-shell correlations.

In figure 5.6, the C2P distribution and correlation function are shown for four coupling parameters between  $\Gamma = 30$  and  $\Gamma = 30\,000$ . This wide range was chosen in order to explore whether the orientation of the two shells is eventually locked at very high coupling. The single peak in the heat capacity suggests that this cluster melts in a one-step process. The reduced heat capacity  $c_\omega^{(2)}$  from the C2P shows only a very broad peak and  $c_\omega^{(1)}$  from the radial density shows one peak. The latter agrees with the radial melting region around  $\Gamma_{\text{R}} = 50$ .

The plots (a)-(h) confirm the one-step melting process. Again, the first radial coordinate  $r_{\text{I}}$  is integrated over a range that corresponds to the inner shell. Even at the highest coupling strength, the orientation of the two shells vary. At the radius  $r_{\text{II}} \approx 2$ , a continuous line indicates that all pair angles are possible for particle pairs with one particle from the inner shell and a second from the outer. The outer particle are again pushed to slightly larger radii when they



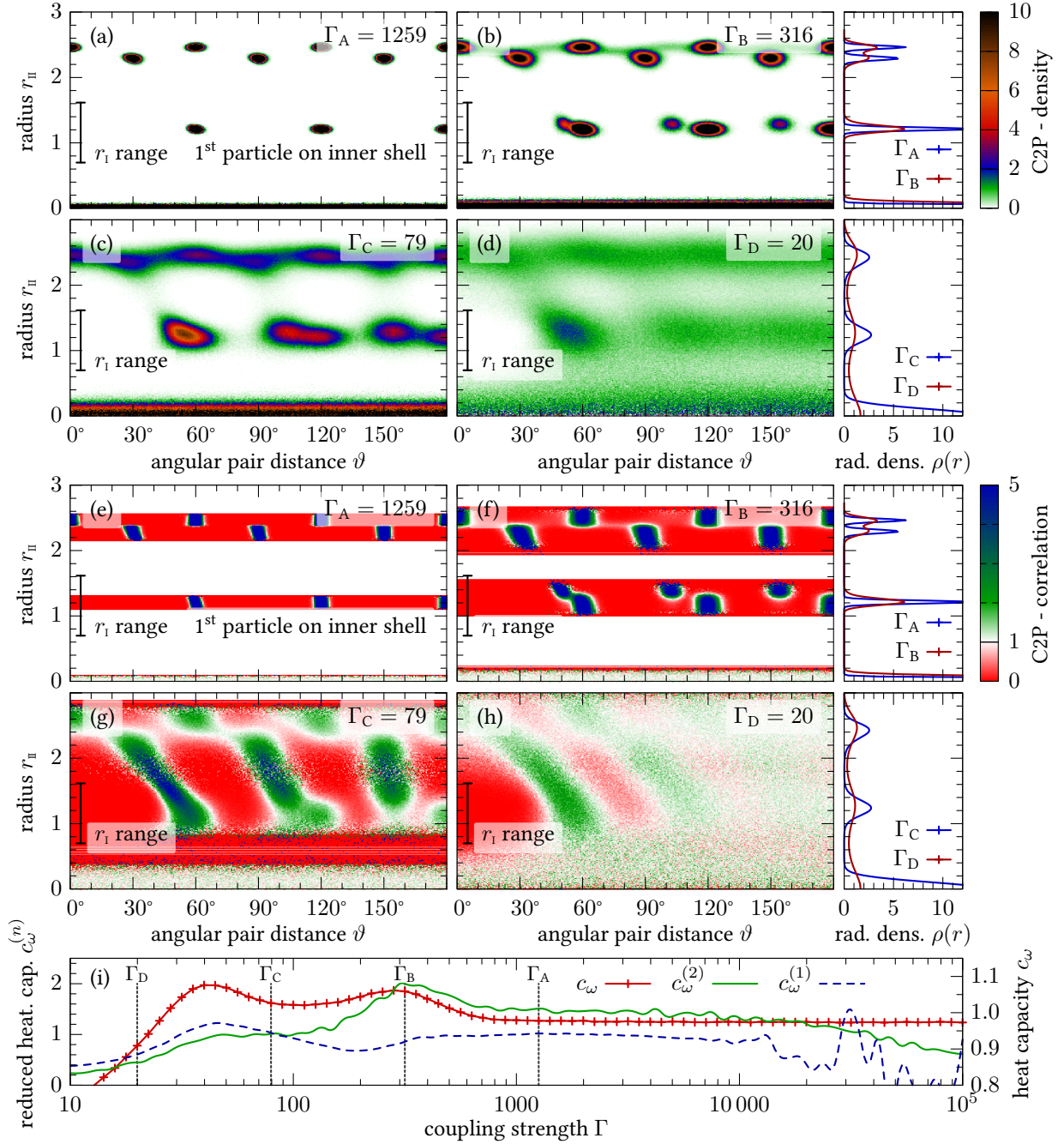


**Figure 5.5:** (a)-(d) Center-two-particle distribution function of a harmonically confined 2D Coulomb cluster with  $N = 19$  particles. The temperature increases from (a) to (d) and the corresponding radial densities are shown on the right hand side. (e)-(h) The corresponding C2P correlation function as defined in Eq. (4.38). (i) The thermodynamic heat capacity  $c_\omega$  is compared to the reduced heat capacities  $c_\omega^{(1)}$  and  $c_\omega^{(2)}$  which are calculated from the reduced entropies of the radial density and the C2P function, respectively. (The oversaturation of the density color at high coupling is accepted for the benefit of a constant color scale over all four plots.)

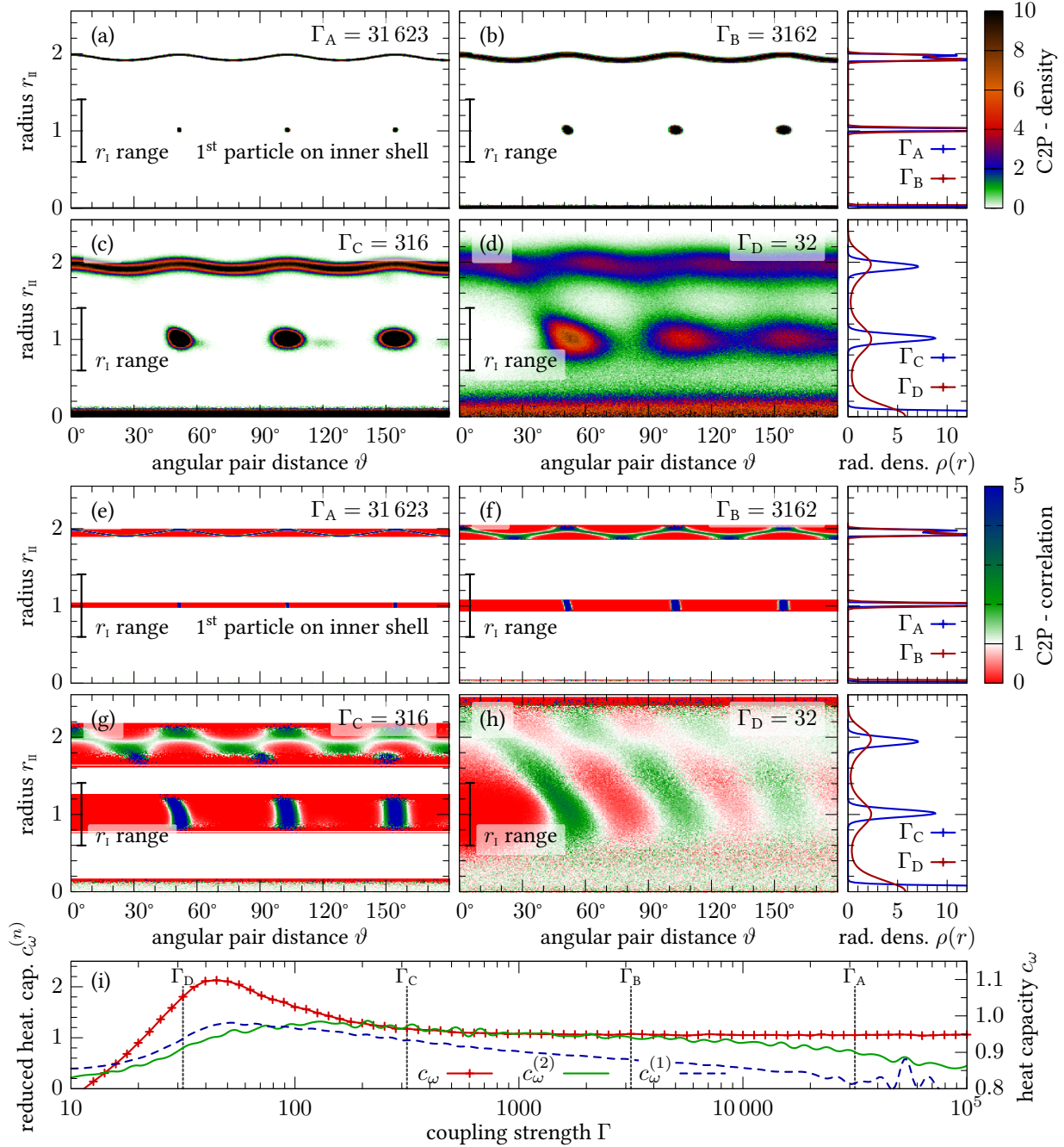


**Figure 5.6:** (a)-(d) Center-two-particle distribution function of a harmonically confined 2D Yukawa cluster ( $\kappa = 1$ ) with  $N = 19$  particles. The temperature increases from (a) to (d) and the corresponding radial densities are shown on the right hand side. (e)-(h) The corresponding C2P correlation function. (i) The thermodynamic heat capacity  $c_\omega$  is compared to the reduced heat capacities  $c_\omega^{(1)}$  and  $c_\omega^{(2)}$  which are calculated from the reduced entropies of the radial density and the C2P function, respectively. This figure corresponds to Fig. 5.6 for Coulomb interaction.

are in line with an inner particle. In plot (c), the weak peaks at  $r_{\text{II}} \approx 1$  and multiples of  $60^\circ$  for the pair angle indicate the occurrence of configurations with six particles on the inner shell. In conclusion, a Yukawa cluster with  $N = 19$  particles and screening parameter  $\kappa = 1$  does not exhibit the inter-shell disorder transition compared to the Coulomb cluster with the same particle number. Inner and outer shell can rotate with respect to each other for the entire range of the coupling parameter  $10 \leq \Gamma \leq 10^5$  in the simulation. The inter-shell disorder transitions first shifts to higher coupling when  $\kappa$  is increased in steps. In contrast, the critical coupling parameter for radial transition does not change significantly.

In the 2D cluster with  $N = 19$  particles, the inter-shell disordering transition was triggered by the emergence of configurations with seven instead of six particles on the inner shell. The remaining question is whether there are situations where such a transition happens without any change in the radial configuration.

This effect can be observed for a 2D Coulomb cluster with  $N = 25$  particles at very strong coupling. The cluster is ground state configuration (13-9-3) for  $\Gamma \geq 400$ . In contrast to the cluster above, the particle number on the outer shell  $N_2 = 13$  does not match the number on the inner shell  $N_1 = 9$ .

In order to investigate the relative orientation of inner and outer shell, the inter-shell pair-angle distribution is extracted from the C2P by integration. The integration ranges for the first and second radial coordinate  $r_1$  and  $r_{\text{II}}$  correspond to the inner and outer shell, respectively. This means that one particle of the pair is from inner shell and the other particle is from the outer shell. The pair-angle distribution function is then normalized by

$$\int_0^\pi d\vartheta \tilde{\rho}_2(\vartheta) = \pi, \quad (5.3)$$

which implies  $\tilde{\rho}_2(\vartheta) \equiv 1$  for two freely rotating shells.

In part (a) of Fig. 5.7, the inter-shell correlations are visualized by this quantity for cluster with  $N = 25$  particles. A strongly peak structure is found at very strong coupling. Since some inter-shell pair angles, e.g.  $\vartheta = 6^\circ$  have zero density, inner and outer shell cannot rotate differentially. However, the amplitude of the peaks decreases quickly when the coupling strength is reduced. For  $\Gamma = 32\,000$ , the density  $\tilde{\rho}_2(\vartheta)$  is finite for all angles, indicating that a differential shell rotation is possible. When the coupling strength is reduced further, only a weak modulation remains at  $\Gamma = 3200$ .

In order to quantify the amount of order in  $\tilde{\rho}_2(\vartheta)$ , the associated entropy  $S^{(2)}(\text{ISC})$  is calculated as

$$S^{(2)}(\text{ISC}) = \frac{1}{\pi} \int_0^\pi d\vartheta \tilde{\rho}_2(\vartheta) \cdot \log \left\{ \frac{1}{2\pi} \tilde{\rho}_2(\vartheta) \right\}, \quad (5.4)$$

where the factor  $\pi$  in the denominator was introduced in order to match the normalization above. Some attention is necessary during the interpretation of this entropy. For an rotational invariant Hamiltonian, the entropy  $S^{(2)}$  of the full center-two-particle is the analogon of the thermodynamic entropy, when replacing the full  $N$ -particle density by the pair-density, see Sec. 4.4. Such an analogy with the thermodynamic entropy is missing for  $S^{(2)}(\text{ISC})$ , which is simply interpreted as a *measure of the inter-shell angular correlations*.

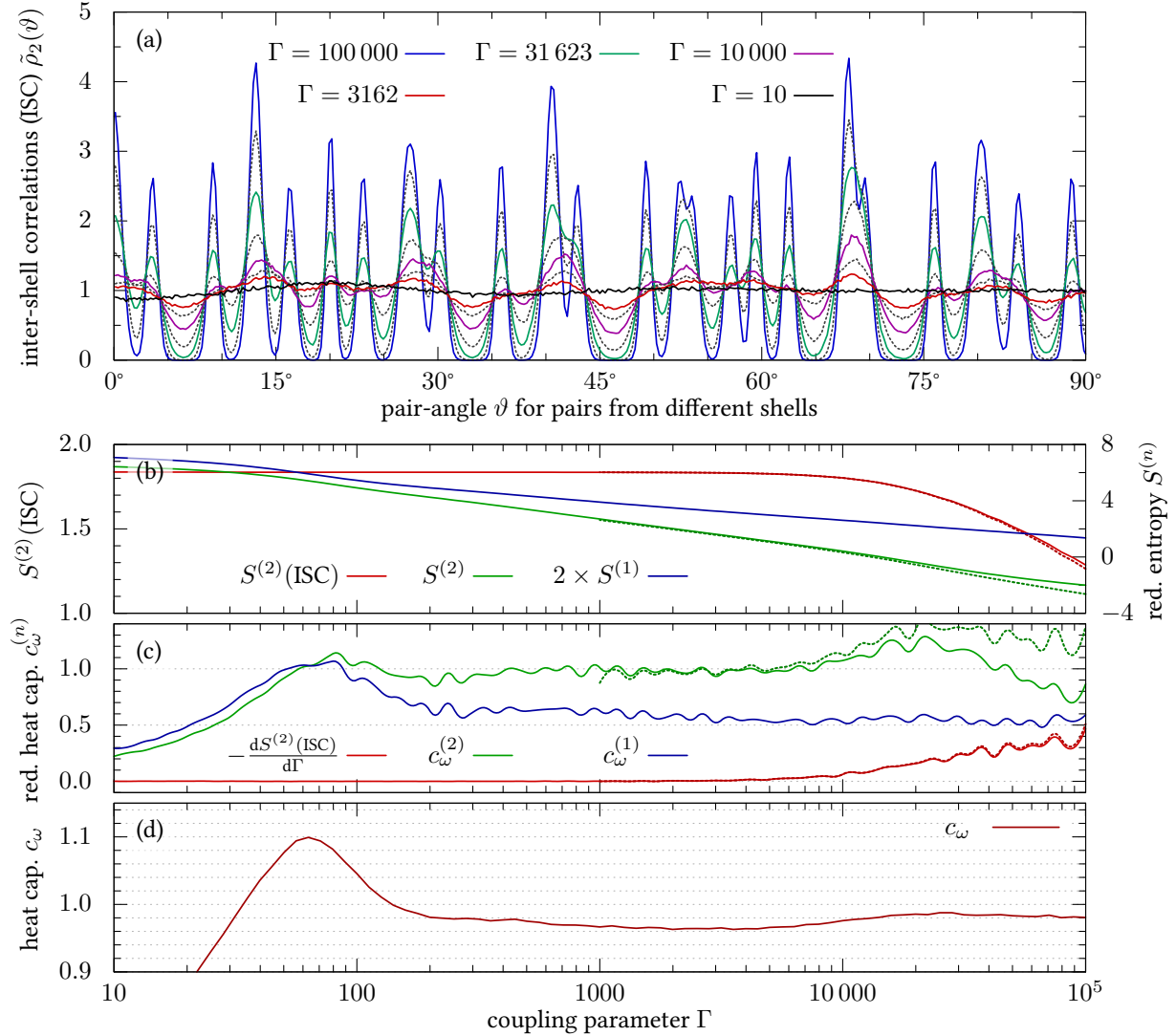


**Figure 5.7:** (a) Inter-shell pair angle distribution for a Coulomb cluster with  $N = 25$  particles. The distribution  $\tilde{\rho}_2(\vartheta)$  was obtained by integrating  $\tilde{\rho}_2(r_I, r_{II}, \vartheta)$  over a range of  $r_I$  ( $r_{II}$ ) that corresponds to the inner (outer) shell. The gray lines are intermediate values of the coupling parameter  $\Gamma$ . (b) The reduced entropy is calculated for the inter-shell correlations, for the full C2P function and for the radial density. For high coupling strengths, calculations with a finer grid for are shown as dotted lines. (b) Reduced heat capacities as the negative derivatives of the entropies with respect to  $\log \Gamma$ . (d) The thermodynamic heat capacity has a pronounced peak around  $\Gamma_R = 65$  and a very flat, broad peak around  $\Gamma_{\text{ISC}} = 35\,000$ .

The entropy  $S^{(2)}(\text{ISC})$  is shown in Fig. 5.7(b) and is found to be constant for  $\Gamma \lesssim 5000$ . The decay of  $S^{(2)}(\text{ISC})$  above this coupling strength means that angular correlations emerge for the two shells. When plotting the entropy of the full C2P function and the associated reduced heat capacity  $c_\omega^{(2)}$  in Fig. 5.7(b), one finds the transition as a broad peak at  $\Gamma_{\text{ISC}} = 35\,000$ . This peak is not found in entropy of the radial density and as discussed above, the occupation number of the three shells (13-9-3) are constant at this coupling.

In order to ensure that the peak in  $c_\omega^{(2)}$  is not simply an artifact of an insufficient resolution when sampling  $\tilde{\rho}_2(r_I, r_{\text{II}}, \vartheta)$  in a histogram, the analysis is repeated with smaller bins. Originally, a three dimensional array was used with  $M_{r_I}^{\text{bin}} = M_{r_{\text{II}}}^{\text{bin}} = 300$  bins for the two radii and  $M_\vartheta^{\text{bin}} = 360$  bins for the pair angle. For the second analysis, these bins numbers were increased to  $M_{r_I}^{\text{bin}} = M_{r_{\text{II}}}^{\text{bin}} = 450$  and  $M_\vartheta^{\text{bin}} = 720$ . The results are shown as dashed lines in Fig. 5.7(b),(c). Indeed, the peak in the reduced heat capacity  $c_\omega^{(2)}$  broadens but does not disappear.

To conclude, the center-two-particle function provides detailed insight into the temperature dependent structure of small 2D dust clusters. It allows to resolve the radial melting process as well as the inter-shell disordering process where the fixed orientation of two shells is lost. In order to identify the critical values of the coupling, the reduced entropy turned out to be well suited. As the entropy drops when structure emerges, its derivative with respect to the logarithm of the coupling parameter shows a peak at this point. While the radial melting process showed only a weak dependence on the particle number and the screening parameter  $\kappa$ , the inter-shell transitions are strongly affected by the precise cluster configuration. These configurations crucially depends on particle number and screening parameter.

## 5.2 Spherical 3D Dust Clusters

When going from planar 2D clusters to spherical dust balls in 3D, the number of possible transitions grows. Compared to the former, the latter cluster have an *intra-shell* order as an additional feature. Disregarding the anisotropy of electric potential caused by the inner particles and the finite width of the shell, the intra-shell order at zero temperature is determined by the minimum interaction energy of  $N_s$  particles on a circular ring or a spherical shell, respectively. This problem is easily solved for the circular ring, where all neighbors have the same distance in the configuration with the minimal energy. For a spherical shell, finding the configuration with the minimal energy is much more complex. In case of Coulomb interaction, this task is called the Thomson problem [100, 104]. Exact analytical solutions of this problem were found for a few specific particle numbers, only [141]. The temperature behavior of the intra-shell order is of central interest when the melting of spherical dust clusters is investigated in the following.

### 5.2.1 Classification of the Intra-Shell Order by the Means of Voronoi Diagrams

This section describes how different particle configurations within a spherical shell can be distinguished by the coordination number calculated in the Voronoi diagram, see Sec 4.1. During this chapter, TCF will provide insight into the intra-shell structure of spherical Coulomb clusters.

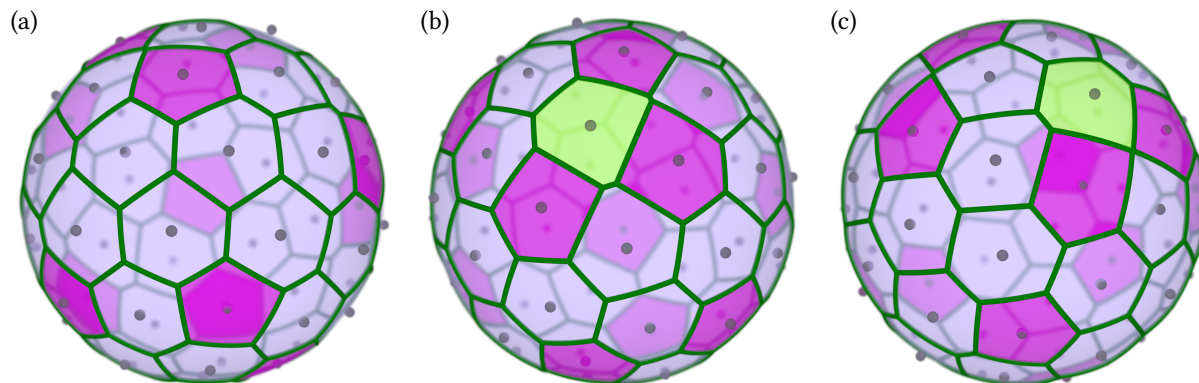


**Figure 5.8:** Examples of three different intra-shell configurations in the outer shell of a 3D Coulomb cluster with  $N = 80$  particles. All three configurations have in common that the shell is occupied by  $N_2 = 59$  particles. (a) Each of the twelve pentagonal Voronoi cells is fully surrounded by deformed hexagons. (b) One heptagonal Voronoi cells appears which is surrounded by three deformed pentagons and four deformed hexagons. (c) The one heptagonal Voronoi cells is surrounded by two deformed pentagons and five deformed hexagons.

The interpretations of the TCF can be verified by applying an independent quantity that resolves the intra-shell structure as well. Therefore, the particle arrangement within a shell is classified by the Voronoi diagram as follows.

In order to characterize the *radial configuration* of a cluster, it is meaningful to give the occupation number of the different shell. A similar scheme is now introduced for the description of the *intra-shell configurations*. Figure 5.8 shows three different intra-shell configuration for the same shell occupation numbers (1-20-59). Since these Voronoi diagrams differ, the shell occupations numbers are not sufficient to describe the entire structure.

A more detailed classification is possible by counting the particles with coordination number five, i.e. particles with five adjacent Voronoi cells, particles with coordination number six, and those with coordination number seven. In the example above, these numbers are (47-12-0) for (a) and (45-13-1) for both (b) and (c). Obviously, the latter two configurations differ with respect to the arrangement of pentagons, hexagons and heptagons. Hence, the first approach is not sufficient to resolve the difference between these two configuration. A suited tuple of numbers should be sensitive to the arrangement of pentagons, hexagons and heptagons.

One way to characterize this arrangement is to count different classes of bonds<sup>2</sup> instead of particles. Each of these bonds is classified by the coordination numbers of the two particles connected by the bond, e.g. a 5-5 bond connects two particles with pentagonal Voronoi cells. When compared to example (b), the number of 5-7 bonds is reduced in example (c), while numbers of 5-6 and 6-7 bonds are both increased by one. Since the class-resolved numbers of particles are easily calculated from the numbers of bonds but not vice versa, the latter numbers carry more information and are better suited to describe the intra-shell configuration.

However, there are still structural differences which cannot be resolved within the frame of bond classes. When a pentagonal Voronoi cell is moved within a field of hexagonal cells, this

<sup>2</sup>The term “bond” at this point is used for the virtual connection between two adjacent particles.

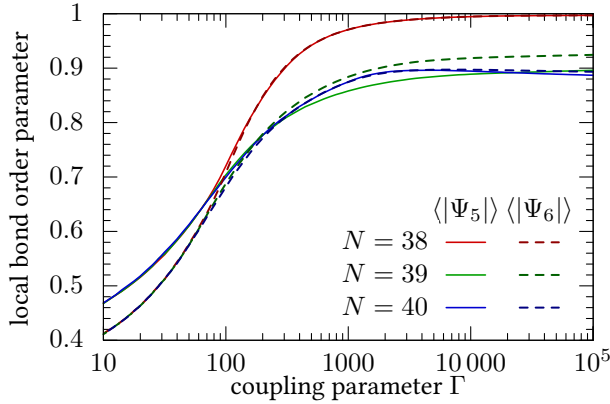


**Figure 5.9:** Local bond order parameters, cf. Sec. 4.2, within the outer shell of three Coulomb balls with different particle numbers. The five-fold parameter  $\langle |\Psi_5| \rangle$  is calculated for the particles with pentagonal Voronoi cells, while  $\langle |\Psi_6| \rangle$  is calculated for those with hexagonal Voronoi cells. The high symmetry of the magic number ( $N = 38$ ) cluster at high couplings results in bond order parameters  $\langle |\Psi_5| \rangle \approx \langle |\Psi_6| \rangle \approx 1$ .

will not result in change of the class-resolved bond numbers although the structure is altered.

### 5.2.2 Small “Magic” Cluster

First, the melting analysis is done for a 3D Coulomb cluster with  $N = 38$  particles. This “magic number” cluster was chosen because of its high symmetry which is well understood [88]. In the ground state, the outer shell is occupied by 32 particles while the inner shell contains six particles [142]. The six particles on the inner shell arrange themselves at the face centers of a cube. The outer particles form a lattice on the shell with twelve pentagonal and twenty hexagonal Voronoi cells. In this lattice, each pentagon is fully surrounded by hexagons which gives the structure a high level of symmetry. Effects of the precise number of particles are investigated in the following by increasing the particle number by one and two, respectively.

The local bond order parameters  $\langle |\Psi_{5/6}| \rangle$ , cf. Sec. 4.2, are good indicators for the perfect symmetry of the magic number cluster. In Figure 5.9, the bond order parameter  $\langle |\Psi_5| \rangle$  was obtained as the average over all particles which have a pentagonal Voronoi cell within the outer shell. Analogously, the parameter  $\langle |\Psi_6| \rangle$  was obtained as the average over all particles with hexagonal Voronoi cells. At strong couplings, both local bond order parameters,  $\langle |\Psi_5| \rangle$  and  $\langle |\Psi_6| \rangle$ , take values which are close to the maximum possible value of unity. This means that the intra-shell Voronoi cells are not deformed. For the two non-magic particle numbers,  $N = 39$  and  $N = 40$ , in Fig. 5.9, the bond order parameters at high couplings are significantly smaller. As expected, this indicates a deformation of the intra-shell Voronoi cells in the ground states of the non-magic number clusters.

When the coupling parameter  $\Gamma$  is reduced, the bond order parameter decreases. In the molten cluster, the dependence on the exact particle number  $N$  is lost as the three  $\langle |\Psi_5| \rangle$ -curves converge towards one common curve. All three  $\langle |\Psi_6| \rangle$ -curves converge towards a second common curve. At a moderate coupling parameter  $\Gamma = 10$ , the values  $\langle |\Psi_5| \rangle \approx 0.47$  and  $\langle |\Psi_6| \rangle \approx 0.41$  are found, regardless of the particle number. Since the decrease of the local bond order parameters takes place over a very broad range of the coupling parameter, these parameters are unsuitable for fixing a transition region in spherical clusters. The discussed parameters capture only the local bond order of adjacent particles. In contrast, the TCF, which is applied to the Coulomb clusters in the following, is sensitive to the global bond order.

In figure 5.10, the triple-correlation function is shown for the outer shell of the magic number cluster and compared to the clusters with one and two additional particles. The ground state configurations of these clusters with are (33-6) for  $N = 39$  particles and (34-6) for  $N = 40$  particles. In the pattern of the TCF, the two add additional particles on the outer shell are found to have a large effect on the intra-shell structure. Figure 5.10(a) shows the TCF for the magic number cluster at strong coupling. Since the three-particle density is integrated over a  $\vartheta_1$  range that corresponds to the nearest neighbor distance within the shell for the plot, those particle triples are selected where particle one and three are nearest neighbors. Several distinct peaks are found around  $\vartheta_{11} = 40^\circ$ . This angular pair distance corresponds to nearest neighbors, which means that particle three is also a neighbor of the first particles for these peaks. The bond angle  $\varphi$  is plotted on the abscissa and the peaks are located at multiples of  $60^\circ$  and at multiples of  $72^\circ$ , respectively. While for the former bond angles, the first particle has a hexagonal Voronoi cell, it has a pentagon Voronoi cell for the latter bond angles, cf. Fig. 5.11.

Interestingly, the peaks that corresponds to a first particle with six nearest neighbors are split into two peaks in the direction of the angular pair distance  $\vartheta_{11}$ . This effect can be understood by considering the intra-shell Voronoi diagram shown in Fig. 5.11. Every hexagonal cell is surrounded by three hexagonal and three pentagonal cells. One finds that the 5-6 bonds that connect one five-fold particle and one six-fold particle are slightly smaller than 6-6 bonds. Therefore, two peaks are found in the TCF for every bond angle, when the first particle has sixfold symmetry. Since every fivefold particle has sixfold neighbors only, no splitting of the peaks in the direction of  $\vartheta_{11}$  is observed here.

At the ten times lower coupling strength  $\Gamma = 1000$ , Fig. 5.10(b), all peaks are broadened but yet still clearly visible. This observation indicates that the particles oscillate around their equilibrium positions with larger amplitude but that the intra-shell lattice persists.

Looking at the TCF for the  $N = 39$  cluster with one additional particle on the outer shell, Fig. 5.10(c), a less ordered pattern is found. Although the nearest neighbor peaks which were discussed above are also visible for this particle number, these are significantly less pronounced. Moreover, a variety of additional peaks are found in those regions that exhibit zero density for the magic number cluster above. All these peaks are embedded into a thready density. At a ten times lower coupling strength, Fig. 5.10(d), the three particle density became continuous. However, several broad peaks as well as void regions persist.

The bottom row of Fig. 5.10 shows the TCF for the cluster with  $N = 40$  particles of which 34 are found on the outer shell at high coupling. Although the pattern is more similar to the cluster with  $N = 39$  particles than to the magic number cluster in the top row, a variety of small peaks is found. Compared to the  $N = 39$  particle cluster with an odd number of particles on the shell, these peaks are separated more clearly. At lower coupling strengths, Fig. 5.10(f), the triple-correlation function shows only slight differences between the two non-magic number clusters.

The discussed plots showed the extraordinary symmetry of the magic number cluster with 32 particles on the outer shell. However, the quantification of one or more transitions points is still missing. For this purpose, it is practical to extract one parameter  $\chi$  from the TCF. Characteristic features, e.g. steps, of the temperature dependence this parameter may then allow one to quantify a transition point.



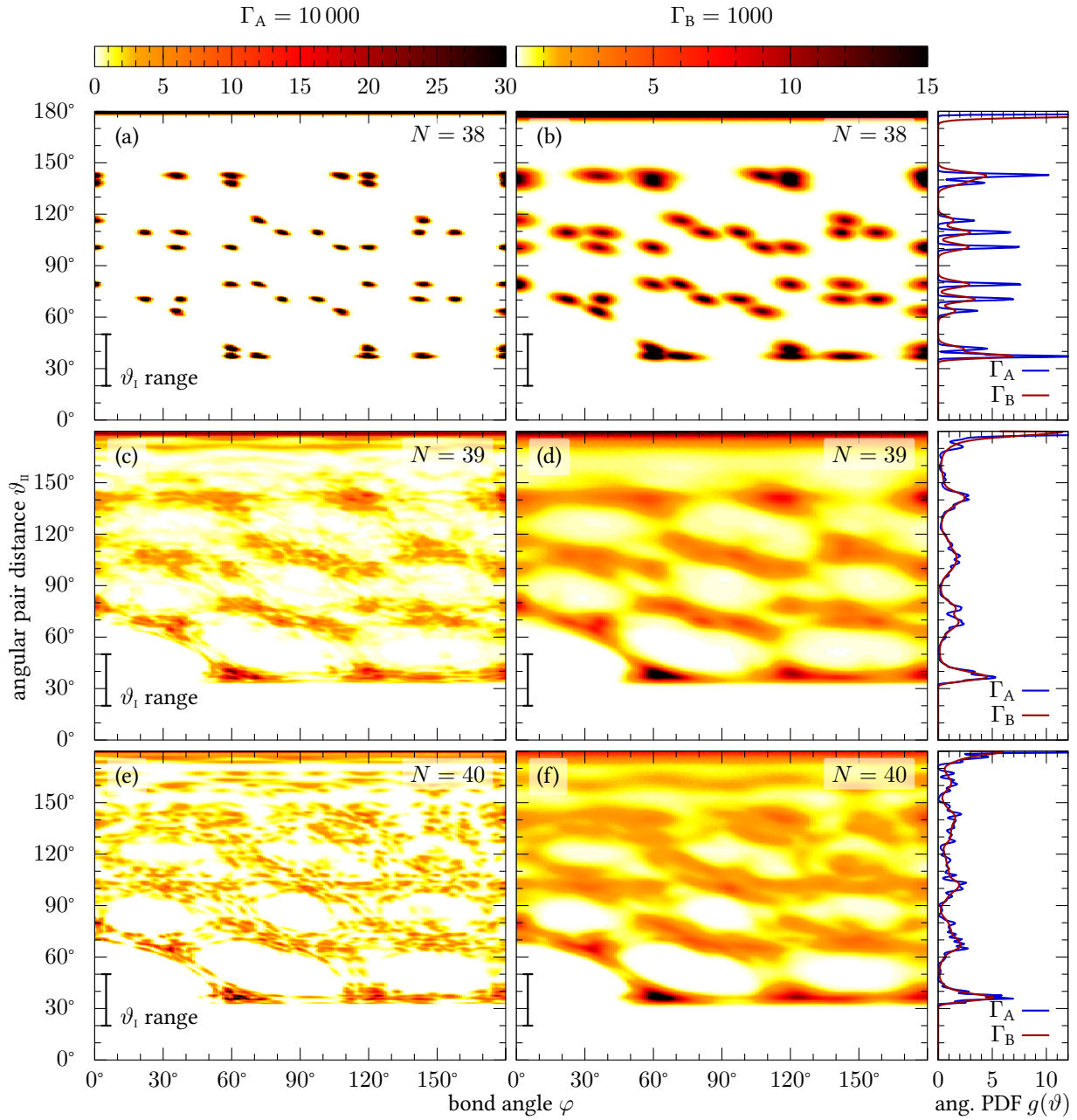
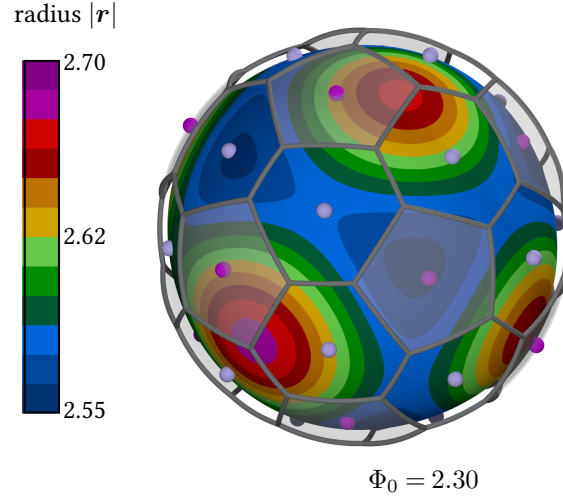


**Figure 5.10:** Triple-correlation function on the outer shell of Coulomb clusters with  $N = 38$  (top row),  $N = 39$  (middle row), and  $N = 40$  (bottom row) particles. The coupling parameter is  $\Gamma = 10\,000$  ( $\Gamma = 1000$ ) for the right (left) column. Through the  $\vartheta_1$ -integration range, intra-shell neighbors were selected for particles one and two. The bond angle  $\varphi$  is on the abscissa, while the angular pair distance of particles one and three is on the ordinate. In the very right column, the corresponding angular pair distribution function within the shell is shown for both coupling strengths. (The oversaturation of the density color  $N = 38$  is accepted for the benefit of a constant color scale over all three particle numbers.)

**Figure 5.11:** Outer shell structure of the magic number Coulomb cluster with  $N = 38$  particles at strong coupling  $\Gamma = 10\,000$ . Pentagonal Voronoi cells are shaded and the corresponding particles are colored in violet. Moreover, the equipotential surface at  $\Phi_0 = 2.30$  in dimensionless units is shown for the Coulomb potential  $\Phi_{\text{inner}}(\mathbf{r})$  caused by the inner particles. The color indicates the radial coordinate of the surface. Blue areas are valleys and violet areas are hills.



One possibility is to use the height of a certain peak for  $\chi$ . This approach is rejected for the following reasons. On the one hand, one has to choose a certain peak which causes a first arbitrariness. On the other hand, the previous plots were obtained by integrating the full triple-correlation function over a certain range of the first angular pair distance  $\vartheta_1$  in order to obtain  $\tilde{\rho}_3(\vartheta_{\text{II}}, \varphi)$ . Although the precise choice of this range has no qualitative influence on the structure of  $\tilde{\rho}_3(\vartheta_{\text{II}}, \varphi)$ , the influence of the  $\vartheta_1$  range had to be checked carefully when a transition point is determined from a peak height of the integrated quantity.

In the following, the *reduced entropy*  $S^{(3)}$  of the three-particle distribution within the shell is used as a melting parameter. The explicit calculation of  $S^{(3)}$  from the sampled histogram is subject to Sec. 4.4. Since the reduced entropy is calculated from the full triple-correlation function as a function of three parameters, no integration ranges have to be chosen. Moreover, the full information of the triple-correlation function enters the entropy  $S^{(3)}$  which can be interpreted as a measure of the disorder. When certain three-particle arrangements, described by two angular pair distances and the bond angle, are preferred, the disorder is lower than in the case when all arrangements occur with similar probability. Even though the plots in Fig. 5.10 only show a small portion of the triple-correlation function due to the integration, one already sees that the disorder is lower for part (a) than for part (b).

For a quantitative analysis, the reduced entropy  $S_{\text{outer}}^{(3)}$ , corresponding to the intra-shell order on the outer shell, is shown in Fig. 5.12(e) for the three clusters. In the liquid regime for  $\Gamma \lesssim 100$ , there is no difference in entropy of the triple-correlation function between the three particle numbers. Around  $\Gamma = 100$ , the curve for the cluster with  $N = 38$  particles is bent down, while the two other curves remain at a high level. This behavior indicates that the intra-shell order freezes around that point for the magic number cluster. For the cluster with  $N = 39$  particles, a decline is found around  $\Gamma = 10\,000$ . Compared to the previous cluster, the required coupling parameter for freezing the intra-shell order is about hundred times larger. Moreover, this disordering transition is significantly broader than for the previous cluster. For the last cluster with  $N = 40$  particles, the decline is found for a coupling parameter  $\Gamma \approx 3000$  in between the previous two

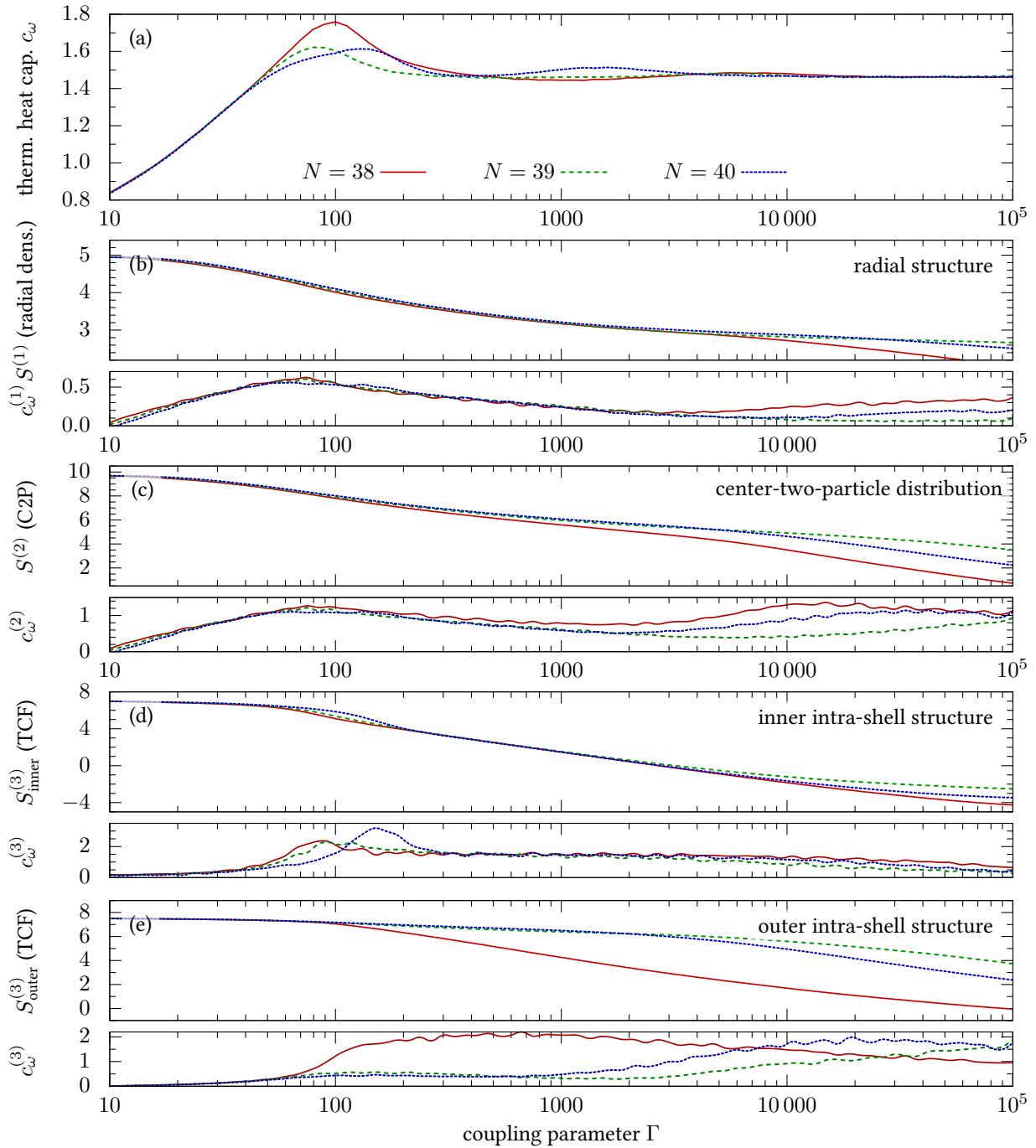


**Figure 5.12:** Comparison of the three Coulomb clusters with  $N = 38, 39$  and  $40$  particles. (a) The specific heat capacity per particle derived from the energy fluctuations in the MC simulation. (b) The reduced entropy of the radial density as a one-particle quantity. Below, the derivative with respect to  $\log T$  as the reduced capacity is shown. (c) The reduced entropy of the center-two-particle distribution as a two-particle quantity and the corresponding capacity. (d),(e) The reduced entropy of the triple-correlation function on the inner and outer shell, respectively, as a three-particle quantity and the corresponding capacities. For strong coupling, the high symmetry of the first cluster's (32-6) configuration is responsible for the low values of the entropies  $S^{(2)}$  (C2P) and  $S_{\text{outer}}^{(3)}$  (TCF) compared to the two other clusters.

critical values. In the lower part of Fig. 5.12(e), the associated capacity  $c_\omega^{(3)}$  as the derivative of the entropy with respect to  $\log T$  is shown. The decline of  $S_{\text{outer}}^{(3)}$  around  $\Gamma = 100$  for  $N = 38$  particles is reflected as a sharp step in the corresponding capacity.

In the same figure 5.12, the entropies from the radial density, the two-particle density, and the three-particle density on the inner shell are shown as well and compared to the total thermodynamic heat capacity  $c_\omega$ . For all three clusters, the capacity  $c_\omega^{(1)}$  has a peak around  $\Gamma = 75$ . Since this capacity is calculated from the entropy of the radial density, this peak is attributed to the radial melting process. In this process, the onion-like shell structure is lost. Only for  $N = 40$ , the peak is broadened towards higher values of  $\Gamma$ . This observation can be explained by the onset of inter-shell transitions. While for  $\Gamma \gtrsim 200$  only the radial isomer (34-6) is found, the radial isomer (33-7) starts to contribute to the thermodynamic ensemble with a significant fraction. The transitions between those isomers can be efficiently sampled in the MC simulation because of the parallel tempering enhancement.

Since the center-two-particle distribution function contains the radial density as well, the capacity  $c_\omega^{(2)}$  shown in Fig. 5.12(c) also shows the peak around  $\Gamma = 100$  which was attributed to the radial melting process. Regarding the cluster with  $N = 38$  particles, a second broad peak is found around  $\Gamma = 14\,000$ . This peak is neither found in the capacities  $c_\omega^{(3)}$  of the inner and outer intra-shell structure nor in the capacity  $c_\omega^{(1)}$  for the radial structure. Therefore, the peak is attributed to an inter-shell angular transition process. When the coupling parameter exceeds the transition point, the angular position of the two shells is locked.

In order to verify this interpretation, the anisotropy of the Coulomb potential  $\Phi_{\text{inner}}(\mathbf{r})$  caused by the six particles on the inner shell is investigated. In figure 5.11, the equipotential surface of this potential is shown at a value  $\Phi_0$  for one snapshot of the configuration at a high coupling strength. The value  $\Phi_0$  was chosen as roughly the electric potential at the radius of the outer shell. Since the harmonic confinement potential is perfectly isotropic, it is neglected for this consideration. The equipotential surface deviates from a perfect sphere by about 5 % in radius. The hills in the equipotential surface represent blockades for the inter-shell rotation and can therefore explain the fixed angular orientation of both shells at high coupling.

Besides the depth of valleys and the height of hills in the equipotential surface caused by the inner particles, the lattice within the outer shell has strong impact on the inter-shell angular transition. The energy barrier for rotating the shells differentially is high when the symmetry of the outer shell fits the symmetry of the inner shell. This mechanism is well understood for 2D clusters, see previous section 5.1. Here, an outer shell with  $N_2 = 12$  particles could perfectly interlock with an inner shell with  $N_1 = 6$  particles. For 3D clusters, the situation is much more complex. Interlocking two spherical shells can be compared with placing one egg carton on top of a second egg carton with different size. For certain size ratios of the two cartons, they can lock in place. Of course, the curvature of the sphere is lacking from this picture.

The comparably high critical coupling strength for the inter-shell locking in 3D results from the additional degree of freedom for twisting the two shells. Somewhere along the twist of two circular shells in 2D, every outer particle is necessarily in line with a particle on the inner shell. As shown in Fig. 5.13, the outer shell of a spherical cluster in 3D can be rotated with respect to the inner shell without passing the arrangement described above. When the outer shell is turned

by fixing the polar angle  $\varphi_{1,2}$  of one particle on the outer shell as a scanning parameter,<sup>3</sup> the shells are twisted along a path in  $(\vartheta, \varphi)$ -space avoiding the bulges in the equipotential surface of the Coulomb potential by the inner particles. Each bulge corresponds to one inner particle. As illustrated in the figures, all of the outer particles move along the gaps between the inner particles during the twist which is, in contrast, impossible in 2D clusters.

The lower symmetry of the lattice on the outer shell of the clusters with  $N = 39$  and  $N = 40$  particles can explain that inter-shell locking requires higher coupling strengths compared to the magic number cluster.

Part (d) of Fig. 5.12 shows the reduced entropy  $S_{\text{inner}}^{(3)}$  obtained from the triple-correlation function of the inner shell. This shell is occupied by six particles for all three clusters in the ground state. For six particles, there exists virtually only one stable intra-shell configuration for which the particles are found at the face centers of a cube. Since this configuration is very stable, the intra-shell disordering process accompanies the radial melting around  $\Gamma = 100$ . A distinctive feature is found for the cluster with  $N = 40$  particles. Here, the corresponding capacity  $c_{\omega}^{(3)}$  has a clear peak for  $\Gamma \approx 160$ . This peak is caused by the appearance of the (33-7) isomers in the thermodynamic ensemble around this coupling parameter. The additional particle on the inner shell has a major impact on the intra-shell configuration and is therefore responsible for the breakdown of the highly symmetric order within the shell. Notably, this peak is also found in the thermodynamic heat capacity  $c_{\omega}$  shown in part (a) of the figure.

With the knowledge of the different melting processes in mind, one can understand most features of the thermodynamic heat capacities  $c_{\omega}$  of the three cluster in Fig. 5.12. Because of the radial melting, one can expect a peak around  $\Gamma_{\text{RM}} \approx 80$ . This peak is clearly visible for  $N = 39$  since no other melting process takes place at similar coupling strength for this particle number which could overlap the radial melting peak.

For the magic particle number  $N = 38$ , the peak is higher and its maximum is found at coupling parameter  $\Gamma_{\text{RM}} = 100$ . This observation can be explained by the intra-shell disordering process in the outer shell which takes places around this coupling strength. Therefore the radial melting peak in the thermodynamic heat capacity is overlapped by a peak connected with the intra-shell disordering process. The inter-shell angular melting process around  $\Gamma_{\text{IS}} = 14\,000$  does not cause a visible peak in the thermodynamic heat capacity.

For the last particle number  $N = 40$ , the radial melting peak appears as a shoulder in the larger peak around  $\Gamma = 160$  which results from the onset of inter-shell transitions. This process is accompanied by an intra-shell disordering process in the inner shell. Since several intra-shell isomers are found for the outer shell configuration of this cluster even at higher coupling strength, the inter-shell transitions have no impact on the intra-shell structure that would be visible in the TCF of this shell. It remains to explain the  $c_{\omega}$  peak around  $\Gamma = 1500$ . The Voronoi analysis within the outer shell provides insight into the intra-shell order. In figure 5.14, the fraction of configurations with  $N_2 = 33$  (or less) particles on the shell is plotted above the zero line, while the fraction of configurations with  $N_2 = 34$  (or more) particles on the shell is plotted below the

<sup>3</sup>For this parameter scan, the arrangement of the inner shell is locked by restricting the position of one particle to the positive  $z$ -axis. The rotation of the inner shell around the  $z$ -axis is subtracted before the evaluation of the particle positions.

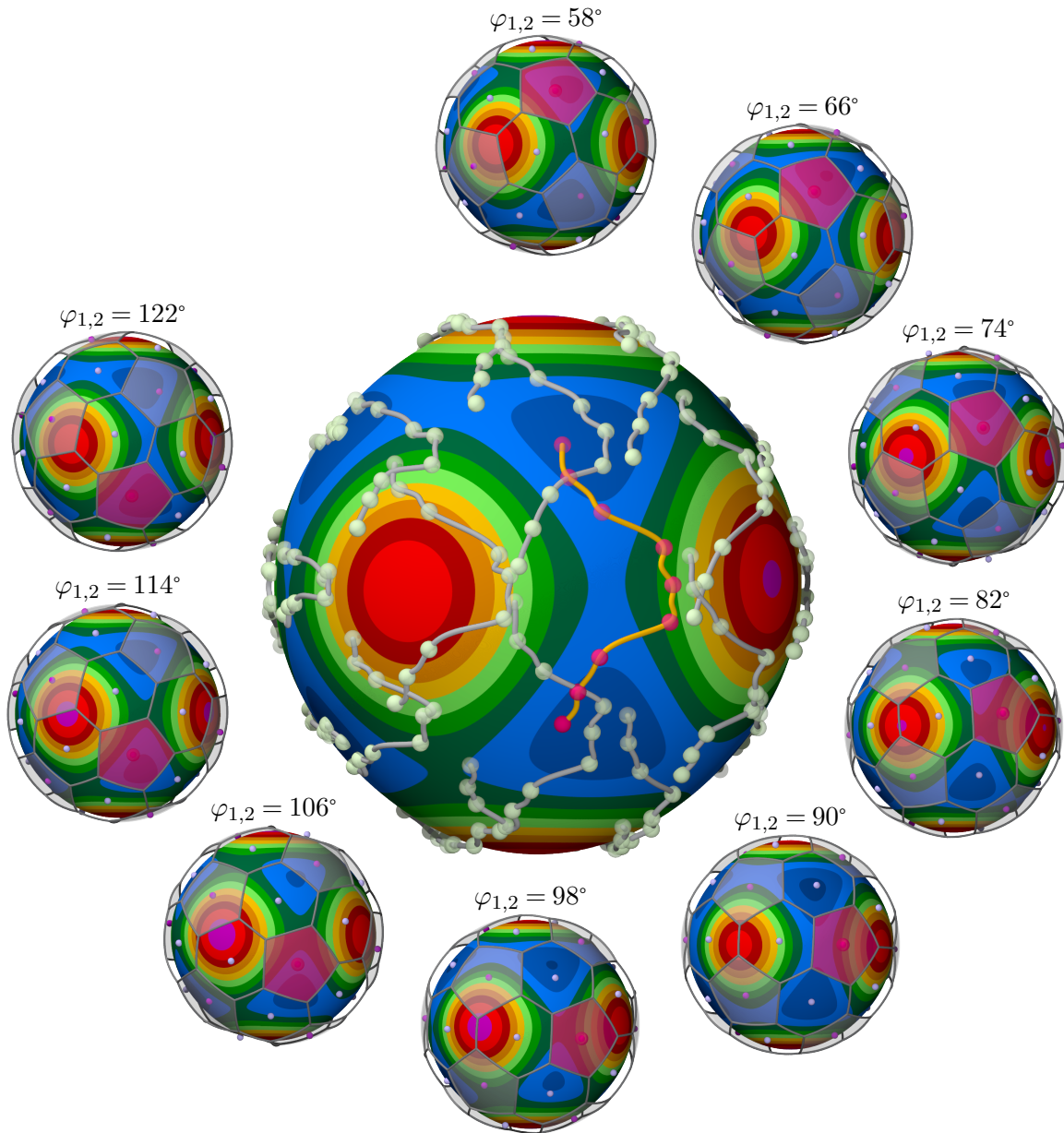


**Figure 5.13:** Inter-shell twisting in the magic number cluster with  $N = 38$  particles. One of the particles on the inner shell was fixed on the positive  $z$ -axis and the polar angle of one particle (highlighted in red) on the outer shell is fixed at  $\varphi_{1,2}$ . This angle  $\varphi_{1,2}$  is then scanned over the interval  $[50^\circ : 122^\circ]$  in the small figures. The colored surface is the equipotential surface at  $\Phi_0 = 2.3$  of the electric potential caused by the inner particles, cf. Fig. 5.11. This surface exhibits six red bulges which are located above the inner particles. As the red particle is twisted with respect to the inner shell, it moves along a path between the bulges. The paths of all outer particles during the twist are shown in the big figure. All these paths pass through the gabs between the inner particles.

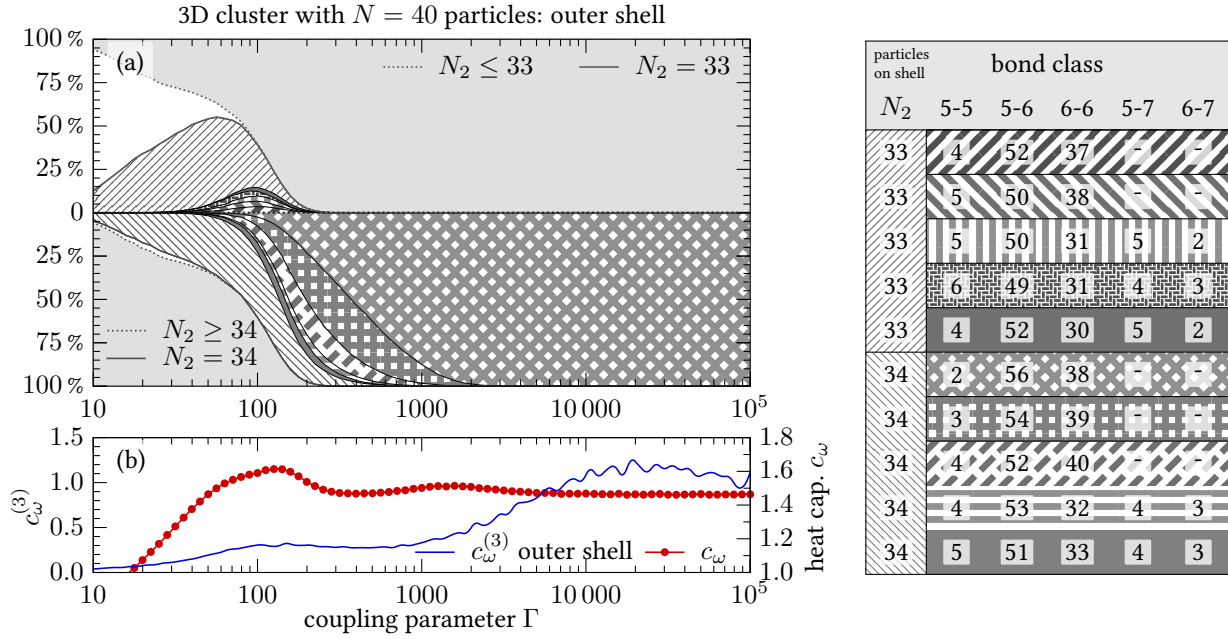


**Figure 5.14:** Voronoi analysis for the outer shell of the Coulomb cluster with  $N = 40$  particles. (a) The intra-shell Voronoi diagram allows to determine the coordination number, i.e. the number of nearest neighbors, for every particle. A bond is then classified by the coordination numbers of the two particles connected by the bond. (b) The thermodynamic heat capacity shows a flat peak around  $\Gamma = 1000$ , while the reduced capacity  $c_\omega^{(3)}$  calculated from the TCF on the shell has a peak at a significantly higher  $\Gamma$ .

zero line. The configurations are additionally distinguished with respect to the arrangement of the Voronoi cells within the cell. While for  $\Gamma \gtrsim 2000$  only the (2-56-38) intra-shell configuration is found, different intra-shell isomers contribute with significant fractions for lower coupling. The critical temperature, where the additional configurations occur, is in good agreement with the position of the peak in the thermodynamic heat capacity  $c_\omega$ . However, the peak in the reduced capacity  $c_\omega^{(3)}$  as the derivative of the entropy of the TCF is found at a ten times higher coupling strength.

### 5.2.3 Melting Processes in Further Coulomb Balls

The Coulomb cluster which was studied in the previous section is outstanding because of its magic particle number. This number allows for the formation of a highly symmetric shell. In contrast, “normal” clusters with non-magic particle numbers are the focus of this section. Therefore, the melting process of further Coulomb balls with different particle numbers is studied by the means of the  $n$ -particle distribution functions in generalized coordinates. As in the section before, the reduced entropies are used as melting parameters.

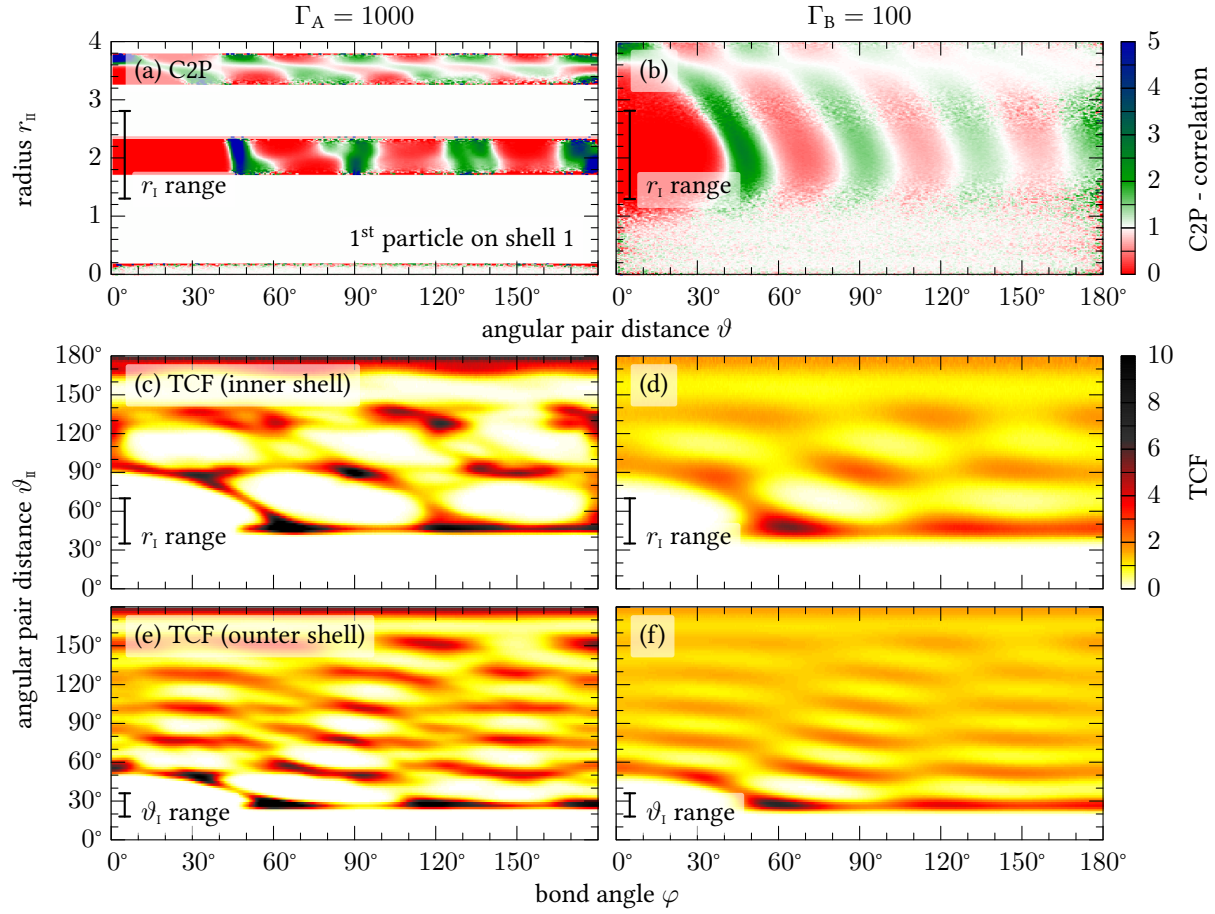


**Figure 5.15:** Spherical 3D Coulomb cluster with  $N = 80$  particles on two shells. Left (right) column:  $\Gamma = 1000$  ( $\Gamma = 100$ ). (a,b) C2P for a reference particle from the inner shell. The reference particle is selected by the  $r_I$ -integration range (bar). (c,d) [(e,f)] TCF on the inner [outer] shell. The first particle pair is selected as nearest neighbors by the  $\vartheta_I$ -integration range (bar). Reprinted from Ref. [143]. Copyright (2015) by the American Physical Society.

**3D Coulomb cluster with  $N = 80$  particles.** This cluster represents a particularly instructive example for the discussion of different transition processes [143]. Two radial isomers play an important role during the melting process of this cluster. At a very high coupling strength, the (60-19-1) radial isomer is found exclusively. This radial isomer consist of 60 particles on the outer shell, 19 particles on the inner shell, and one particle in the center. The (59-20-1) radial isomer becomes important at lower coupling.

Figure 5.15 shows an overview of the center-two-particle correlation function and triple-correlation function for this cluster at two different values of the coupling parameter. In part (a) of the figure, the C2P is shown for a reference particle from the inner shell. Therefore the three dimensional densities  $\tilde{\rho}_2(r_I, r_{II}, \vartheta)$  and  $\tilde{\rho}_2^{\text{id}}$  were both integrated over a range that corresponds to this shell. Intra-shell correlations are visible as sequence of clear minima and maxima in the direction of the angular pair distance  $\vartheta$  at  $r_{II} \approx 2$ . This value of the second radial coordinate means that the second particle is located on the inner shell as well.



In addition to these intra-shell correlations, we find pronounced inter-shell angular correlations which are seen as minima and maxima at values of  $r_{\text{II}}$  that correspond to the outer shell. For example, the clear peak at  $\vartheta = 0^\circ$  and  $r_{\text{II}} = 3.7$  indicates that the particles on the outer shell are pushed towards higher radii when they are in line with an inner particles. When an outer particle is located above the void between two particles on the inner shell, it is slightly closer to the trap center. This observation is in good agreement with the equipotential picture, Fig. 5.11, discussed for the smaller Coulomb cluster in Sec. 5.2.2 above.

For the ten times lower coupling parameter  $\Gamma = 100$  in Fig. 5.15, the intra-shell correlations are still clearly visible. However, the height of the peaks—indicated by the color—decreases rapidly with the angular pair distance. Weak inter-shell angular correlations are found only for small angular pair distances  $\vartheta \lesssim 60^\circ$  at this temperature.

The second row of Fig. 5.15 shows the TCF on the inner shell of the cluster. For all plots, one pair of nearest neighbors was chosen as the reference by the integration range of the first angular pair distance  $\vartheta_1$ . In part (b), the pattern shows clear peaks which are connected by a thready density. On the one hand, the pattern has characteristic features of a hexagonal lattice, such as for example the peak at the bond angle  $\varphi = 60^\circ$  when particle three is also a neighbor of the first particle ( $\vartheta_{\text{II}} \approx 50^\circ$ ). On the other hand, the pattern is distinctively different from the TCF in the extended 2D system, Fig. 5.2, as a consequence of the small number of particles  $N_1 = 19 - 20$  on this shell. The peak at bond angles  $\varphi = 120^\circ$  for second nearest neighbors is for example missing in this spherical system.

When the coupling strength is decreased in Fig. 5.15(d), the overall structure of the TCF is the same. The peaks are, however, smeared out and their sub-structure is lost.

In Fig. 5.15(e), the TCF of the outer shell shows noticeable similarities with the extended 2D system. Multiplies of  $60^\circ$  are preferred bond angles  $\varphi$  of nearest neighbors and multiplies of  $30^\circ$  stick out for second neighbors. These features indicate a pseudo-hexagonal order within the shell. In contrast to the planar 2D systems, the hexagons are deformed and a finite number of pentagonal Voronoi cells, i.e. particles with five nearest neighbors, exist due to the curvature of the sphere. Therefore, the peaks are smeared out in the  $\varphi$ -direction. As a “long”-range feature of this structure at strong coupling  $\Gamma = 1000$ , one also sees a distinct peak for distant particles. For example, a peak at fourth neighbors ( $\vartheta_{\text{II}} \approx 102^\circ$ ) and a bond angle of  $\varphi = 95^\circ$  signifies the existence of a bond-angular order beyond nearest neighbors. When compared to the TCF of a planar 2D system, Fig. 5.2, the similarities between the patterns are striking for the solid as well as for the liquid system. Since the phase transition is much sharper in the extended system, a qualitative change of the TCF was found between  $\Gamma = 174$  in Fig. 5.2(c) and  $\Gamma = 193$  in Fig. 5.2(d), while the shown values of  $\Gamma$  differ by a factor of ten for the spherical cluster.

After Fig. 5.15 revealed the loss of intra-shell order, the transitions will now be quantified. For this purpose, the reduced entropies  $S^{(n)}$  are calculated for the radial density, for the C2P, and for TCF on both inner and outer shells, see Fig. 5.16(a).

The entropy  $S^{(1)}$ , which is obtained from the radial density, shows its steepest decrease at approximately  $\Gamma_{\text{RM}} = 120$  and becomes flat for higher coupling strengths. For low coupling, the entropy  $S^{(2)}$ , which is obtained from the C2P distribution function, has nearly twice the value of  $S^{(1)}$ . Hence, the knowledge of the positions of one particle does not significantly reduce the uncertainty about the position of a second randomly chosen particle. The situation changes

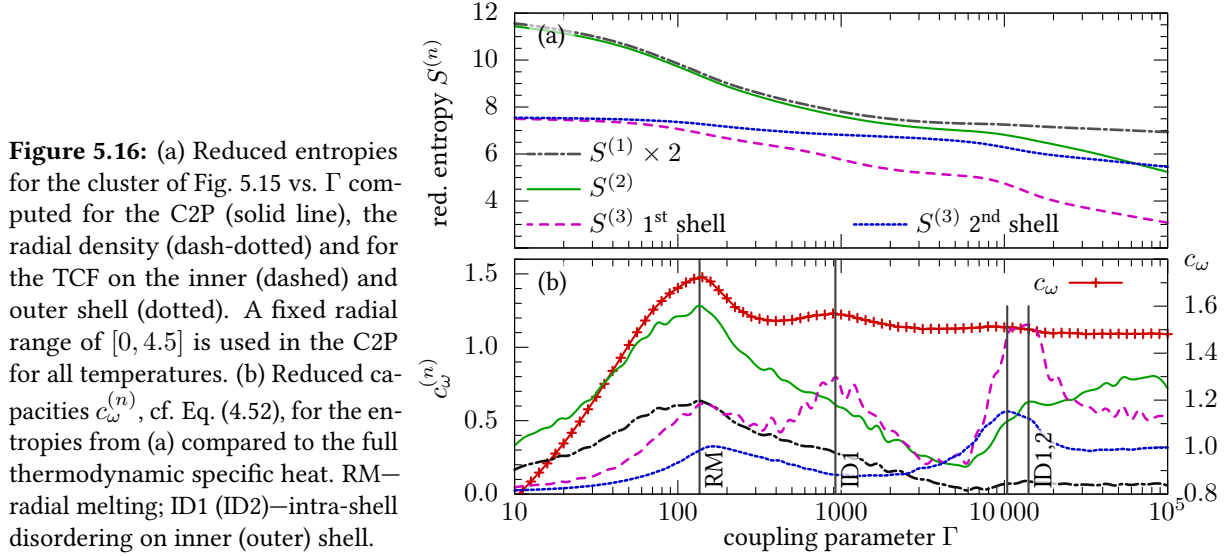


**Figure 5.16:** (a) Reduced entropies for the cluster of Fig. 5.15 vs.  $\Gamma$  computed for the C2P (solid line), the radial density (dash-dotted) and for the TCF on the inner (dashed) and outer shell (dotted). A fixed radial range of  $[0, 4.5]$  is used in the C2P for all temperatures. (b) Reduced capacities  $c_\omega^{(n)}$ , cf. Eq. (4.52), for the entropies from (a) compared to the full thermodynamic specific heat. RM—radial melting; ID1 (ID2)—intra-shell disordering on inner (outer) shell.

when the coupling parameter exceeds  $\Gamma \approx 10\,000$  where  $S^{(2)}$  bends down and, hence, indicates the relevance of angular correlations.

The entropy  $S^{(3)}$  of the TCF on the outer shell shows a small kink near the radial melting temperature and a stronger pronounced kink near  $\Gamma_{\text{ID}} = 10\,000$ . These two kinks are found in for the TCF on the inner shell as well and even more pronounced. An additional kink is found at  $\Gamma_{\text{ID}_2} = 1000$  for the inner shell.

Figure 5.16 shows the reduced heat capacities  $c_\omega^{(n)}$  which are calculated by cubic spline interpolations of reduced entropy as a function of the logarithm of the coupling parameter. These are compared with the full thermodynamic heat capacity calculated from the energy fluctuations in the same simulation.

The reduced heat capacity  $c_\omega^{(1)}$  shows a clear peak around  $\Gamma_{\text{RM}} = 120$ . Since  $c_\omega^{(1)}$  is obtained from the radial density, this peak can be associated with the radial melting process. At this coupling strength, the onion-like shell structure vanishes. The thermodynamic heat capacity  $c_\omega$  shows its highest peak for this transition and a second, weaker peak for  $\Gamma_{\text{ID}_2} = 840$ . A third, very weak peak of  $c_\omega$  is found for high coupling around  $\Gamma = 9000$ . The reduced capacities  $c_\omega^{(3)}$  of the TCF on both inner and outer shell help to explain these additional peaks in the following.

For both shells,  $c_\omega^{(3)}$  shows a peak at  $\Gamma_{\text{ID}} \approx 10\,000$ , where the peak for the inner shell is found at a slightly higher coupling strength than for the outer shell. Hence, an intra-shell disordering transition takes place simultaneously on both shells. This interpretation is strengthened by the Voronoi analyses of the two shells, cf. Fig. 5.17.

At high coupling  $\Gamma \gtrsim 20\,000$ , the cluster is found exclusively as the (60-19-1) radial isomer and on both inner and outer shell, only one intra-shell isomer is observed. For lower coupling strengths, the radial isomer with 59 and 20 particles on the inner and outer shell, respectively, becomes important as well. The Voronoi analysis, Fig. 5.17(a) reveals that two different intra-shell isomers contribute with similar fractions for the inner shell when it is occupied by 20 particles. On the other hand, only one intra-shell isomer is realized when the shell is occupied by 19 particles for  $\Gamma \gtrsim 1000$ . Several intra-shell isomers start to contribute with a significant

fraction for  $N_1 = 19$  at the second intra-shell disordering transition around  $\Gamma_{\text{ID}2} = 840$ . An open question is whether the splitting of the inner shell's configuration into several isomers is the cause of the recurrence of radial configurations with  $N_1 = 19$  particles on the inner shell.

Interestingly, the reduced capacity  $c_\omega^{(3)}$  shows only one high-coupling disordering transition for the outer shell around  $\Gamma_{\text{ID}}$  even though the intra-shell configuration splits into several isomers between  $\Gamma = 1000$  and 10 000 depending on the occupation number of the shell  $N_2$ .

Summarizing it can be said that the Coulomb cluster with  $N = 80$  particles shows at least three different disordering processes: Starting with one single radial isomer and exclusive intra-shell isomers for both shells, the transition between two radial isomers is accompanied by first intra-shell disordering processes in both shell. A second intra-shell disordering transition is found for the inner shell at lower coupling. Finally, both radial and angular<sup>4</sup> order are lost for  $\Gamma_{\text{RM}}$  in the same region as the critical coupling strength for melting in extended systems.

**3D Coulomb Cluster with  $N = 120$  Particles.** The previously considered clusters exhibited intra-shell disordering transitions which were accompanied by an inter-shell transition. When one particle is added to or removed from a shell, this causes a reordering of the particles within that shell. An interesting question is whether there exist certain clusters that exhibit an intra-shell transition without any change in the radial configuration. Such a process is observed for the Coulomb cluster with  $N = 120$  particles which will be described in the following. The ground state configuration for this particle number consists of three spherical shells which are occupied by  $N_3 = 82$ ,  $N_2 = 32$  and  $N_1 = 6$  particles. This configuration is referred to as the (82-32-6) radial isomer.

The intra-shell disordering process takes place at notably higher couplings of approximately  $\Gamma_{\text{ID}} = 50\,000$ , as shown by the Voronoi analysis in Fig. 5.18(a). At a very high coupling strength,  $\Gamma = 10^5$ , only one intra-shell isomer is found for the outer shell in the MC simulation. The Voronoi analysis of this shell shows a lattice with 14 pentagonal cells, and two heptagonal Voronoi cells. The remaining 56 particles have hexagonal Voronoi cells. One of the heptagonal cells is paired with two pentagonal cells, while the second heptagonal cell is encircled by three pentagonal cells. Therefore, five bonds of the 5-7 class—bonds that connect two particles with coordination number five and seven—are found. This intra-shell isomer is referred to as (62-171-3-4), where the four numbers refer to the number of bonds of class 5-6, 6-6, 5-7 and 6-7, cf. Fig. 5.18.

The relative position of the two heptagons within the shell could still vary with respect to the other pentagonal cells. These differences cannot be resolved by counting the bonds of different classes. However, by visually inspecting a number of independent realizations, this arrangement was found to be dominant, save for a few mirrored realizations. At a ten times lower coupling strength  $\Gamma = 10\,000$ , at least four different intra-shell isomers occur with significant fractions. The four most important isomers are (65-161-5-9) with a fraction of 64.5 %, (63-170-2-5) with 17.3 %, (62-171-3-4) with 9.3 % and (67-152-8-13) with 4.1 %.

<sup>4</sup>Since the term “intra-shell” order is misleading when the radial shell structure is lost, the term “angular” order is used here instead.

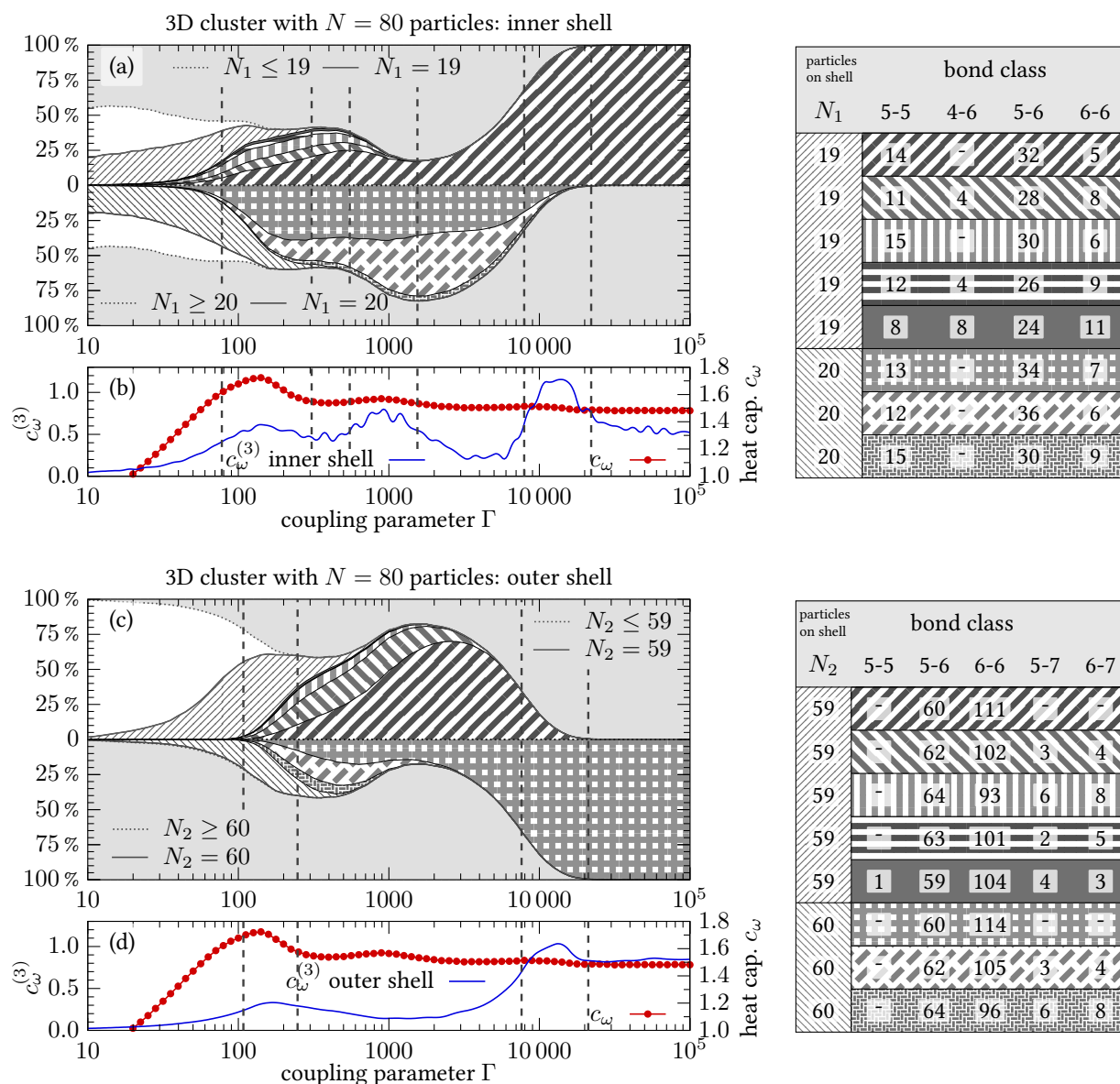


**Figure 5.17:** Voronoi analysis for both shells of the Coulomb cluster with  $N = 80$  particles. The inner shell is subject to the first two parts of the figure, while the outer shell is subject to the last two parts.

The upper graph of (a) and (c) shows the fractions of different intra-shell isomers of the inner shell and of the outer shell, respectively. A bond is further classified by the coordination numbers of the two particles connected by the bond.

The lower graph of (b) and (d) shows the thermodynamic heat capacity and reduced heat capacity from the TCF of the inner shell and of the outer shell, respectively. After Ref. [143].

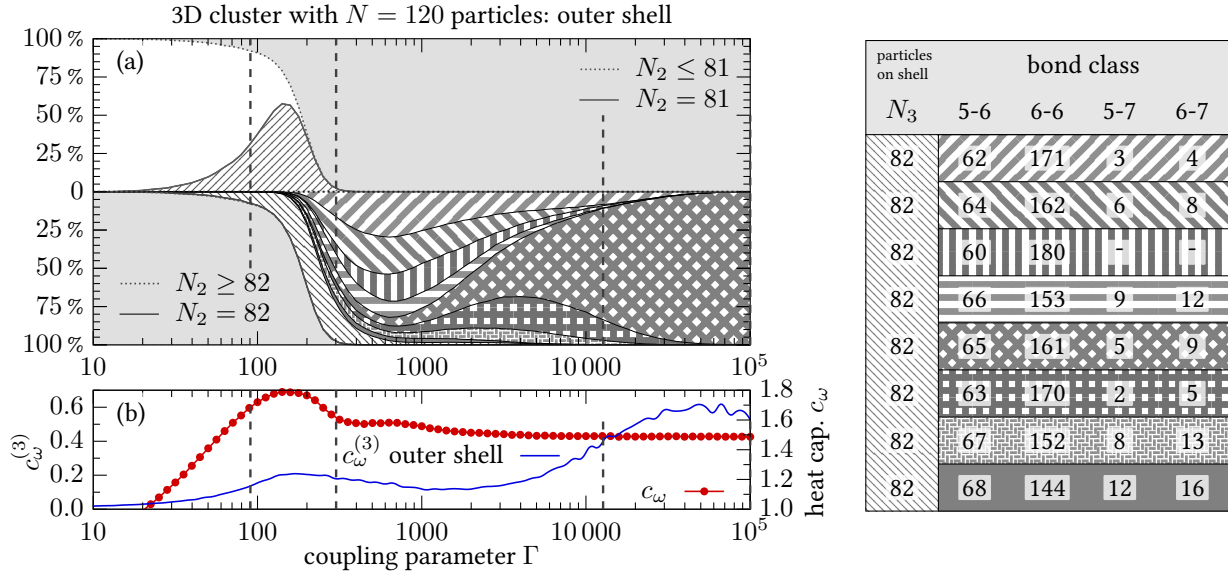


**Figure 5.18:** Intra-shell disordering transition (ID) in the outer shell of a spherical Coulomb cluster with  $N = 120$  particles around  $\Gamma_{ID} = 50\,000$ . (a) The particle number on the outer shell is constant for  $\Gamma \gtrsim 400$  while transitions between different intra-shell isomers take place at higher  $\Gamma$ . The intra-shell Voronoi analysis allows for a classification of these isomers. (b) While the thermodynamic heat capacity  $c_\omega$  captures only the radial melting (RM) at  $\Gamma \approx 165$ , the reduced heat capacity  $c_\omega^{(3)}$  computed from the entropy of the TCF captures also the intra-shell disordering. After Ref. [143].

Notably, the (60-180-0-0) configuration with twelve pentagons and 70 hexagons is not realized at very high coupling strength although this configuration is the solution of the Thomson problem for 82 electrons [144]. This finding is no contradiction but discloses qualitative differences between a Thomson sphere and a spherical shell of a Coulomb cluster.<sup>5</sup> One difference is the anisotropy of the Coulomb potential caused by the inner particles, cf. Sec. 5.2.2. Although the anisotropy is small, it may have an effect on the particle configuration within the shell especially at low temperature. Moreover, the radial confinement is finite for Coulomb clusters in contrast to the Thomson problem. The finite width of the spherical cluster shells even at strong coupling grants an additional degree of freedom. Due to this degree of freedom, configurations other than the solution of the Thomson problem can become energetically favorable.

As shown in Fig. 5.18(b), the reduced entropy of the TCF is suited to resolve the intra-shell shell disordering process around  $\Gamma_{ID} = 50\,000$ . In order to understand the sensitivity of the TCF to this transition, this quantity is shown for one value of the coupling parameter in the totally ordered phase and one in the partially disordered phase as a mixture of multiple intra-shell isomers in Fig. 5.19. The triple-correlation function was sampled from 37 500 configurations, where  $M = 1000$  MC steps were performed between every two samples. In figure 5.19(a), a fine structure with several sharp peaks is found. These fine peaks of the shown TCF present the

<sup>5</sup>As a check for the MC program, a simulation was performed for  $N = 82$  particles with Coulomb interaction placed on a sphere. This simulation could reproduce the correct configuration at high coupling strength.

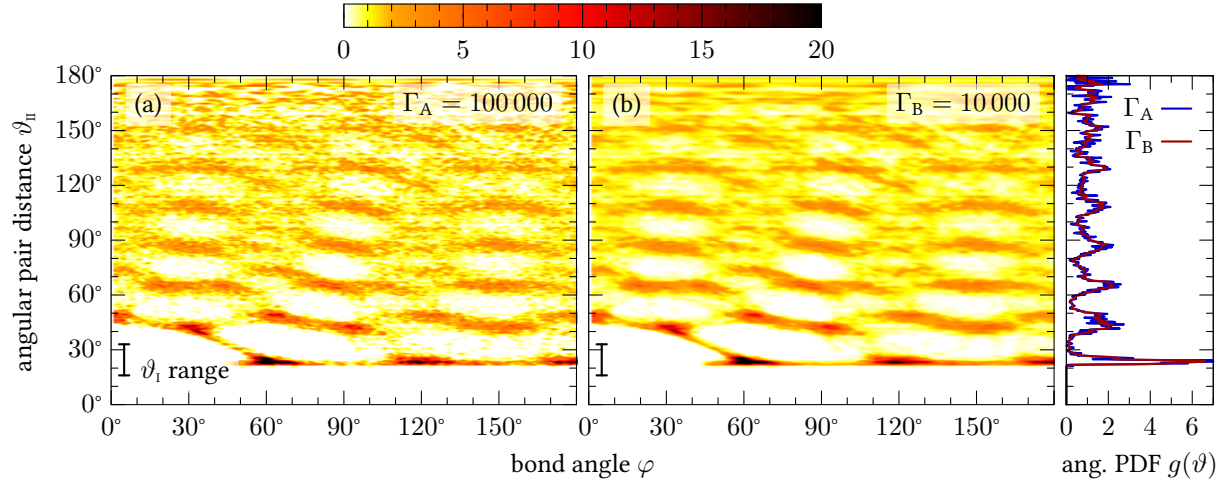


**Figure 5.19:** TCF on the outer shell of the Coulomb cluster with  $N = 120$  particles for two different values of the coupling strength  $\Gamma$ . The right column shows the angular pair distribution function within the shell for both coupling parameters.

characteristics of the intra-shell structure. One has to keep in mind that the plot represents the *average* probability distribution to find a third particle at a certain distance  $\vartheta_{II}$  and under a bond angle  $\varphi$  with respect to one nearest neighbor bond. The sampling procedure and the subsequent  $\vartheta_I$  integration imply averaging over all nearest neighbor bonds as the reference direction. For this reason, a multitude of small peaks is found in Fig. 5.19(a). These fine peaks become smeared out when the temperature is increased by a factor of ten in part (b) of the same figure. At this increased temperature, several different intra-shell isomers contribute to the thermodynamic ensemble, cf. Fig. 5.18.

Since the reduced entropy  $S^{(3)}$  is sensitive to the fine structure of TCF, this quantity can resolve the intra-shell disordering transition at high coupling. During this transition, the order within the shell is not lost completely. Every configuration shows a well-defined pattern of hexagons, several pentagons, and a few heptagons in the intermediate regime. However, different isomers occur with significant fractions in this regime. Finally, the reduced capacity  $c_\omega^{(3)}$  shows a second peak around  $\Gamma_{RM} = 165$  where both radial and intra-shell order are completely lost.

### 5.3 Particles on a Unit Sphere

This section is concerned with the melting process for particles on a Thomson sphere [100]. In the previous section, different melting processes were studied for spherically confined dust clusters. Due to their onion-like shell structure, these clusters exhibit intra-shell disordering processes at coupling parameters which are significantly higher than the critical coupling parameter for the radial melting.

While the spherical clusters shells are similar to the Thomson problem in some sense, there exist at least two qualitative differences. For spherical cluster shell, the radial potential is a superposition of the repulsive Coulomb potential by the inner particles and confining trap potential.

Due to the finite force by this potential, the spherical shells can have a finite width. Moreover, the Coulomb (or Yukawa) potential exerted by the particles on the inner shells is not exactly isotropic in general as seen in Fig. 5.11. The equipotential surface of this potential is a sphere with hills and valleys. Even though the relative derivations from a perfect sphere are small, they can have an impact on the precise intra-shells structure especially at high coupling strengths.

In contrast, the Thomson problem describes distribution of  $N_s$  Coulomb interacting particles on the surface on a sphere. This surface has zero extension in radial direction and, moreover, no anisotropic potential is present in this setup. Although the problem was originally considered for bare Coulomb interaction, it can be generalized by using a different pair interaction potential  $W(|\mathbf{r}_{(j)} - \mathbf{r}_{(i)}|)$ . The coupling parameter  $\Gamma$  for these system is defined in Sec. 3.2.1 using spherical caps as the equivalent of the Wigner-Seitz cell.

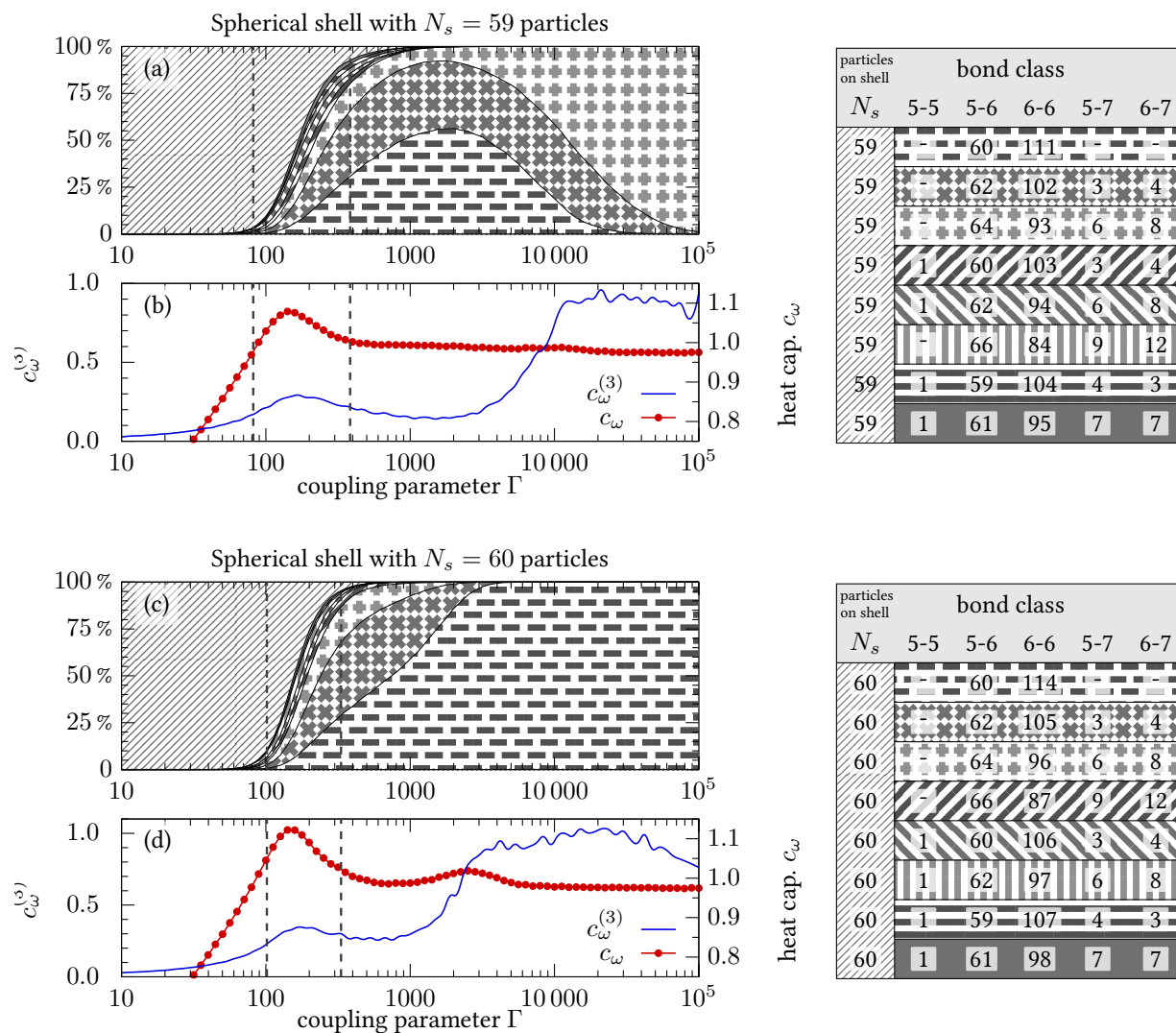
The intention of this section is to elucidate the impact of the finite shell width and the interaction with the particles of the inner shells on the intra-shell disordering process. Section 5.2.3 already detailed the differences between the ground-state configurations of a Thomson sphere and the outer shell of the Coulomb ball with  $N = 120$  particles.

Figure 5.20 shows the result of the Voronoi analysis for  $N_s = 59$  and  $N_s = 60$  particles on a spherical surface as well as reduced capacity  $c_\omega^{(3)}$  which is obtained from the TCF. The first three intra-shell isomers for each particle number are the same that were already found for the outer shell of a full 3D Coulomb cluster with  $N = 80$  particles in total, cf. Fig. 5.17.

When  $N_s = 59$  particles are placed on the spherical surface, basically one isomer with 14 pentagonal, 43 hexagonal and two heptagonal Voronoi cells [curve filled with crosses in Fig. 5.20(a)] is found at high coupling strength. This configuration is the solution of the Thomson problem for 59 particles [100, 101, 144]. However, the isomer with only one pentagonal Voronoi cell [curve filled with diagonal crosses in Fig. 5.20(a)] has a significant contribution in the canonic ensemble, even at the highest value of  $\Gamma = 10^5$ . The fraction of this isomer increases with decreasing coupling, and a third isomer with no heptagonal Voronoi cell [curve filled with dashes in Fig. 5.20(a)] becomes important for  $\Gamma \lesssim 3 \times 10^4$ . For  $\Gamma \approx 2000$  the later isomer is even found in the majority of cases. When the coupling parameter is decreased further, several different isomers start to contribute until the structure is completely lost near  $\Gamma_M = 150$ . The transition causes a peak in the thermodynamic heat capacity  $c_\omega$  whose position is in reasonable agreement with the critical coupling strength for melting in flat, extended 2D systems.

For the reduced capacity  $c_\omega^{(3)}$  obtained from the TCF, cf. Fig. 5.20(b), the peak is shifted towards a slightly higher value of  $\Gamma = 185$ . As a second prominent feature, the reduced capacity shows a more or less sharp increase from  $c_\omega^{(3)} = 0.2$  to 0.9 between  $\Gamma = 3000$  and 12 000. The explanation of this feature is still an open question since several isomers are import already at higher coupling strength as shown in the upper part of the figure.

When one particle is added, the isomer with twelve pentagonal and 48 hexagonal Voronoi cells dominates the structure for  $\Gamma \gtrsim 4000$  as shown in Fig. 5.20(c). This finding also agrees with the solution of the Thomson problem [144]. When the coupling strength is decreased, two additional isomers occur with significant fractions. Between  $\Gamma = 1200$  and 3500, the reduced capacity shows a distinct increase from  $c_\omega^{(3)} = 0.34$  to 0.89 in the strong coupling regime, cf. Fig. 5.20(d). The position of this step coincides with the critical coupling strength



**Figure 5.20:** (a,c) Voronoi analysis for a Thomson setup of  $N_s = 59$  and 60 particles on a spherical surface. (b,d) Thermodynamic heat capacity  $c_\omega$  and reduced heat capacity  $c_\omega^{(3)}$  obtained from the TCF for both particle numbers.



for the transition where different isomers become important. Moreover, a small peak of the thermodynamic heat capacity  $c_w$  is found at  $\Gamma_{\text{ID}} = 2450$ .

A further decrease of the coupling strength results in a melting process around  $\Gamma_{\text{M}} = 150$  where the order within the spherical surface is completely lost. The number of isomers found increases drastically during this transition from about 100 different isomers at  $\Gamma = 300$  to about 4000 different isomers at  $\Gamma = 100$ . As for the previously considered particle number, the corresponding peak in the reduced capacity from the TCF is shifted towards a slightly higher value of  $\Gamma = 200$ .

The MC simulations for Coulomb particles on a spherical surface revealed that neither an anisotropic potential nor a finite shell width is essential for a two-step intra-shell disordering process. The transition between the partially disordered and fluid-like states is observed at  $\Gamma = \mathcal{O}(100)$  for all particle numbers. On the other hand, the exact particle number  $N_s$  crucially affects the critical coupling parameter for the transition between a completely mono-isomer intra-shell configuration and a partially disordered system with several isomers.

In addition, the above analysis of order within the spherical surface helps to understand the intra-shell disordering processes in the outer shell of the Coulomb cluster with  $N = 80$  particles discussed in Sec. 5.2.3. At high coupling strength  $\Gamma = 10^5$ , the outer shell is occupied by  $N_2 = 60$  particles and the ground-state intra-shell isomer with twelve pentagonal Voronoi cells is realized. The analysis of the spherical surface, Fig. 5.20(c), suggests that different isomers become important for  $\Gamma \lesssim 4000$ . Even though this transition is observed in the full cluster as well, a different kind transition takes place already at higher coupling strength around  $\Gamma = 15\,000$ . At this point, the most probable number of particles on the shell decreases by one. Therefore, isomers with  $N_2 = 59$  dominate the structure within the outer shell in the  $\Gamma$ -region between 500 and 5000.

Interestingly, a qualitative difference is observed between  $N_2 = 59$  particle on a cluster shell and the same number of particles on a perfect spherical surface. The ground-state isomer of the latter includes two heptagonal Voronoi cells. In contrast, this isomer is not observed for high coupling strength  $\Gamma \gtrsim 2000$  for the cluster shell, but an isomer with twelve pentagonal cells and no heptagonal cell is found predominantly in this regime.

**Related Journal Publications and Book Chapters**

- P. Ludwig, H. Thomsen, K. Balzer, A. Filinov, and M. Bonitz *Tuning correlations in multi-component plasmas*, Plasmas Phys. Controlled Fusion **52**, 124013 (2010)
- A. Schella, T. Miksch, A. Melzer, J. Schablinski, D. Block, A. Piel, H. Thomsen, P. Ludwig, and M. Bonitz *Melting scenarios for three-dimensional dusty plasma clusters*, Phys. Rev. E **84**, 056402 (2011)
- J. Wrighton, H. Kählert, T. Ott, P. Ludwig, H. Thomsen, J. Dufty and M. Bonitz *Charge Correlations in a Harmonic Trap*, Contrib. Plasma Phys. **52**, 45 (2012)
- A. Melzer, A. Schella, T. Miksch, J. Schablinski, D. Block, A. Piel, H. Thomsen, H. Kählert, and M. Bonitz *Phase Transitions of Finite Dust Clusters in Dusty Plasmas*, Contrib. Plasma Phys. **52**, 795 (2012)
- H. Thomsen, J. Schablinski, and M. Bonitz *Phase Transitions in Dusty Plasmas* in *Complex Plasmas: Scientific Challenges and Technological Opportunities* edited by M. Bonitz, J. Lopez, K. Becker and H. Thomsen (Springer, New York, 2014)
- H. Thomsen, and M. Bonitz *Resolving structural transitions in spherical dust clusters*, Phys. Rev. E **91**, 043104 (2015)

## Chapter 6

# Laser Excitation of 2D Dust Clusters

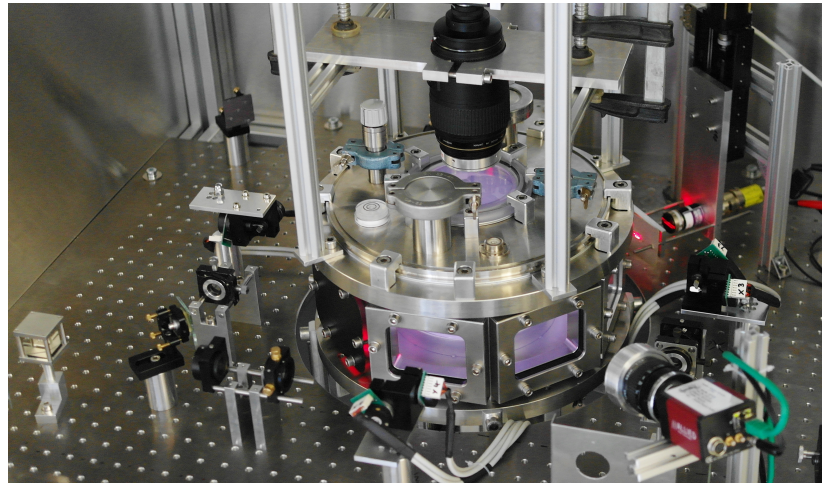
**L**aser beams offer a reliable manipulation method which is essential for the study of structural transitions in dusty plasma experiments. As manipulation tools, laser beams with moderate intensities of several watts were suggested many years ago [92, 93] and have since then proven ideally suited for this purpose. An important reason for the success of this method is that it allows for a manipulation of the dust particles without any significant effect on the plasma parameters such as electron temperature or pressure.

Due to the momentum transfer by the radiation pressure, a focused modest intensity laser beam is well capable of accelerating single dust particles. In that manner, stationary laser beams were used to excite shear flows in monolayer dust crystals [145, 146] as well as to excite rotations in finite 2D clusters [45]. In extended 2D dust crystals, Mach cones were excited by moving the laser spot through a crystal with a moderate velocity [36, 97]. Here, it will be demonstrated that moving laser spots can be used as a heat source for the dust component [4, 5, 40, 147, 148].

The systematic experiments of WOLTER and MELZER [4] and NOSENKO *et al.* [5, 147] can be regarded as pioneering works for heating dusty plasmas with lasers. WOLTER and MELZER used a technique [4] where the spot of a laser beam is rapidly moved via scanning mirrors to one position in a 2D dust cluster, where it remains at for about one tenth of a second, accelerating dust grains during this time. The laser spot is then rapidly moved to the next randomly chosen position. A similar heating scheme for spherical 3D dust balls was developed in Greifswald [56]. In this experiment, the cluster is manipulated by one laser beam in the horizontal direction using this ‘point and shoot’ technique. A near Maxwellian velocity distribution of the particles is realized with one single beam. However, the kinetic temperature in the beam direction is different from the one perpendicular to the beam.

NOSENKO *et al.* exploited two opposing laser beams that were directed onto a 2D plasma crystal using scanning mirrors [5, 147]. These scanners were driven with a sinusoidal signal at an irrational frequency ratio for the  $x$ - and  $y$ -directions. This setups allows them to scan (i.e., heat) a well-defined area of the plasma crystal in a Lissajous figure-like pattern. In addition, the opposing beam setup assures that the transferred momenta cancel on average, while the kinetic energy of each particle is raised as a result of non-compensated momentum fluctuations.

**Figure 6.1:** Photographic image of the laser manipulation experiment in Kiel with the plasma chamber in the center. The top view camera is found above the experiment, and the beam guidances for the manipulation lasers are mounted around the chamber. Photographic image kindly provided by J. Schablinski.



With their laser manipulation tool, NOSENKO *et al.* were able to generate a Maxwellian velocity distribution parallel and perpendicular to the optical axis. Since the direction perpendicular to the beams is heated only indirectly, the kinetic temperature in that direction was found to be significantly lower than the temperature in the beam direction. One can conclude that the energy is transferred to the neutral gas by the viscous damping before collisions between the particles can redistribute sufficient energy in the perpendicular direction.

In Kiel, SCHABLINSKI *et al.* used the above method for finite 2D dust clusters with approximately ten to 50 particles [40, 49]. Their experiment was supplemented by a second pair of opposing laser beams in the perpendicular direction in order to overcome the anisotropy in the velocity distribution. Moreover, different scanning patterns of the laser spots were tested, and a significant impact on the quality of the laser manipulation technique as a heating tool was found. The Langevin molecular dynamics (LMD) simulations of this thesis are closely connected to this experiment. Their purpose is to verify the excellent quality of the elaborated heating method as a true heat source and to suggest further possible application of the laser manipulation technique. In the following section, the experimental setup is described as well as the used scanning pattern. Thereafter, the inclusion of the heating laser in the LMD simulation is concerned.

## 6.1 Laser Heating Method

In order to investigate the melting behavior of small 2D dust clusters, a laser manipulation experiment with two manipulation axes was set up by the group of PIEL in Kiel [40, 149]. The setup consists of two laser beams with a power of about 5 W, which are split up into four single beams. The two beams from one laser source are referred to as a beam pair. Guided by the optical setup, the two beams of one pair manipulate the cluster from opposite sides. The beam pair of one laser accelerates the particles in  $\pm x$ -direction, and the beam pair of the other laser accelerates them in  $\pm y$ -direction. Isotropic heating is achieved by adjusting and stabilizing the power output of each laser by a feedback control. The beams hit the particles from above the levitation plane with an angle  $\alpha \approx 10^\circ$ , cf. Fig. 6.4 (p. 93). Each spot position within the levitation plane is controlled by a pair of scanning mirrors. A sketch of this setup is shown in Fig. 6.2.

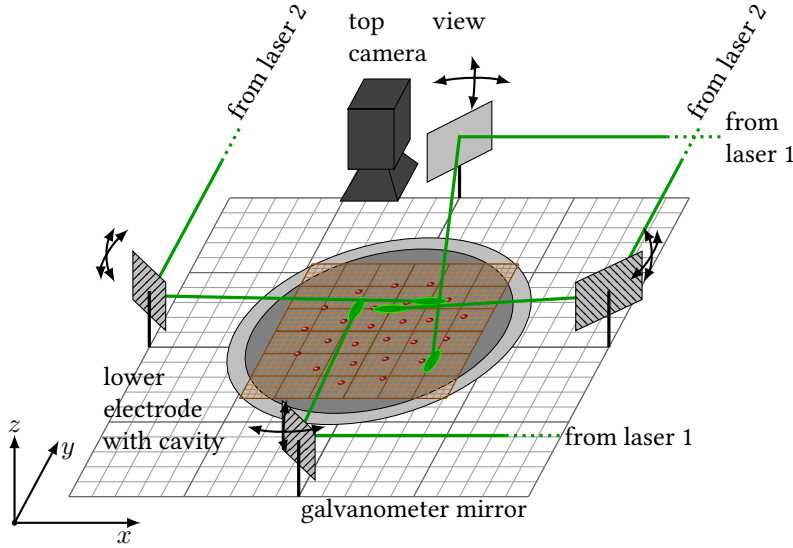


**Figure 6.2:** Sketch of the experimental setup of the laser manipulation technique described in Ref. [40]. Four laser spots (green) are moved individually within the levitation plane (orange) by the galvanometer mirrors. The dust cluster (red points) is levitated above the lower electrode (gray) and is observed with the top view camera.

method	A-I	A-II	B
laser beams	2	2	4
frequency ratio	pseudo-irrational	rational	random frequencies
$f_{\parallel}$	14.5623 Hz	300 Hz/375 Hz	50 Hz to 300 Hz
$f_{\perp}$	9.0 Hz	12 Hz/15 Hz	15 Hz to 60 Hz

**Table 6.1:** Parameters defining the pattern which is scanned by the lasers. Since both beams are oriented in  $\pm x$ -direction for the two methods A,  $f_{\parallel} = f_x$  in that case.

Each of the four galvanometer scanners is driven by two triangular signals, one controls the spot position in the beam direction and the second controls the spot position in the perpendicular direction. Using a triangular driver signal is essential to achieve a homogeneous average intensity distribution over the entire rectangle that is scanned. A heating scheme is characterized by the frequencies of the driver signals.

Three heating methods were investigated in the experiment by SCHABLINSKI *et al.* For the first two methods, only one beam pair is used and the scanners are driven with fixed frequencies. Method A-I is inspired by the experiment of NOSENKO *et al.* [5], where a pseudo-irrational frequency ratio is used. For method A-II, the scanner frequencies are increased by about one order of magnitude, and the rational frequency ratio 1:25 is chosen for both lasers. Therefore, both lasers scan exactly the same closed pattern several times per second. Finally, both laser pairs are used in the elaborated method B and the scanner frequencies are dynamically changed. Whenever a laser spot reaches the border of the scanned area, a new random frequency chosen within a given range. The parameters of the three methods are summarized in Tab. 6.1, and Fig. 6.3 sketches the patterns that are scanned by the different laser spots.

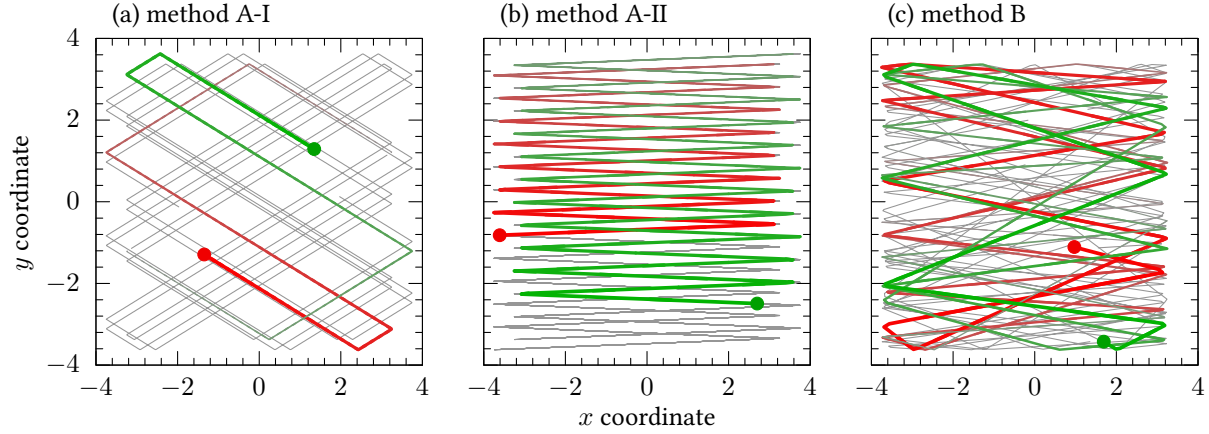


**Figure 6.3:** Trajectories of the laser spots (red/green:  $\pm x$ -direction) for the three investigated heating methods. (a) Method A-I uses a pseudo-irrational frequency ratio. (b) Method A-II uses a rational frequency ratio. (c) Using method B, a new scanning frequency is randomly chosen each time a laser spot reaches the border. Here, the two additional spots of the laser oriented in the  $\pm y$ -direction are omitted, for the sake of clarity [6].

Although the rational frequency method A-II was found to be inadequate as a heating tool, it is listed here for completeness. During the work of this thesis, LMD simulations were also performed for that method. In the related publications [40, 49], it is shown that the heating effect depends crucially on the exact relative position of the patterns scanned by the two laser spots. As discussed in my diploma thesis [150], the entire pattern is repeated several times within  $t_0 = \omega_0^{-1}$  as the typical time scale for the dust dynamics. Therefore the dust grains see a force field which is virtually constant in time. This average force field is controlled by the spot offset as the relative position of the scanned patterns, and it vanishes for zero spot offset. Since controlling the spot offset with the required accuracy is challenging in the experiment, it is difficult to reproduce a specific heating power.

### 6.1.1 Including Heating Lasers in the Model System

An computer experiment aimed at describing the laser heating methods is performed by including the momentum transfer by the manipulation lasers in the LMD simulation scheme. The Metropolis MC technique is less appropriate for this task due to the non-equilibrium character of the experiment and due to the time dependence of the spot positions. During the acceleration, energy is transferred from the lasers to the dust particles, and the dust particles lose energy to the neutral gas by friction. The equilibrium temperature of the dust  $T_{\text{eq}}$  is determined by the balance of both energy currents. Since  $T_{\text{eq}}$  is *a priori* unknown, its dependence on the laser power and on the scanned pattern is of central interest. At this point, the neutral gas is considered as a thermostat at fixed temperature  $T_0$  due to its large heat capacity compared to the dust particles. Moreover, the neutral gas is in thermal contact with the plasma chamber.

The laser-matter interaction itself, which allows to accelerate the dust grains, is not subject of this thesis. In this paragraph it is described how the momentum transfer due to the radiation pressure is modeled in the LMD simulation. A possible heating of the bulk material of the dust

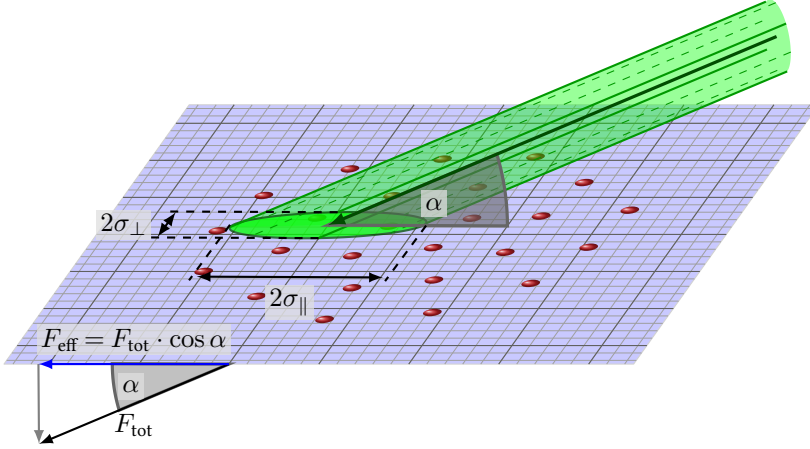


**Figure 6.4:** The angular striking of the laser spots results in an anisotropic spot profile within the levitation plane. Due to the strong vertical confinement, only the in-plane component of the force  $F_{\text{eff}}$  can accelerate the dust particles. For the sake of clarity, only one laser beam is shown.

grains as solid bodies as well as effects like “rocket forces” by laser-induced evaporation of material [151] are beyond the scope of this thesis. Here the focus lies on the center-of-mass motion of the dust particles. When a dust particle with a radius  $r_d$  is placed in a beam of light with intensity  $I_{\text{laser}}$ , there is a force in beam direction with an amplitude [152, 153]

$$F_{\text{light press.}} = q \cdot \frac{n_1 I_{\text{laser}} \pi r_d^2}{c}, \quad (6.1)$$

where  $n_1$  is the refractive index of the surrounding medium, i.e., the plasma. The vacuum speed of light is denoted by  $c$  and  $q$  is a dimensionless quality factor that describes the relevant optical properties of the dust grain. This factor is unity for a perfect absorber, it is zero for a fully transparent particle, and the factor  $q$  of a flat mirror is two. In reality, all these three processes, absorption, transmission and reflection of the laser light play a role. For melamine-formaldehyde microspheres, which are used in many dusty plasma experiments, a factor  $q = 0.94 \pm 0.11$  was determined experimentally [154].

The intensity at a position  $\mathbf{r}$  in the levitation plane is modeled by an anisotropic Gaussian,

$$I_{\text{laser}}(\mathbf{r}) = \frac{P_{\text{laser}}}{2\pi \sigma_x \sigma_y} \cdot \exp \left\{ -\frac{\Delta x^2}{2\sigma_x^2} - \frac{\Delta y^2}{2\sigma_y^2} \right\}, \quad (6.2)$$

where  $(\Delta x, \Delta y)$  is the distance between  $\mathbf{r}$  and the beam center. The total power  $P_{\text{laser}}$  of the beam is given by the integral of its intensity. The anisotropy of the profile results from the angular striking of the levitation plane under an angle  $\alpha$ , see Fig. 6.4.

For 2D dust clusters, the vertical confinement is very strong compared to the inter-particle forces. Therefore, the vertical component of the laser force has no impact on the particles' motion and only the in-plane component is included in the simulation as the effective force  $F_{\text{eff}}$ . Using the intensity profile [Eq. (6.2)] in the expression for light pressure [Eq. (6.1)], the effective force by one laser beam  $l$  acting on a particle at  $\mathbf{r} = (x, y)$  is given by

$$\mathbf{F}_l(\mathbf{r}, t) = \underbrace{qn_1 \frac{\pi r_d^2}{c} P_{\text{laser}} \cos \alpha}_{=F_l} \frac{1}{2\pi \sigma_x \sigma_y} \exp \left\{ -\frac{1}{2} \left[ \left( \frac{x - x_l(t)}{\sigma_x} \right)^2 + \left( \frac{y - y_l(t)}{\sigma_y} \right)^2 \right] \right\} \mathbf{e}_l. \quad (6.3)$$

The trajectory of the spot center is described by  $\mathbf{r}_l(t) = (x_l(t), y_l(t))$ , and the beam direction is denoted by  $\mathbf{e}_l$ . In principle, the direction of a beam changes when the spot is moved perpendicular to the beam direction by turning the galvanometer mirror. Since the distance between the cluster and the galvanometer mirrors is large compared to the extension of cluster, the small change of the direction is neglected. Moreover the laser intensity is assumed to be constant over the extension of the dust particle. This is justified since the typical sizes of the dust grains are  $d_d \approx 6 \mu\text{m}$  while the typical spot width is on the order of several hundred micrometers.

In the model system, the heating lasers are included as four additional time and space-dependent forces of the form of Eq. (6.3). The total power of a beam at the position of the cluster, is converted into a force amplitude  $F_L$  in dimensionless units. Strictly speaking,  $F_L$  has the dimension *force*  $\times$  *area*. Therefore, this parameter is given in units of  $F_0 = m_d \omega_0^2 r_0^3 = E_0 r_0$  in the following. As  $F_L$  is proportional to the total power  $P_{\text{laser}}$  of the laser beam, it is referred to as *dimensionless heating power*. Together with the spot size in the denominator, the pre-factor in Eq. 6.3 is a force.

### 6.1.2 The Effect of Different Heating Methods on Structure and Dynamics of a Dust Cluster

The velocity power spectra, the velocity distributions of the particles as well as the spatial densities are compared for the three heating methods in Fig. 6.5. For heating method A-I, which uses one pair of laser beams in  $\pm x$ -direction and a pseudo-irrational frequency ratio, multiple sharp peaks are found in the velocity power spectrum (a) for  $v_x$  at the scanner frequencies and combinations of them. Moreover, the power transfer from  $x$ - to  $y$ -direction works efficiently only for low frequencies  $f \lesssim 10$  Hz. As the spectral power coincides with the one of the unheated clusters for higher frequencies in  $y$ -direction, these frequencies are not excited by this heating method. The anisotropy of the heating effect is also visible as a significantly broader velocity distribution for the actively heated  $x$ -direction compared to the passive  $y$ -direction, even though the velocity distribution in the latter direction is also broadened, Fig. 6.5(d). The non-Maxwellian character of the profile of  $v_x$  is visible as an over-population of the high velocities. Despite the velocity distribution that is broader than for the random frequency method, method A is less effective in destroying the spatial order as clear peaks are still visible in the spatial density, Fig. 6.5(g). In addition, a slight anisotropy appears to be embossed to the structure by heating method A-I.

The rational frequency ratio method A-II with one beam pair reveals even more inferior heating properties. Apart from the striking peaks at different combinations of the scanner frequencies in the spectrum for  $v_x$ , only low frequencies  $f \lesssim 5$  Hz are excited by this heating scheme for both directions. This observation is explained by the picture of a virtually time-independent force field due to the standing pattern scanned by the laser. Such a field is expected to excite predominately those modes with low frequencies. In the velocity distribution the deviation from a Maxwellian profile is less pronounced than for the previous heating scheme,

<sup>1</sup>Note that  $F_L$  is proportional to the power of one single laser beam. Due to the doubled number of spots, the total laser power is two times higher for method B compared to methods A-I and A-II.



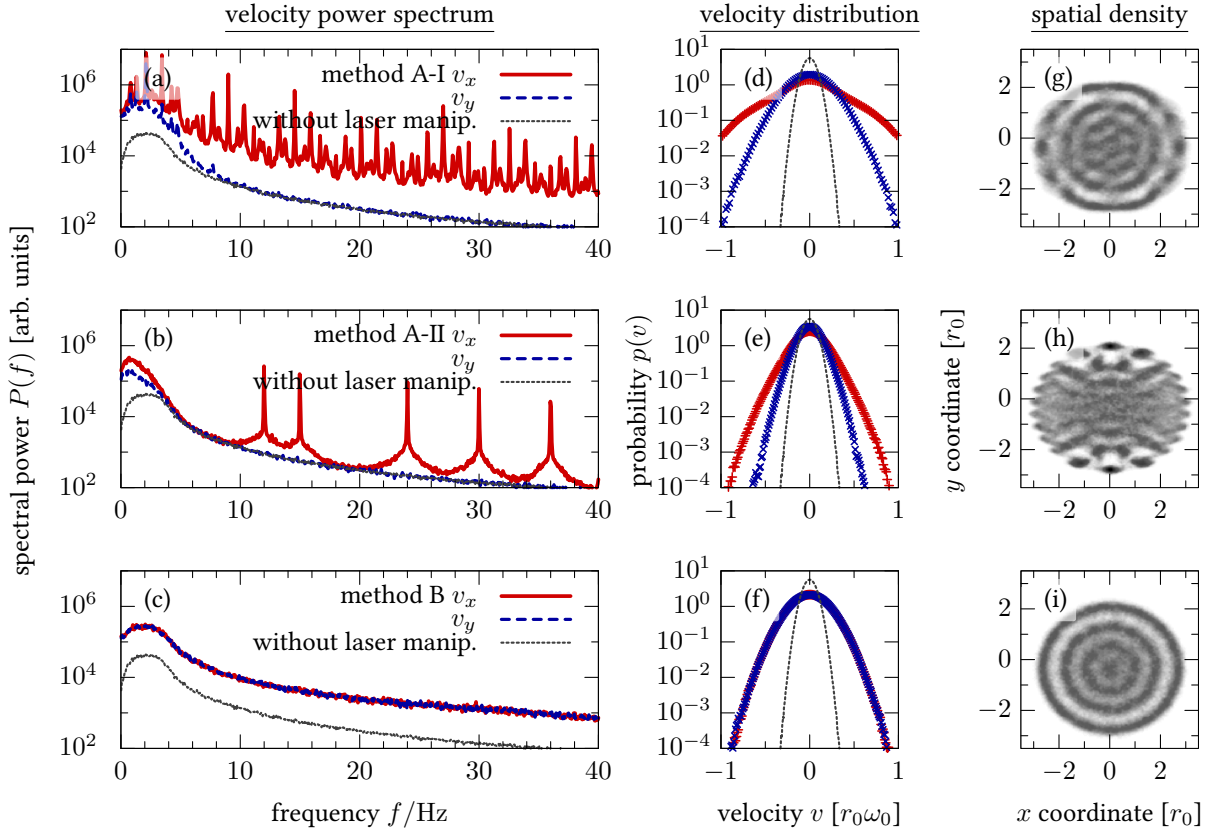


**Figure 6.5:** Results from an LMD simulation for a 2D Yukawa cluster ( $\kappa = 1$ ) with  $N = 38$  particles applying the three different heating methods with a dimensionless heating power  $F_L = 20$  (trap frequency  $\omega_0 = 5.5 \text{ s}^{-1}$ ) [6]. Methods A-I and A-II use only one pair of laser beams in  $\pm x$ -direction, while method B also uses a second beam pair in  $y$ -direction.<sup>1</sup>(a-c) Velocity power spectra for the motion in both  $x$ - (red) and  $y$ -direction (blue) and for an unheated cluster (gray). (d-f) Velocity distributions for both directions compared to a cluster without manipulation lasers. A Maxwellian velocity distribution appears as a parabola due to the logarithmic probability scale. (g-i) Spatial density averaged over  $\Delta t = 1000 \text{ s}$ .

yet still an overpopulation of fast particles is visible for  $v_x$ . The average density in Fig. 6.5(h) shows that the heating method A-II embosses a spatial structure to the cluster, since both lasers scan a closed pattern. While the unheated cluster rotates due to the thermal excitation of the corresponding collective mode, the rotation is stopped here. Hence, localized density peaks are found in the both north and south regions of the cluster. In contrast, the dust cluster is clearly molten along the central stripe. A zig-zag structure at both right and left sides is caused by the superposition of the harmonic trap potential and the quasi-constant force field by the two fast moving laser spots [49].

Finally, the excellent heating properties of the random frequency method B with four laser spots in total result in a constant shift of the entire velocity spectrum towards higher powers in Fig. 6.5(c). Since no frequency is preferred by this excitation scheme, the shape of the spectrum is conserved. Besides, neither the spectral power nor the velocity distribution in Fig. 6.5(f) indicate any difference between the  $x$ - and the  $y$ -direction. The velocity distribution

is broadened compared to the unheated cluster, whereat isotropy and Maxwellian shape are conserved. Unlike the previous methods, this heating method B does not impose an artificial pattern to the dust system as indicated by an rotationally invariant density with several circular shells in Fig. 6.5(i). Even tough shells are clearly visible as a radial modulation of density in the radial direction, frequent particle transitions between different shells are visible as a finite density in between the shells. To conclude, the combination of each one beam pair per direction and dynamically changed random scanner frequencies is well suited to heat a 2D dust cluster thermodynamically [49].

### 6.1.3 Analytical Model of the Laser Heating Process

The laser heating method is a well approved technique to control the dust kinetic temperature in a dusty plasma. WOLTER *et al.* derived an analytic approximation for the equilibrium temperature  $T_{\text{eq}}$  in a setup with one laser spot that was rapidly moved to one position, remained there for a dwell time of a few microseconds and was then moved to the next position [4]. In this section the elaborated heating method B with two beams direction is considered in particular.

In the following, an analytic expression is derived which describes the dependence of the equilibrium temperature  $T_{\text{eq}}$  of the dust system on the specific parameters of the laser heating method, namely the intensity, the spot size, the scanner frequencies and the size of the scanned area.

Considering one pair of laser spots, the beam direction is  $+x$  for the first and  $-x$  for the second beam. Therefore, only forces, momenta, etc. in  $x$ -direction are considered. These quantities are then treated as scalars and no indices  $x$  and  $y$  have to be added. The accelerating forces by the two laser beams, Eq. (6.3), are hence given by

$$F(\Delta x, \Delta y) = \pm F_L \frac{1}{2\pi} \frac{1}{\sigma_x \sigma_y} \exp \left\{ -\frac{1}{2} \left( \left( \frac{\Delta x}{\sigma_x} \right)^2 + \left( \frac{\Delta y}{\sigma_y} \right)^2 \right) \right\}, \quad (6.4)$$

as a function of the particle's distance from the spot center, which is denoted by  $\Delta x$  and  $\Delta y$ .

Each spot moves randomly through the levitation plane. Thereby, it follows a pattern with following the properties. The spot velocity is randomly chosen within a range  $v_x \in [v_x^{\min}, v_x^{\max}]$  and  $v_y \in [v_y^{\min}, v_y^{\max}]$  and the spot then moves *uniformly* until it reaches an edge of the scanned rectangle. As the length  $X$  and the width  $Y$  of the scanned area are fixed and the scanners are driven by a triangular signal, the conversion between spot velocities and scanner frequencies is straightforward,  $v_x = 4X f_x$  and  $v_y = 4Y f_y$ . The ranges of the spot velocity are given by the ranges of the scanning frequencies, see Tab. 6.1, multiplied by the width of the scanned rectangle.

When the right edge is reached, then the motion in  $x$ -direction is changed from forward to backward and a new  $v_x$  is chosen randomly. The procedure is analogous when reaching any other edge. Except for points near the edges, the spot motion can be treated as uniform at any time. Hence, the momentum transfer to a particle is calculated for a laser spot that passes with a constant velocity  $v_x, v_y$ .

### Time-Dependent Force of the Passing Spot

In order to calculate the momentum transfer to a single dust particle, the first task is to describe the time-dependent force on a particle when a spot passes with constant velocity  $v_x, v_y$ . Since the velocity of the particles  $|\mathbf{v}_d| \ll |\mathbf{v}_{\text{laser}}|$  is small compared to the laser spots, the change of the dust particle's position during the acceleration event is neglected. Even at a very moderate coupling strength  $\Gamma = 1$ , the thermal velocity of the dust grains is on the order of  $v_{\text{d,th}} \approx 13 \text{ mm s}^{-1}$ , while the lowest spot velocity is still  $v_{\text{laser}}^{\text{min}} > 1000 \text{ mm s}^{-1}$  for typical plasma parameters<sup>2</sup>. In general, the trajectory of the spot center does not hit the particle directly but passes it within a finite distance. Nonetheless, the particle is accelerated due to the spatial extension of the spot. In the following, the length  $\Delta y_0$  is used to parameterize the passing distance. This length is defined as the distance in  $y$ -direction at the point where the particle and the spot center are in-line with respect to their  $x$ -position,<sup>3</sup> cf. Fig. 6.6. Defining the origin of the time axis as  $t = 0$  at this point, the time dependent distances can be written as

$$\Delta x(t) = v_x \cdot t \quad \text{and} \quad \Delta y(t) = \Delta y_0 + v_y \cdot t. \quad (6.5)$$

Using the time-dependent distances from the above equation (6.5) in Eq. (6.4), the time-dependent force acting on the particle reads

$$\begin{aligned} F(t) &= \pm F_L \frac{1}{2\pi} \frac{1}{\sigma_x \sigma_y} \exp \left\{ -\frac{1}{2} \left[ \left( \frac{v_x t}{\sigma_x} \right)^2 + \left( \frac{\Delta y_0 + v_y t}{\sigma_y} \right)^2 \right] \right\} \\ &= \pm F_L \frac{1}{2\pi} \frac{1}{\sigma_x \sigma_y} \exp \left\{ -\frac{1}{2} \left[ \frac{v_x^2}{\sigma_x^2} t^2 + \frac{v_y^2}{\sigma_y^2} t^2 + 2 \frac{\Delta y_0 v_y}{\sigma_y^2} t + \frac{\Delta y_0^2}{\sigma_y^2} \right] \right\} \\ &= \pm F_L \frac{1}{2\pi} \frac{1}{\sigma_x \sigma_y} \exp \left\{ -\frac{1}{2} \left[ \left( \frac{v_x^2}{\sigma_x^2} + \frac{v_y^2}{\sigma_y^2} \right) t^2 + 2 \frac{\Delta y_0 v_y}{\sigma_y^2} t + \frac{\Delta y_0^2}{\sigma_y^2} \right] \right\}, \end{aligned} \quad (6.6)$$

where one can introduce the time scale  $\tau$  as

$$\frac{1}{\tau^2} = \frac{v_x^2}{\sigma_x^2} + \frac{v_y^2}{\sigma_y^2}. \quad (6.7)$$

With this time scale  $\tau$ , equation (6.6) is simplified as

$$\begin{aligned} F(t) &= \pm F_L \frac{1}{2\pi} \frac{1}{\sigma_x \sigma_y} \exp \left\{ -\frac{1}{2} \frac{1}{\tau^2} \left[ t^2 + 2\tau^2 \frac{\Delta y_0 v_y}{\sigma_y^2} t + \tau^2 \frac{\Delta y_0^2}{\sigma_y^2} \right] \right\} \\ &= \pm F_L \frac{1}{2\pi} \frac{1}{\sigma_x \sigma_y} \exp \left\{ -\frac{1}{2} \frac{1}{\tau^2} \left[ \left( t + \tau^2 \frac{\Delta y_0 v_y}{\sigma_y^2} \right)^2 + \tau^2 \frac{\Delta y_0^2}{\sigma_y^2} - \tau^4 \frac{\Delta y_0^2 v_y^2}{\sigma_y^4} \right] \right\}, \end{aligned} \quad (6.8)$$

<sup>2</sup>This evaluation of  $v_{\text{d,th}} = \sqrt{2k_B T / m_d}$  was done for a particle diameter  $d_d = 6 \mu\text{m}$ , a dust charge  $Q_d = 10\,000 e$  and a trap frequency  $\omega_0 = 5.5 \text{ s}^{-1}$ . The minimal spot velocity was calculated using the lower limits of the scanner frequency ranges  $f_{\parallel}^{\text{min}} = 50 \text{ Hz}$  and  $f_{\perp}^{\text{min}} = 15 \text{ Hz}$  plus  $X = Y = 3.5 r_0$  for the size of the scanned rectangle.

<sup>3</sup>The choice of  $\Delta y_0$  for parameterizing the passing distance of the laser spot is somewhat arbitrary. Choosing the distance  $\Delta x_0$  in the  $x$ -direction leads to an equivalent description.

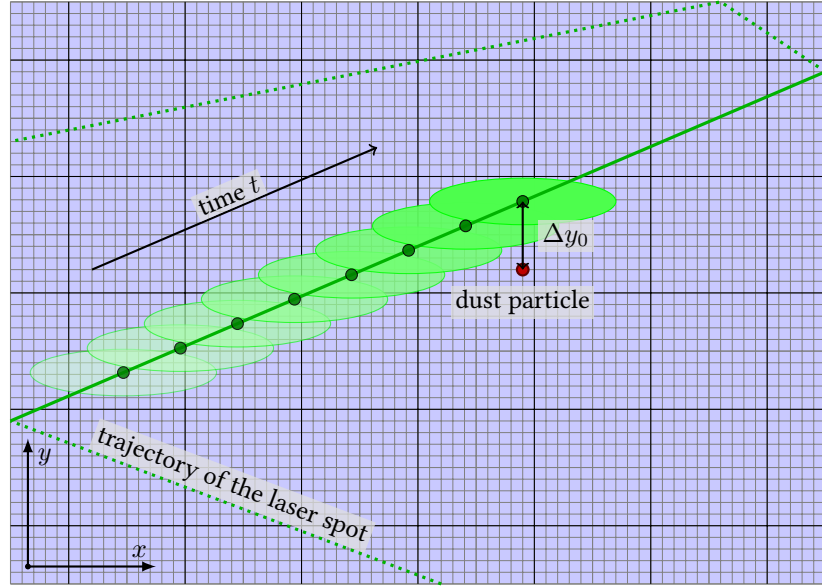


**Figure 6.6:** Illustration of the laser spot's trajectory: The spot profile at different times is sketched as a fading ellipse. When the dust particle and then spot center are aligned parallel to the  $y$ -axis, their distance is defined as  $\Delta y_0$ .

where one can substitute  $t' = t + \tau^2 \frac{\Delta y_0 v_y}{\sigma_y^2}$ , which means re-defining the origin of the time axis. The time-dependent force then reads

$$F(t') = \pm F_L \frac{1}{\sqrt{2\pi}} \exp\left\{-\frac{1}{2} \frac{t'^2}{\tau^2}\right\} \cdot \underbrace{\frac{1}{\sqrt{2\pi}} \frac{1}{\sigma_x \sigma_y} \exp\left\{-\frac{1}{2} \left[ \frac{\Delta y_0^2}{\sigma_y^2} - \tau^2 \frac{\Delta y_0^2 v_y^2}{\sigma_y^4} \right] \right\}}_{:=\Sigma}. \quad (6.9)$$

Here, the spatial factor  $\Sigma$  is time independent and depends on the distance between the laser trajectory and the particle position. This factor can be simplified to

$$\Sigma = \frac{1}{\sqrt{2\pi}} \frac{1}{\sigma_x \sigma_y} \exp\left\{-\frac{1}{2} \frac{\Delta y_0^2 v_x^2 \tau^2}{\sigma_y^2 \sigma_x^2}\right\}, \quad (6.10)$$

as shown in Eqs. (B.2)–(B.3) in Sec. B.1 of the appendix.

At time  $t' = 0$  the dust particle experiences the strongest acceleration. This is also the geometrically closest point for an isotropic spot profile  $\sigma_x = \sigma_y$  and  $\Sigma$  is the relative force at this point. Finally, the time-dependent force is written in a compact form as

$$F(t') = \pm F_L \Sigma \cdot \frac{1}{\sqrt{2\pi}} \exp\left\{-\frac{1}{2} \frac{t'^2}{\tau^2}\right\}. \quad (6.11)$$

The dust particle experiences a force pulse which has a Gaussian shape, independently of the passing distance. However, the passing distance defines the amplitude of this force pulse.

### Momentum Transfer during one Passing Event

The momentum transferred to a dust grain during a single passing event can be approximated by integrating the time-dependent force  $F(t')$  from  $-\infty$  to  $+\infty$ , as only times around  $t' = 0$

give a significant contribution to the integral. The extension to infinite times is reasonable for all particle positions far away from the edges of the scanned rectangle. Far away means in this context that the distance from the edge is large compared to the spot width. The approximation that the spot moves linearly for all times is valid since the force at the particle's position is practically zero due to the exponential function when the motion of the spot changes its direction at the edges of the scanned rectangle.

The transferred momentum is then simply given by the expression

$$\Delta p = \int_{-\infty}^{\infty} dt' F(t') = \pm F_L \Sigma \cdot \frac{1}{\sqrt{2\pi}} \int_{-\infty}^{\infty} dt' \exp \left\{ -\frac{1}{2} \frac{t'^2}{\tau^2} \right\} \quad (6.12)$$

$$= \pm F_L \Sigma \cdot \tau, \quad (6.13)$$

which depends on the spatial factor  $\Sigma$  besides the characteristic time  $\tau$ .

Since the passing distance  $\Delta y_0$  varies,  $\Sigma$  has to be averaged over all possible values. During its motion in  $x$ -direction from one edge of the scanned rectangle to the opposite edge, the laser trajectory passes the particle at a point  $y \in [-Y : Y]$ . The interval of the possible passing point  $[-Y : Y]$  is the spatial extend of the scanned rectangle in  $y$ -direction. The particle is considered to be located a  $x_d, y_d$  within this rectangle.  $\Delta y_0$  can then take values from the interval  $[-Y - y_d : Y - y_d]$ , where  $y_d$  is the  $y$  coordinate of the dust particle. As the particle is considered to be far inside the scanned area, the integral over  $\Delta y_0$  is again extended to infinity since large values of  $\Delta y_0$  give no contribution due to rapid decay of the exponential function. The average of the spatial factor from Eq. (6.10) is then derived as

$$\begin{aligned} \langle \Sigma \rangle_y &= \frac{1}{2Y} \frac{1}{\sqrt{2\pi}} \frac{1}{\sigma_x \sigma_y} \int_{-Y-y_d}^{Y-y_d} d\Delta y_0 \exp \left\{ -\frac{1}{2} \frac{\Delta y_0^2 v_x^2 \tau^2}{\sigma_y^2 \sigma_x^2} \right\} \\ &\approx \frac{1}{2Y} \frac{1}{\sqrt{2\pi}} \frac{1}{\sigma_x \sigma_y} \int_{-\infty}^{\infty} d\Delta y_0 \exp \left\{ -\frac{1}{2} \frac{\Delta y_0^2 v_x^2 \tau^2}{\sigma_y^2 \sigma_x^2} \right\} \\ &= \frac{1}{2Y} \frac{1}{\sqrt{2\pi}} \frac{1}{\sigma_x \sigma_y} \cdot \sqrt{2\pi} \frac{\sigma_x \sigma_y}{v_x \tau} = \frac{1}{2Y} \cdot \frac{1}{v_x} \cdot \frac{1}{\tau}. \end{aligned} \quad (6.14)$$

In the same manner, one calculates the average of the square of spatial factor  $\Sigma$  for different passing parameters  $\Delta y_0$ . These averages are later employed during the calculation of the average energy transfer to the particle during one passing event,

$$\begin{aligned} \langle \Sigma^2 \rangle_y &\approx \frac{1}{2Y} \frac{1}{2\pi} \frac{1}{\sigma_x^2 \sigma_y^2} \int_{-\infty}^{\infty} d\Delta y_0 \exp \left\{ -\frac{1}{2} \frac{\Delta y_0^2 v_x^2 \tau^2}{\sigma_y^2 \sigma_x^2} \cdot 2 \right\} \\ &= \frac{1}{2Y} \cdot \frac{1}{2\sqrt{\pi}} \cdot \frac{1}{\sigma_x \sigma_y} \cdot \frac{1}{v_x} \cdot \frac{1}{\tau}. \end{aligned} \quad (6.15)$$

### Time Averages

In the following, the average momentum transfer and the *average energy transfer per time* are of central interest in order to calculate the dust kinetic temperature. Assuming that the

average momentum and the average energy transfer during one passing event are given, these numbers have to be multiplied by average number of passing events per time. Each time the laser crosses the levitation plane in  $x$ -direction, it passes the particle position once. Then, the “passing rate”  $\chi$  is given by the inverse crossing time in  $x$ -direction as

$$\chi = \left( \frac{2X}{v_x} \right)^{-1} = \frac{v_x}{2X}. \quad (6.16)$$

Using Eqs. (6.13), (6.14) and (6.16), the average momentum transfer per time is calculated as

$$\begin{aligned} \left\langle \frac{\Delta p}{\Delta t} \right\rangle &= \pm F_L \cdot \chi \cdot \langle \Sigma \rangle_y \cdot \tau \\ &= \pm F_L \cdot \frac{v_x}{2X} \cdot \frac{1}{2Y} \cdot \frac{1}{v_x} \cdot \frac{1}{\tau} \cdot \tau \\ &= \pm F_L \cdot \frac{1}{4XY}, \end{aligned} \quad (6.17)$$

which is found to depend on the *force amplitude*  $F_L$  and the *size of the scanned area*  $4XY$ , only.

The magnitude of the momentum transfer is the same for both lasers, but the sign alternates. Hence, the average momentum transfer from the laser in  $+x$ -direction cancels the one of the laser in  $-x$ -direction as one would expect.

### Average Energy Transfer

In the previous paragraph, the momentum transfer of each laser was found to depend on the force amplitude and the size of the scanned area only. Furthermore, it could be shown that the gross momentum transfer of two opposing lasers with the same amplitude cancels. In this section, the average energy transfer to a dust particle per time is analyzed. Considering one crossing event, the particle’s energy before ( $E$ ) and after ( $E'$ ) the laser-particle interaction is given by

$$E = \frac{m}{2} v_d^2 \quad (6.18)$$

$$E' = \frac{m}{2} \left( v_d + \frac{\Delta p}{m} \right)^2, \quad (6.19)$$

where  $v_d$  is the initial velocity of the dust particle before the interaction with the laser. At this point, the deceleration due to friction during the acceleration event is ignored. As discussed below, see Tab. 6.2, this is well justified for the typical laser heating parameter. The energy transfer can be written as

$$\Delta E = E' - E = v_d \Delta p + \frac{(\Delta p)^2}{2m}, \quad (6.20)$$

where the momentum transfer  $\Delta p$  is given by Eq. (6.13). Using the expression from Eq. (6.13) to express  $(\Delta p)^2$ , the following expression is obtained for the energy transfer during a single passing event,

$$\Delta E = v_d \Delta p + \frac{1}{2m} F_L^2 \Sigma^2 \cdot \tau^2, \quad (6.21)$$

which depends on the passing distance  $\Delta y_0$  via  $\Sigma$ . In order to calculate the average energy transfer per time, the average over all possible passing distances is multiplied by the passing rate  $\chi$ . Since the average momentum transfer vanishes as shown in section 6.1.3, the first term in the above equation cancels under the average. Using the average squared spatial factor from Eq. (6.15), the result for the average energy per time is

$$\begin{aligned} \left\langle \frac{\Delta E}{\Delta t} \right\rangle &= \frac{1}{2m} F_L^2 \cdot \chi \cdot \langle \Sigma^2 \rangle_y \cdot \tau^2. \\ &= \frac{1}{2m} \cdot \frac{1}{2\sqrt{\pi}} \cdot F_L^2 \cdot \frac{1}{4XY} \cdot \frac{1}{\sigma_x \sigma_y} \cdot \tau, \end{aligned} \quad (6.22)$$

where the current spot velocity enters via  $\tau$ .

Until now, a constant spot velocity  $v_x, v_y$  was assumed. In contrast, the spot velocity is randomly varied in the experiment. Therefore, the effective time scale  $\tau_{\text{eff}}$  is introduced by averaging  $\tau$  over all possible spot velocities. The expression for this time scale is given in Sec. B.2 in the appendix.

### Equilibrium Temperature

Now that the average energy transfer by the laser per time, Eq. (6.22), is known, the equilibrium temperature of the dust system is calculated in the Langevin model. The equilibrium temperature  $T_{\text{eq}}$  results from the balance between *power input by the lasers*  $P_{\text{laser}}$ , *power input by the stochastic force*  $P_{\text{stochastic}}$  and *power loss due to friction*  $P_{\text{friction}}$ ,

$$P_{\text{laser}} + P_{\text{stochastic}} + P_{\text{friction}} = 0. \quad (6.23)$$

The average power loss due to friction of particles with mass  $m$  distributed according to a (1D) Maxwellian velocity distribution with temperature  $T_{\text{eq}}$ ,

$$\mathcal{P}(v) = \sqrt{\frac{m}{2\pi k_B T_{\text{eq}}}} e^{-\frac{mv^2}{2k_B T_{\text{eq}}}}, \quad (6.24)$$

is calculated using the relation  $\dot{v} = -\gamma v$ , where  $\gamma$  is the friction coefficient. The power loss,

$$\begin{aligned} P_{\text{friction}} &= \left\langle \frac{d}{dt} \frac{m}{2} v^2 \right\rangle = -m\gamma \langle v^2 \rangle = -m\gamma \frac{k_B T_{\text{eq}}}{m} \\ &= -\gamma k_B T_{\text{eq}}, \end{aligned} \quad (6.25)$$

is proportional to the temperature. In order to obtain the power input by the stochastic force, an equilibrium system without laser heating,  $P_{\text{laser}} = 0$ , is considered. The temperature of this

system is given by the temperature of Langevin thermostat,  $T_0$ . In equilibrium, the power loss due to friction has to be compensated by the power gain due to the stochastic force. Therefore, the stochastic power input is given by,

$$P_{\text{stochastic}} = -P_{\text{friction}} = \gamma k_B T_0, \quad (6.26)$$

and is independent of the presence of manipulation lasers. Using the energy balance equation (6.23) and the power input by the lasers from Eq. (6.22) with  $\tau_{\text{eff}}$  from Eq. (B.4) in the appendix (p. 142), one obtains

$$\begin{aligned} 0 &= \frac{1}{2m} \cdot \frac{1}{\sqrt{\pi}} \cdot F_L^2 \cdot \frac{1}{4XY} \cdot \frac{1}{\sigma_x \sigma_y} \cdot \tau_{\text{eff}} + \gamma k_B T_0 - \gamma k_B T_{\text{eq}} \\ \Leftrightarrow \quad T_{\text{eq}} &= T_0 + \frac{1}{2m\gamma k_B \sqrt{\pi}} \cdot F_L^2 \cdot \frac{1}{4XY} \cdot \frac{1}{\sigma_x \sigma_y} \cdot \tau_{\text{eff}}, \end{aligned} \quad (6.27)$$

as the equilibrium temperature in the heated system. The power input,

$$P_{\text{laser}} = 2 \cdot \left\langle \frac{\Delta E}{\Delta t} \right\rangle \quad (6.28)$$

was multiplied by the factor two since there are two laser spots for each  $x$ - and  $y$ -direction heating the particles.

### Comparison with Simulation Results

In this section, the equilibrium temperatures estimated by Eq. (6.27) are compared with those of a Maxwellian fit to the simulation data. The simulations were performed as LMD simulations with  $N = 25$  particles over  $t = 1000$  s with a laser power  $F_L = 10$  in dimensionless units. In the appendix, the results for different spot sizes and different friction coefficients  $\gamma$  are listed in tables B.1, B.2 and B.3.

The agreement of the analytic approximation formula and the simulation results is good for small laser spots ( $\sigma_x \lesssim 0.4$ ,  $\sigma_y \lesssim 0.08$ ) as shown in Fig. 6.7. For large spots ( $\sigma_x = 0.7$ ), the error in the temperature can make up to 30 %. The formula in general overestimates the temperature (underestimates the coupling strength), and, hence, overestimates the heating effect of the lasers. The only exception is a slight underestimation of the temperature by 1.5 % for one simulation with small spot size and low friction. However, the error of 1.5 % is within the error of the determination of the temperature in the simulation. Furthermore, the velocity profile shows significant deviation from a Maxwellian distribution for the smallest spot size. Here, the fraction of fast particles in the simulation is larger than predicted by an ideal Maxwellian distribution.

Excluding the smallest two spots, the deviation of the analytic formula is found to become smaller for larger friction coefficients  $\gamma$ . Since the characteristic decay time  $\tau_v$  of the velocity autocorrelation function is proportional to the inverse friction coefficient  $\gamma^{-1}$ , the analytic formula appears to become improper for longer temporal correlations of the particle velocity. The analytical model does not take into account the autocorrelation particle velocity. The particle velocity at the beginning of each acceleration event was assumed to be distributed according to a Maxwellian distribution with temperature  $T_{\text{eq}}$ . This means that the particles are assumed to have equilibrated *before* the next interaction with a laser spot.



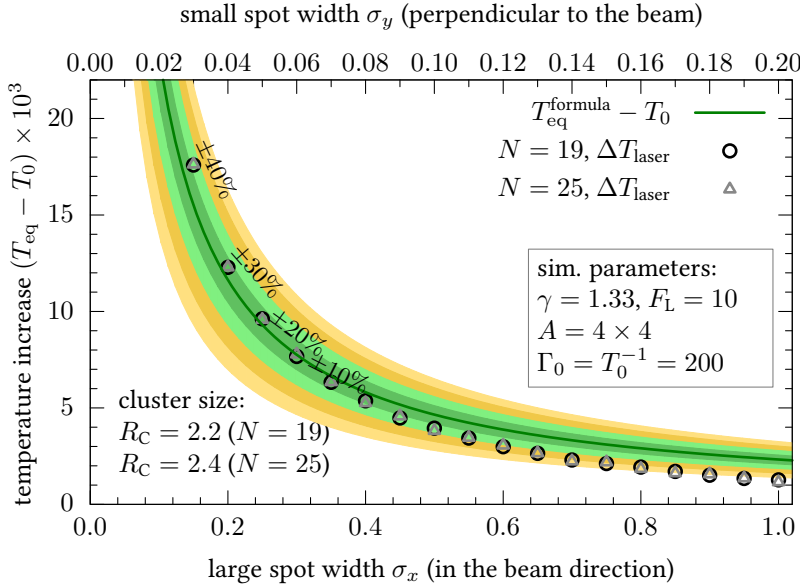


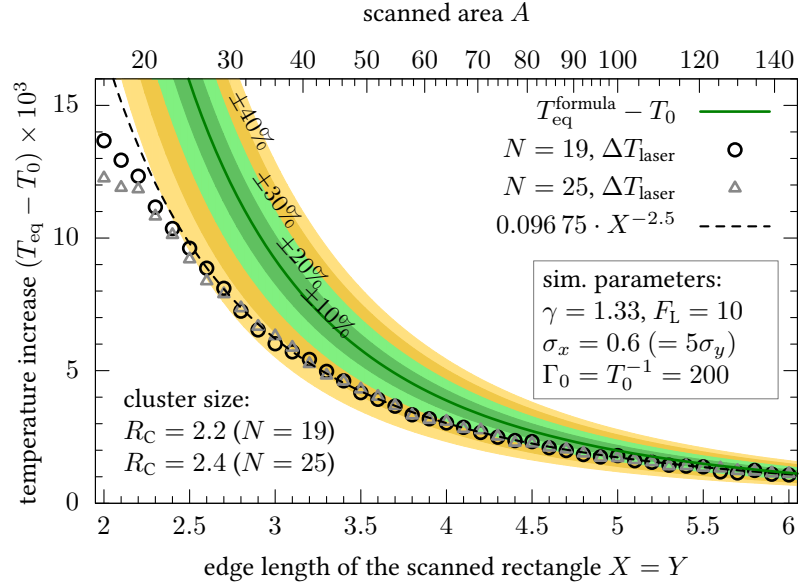
**Figure 6.7:** Temperature increase due to the heating lasers as a function of the spot width (symbols) and in the analytic model, Eq. (6.27) (solid green line). The spot width  $\sigma_x$  in the beam direction is always five times larger than  $\sigma_y$  in the perpendicular direction. The deviation from the analytical model, shown by the shaded area, is related to the difference  $T_{\text{eq}}^{\text{formula}} - T_0$ , here.

### Functional Connection between the Equilibrium Temperature $T_{\text{eq}}$ and the Laser Heating Parameters

In this section, the functional form of the analytic approximation for the equilibrium temperature  $T_{\text{eq}}$  in a laser heating experiment with four randomly moving laser spots is discussed. By introducing dimensionless units, cf. Sec. 3.1.4, the equilibrium temperature  $k_{\text{B}}T_{\text{eq}}$  in units of  $E_0$ , Eq. 6.27, was found to be fixed by the following parameters.

- The temperature of the background gas  $k_{\text{B}}T_0$  causes a constant offset of the equilibrium temperature, which is the sum of the background temperature and the temperature increase  $\Delta T_{\text{laser}}$  caused by the laser heating. In the following, the discussion of the heating effect refers to this temperature increase.
- The temperature increase  $\Delta T_{\text{laser}}$  is inversely proportional to the damping parameter  $\lambda = m_{\text{d}}\gamma$  as the product of the particle mass and the friction coefficient  $\gamma$ . This behavior can be explained by the fact that the parameter  $\lambda$  quantifies the strength of the coupling between the dust cluster and the neutral gas at temperature  $T_0$ . The equilibrium temperature of the dust particles results from the energy input by the acceleration due to the manipulation lasers and the energy loss due to damping as two competing processes. Since  $m_{\text{d}}$  serves as the unit of mass in the dimensionless system units, both the damping parameter  $\lambda$  in units of  $m_{\text{d}}t_0^{-1}$  and the friction coefficient  $\gamma$  in units of  $t_0^{-1}$  are described by the same number.
- The heating power  $P_{\text{laser}}$ , which is proportional to the total power of a laser beam, enters *quadratically* in the temperature increase. This functional relation was also found by WOLTER *et al.* for their “point and shoot” heating method with one laser beam [4]. The quadratic dependence of the temperature increase can be understood, as  $\Delta T_{\text{laser}}$  is proportional to the mean square of the momentum transfer by the laser beams.

**Figure 6.8:** Temperature increase due to the heating lasers as a function of the length  $X = Y$  of the square which is scanned by the laser spots from an LMD simulation (symbols) and in the analytic model, Eq. (6.27) (solid green line). The deviation from the analytical model, shown by the shaded area, is related to the difference  $T_{\text{eq}}^{\text{formula}} - T_0$ , here.



- The scanner frequencies enter the temperature increase inversely via the time scale  $\tau_{\text{eff}}$ . When changing the limits of the scanning frequency ranges  $[v_x^{\min}, v_x^{\max}]$  and  $[v_y^{\min}, v_y^{\max}]$  for the spot motion individually, the impact on  $\tau_{\text{eff}}$  is, however, more complicated, cf. Eq. B.4 in Sec. B.2 of the appendix. Yet, scaling both frequency ranges by a constant factor reduces the effective time scale by this factor as one expects. While the inverse relation of scanning frequencies and effective time scale  $\tau_{\text{eff}}$  is trivial, the proportionality of  $\Delta T_{\text{laser}}$  and  $\tau_{\text{eff}}$  should be discussed. On the one hand, one would expect a quadratic increase of  $\Delta T_{\text{laser}}$  with  $\tau_{\text{eff}}$ , as the momentum transfer scales linearly with the duration of the acceleration provided that the force remains unchanged. On the other hand, the mean time between two acceleration events scales also with  $\tau_{\text{eff}}$ , which explains the weaker linear dependence of  $\Delta T_{\text{laser}}$  on the time scale.
- When a square with edge length  $X = Y$  is scanned by the lasers, the temperature increase is expected to scale as  $\Delta T_{\text{laser}} \propto X^{-3}$ . First, the size of rectangle in the denominator scales as  $X^2$  and, second, the effective time scale is inversely proportional to the edge length  $X$ . As shown by the comparison with LMD simulation results in Fig. 6.8, the analytic model, Eq. 6.27, overestimates the temperature significantly for small scanned squares.
- For a given striking angle  $\alpha$  of the lasers, the spot width ratio  $\sigma_x : \sigma_y$  is constant. Increasing the spot width then has two opposing effects since the spot cross-sectional area in the denominator grows quadratically with  $\sigma_x$ , but the effective time scale  $\tau_{\text{eff}}$  is proportional to  $\sigma_x$ . The overall effect is that the temperature increase is proportional to the spot width  $\Delta T_{\text{laser}} \propto \sigma_x$ , for a constant spot anisotropy.

### Discussion of the Deviation

The comparison with LMD simulations revealed that the analytic formula for the equilibrium temperature  $T_{\text{eq}}$ , Eq. (6.27), works best for small spot sizes. The deviations for very small spots and high friction can be explained by the non-equilibrium character of this system. Here, the energy input by the lasers is high and the power loss due to friction is also high. This results in a non-Maxwellian velocity profile making the assumptions about energy loss and gain invalid. The deviations for larger spot sizes and moderate heating powers, however, occur although the Maxwellian velocity profile is conserved. Even the high-velocity tail is well represented and does not show significant deviations from the Maxwellian distribution even in a logarithmic plot. Hence, there has to be another explanation for the temperature difference between the analytic prediction and the simulation result.

One possible reason for the overestimation of the resulting equilibrium temperature  $T_{\text{eq}}$  is the *overlap of different laser spots*. Therefore, the validity of the simple summation of the power input from both lasers is checked. The picture in which the analytic model was derived neglects the possibility that both laser spots overlap and the net force cancels or is at least reduced. Since the average overlap grows with the spot size, one can expect this effect to become more important for larger spots. In the appendix, Sec. B.4, the average overlap of the two spots of a beam pair is calculated as the folding integral of the intensities averaged over all possible position for both spots. The result is related to the integral of the squared force of both beams individually in order to obtain the correction factor

$$\epsilon_0 = \frac{\langle f_- \otimes f_+ \rangle}{2|f_{\pm}^2|} = -\frac{\pi}{2} \left( X - \frac{\sigma_x}{\sqrt{\pi}} \right) \cdot \left( Y - \frac{\sigma_y}{\sqrt{\pi}} \right) \cdot \frac{\sigma_x \sigma_y}{X^2 Y^2}. \quad (6.29)$$

This factor is of the order of  $\epsilon_0 \approx -1\%$  even for large spots ( $\sigma_x = 0.7$ ,  $\sigma_y = 0.14$  and a scanned area  $X = Y = 3.5$ ). The overlap of both laser spot cannot explain the difference of 30% in the equilibrium temperature between simulation and analytic formula. This is also verified by switching off the  $-x$ -directed laser in the simulation and increasing the  $+x$ -directed laser by a factor  $\sqrt{2}$ . The deviation between simulation and formula remains, and the resulting temperature agrees with the case with both laser spots.

Until now, the friction during the acceleration event was not taken into account. In section 6.1.3, the momentum transfer to the particle by the laser was calculated first, and the energy transfer was then obtained as the squared momentum transfer divided by twice the mass of a dust particle,  $2m_d$ . Afterwards, the friction was taken into account for the energy balance equation (6.23) in section 6.1.3. Strictly speaking, this procedure is valid for an instantaneous acceleration, only. In section B.5 of the appendix, the equation of motion is solved for a damped dust particle accelerated by a Gaussian force pulse. The solution for a particle which is at rest before the acceleration event is found as

$$v(t) = \frac{F_L}{2m} \cdot e^{\frac{\gamma^2 \tau^2}{2}} \cdot e^{-\gamma t} \cdot \left[ 1 - \operatorname{erf} \left\{ \frac{-t + \gamma \tau^2}{\sqrt{2}\tau} \right\} \right]. \quad (6.30)$$

The analytic integration of  $v^2(t)$  is however not possible for finite acceleration times. Due to the scaling relation  $v(t, \tau, \gamma) = v(\gamma t, \gamma \tau)$ , the total energy transfer depends on the product  $\gamma \tau$  and

$\gamma \backslash \tau$	0	0.001	0.002	0.005	0.01	0.02	0.05	0.1	0.2	0.5
0.1	1.0	1.000	1.000	0.999	0.999	0.998	0.994	0.989	0.978	0.946
0.2	1.0	1.000	0.999	0.999	0.998	0.996	0.989	0.978	0.956	0.896
0.5	1.0	0.999	0.999	0.997	0.994	0.989	0.972	0.946	0.896	0.770
1.0	1.0	0.999	0.997	0.994	0.989	0.978	0.946	0.896	0.809	0.616

**Table 6.2:** Total energy transfer for different combinations of acceleration time  $\tau$  and friction coefficient  $\gamma$  in units of  $E(\tau = 0) = \frac{m_d}{2} v_0^2$  as the energy transfer for instantaneous acceleration.

not on these two parameters individually. Table 6.2 shows some values of the energy transfer for different acceleration times compared to an instantaneous acceleration. Even for large laser spots ( $\sigma_x = 0.7$ ,  $\sigma_y = 0.14$ ), the acceleration time is  $\tau_{\text{eff}} \approx 0.001$  and cannot explain the deviation of about 30 % between simulation and formula (6.27). One should keep in mind that the particle is considered to be at rest at the beginning of the acceleration process. In the simulation and in the experiment, the initial particle velocity follow a Maxwellian distribution in contrast.

Another important point is that the entire derivation of Eq. (6.27) assumed a single free particle. Obviously, that assumption does not conform to solid dust clusters where the coupling between the particles plays an essential role. The comparison of simulation data and analytic formula reveals that at constant friction coefficient  $\gamma$ , both the deviation of the formula and the coupling parameter  $\Gamma$  increase when moving from small to large spots. This observation substantiates that the particle interactions are responsible for the overestimation of the heating power. Without solving the equation of motion for a caged particle, the sign of the correction on the power input to the dust system can be rated by the following consideration: The power transfer from the laser beam to the dust particle is given by the integral over the product of accelerating force and displacement of the dust particle. While the force is the same for both free and caged particle, the displacement is smaller for the caged particle which results in a reduced energy transfer.

Although the derived expression for the equilibrium temperature  $T_{\text{eq}}$  in a laser heating experiment, Eq. (6.27), shows weaknesses for large laser spots, it can provide a reliable estimate for the temperature without extensive calculations. Except for situations with both low friction and very large laser spots, it allows to characterize  $T_{\text{eq}}$  with an accuracy of 20 % which is remarkable due to the keen assumptions during the derivation.

## 6.2 Inhomogeneous Excitation and Heat Transport

The laser manipulation method is not only suited to serve as a homogeneous heat source for the entire cluster, but it can, in addition, be used to realize a spatially inhomogeneous heat source. Since the position of a laser spot within the levitation plane can be controlled with high accuracy by the galvanometer mirrors, the manipulation of the dust grains can be restricted to a certain area.

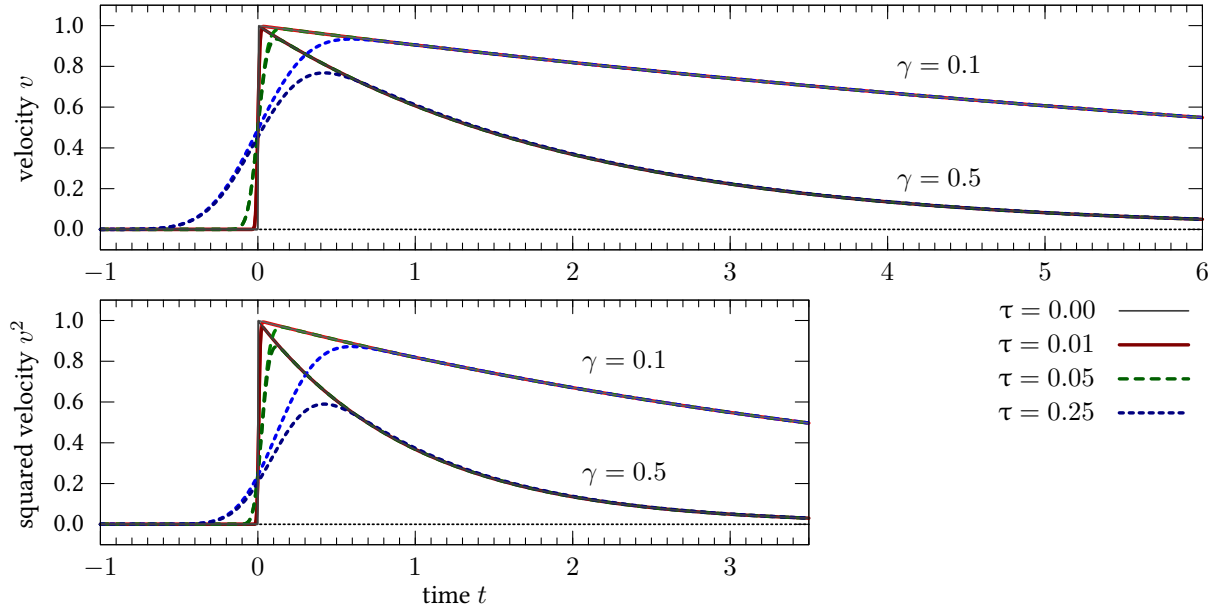


**Figure 6.9:** Time-dependent velocity (top) and its square (bottom) for different combinations of acceleration time  $\tau$  and friction coefficient  $\gamma$ . All curves are calculated for particle mass  $m = 1$  and force amplitude  $F_L = 1$  in units of  $r_0$  and  $t_0 = \omega_0^{-1}$ . The instantaneous acceleration case is shown by the black dashed line.

In the following, a setup for future experiments is suggested, where only the central region of a 2D cluster is heated. This inhomogeneous excitation scenario is considered for a relatively large cluster with a particle number on the order of hundreds, so that the spatial extension is sufficient for recording a radial temperature profile that covers several shells.

At this point, I would like to thank Giedrius Kudelis who visited Kiel in summer 2012 for twelve weeks. During his internship under the DAAD (German Academic Exchange Service) RISE program, we extended my LMD code for inhomogeneous heating, generated first simulation results and derived the analytic form for the temperature profile of a circular 2D dust cluster in the fluid model.

Figure 6.10(a) shows the velocity distributions at different radii for a 2D Yukawa cluster with  $N = 200$  particles which is heated in the central region. The laser spots were randomly moved within a central square with edge length  $2a = 1.0$ . This square holds three to four particles,  $\langle N_{\text{cen}} \rangle = 3.55$ , and the variance of this number was determined as  $\sigma(N_{\text{cen}}) = 0.76$  for the simulation shown in the figure. Due to the finite width of the laser spots, particles outside but near the square, in which the spot centers move, can be accelerated as well. This effect is taken into account by considering an additional stripe at each border of the square. The width of the stripe is considered equal to the larger width of the anisotropic laser spot in beam direction  $\sigma_{\parallel} = 0.5$ . For the simulation results shown, this extended area then holds seven to nine particles. Hence, only a few percent of the dust grains are accelerated directly by the manipulation lasers. The major fraction of the particles is heated indirectly as energy is transferred between different particles via collisions. In the following the heat transport mechanism in the dust system will be investigated.

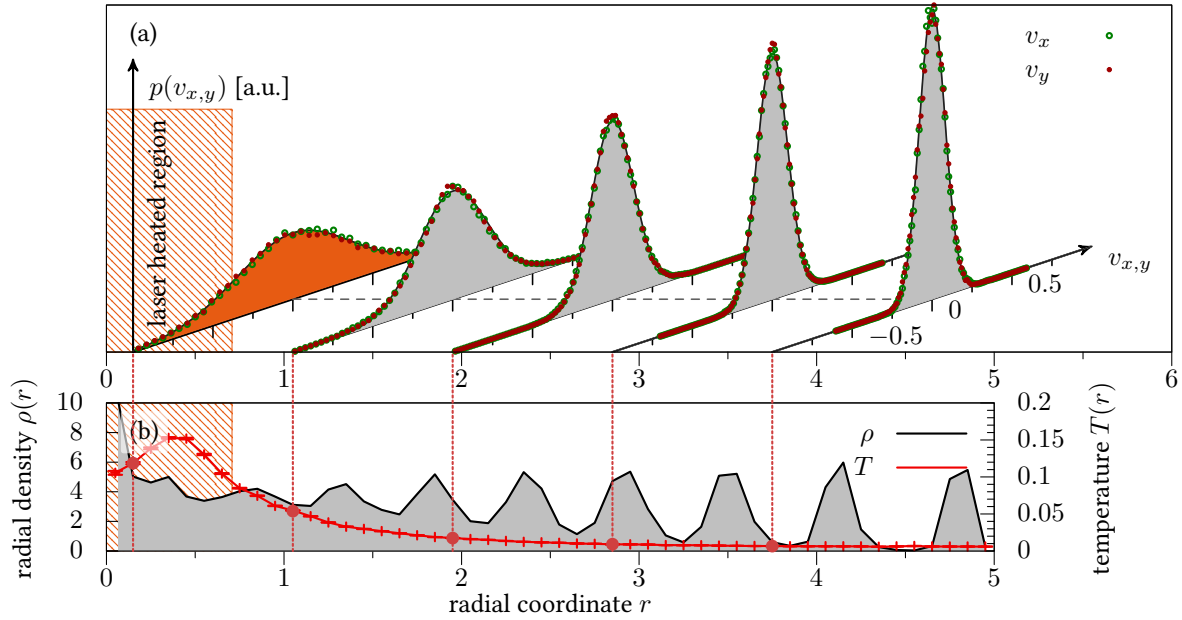


**Figure 6.10:** LMD simulation for a 2D Yukawa ( $\kappa = 1$ ) cluster with  $N = 200$  particles which is heated in the center by four lasers with a power  $F_L = 40$ , a background temperature  $T_0 = 0.005$  and a friction coefficient  $\gamma = 0.5$  in dimensionless units. The heated region is indicated by the shaded, orange area. (a) The velocity distributions for  $v_x$  and  $v_y$  were recorded at different radii. (b) The radial temperature profile (red curve) is obtained from the random motion of the particles. Five temperatures are highlighted at the radii that correspond to the velocity distributions shown in (a). The filled curve shows the radial density [155].

The velocity distributions in Fig. 6.10(a) were calculated by dividing the cluster into circlets of width  $\Delta r = 0.3$  and sampling the velocities of all particles within one circlet. While Maxwellian shape and isotropy are well conserved over the entire radius, the width of the distribution decreases monotonically with distance from the center. This observation indicates that the temperature decreases with the radius as a consequence of the selective heating at the center.

In order to quantify the temperature decrease, the radial temperature profile is recorded with a finer resolution  $\Delta r = 0.1$  in Fig. 6.10(b). Although the temperature in the strict thermodynamic sense is defined only for a system that is in equilibrium with a heat bath, the kinetic theory approach to temperature allows one to determine  $T$  from the particle velocities. The *equipartition theorem* states that for a classical particle every degree of freedom stores an energy portion of  $\frac{1}{2}k_B T$  on average. Considering the random motion of the dust particles in 2D with two degrees of freedom, the kinetic temperature is obtained from

$$k_B T = \frac{m}{2} (\langle v^2 \rangle - \langle \mathbf{v} \rangle^2), \quad (6.31)$$

where the mean velocity  $\langle \mathbf{v} \rangle$  cancels for a system without flows. The radial velocity profile  $T(r)$  is sampled from the LMD simulation by selecting only particles within a certain ring in Eq. (6.31). On the one hand, a small radial width of the ring  $\Delta r$  is preferable to obtain a sufficient radial resolution. On the other hand, the width has to be large enough to obtain a sufficient number of data points per ring. For these requirements,  $\Delta r \approx 0.1 - 0.3$  turned out to be a proper choice.

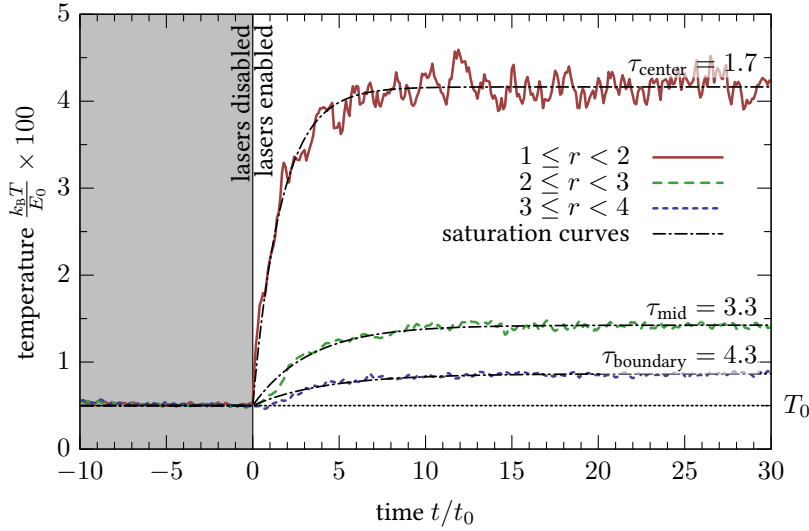


**Figure 6.11:** Time evolution of the local temperature in the LMD simulation at three different radii. The lasers were “turned on” at  $t = 0$ . For  $t > 0$ , the data are fit by saturation curves with different time scales  $\tau$  for the three regions. The relaxation takes longer for the outer, indirectly heated particles. The temperatures were averaged over 40 independent simulations.

Parameters:  $N = 200$ ,  $\kappa = 1$ ,  $\Gamma_0 = T_0^{-1} = 200$ ,  $\gamma = 0.5$ , and  $F_L = 50$ . Prior to heating the cluster is in the crystal state. From Ref. [155].

After a slight increase of  $T(r)$  within the heated center, the temperature decreases monotonically with the radius. Since energy is transferred to dust in the central region and is then transported to the outside of the cluster, the decrease in the curve is readily understood.

In contrast, the positive slope in the very inside requires a discussion. Compared to the outer region, the statistics is weaker for the inner rings due to their small area that results in a low number of particles within the ring on average. However, the increase is still significant as indicated by the error bars.

A possible reason for the lower temperature in the center is an increased energy input at the frame of the heated square. At the borders of this square, the motion of an incoming laser spot is reversed. When a particle is located in the vicinity of the border, the laser spot passes this particle on its way to the border and shortly after again, moving in the opposite direction. This dust grain is then accelerated by the same laser spot and, therefore, in the same direction two times within a short time. Due to the fast motion of the laser spot compared to the time scales  $\gamma^{-1}$  for the friction caused by the neutral gas and  $t_0 = \omega_0^{-1}$  for the dust motion, the grain cannot transfer its momentum to the neutral gas background and other dust grains before the spot passes for the second time. The fact that the spot motion parallel to the border is not reversed softens the effect, but still an enhanced acceleration takes place at the edges. In the central region, however, an accelerated particle is thereafter equiprobable accelerated again by the same laser beam or decelerated by the opposite laser beam.

While the radial density is flat in the central region, shells are visible in the colder outer region. In contrast, the radial density of the same cluster without manipulation lasers, which is not shown in the figure, consists of distinct peaks over the entire range of  $r$ . The spatially inhomogeneous energy input offers the ability to melt the central region, while the outer parts of the cluster remain solid.

Recording the radial temperature  $T(r)$  requires that this profile has already reached a steady state. This is ensured by equilibration of the cluster over  $t_{\text{eq}} = 20 t_0$  with enabled laser, before data is recorded. The time-resolved temperatures for different radii in Fig. 6.11 reveal that the

saturation takes place on time scales  $\tau \lesssim 5 t_0$ . Moreover, the saturation is found to pass off faster for the central region with  $\tau_{\text{center}} < 2 t_0$ . Particles in the central region are directly accelerated by the laser spots, while outer regions are indirectly heated when the energy is transported via collisions. This heating mechanism explains the slower relaxation at the cluster boundary.

The inhomogeneous excitation setup represents a non-equilibration situation as a macroscopic heat current is involved. On the one hand, the heating lasers serve as a local source of heat for the dust system at the center of the cluster. On the other hand, the neutral gas background, modeled as the Langevin thermostat, serves as a global drain of heat.<sup>4</sup> This results in an outward energy current  $\mathbf{j}_e$  and in a global loss of heat. The amplitude of the heat current has to decrease with the radius for two reasons: First, the integrated energy current  $J_e$  through a ring around the heated center can only decrease as a function of  $r$  but never increase when energy is lost to the background gas. Second, since the circumference of the circle grows with the radius, the outward energy current  $\mathbf{j}_e$  decreases as  $r^{-1}$ , even at a constant integrated energy current  $J_e$ . In a way, this situation can be compared to spilling a bucket of water on desert ground. While the water flows outward, part of it is lost to the ground.

In the dust cluster, the energy current is connected to the radial temperature gradient via the thermal conductivity  $k$ . Both the friction coefficient  $\gamma$  and the temperature difference between dust particles and the neutral gas, determine the energy losses from the dust to the latter. The interplay of thermal conductivity and loss rate determines the resulting temperature profile and is considered in a simple analytic model in the following section.

### 6.2.1 Analytical Model for the Temperature Profile

This section aims at describing the radial dependence of the stationary temperature profile  $T(r)$  in an analytical model. The goal is to describe the dust temperature only outside the central heated region. Motivated by the smooth temperature curve found in Fig. 6.10, an incompressible fluid model is considered for the transport process. The time-dependent heat transport equation [7] is supplemented by the thermal coupling to the background gas with temperature  $T_0$  as an additional energy source or drain,

$$c_P n k_B \left( \frac{\partial T}{\partial t} + \mathbf{v} \cdot \nabla T \right) = \text{div} (k \nabla T) + S_{\text{vis}} - 2\gamma n k_B (T - T_0) , \quad (6.32)$$

where  $n$  is the average areal particle number density,  $c_P$  is the specific heat capacity at constant pressure per particle, and  $\mathbf{v}$  is the collective flow velocity [147]. The left-hand side of Eq. (6.32) represents the (convective) time derivative of the temperature. On the right-hand side, the first term describes the thermal conduction, where the proportionality factor between the energy current and the temperature gradient is called *heat* or *thermal conductivity*  $k$ . The *viscous stress tensor* is a function of the spatial derivative of the velocity vector field of the form

$$\sigma'_{ik} = \eta \left( \frac{\partial v_i}{\partial x_k} + \frac{\partial v_k}{\partial x_i} - \frac{2}{2} \delta_{ik} \frac{\partial v_l}{\partial x_l} \right) + \zeta \delta_{ik} \frac{\partial v_l}{\partial x_l} , \quad (6.33)$$

<sup>4</sup>Of course, single particles can also gain energy from the thermostat, but the overall effect is a cooling since the particles are externally heated by the lasers to a temperature above  $T_0$ .



for an isotropic fluid in 2D. The indices  $i$ ,  $k$  and  $l$  take values 1, 2 in two dimensions, and the Einstein summation convention is used. Since the divergence of the velocity field must vanish for an incompressible fluid,  $\nabla \cdot \mathbf{v} = 0$ , the viscous heating due to shear flows is described by

$$S_{\text{vis}} = \sigma'_{ik} \frac{\partial v_i}{\partial x_k} = \frac{\eta}{2} \left( \frac{\partial v_i}{\partial x_k} + \frac{\partial v_k}{\partial x_i} \right)^2, \quad (6.34)$$

where  $\eta$  is called the *(first) coefficient of viscosity* [7]. In Eq. (6.34), the expressions in the brackets is twice the *strain rate tensor*, and the squaring implies summation over the indices  $i$  and  $k$ .

Finally, the last term on the right-hand side of Eq. (6.32) describes the losses to the neutral gas via friction, which are modeled by the damping term and the stochastic force in the Langevin model. If the model was to describe the central region, where the dust is heated by the lasers, an additional source term would have to be added.

As discussed above, the temperature profile becomes constant after a few dust plasma periods  $t_0 = \omega_0^{-1}$  and the partial time derivative  $\frac{\partial T}{\partial t}$  vanishes. The *stationary* heat transport equation then reads

$$c_P n \mathbf{v} \cdot \nabla k_B T = \text{div}(k \nabla T) - 2\gamma n k_B (T - T_0) + S_{\text{vis}}. \quad (6.35)$$

While the background temperature  $T_0$  and the friction coefficient  $\gamma$  are input parameters, the heat conductivity  $k$  is unknown and must be determined from the simulation.

Since no collective flow is observed in the simulation data, both the convective heat transport on the left side of Eq. (6.35) and heat input by viscous conversion of energy from a shear flow  $S_{\text{vis}}$  are neglected in the following. The validity of these assumptions is checked later by comparing the temperature profiles in the simulations with the analytic solution. Under these assumptions, the heat transport equation (6.35) simplifies to

$$\text{div}(k \nabla T) = 2\gamma n k_B (T - T_0). \quad (6.36)$$

Due to the cylindrical symmetry of the dust cluster, the temperature profile is expected to depend only on the radial coordinate  $r$  and the above equation reduces to

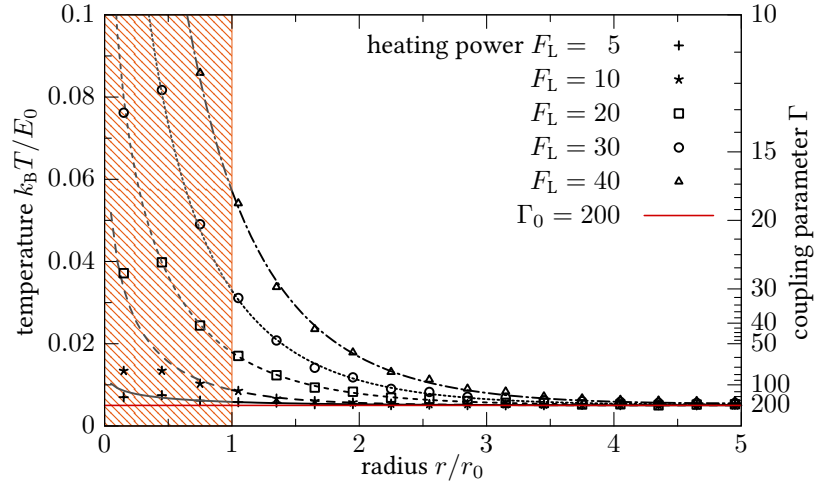
$$\frac{1}{r} \frac{d}{dr} \left( r k \frac{dT}{dr} \right) = 2\gamma n k_B (T - T_0), \quad (6.37)$$

in polar coordinates. Provided the thermal conductivity  $k$  is independent of the radius  $r$  and neglecting the spatial dependence of the areal number density, the general solution of Eq. (6.37) is readily found as zero order modified Bessel functions of the first kind  $I_0$  and the second kind  $K_0$ ,

$$T - T_0 = AK_0(\sqrt{b}r) + BI_0(\sqrt{b}r) \quad \text{with} \quad b = \frac{2\gamma n k_B}{k}. \quad (6.38)$$

Since the dust cluster has a finite radial extension  $R$ , heat cannot be transferred further outside. A heat flow equal to zero at this radius is ensured in the solution, when the temperature gradient

**Figure 6.12:** Simulation data (points) and fits by modified Bessel functions (lines), Eq. (6.38), for different laser heating powers. The central region (orange shade) was always excluded for fitting. The background temperatures corresponds to  $\Gamma_0 = 200$  in all cases.



vanishes. Differentiation of Eq. (6.38) with respect to the radius  $r$  sets up a condition for the second coefficient, which is then found to be  $B = AK_1(\sqrt{b}R)/I_1(\sqrt{b}R)$ .

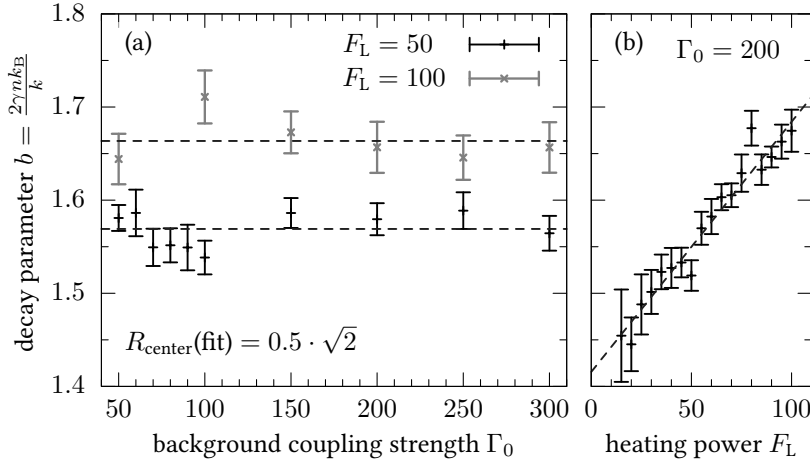
The solution for the stationary radial temperature profile Eq. (6.38) has two free parameters,  $A$  and  $b$ , which are connected to transport properties of the dust cluster and the power input in the center. While the amplitude  $A$  is connected to the total power input, the parameter  $b$  describes the slope of the temperature decay and is therefore closely linked to the heat conductivity of the cluster.

Figure 6.12 shows the decaying temperature over the radius in a Yukawa ( $\kappa = 1.0$ ) cluster with  $N = 200$  particles for different heating powers. When fitting the data points by Eq. (6.38), the central region with radius  $R_{\text{cen}} = 1.0$  is excluded since the power input by the lasers takes place in this area. The simulation data and the analytic temperature profile are in good agreement for all given values of the heating power  $F_L$ .

The resulting fit parameters are listed in Tab. 6.3. The parameter  $A$  scales roughly quadratically with the heating power. As the total power input is expected to increase quadratically with the intensity of the laser beams, i.e., the heating power  $F_L$ , see Eq. 6.22, this observation supports the statement that  $A$  describes the total heat input. Table 6.3 does not allow one to identify a clear trend of the decay parameter  $b$ . Within the statistical errors, this parameter

**Table 6.3:** Fit parameters  $A$  and  $b$  corresponding to Fig. 6.12 for an inhomogeneously heated 2D cluster of  $N = 200$  particles. The parameter  $A$  is the amplitude of the temperature profile and is connected to the total power input by the lasers. The second parameter  $b$  describes the decay of the profile and is, therefore, connected to the ratio of the thermal conductivity  $k$  of the dust cluster and the friction with the neutral gas background  $\gamma$ . For fitting the temperature outside  $R_{\text{cen}} = 1.0$ , the `curve_fit` function from `scipy` was used.

$F_L$	$A$	$b$
5	0.001 63(45)	0.722(230)
10	0.0172(35)	2.22(39)
15	0.0240(17)	1.410(99)
20	0.0402(24)	1.430(87)
25	0.0669(67)	1.58(15)
30	0.0884(63)	1.46(10)
35	0.1270(98)	1.46(11)
40	0.1590(92)	1.390(81)



**Figure 6.13:** Decay parameter  $b$  for different background temperatures of the Langevin thermostat  $\Gamma_0$  (a) and for different heating powers  $F_L$  (b). Each symbol represents the average from fitting the temperature outside  $R_{\text{cen}} = 0.5 \cdot \sqrt{2}$  in 20 independent simulations by Eq. (6.38) using the `leasqr` function from GNU Octave. From Ref. [155].

appears to be constant, at least for larger values of the heating power. The values for the two lowest heating powers have a very high uncertainty which is due to the small overall decrease of the temperature outside the heated region.

While the agreement of the fit with the data is good at small radii, a closer inspection of the curves in Fig. 6.12 reveals that the analytic curves systematically underestimate the temperature in the outer region with  $r \gtrsim 3$ . At least two possible reasons can be considered for this observation:

- While the mean areal number density  $n$  was assumed as constant in the fluid model, Eq. (6.38), it is found to decrease with the radius in the simulations. The radial decrease of the density can, in turn, affect the thermal conductivity  $k$  via an increased inter-particle distance. Moreover, the number of particles within a ring of constant area does no longer grow linearly with the distance from the trap center.
- The thermal conductivity  $k$  is considered as constant over the temperature range of the outer cluster, where the heat transport takes place. Especially at large heating powers,  $F_L = 40$ , this assumption may be violated due to the large temperature range covering one order of magnitude.

### 6.2.2 Influence of the Background Temperature $T_0$ and the Heating Power $F_L$

This section is concerned with the dependence of the parameter  $b$ , which describes the decay of the temperature profile on both the background temperature  $T_0$  and the laser heating power  $F_L$ . The background Coulomb coupling parameter is given by the inverse of the temperature  $k_B T_0$  in units of  $E_0$  for the used system of units, cf. Sec. 3.1.4. Therefore, both terms *coupling parameter* and *temperature* are used in the following discussion. At constant neutral gas friction coefficient  $\gamma$  and mean density  $n$ , the parameter  $b$  is inversely proportional to the thermal conductivity  $k$ , cf. Eq. (6.38).

**Figure 6.14:** Decay parameter  $b$  obtained by a fit that excludes a larger central region with  $R_{\text{center}} = 1$  (color). The results from the original fit with  $R_{\text{center}} = 0.5 \cdot \sqrt{2}$ , Fig. 6.13, are shown for comparison (gray).

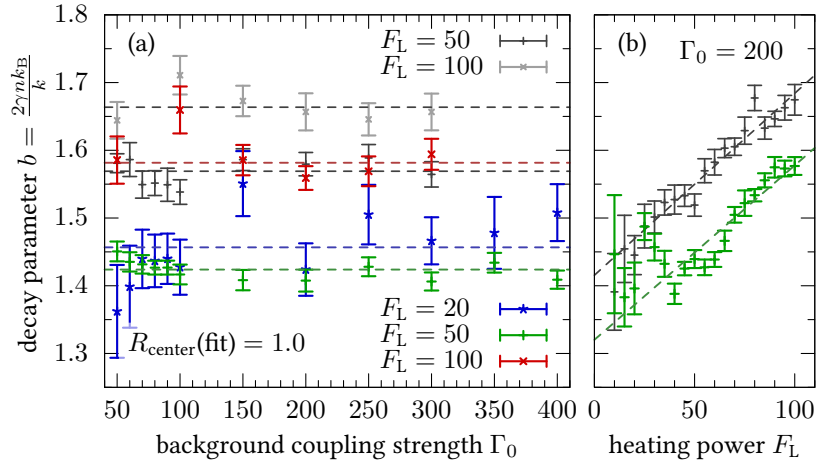


Figure 6.13 shows the results for  $b$  for a 2D Yukawa cluster (parameters:  $N = 200$ ,  $\kappa = 1$ ,  $\gamma = 0.5$ ) which were published in the joint paper with KUDELIS [155]. The left part of the figure indicates that  $b$  is constant over the investigated range of the background temperature  $T_0$  within the accuracy of the simulation. As a consequence, the thermal conductivity is also constant over  $T_0$ , as the mean density does not change during that parameter scan. In Fig. 6.13(a), the horizontal dashed lines denote the mean values of  $\bar{b} = 1.57(1)$  for a heating power of  $F_L = 50$  in dimensionless units and  $\bar{b} = 1.66(1)$  for  $F_L = 100$ , respectively.

In Fig. 6.13(b), the laser heating power  $F_L$  is varied while the temperature of the Langevin thermostat is kept constant at  $\Gamma_0 = 200$ . Here, the power dependence is well reproduced by a linear increase,  $b = b_0 + m \cdot F_L$ , with  $b_0 = 1.42(1)$  and  $m = 2.68(18) \times 10^{-3}$ . This means that the thermal conductivity decreases as a function of the laser heating power.

When fitting the temperature, a circular region in the center, where the heating takes place, was excluded. The diameter of this region is the diagonal of the square in which the spot centers of the laser beams move,  $2R_{\text{center}} = \sqrt{2}$ . Because of the radial bin width  $\Delta r = 0.3$ , this means that the inner two temperature values do not enter the fit. As discussed above, particles outside but near this square can be accelerated as well, due to the finite width of the laser spots. Since the analytic solution for  $T(r)$ , Eq. (6.38), is valid only outside the heated region, this choice of  $R_{\text{center}}$  during the fit may be too small.

For this reason, the results from the paper [155] are compared to supplementary results for  $b$  with a larger region being excluded from the fit. Here, the function `curve_fit` from the scientific python library `scipy` was used instead of GNU Octave. The only reasons for this choice are the higher convenience and the flexibility of the python programming language. Both routines yield the same results provided that the same region is excluded from the fit.

The new results for the parameter  $b$  are shown in Fig. 6.14 and are compared to the original results where the excluded center was supposedly chosen to be small during the fit. Although the quantitative results are biased by the choice of  $R_{\text{center}}(\text{fit})$ , the two qualitative conclusions are still valid. The thermal conductivity is independent of the background temperature  $T_0$  in the investigated parameter range, but it decreases with the laser heating power  $F_L$ . For moderate heating powers  $F_L \lesssim 40$  in dimensionless units, the obtained values for  $b$  appear to deviate from

the linear increase towards higher values. However, the uncertainties are large in this case due to the small overall slope of the radial temperature profile. In figure 6.14, the results are complemented by a scan of the background coupling strength  $\Gamma_0$  at a lower constant heating power  $F_L = 20$ . The obtained values of  $b$  exhibit high fluctuations at this relatively low heating power.

Choosing a too small value of  $R_{\text{center}}(\text{fit})$  for the fit biases the resulting parameter  $b$  towards higher values, i.e., a lower thermal conductivity is obtained. The dashed lines in the plot indicate mean values of  $\bar{b} = 1.46(1)$  for  $F_L = 20$ ,  $\bar{b} = 1.424(4)$  for  $F_L = 50$ , and  $\bar{b} = 1.58(1)$  for  $F_L = 100$ . This finding is discussed in the following, since the unaccounted source of heat in the fitted range should result in an overestimation of the thermal conductivity. A possible reason for the contrary effect is that the relative weight of the outer temperature measurements is reduced by the additional measurements in the hot central region. As discussed at the end of section 6.2.1, the analytical solution underestimates the temperature at the outer cluster, and extending the fit range towards smaller inner radii increases this bias. While the absolute deviation between the sampled temperature profile and the analytic profile is small, the difference  $T(r) - T_0$  at the outer cluster too small by a factor of two at parameters  $T_0 = 400^{-1}$  and  $F_L = 50$  when fitting with the small excluded center. Since the energy losses to the neutral gas are proportional to this temperature difference, the thermal conductivity of the outer cluster is underrated by the fitted solution. A higher weight of the (temperature) data points at the outer cluster results in a value for  $b$  that is approximately 30 % lower. This clearly shows the limits of the assumption of a constant  $b = \frac{2\gamma n k_B}{\kappa}$  in the analytic model.

The major impact of the high temperature data points near the heated center on the identified parameter  $b$  can explain the independence of the latter of the background temperature  $T_0$ , found in Figs. 6.13 and 6.14. For the shown parameter range, the actual value of  $T_0$  mainly influences the temperature of the outer cluster, while the temperature of the inner cluster predominately follows from the heating power  $F_L$ .

When the heating power is increased, the absolute temperature increase in the central region is much higher than the absolute temperature increase in the outer regions. Since the fit minimizes the absolute deviation between the analytical temperature profile and the sampled temperatures, this increases the relative weight of the inner data points in the obtained parameter  $b$ . As discussed above, the increased weight of the inner region results in a smaller decay parameter  $b$ .

### 6.2.3 Discussion of the Results

The parameter  $b$ , as introduced in Eq.(6.38), has the dimension of an inverse length squared. Hence,  $L = 1/\sqrt{b}$  can be interpreted as characteristic length for the heat transport. For arguments  $x > 2$ , the modified Bessel function  $K_1(x)$  is well approximated by an exponential decay, and the temperature difference  $T(r) - T_0$  is found to drop by a factor  $\approx 2.5$  over a distance  $L$  in the radial direction. The mean value  $\bar{b} = 1.424$  ( $F_L = 50$ ), Fig. 6.14, corresponds to  $L = 0.84 \cdot r_0 = 1.37$  mm. The conversion from dimensionless units into SI units was done for melamine dust particles with a diameter  $d_d = 6 \mu\text{m}$  carrying a charge of  $Q_d = 10\,000 e$ , a trap frequency  $\omega_0 = 5.5 \text{ s}^{-1}$  and a friction frequency  $\gamma = \omega_0/2$  as representative plasma parameters [46].

The stationary temperature profile is governed by two competing processes: (i) heat transport within the dust system (proportional to the thermal conductivity  $k$ ), and (ii) energy loss to the neutral gas (proportional to the neutral gas friction coefficient  $\gamma$ ). Rearranging Eq. (6.38), the decay length can be written as

$$L = \frac{1}{\sqrt{b}} = \frac{1}{\sqrt{nk_B}} \sqrt{\frac{k}{2\gamma}}. \quad (6.39)$$

While a high thermal conductivity in the cluster leads to a flat temperature profile with a large length scale  $L$ , a high neutral gas friction leads to a temperature profile with a fast decay characterized by a small length scale  $L$ .

The two competing processes were assumed as independent. In Ref. [155], it is shown that this picture holds well except for low friction frequencies  $\gamma \lesssim 0.4\omega_0$ . For low friction frequency, the thermal conductivity  $k$  increases with reduced  $\gamma$ . This increase is attributed to the increased mobility of the dust grains, which was verified by the investigation of their mean square displacement. In the case of high mobility, long-range particle motion can become important in addition to the energy transfer via vibrations.

A quantity that is often calculated in experiments [147, 156, 157] is the *thermal diffusivity*, denoted by  $\chi$ . This quantity relates the thermal conductivity and the areal heat capacity as  $\chi = k/nc_P$ , where  $c_P$  is the specific heat capacity (heat capacity per particle) at constant pressure. The latter can be estimated by the Dulong-Petit limit. To this end, the excitations of a strongly correlated 2D dust cluster are approximated by  $2N$  normal modes, one of which—the rigid rotation of the entire cluster—does not contribute,  $\omega_{\text{rot}} = 0$ . With  $c_P \approx (2N - 1)/N \approx 2$  as heat capacity per particle, the thermal diffusivity for  $\bar{b} = 1.424$  ( $F_L = 50$ ) is [155]

$$\chi = \frac{k}{nc_P} = \frac{2\gamma nk_B}{bnc_P} = \frac{\gamma k_B}{b} \approx 5.2 \text{ mm}^2 \text{ s}^{-1}, \quad (6.40)$$

for typical plasma conditions as described above. This result is in reasonable agreement with experimental findings for 2D complex plasmas between  $\chi \approx 9 \text{ mm}^2 \text{ s}^{-1}$  and  $\chi_{\text{tr}} \approx 30 \text{ mm}^2 \text{ s}^{-1}$  (transverse),  $\chi_l = 50 \text{ mm}^2 \text{ s}^{-1}$  (longitudinal) [147, 156]. A lower thermal diffusivity  $\chi \approx 1 \text{ mm}^2 \text{ s}^{-1}$  was found for a liquid 3D complex plasmas [157]. The uncertainty of these values is predominately caused by different friction values.

An increased weight of the outer temperature data points, which is achieved by using the temperature fluctuations recorded in the simulations as inverse weights during the fits, increases the obtained thermal conductivity  $k$  by about 30%. Hence, taking into account the temperature fluctuations affects the result for the thermal diffusivity in the correct direction.

Determining the thermal conductivity  $k$  by fitting an analytic model to the temperature profile involves a conceptual challenge. Since  $k$  is obtained from the slope of the temperature, a high power input is beneficial as it results in a strong decay. This allows one to determine the slope with a small relative error, while this error becomes large for a shallow radial temperature profile. On the other hand, a shallow temperature profile is advantageous in order to resolve any temperature dependence of the thermal conductivity  $k$ . As the model in Eq. (6.38) assumes

that  $k$  is constant over the fitted temperature range, this range sets an upper limit for resolvable temperature dependences.

The standard method to determine the linear-response transport coefficient of an *infinite* system in an equilibrium simulation is the Green-Kubo formula [158–160]. The basic idea of this approach is to calculate the thermal conductivity or other transport coefficients via the integrated autocorrelation function of the total energy current, or the current that corresponds to the transport coefficient, respectively. However the standard Green-Kubo formula is problematic in finite systems as it involves the limit of infinite system length  $L_{\text{sys}} \rightarrow \infty$  and is, for this reason, not suited for harmonically confined dust clusters. KUNDU *et al.* presented a formula for the heat conduction in open systems [161], in which the energy current is obtained by coupling the left and the right side of the system to heat baths with different temperatures. This approach is promising for future stimulations with circular or spherical dust clusters where single particles can be selectively coupled to different heat baths. On the contrary, the neutral gas background acts as a heat bath for all particles in experiments. For this reason, it should be easier to determine the thermal conductivity  $k$  via the slope of the temperature profile in a dusty plasma experiment.

#### 6.2.4 Heat Transport in a Magnetized Cluster

The influence of a magnetic field  $\mathbf{B}$  on the transport properties of the dust cluster is subject of this section. This magnetic field is considered perpendicular to the cluster plane. While a static magnetic field does not have any impact on the static properties of a classical system due to the Bohr-van Leeuwen theorem, it can modify the dynamic properties. For example, magnetized dust particles cannot follow an electric field directly but they are constrained onto Larmor orbits. This constraint may hinder the transfer of momentum and energy from one dust particle to a second particle and could therefore result in a reduced thermal conductivity. In experiments, the dust particles can be strongly magnetized by rotation of the cluster together with the neutral gas, as shown by KÄHLERT *et al.* [39]. In the rotated frame, the Coriolis force has the same form as the Lorentz force and represents a pseudo-magnetic field.

An efficient numerical handling of the magnetic field requires a modification of the Langevin molecular dynamics (LMD) algorithm. The straightforward implementation includes the Lorentz forces  $\mathbf{F}_i = Q_d \mathbf{v}_i \times \mathbf{B}$  as additional accelerations for all particles  $i$ . However, this implementation becomes inefficient for large magnetic fields as a small time step  $\Delta t$  is necessary to resolve the circular motion of each dust particle. SPREITER and WALTER proposed a classical MD algorithm that allows one to include arbitrarily strong static homogeneous external magnetic fields [162]. In their scheme, the magnetic field is built into the propagation equations in a way such that the Larmor oscillations are correctly reproduced, independently of the chosen time step. This allows one to choose the time step according to the physical properties of the investigated dust cluster, regardless of the magnetic field strength. In order to combine this scheme with the quasi-symplectic integration of the Langevin equation of motion [122], the Langevin operator for the propagation of the velocity is split into two parts with half time step [163, 164].

In the following, the strength of the magnetic field  $\mathbf{B}$  is characterized by the *cyclotron frequency* of the dust grains  $\omega_c = \frac{Q_d |\mathbf{B}|}{m_d}$  in units of the trap frequency  $\omega_0$ . This way of quantifying  $\mathbf{B}$

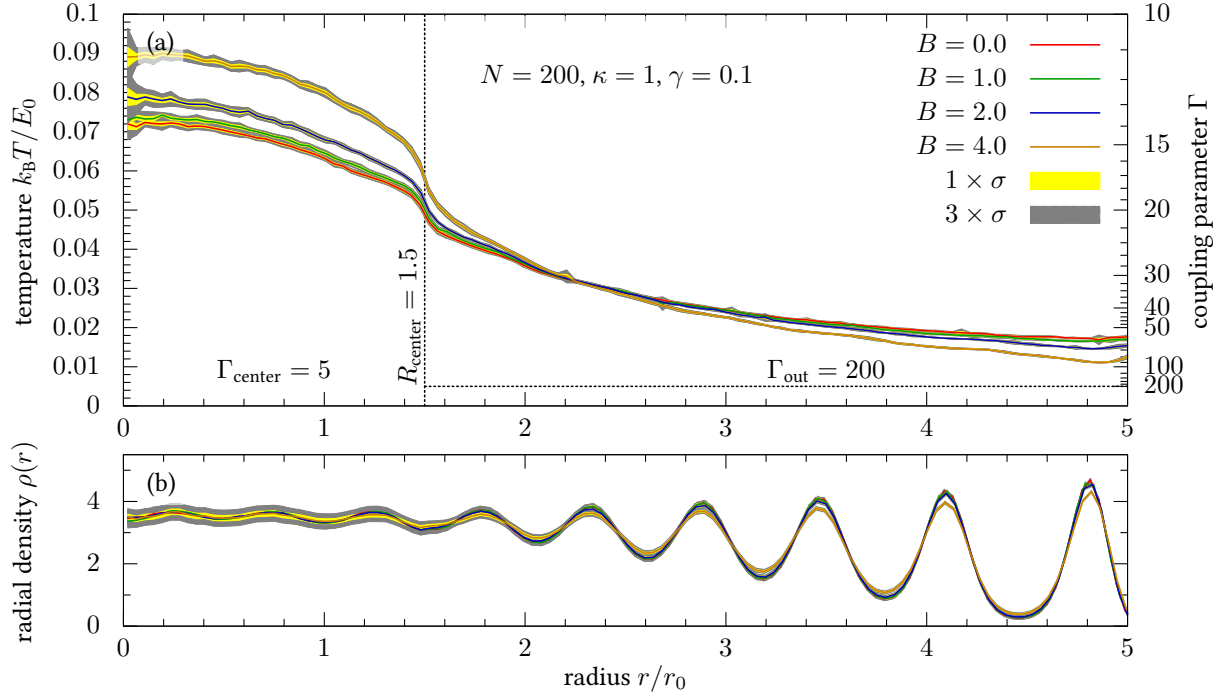


**Figure 6.15:** (a) Radial temperature profile of a 2D cluster for different magnetization characterized by the cyclotron frequency in units of the trap frequency  $B = \omega_c/\omega_0$ . The magnetic field is considered perpendicular to the cluster,  $\mathbf{B} = B \cdot \mathbf{e}_z$ . The inner part of the cluster (vertical line at  $R_{\text{center}} = 1.5$ ) is coupled to a hotter thermostat than the outer part. The curves are obtained as an average over 20 independent simulation runs and the standard deviation  $\sigma$  ( $3 \times \sigma$ ) is shown in yellow (gray). (b) The radial density shows virtually no dependence on the strength of the magnetization.

is equivalent to defining  $B_0 = m_d \omega_0 / Q_d$  as unit of magnetic field strength. As discussed in the first part of this chapter, the random frequency laser heating method B is appropriate to realize a source of heat, which can be tailored for inhomogeneous heating of the cluster's center. In section 6.2, the heating lasers were included as time-dependent forces that accelerate the dust grains in the central region. In contrast, this heating mechanism is not included explicitly in the simulations addressed in this section. Instead, the inhomogeneous heating is modeled by a Langevin thermostat with an increased temperature in the central region. The background temperature of the thermostat is given by

$$T_0(r) = \begin{cases} T_{\text{center}} & : r \leq R_{\text{center}} \\ T_{\text{out}} & : r > R_{\text{center}} \end{cases} . \quad (6.41)$$

Figure 6.15(a) shows the variation the radial temperature profile with the strength of the magnetic field  $B$  perpendicular to the cluster plane. The temperature decreases monotonically with the radius over the entire cluster, and the steepest decrease is found at the intersection of the



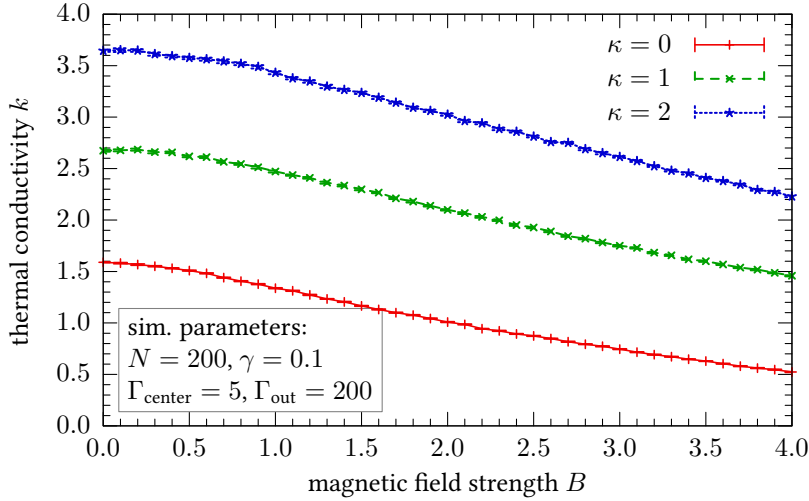


**Figure 6.16:** Thermal conductivity  $k$  as a function of the magnetic field strength  $B$  for different screening parameters  $\kappa$ . The radial temperature profile of the outer cluster, cf. Fig. 6.15, was fit by Eq. (6.38) in order to obtain the decay parameter  $b = \frac{2n\gamma}{k}$  which allows one to determine  $k$  using the average particle density of the outer cluster  $\bar{n}$ .

heated and cooled regions.<sup>5</sup> Note that the comparably low neutral gas friction coefficient  $\gamma = 0.1$  allows for the transport of heat over large distances with a low temperature gradient. Therefore, all radial temperature profiles have a small slope when compared to Fig. 6.10.

In comparison with the unmagnetized cluster, the kinetic temperature [Eq. (6.31)] in the central region with a warm background temperature  $T_0 = T_{\text{center}} = 0.2$  increases with the magnetic field strength. This trend is reversed in the outer regions with  $r \gtrsim 3$  and a cold background temperature  $T_0 = T_{\text{out}} = 0.005$ . Only the curve for  $B = 4$  stands out from the other curves. Figure 6.15(a) indicates that the thermal conductivity  $k$  within the 2D dust cluster is *reduced* by a perpendicular magnetic field. If the cluster was a perfect heat conductor with  $k = \infty$ , the temperature profile would be constant, with  $T$  between  $T_{\text{center}}$  and  $T_{\text{out}}$ . The actual value of  $T$  would depend on the size of the heated center  $R_{\text{center}}$ . If the cluster was yet a perfect heat isolator with  $k = 0$ , the dust temperature would be  $T_{\text{center}}$  in the center and would abruptly drop to  $T_{\text{out}}$  at the radius of the heated center,  $R_{\text{center}}$ .

The lower part (b) of the figure shows the radial density  $\rho(r)$  for the different values of  $B$ . Within the statistical error, the radial densities coincide for  $B = 0, 1$  and  $2$ , but a slight deviation is found for the largest field strength  $B = 4$ . Interestingly, the latter curve for the strongest magnetic field has lower maxima and higher minima in the outer region compared to weaker magnetic fields, even though this system has the lowest kinetic temperature in this region. This observation suggests that the magnetic field has also an impact on the interchange between kinetic and potential energy [165].

In order to quantify the effect of the magnetic field on the heat transport, the thermal conductivity  $k$  as a function of  $B$  is determined from the LMD simulation results. For this purpose, the radial temperature profile outside the heated core is fitted by the analytical temperature profile, Eq. (6.38). In addition to the results shown in Fig. 6.15, LMD simulations were performed

<sup>5</sup>In this model, a monotonic decrease of the temperature with the radius is found, both in the heated center and in the outer region. In contrast, the temperature increased towards the edges of the heated square when the lasers were explicitly included in the simulation in Fig. 6.11. This observation indicates that the increase is an artifact of the laser excitation mechanism.

for the intermediate magnetic field strengths. Each data point in Fig. 6.16 was obtained as the average over 21 independent simulation runs for the same  $B$ . The thermal conductivity  $k$  is evaluated for one Coulomb cluster ( $\kappa = 0$ ) and for two Yukawa clusters ( $\kappa = 1$  and  $\kappa = 2$ ).

The absolute value of  $k$  is strongly dependent on the screening parameter  $\kappa$ . When  $\kappa$  is increased, the cluster becomes smaller and the thermal conductivity increases. When a magnetic field is applied, the thermal conductivity  $k$  decreases. This tendency is found regardless of the screening and means that the magnetization hinders the radial heat transport. Compared with the unmagnetized case, a magnetic field strength  $B = 4$  causes a decrease of  $k$  by 40–70 % depending on the screening parameter, where the strongest relative decrease is found for the Coulomb cluster.

### Related Journal Publications and Book Chapters

- J. Schablinski, D. Block, A. Piel, A. Melzer, H. Thomsen, H. Kählert and M. Bonitz *Laser heating of finite two-dimensional dust clusters: A. Experiments*, Phys. Plasmas **19**, 013705 (2012)
- H. Thomsen, H. Kählert, M. Bonitz, J. Schablinski, D. Block, A. Piel and A. Melzer *Laser heating of finite two-dimensional dust clusters: B. Simulations*, Phys. Plasmas **19**, 023701 (2012)
- G. Kudelis, H. Thomsen and M. Bonitz *Heat transport in confined strongly coupled two-dimensional dust clusters*, Phys. Plasmas **20**, 073701 (2013)
- A. Schella, A. Melzer, P. Ludwig, H. Thomsen and M. Bonitz *Introduction to Streaming Complex Plasmas A: Attraction of Like-Charged Particles in Complex Plasmas: Scientific Challenges and Technological Opportunities* edited by M. Bonitz, J. Lopez, K. Becker and H. Thomsen (Springer, New York, 2014)
- H. Thomsen, P. Ludwig, M. Bonitz, J. Schablinski, D. Block, A. Schella and A. Melzer *Controlling strongly correlated dust clusters with lasers*, J. Phys. D: Appl. Phys. **47**, 383001 (2014)

## Chapter 7

### Conclusion

**T**his work has been grouped into two main topics. Its first part was concerned with the structural transitions during the melting process of finite dust clusters. In this context the focus was on spherical dust balls in 3D. The second part of this work was concerned with the laser excitation of circular 2D clusters.

#### Melting Process of Finite Dust Clusters

The thermodynamic properties of harmonically confined dust clusters were investigated by the means of finite temperature Monte Carlo (MC) simulations. This method was chosen because of its ability to sample the accessible phase space efficiently over a broad range of coupling strength  $\Gamma$ . In order to ensure an ergodic sampling of the entire phase space across energy barriers at very high couplings, the parallel tempering enhancement was used. The parallel tempering method assists the transitions between different isomers. However, the resultant sequence of configurations grants only very limited statements about the dynamics of the dust particles, in particular because of the configuration swaps.

In spherical 3D clusters, the radial structure, the intra-shell structure and the inter-shell angular order are subject to the melting process. For this reason, the development of melting parameters was required in order to distinguish between the different disordering processes. As an additional requirement, these parameters should not depend on dynamic information but only on the  $N$ -particle phase space distribution which is accessible in equilibrium MC simulations. The center-two-particle (C2P) and the triple-correlation function (TCF) were introduced as the pair-density and the three-particle density in generalized coordinates, respectively, and were found to excellently meet these requirements. Due to the choice of the generalized coordinates, the C2P and the TCF take into account the spherical symmetry of the Hamiltonian of the dust system. In order to obtain a reliable melting criterion based on these quantities, the reduced entropy  $S^{(n)}$  was introduced as a measure for the disorder in the  $n$ -particle distribution. Moreover, this reduced entropy is closely linked to the thermodynamic Boltzmann entropy  $S$ .

The C2P was first tested in small 2D clusters, where it could resolve the intra-shell angular melting process. Since the cluster shells can interlock for certain magic particle numbers, the

cluster is then very stable against this disordering process.

Spherical Coulomb balls in 3D exhibited an even broader spectrum of transitions. The inter-shell angular melting process was found to occur at relatively high coupling strength even for magic number clusters. On the other hand, the intra-shell order turned out to be very stable. Even though, transitions between different intra-shell isomers can occur at high coupling, a well ordered pattern of the intra-shell particle positions persists. The critical coupling strength for this kind of transition strongly depends on the precise particle number. While these intra-shell transitions are often accompanied by particle transitions between two shells, they can occur without any change of the radial configuration. This finding was confirmed by the consideration of a system of charges on a Thomson sphere. The order within the shell is completely lost at coupling strengths around the radial melting point.

In this work, the C2P and the TCF have been applied as two novel melting parameters in the context of dusty plasmas in order to resolve structural transitions in a system of classical particles. However, these quantities should be applicable also for quantum systems where the  $n$ -particle density has to be replaced by the  $n$ -particle density operator. This density operator can be evaluated in most quantum simulation methods.

As an independent access towards the order within a spherical shell, the intra-shell Voronoi diagrams were evaluated. These diagrams allowed for the distinction of the different intra-shell isomers by the configuration of hexagonal and pentagonal cells.

## Laser Excitation of 2D Dust Clusters

In the first part of the laser excitation section, the properties of the elaborated heating method with four randomly moving laser spots were proved in Langevin molecular dynamics simulations. By the means of this method, a 2D dust cluster is heated spatially homogeneously, no artificial pattern is impressed to the structure, and the energy is equally distributed over the entire velocity spectrum. In a simple analytical model for the laser heating process, the resultant dust temperature could be estimated from the balance of the energy gain from the momentum transfer via radiation pressure on the one hand and the energy loss due to the neutral gas friction on the other hand.

Furthermore, an inhomogeneous scenario has been proposed for future experiments. In this scenario, a cluster is laser heated selectively in the central region. Langevin molecular dynamics (LMD) simulations were carried out for this scenario and the resultant temperature profiles were reproduced in a fluid model for the heat transport. By fitting the analytical temperature profile to the simulation data, the thermal conductivity  $k$  was extracted from the numerical experiment. The thermal conductivity was found to be independent of the coupling strength  $\Gamma$  for the investigated parameters. In contrast, a magnetic field  $B$  perpendicular to the cluster plane was capable to weaken the radial heat transport.

The applied method for the determination of the thermal conductivity  $k$  has the advantage to be suitable for experiments since the spatial area, in which the heating laser spots move, can be adjusted with high precision. Moreover, the radial temperature profile is experimentally accessible through the recorded particle velocities and a pseudo-magnetic field for the dust grains can be realized by rotating the cluster together with the neutral gas.

# Appendix A

## Distribution Functions in Generalized Coordinates and Reduced Entropy

### A.1 Jacobi Determinants for Spherical Coordinate Systems

When sampling the  $n$ -particle density in generalized coordinates  $Q$ , it is sufficient to know how these coordinates are obtained from the positions  $(\mathbf{r}_1, \dots, \mathbf{r}_n)$  of  $n$  particles in Cartesian coordinates. However, the calculation of the center-two-particle and the triple-correlation function involves the geometric factors  $V_2$  and  $V_3$ , respectively. The geometric factors are obtained by integrating the Jacobi determinant over the irrelevant coordinates  $B$ . For this purpose, the Jacobi determinants are calculated for the coordinate systems used in the C2P, the TCF in flat extended systems and the TCF in spherical systems in the following.

#### A.1.1 Center-Two-Particle Coordinates $(r_I, r_{II}, \vartheta)$

The appropriate coordinate system for describing the two particle density contains  $r_I$  as the radial coordinate of first particle,  $r_{II}$  as the radial coordinate of the second particle and the angle  $\vartheta$  between both particles with respect to the origin as coordinates. This coordinate system allows one to describe the pair density by the center-two-particle (C2P) distribution function, cf. Sec. 4.3.2.

In order to calculate the C2P correlation function  $g_2(r_I, r_{II}, \vartheta)$  or the *reduced* entropy  $S^{(2)}$  in a spherical systems, the functional determinant of the transformation  $\Phi_{\text{C2P}}^{\text{3D}} : (Q, B) \mapsto (\mathbf{r}_1, \mathbf{r}_2)$  has to be known. The transformation  $\Phi_{\text{C2P}}^{\text{3D}}$  can be described by usual spherical coordinates as

$$\mathbf{r}_1 = r_I \cdot \begin{pmatrix} \sin(\vartheta_1) \cos(\varphi_1) \\ \sin(\vartheta_1) \sin(\varphi_1) \\ \cos(\vartheta_1) \end{pmatrix} \quad \mathbf{r}_2 = \mathbf{R}(\vartheta_1, \varphi_1) r_{II} \cdot \begin{pmatrix} \sin(\vartheta) \cos(\varphi_2) \\ \sin(\vartheta) \sin(\varphi_2) \\ \cos(\vartheta) \end{pmatrix}, \quad (\text{A.1})$$

where  $\mathbf{R}(\vartheta_1, \varphi_1)$  is the rotational matrix that transforms the  $z$ -axis to the direction of  $\mathbf{r}_1$ . The relevant coordinates are  $Q = (r_I, r_{II}, \vartheta)$  while the two particle density must not depend on the irrelevant coordinates  $B = (\vartheta_1, \varphi_1, \varphi_2)$  due to the rotational invariance of the Hamiltonian.

Neither the detailed form of  $\mathbf{R}$  nor the direction of the  $y$ -axis after the rotation are of central interest. The only important fact is that, after the rotation,  $\vartheta$  describes the angle between  $\mathbf{r}_1$  and  $\mathbf{r}_2$ . The Jacobi matrix has the form

$$\mathcal{J}\Phi_{\text{C2P}}^{3\text{D}}(r_1, \vartheta_1, \varphi_1, r_{\text{II}}, \vartheta, \varphi_2) = \begin{pmatrix} \frac{\partial x_1}{\partial r_1} & \frac{\partial x_1}{\partial \vartheta_1} & \frac{\partial x_1}{\partial \varphi_1} & \frac{\partial x_1}{\partial r_{\text{II}}} & \frac{\partial x_1}{\partial \vartheta} & \frac{\partial x_1}{\partial \varphi_2} \\ \frac{\partial y_1}{\partial r_1} & \ddots & & & & \vdots \\ \frac{\partial z_1}{\partial r_1} & & \ddots & & & \vdots \\ \frac{\partial x_2}{\partial r_1} & & & \ddots & & \vdots \\ \frac{\partial y_2}{\partial r_1} & & & & \ddots & \vdots \\ \frac{\partial z_2}{\partial r_1} & \dots & \dots & \dots & \dots & \frac{\partial z_2}{\partial \varphi_2} \end{pmatrix}. \quad (\text{A.2})$$

The upper left part is identified as the Jacobi matrix of usual spherical coordinates  $\mathbf{A} = \mathcal{J}_1\Phi(r_1, \vartheta_1, \varphi_1)$ .  $\mathcal{J}_1$  is the Jacobi matrix of the transformation  $(r_1, \vartheta_1, \varphi_1) \mapsto \mathbf{r}_1$  from spherical to Cartesian coordinates and  $\mathcal{J}_2$  is analogous for the second triple of spherical coordinates  $(r_{\text{II}}, \vartheta, \varphi_2)$  excluding the rotation  $\mathbf{R}$ .

Since  $\mathbf{r}_1$  does not depend on  $r_{\text{II}}$ ,  $\vartheta$  or  $\varphi_2$ , the upper right part of the Jacobi matrix vanishes. In the following, the lower left part is referred to as  $\mathbf{C}$ . Finally, the lower right part can be simplified as

$$\mathbf{D} = \mathcal{J}_2\mathbf{R}(\vartheta_1, \varphi_1) \Phi(r_{\text{II}}, \vartheta, \varphi_2) = \mathbf{R}(\vartheta_1, \varphi_1) \mathcal{J}_2\Phi(r_{\text{II}}, \vartheta, \varphi_2), \quad (\text{A.3})$$

since the rotational matrix  $\mathbf{R}$  does not depend on the coordinate of the second triple  $r_{\text{II}}$ ,  $\vartheta$  and  $\varphi_2$ . Applying these simplifications, the full Jacobi matrix is now written as the block matrix

$$\mathcal{J}\Phi_{\text{C2P}}^{3\text{D}}(r_1, \vartheta_1, \varphi_1, r_{\text{II}}, \vartheta, \varphi_2) = \begin{pmatrix} \mathcal{J}_1\Phi(r_1, \vartheta_1, \varphi_1) & 0 \\ \mathbf{C} & \mathbf{R}(\vartheta_1, \varphi_1) \mathcal{J}_2\Phi(r_{\text{II}}, \vartheta, \varphi_2) \end{pmatrix}, \quad (\text{A.4})$$

of which the determinant is calculated as the next step. Since the upper off-diagonal block is zero, the lower off-diagonal block  $\mathbf{C}$  has no contribution in the determinant. Furthermore, the determinant of any rotational matrix is unity, so that the final result is

$$\begin{aligned} |\mathcal{J}\Phi_{\text{C2P}}^{3\text{D}}(r_1, \vartheta_1, \varphi_1, r_{\text{II}}, \vartheta, \varphi_2)| &= |\mathcal{J}_1\Phi(r_1, \vartheta_1, \varphi_1)| \cdot |\mathbf{R}(\vartheta_1, \varphi_1)| \cdot |\mathcal{J}_2\Phi(r_{\text{II}}, \vartheta, \varphi_2)| \\ &= r_1^2 \sin \vartheta_1 \cdot r_{\text{II}}^2 \sin \vartheta. \end{aligned} \quad (\text{A.5})$$

In the last step, the well-known result  $|\mathcal{J}\Phi(r, \vartheta, \varphi)| = r^2 \sin \vartheta$  was used for the Jacobi determinant of spherical coordinates.

This result is readily transferred to 2D systems, where the two positions are described by

$$\mathbf{r}_1 = r_1 \cdot \begin{pmatrix} \cos(\varphi_1) \\ \sin(\varphi_1) \end{pmatrix} \quad \mathbf{r}_2 = r_{\text{II}} \cdot \begin{pmatrix} \cos(\varphi_1 + \vartheta) \\ \sin(\varphi_1 + \vartheta) \end{pmatrix}, \quad (\text{A.6})$$

with the relevant coordinates being again  $Q = (r_1, r_{\text{II}}, \vartheta)$ , and with the irrelevant coordinate being  $B = (\varphi_1)$ . The Jacobi determinant is then found as  $|\mathcal{J}\Phi_{\text{C2P}}^{2\text{D}}(r_1, \varphi_1, r_{\text{II}}, \vartheta)| = r_1 \cdot r_{\text{II}}$  for the C2P function in finite 2D systems.

### A.1.2 Triple-Correlation Function Coordinates in Extended Systems $(d_1, d_{\parallel}, \vartheta)$

Similarly to the above section, the Jacobi determinant is now calculated for the triple-correlation function (TCF) in planar 2D systems. The coordinate system, which was introduced for the TCF in Sec. 4.3.3, contains  $d_1$  as the Euclidean pair distance of the first and the second particle,  $d_{\parallel}$  as the Euclidean pair distance of the first and the third particle and  $\varphi$  as the “bond angle” between the two pair-distances. The coordinate transformation  $\Phi_{\text{TCF}}^{2\text{D}}$  with

$$\mathbf{r}_1 = \begin{pmatrix} x_1 \\ x_2 \end{pmatrix} \quad \mathbf{r}_2 = \mathbf{r}_1 + d_1 \cdot \begin{pmatrix} \cos(\varphi_2) \\ \sin(\varphi_2) \end{pmatrix} \quad \mathbf{r}_3 = \mathbf{r}_1 + d_{\parallel} \cdot \begin{pmatrix} \cos(\varphi_2 + \vartheta) \\ \sin(\varphi_2 + \vartheta) \end{pmatrix}, \quad (\text{A.7})$$

describes how the three particle positions in Cartesian coordinates are obtained from the generalized coordinates  $(Q, B)$ . The relevant coordinates are  $Q = (d_1, d_{\parallel}, \vartheta)$  while the three-particle density must not depend on the irrelevant coordinates  $B = (x_1, y_1, \varphi_2)$  due to the assumed invariances of the Hamiltonian under rotation and translation.

The Jacobi matrix for the coordinate transformation reads

$$\mathcal{J}\Phi_{\text{TCF}}^{2\text{D}}(x_1, x_2, d_1, \varphi_2, d_{\parallel}, \vartheta) = \begin{pmatrix} \frac{\partial x_1}{\partial x_1} & \frac{\partial x_1}{\partial y_1} & \frac{\partial x_1}{\partial d_1} & \frac{\partial x_1}{\partial \varphi_2} & \frac{\partial x_1}{\partial d_{\parallel}} & \frac{\partial x_1}{\partial \vartheta} \\ \frac{\partial y_1}{\partial x_1} & \ddots & & & & \vdots \\ \frac{\partial x_2}{\partial x_1} & & \ddots & & & \vdots \\ \frac{\partial y_2}{\partial x_1} & & & \ddots & & \vdots \\ \frac{\partial x_3}{\partial x_1} & & & & \ddots & \vdots \\ \frac{\partial y_3}{\partial x_1} & \dots & \dots & \dots & \dots & \frac{\partial y_3}{\partial \vartheta} \end{pmatrix}, \quad (\text{A.8})$$

which can be decomposed into nine  $2 \times 2$  blocks. Again, the blocks above the diagonal vanish, since the first position  $\mathbf{r}_1$  is independent of the last two pairs of generalized coordinates, and since the second positions is independent of the last coordinate pair. Moreover, the blocks in the left column are all unit matrices, because  $\mathbf{r}_1$  represents a translation of all three positions. The simplified block matrix reads,

$$\mathcal{J}\Phi_{\text{TCF}}^{2\text{D}}(x_1, x_2, d_1, \varphi_2, d_{\parallel}, \vartheta) = \begin{pmatrix} \mathbf{1} & \mathbf{0} & \mathbf{0} \\ \mathbf{1} & \mathcal{J}_2\Phi(d_1, \varphi_2) & \mathbf{0} \\ \mathbf{1} & \mathbf{A} & \mathcal{J}_3\Phi(d_{\parallel}, \varphi_2 + \vartheta) \end{pmatrix}, \quad (\text{A.9})$$

where  $\mathcal{J}_2$  and  $\mathcal{J}_3$  are the Jacobi matrices of the transformations from polar coordinates  $(d_1, \varphi_2)$  and  $(d_{\parallel}, \varphi_2 + \vartheta)$  to Cartesian coordinates of the second two positions excluding the translation by  $\mathbf{r}_1$ .

Due to the zeros in the upper half, the full Jacobi determinant is given by the product of the diagonal determinants,

$$\begin{aligned} |\mathcal{J}\Phi_{\text{TCF}}^{2\text{D}}(x_1, x_2, d_1, \varphi_2, d_{\parallel}, \vartheta)| &= |\mathbf{1}| \cdot |\mathcal{J}_2\Phi(d_1, \varphi_2)| \cdot |\mathcal{J}_3\Phi(d_{\parallel}, \varphi_2 + \vartheta)| \\ &= d_1 \cdot d_{\parallel}, \end{aligned} \quad (\text{A.10})$$

where the well-known result  $|\mathcal{J}\Phi(r, \varphi)| = r$  was used for the Jacobi determinant of polar coordinates.

This result is readily transferred to 3D systems by introducing rotational matrices and using the Jacobi determinant of spherical polar coordinates as in Sec. A.1.1. The derivation is straight forward and gives

$$\mathcal{J}\Phi_{\text{TCF}}^{3\text{D}}(x_1, y_1, z_1, d_1, \vartheta_2, \varphi_2, d_{\text{II}}, \vartheta, \varphi_3) = d_1^2 \sin \vartheta_2 \cdot d_{\text{II}}^2 \sin \vartheta. \quad (\text{A.11})$$

as the Jacobi determinant for the coordinate system of the TCF in extended 3D systems.

### A.1.3 Coordinates of the Triple-Correlation Function in Spherical Systems $(\vartheta_1, \vartheta_{\text{II}}, \varphi)$

In Sec. 4.3.4 the triple-correlation function and the associated reduced entropy  $S^{(3)}$  were introduced for a spherical cluster shell. To this end, the spatial three-particle distribution within the shell is described in a coordinate system that contains  $\vartheta_1$  as the angular pair distance of the first and the second particle,  $\vartheta_{\text{II}}$  as the angular pair distance of the first and the third particle and  $\varphi$  as the ‘‘bond angle’’ on the sphere. The corresponding coordinate transformation  $\Phi_{\text{TCF}}^{\text{sphere}} : (Q, B) \mapsto (\mathbf{r}_1, \mathbf{r}_2, \mathbf{r}_3)$  is defined by

$$\begin{aligned} \mathbf{r}_1 &= r_1 \cdot \begin{pmatrix} \sin(\vartheta_0) \cos(\varphi_0) \\ \sin(\vartheta_0) \sin(\varphi_0) \\ \cos(\vartheta_0) \end{pmatrix} & \mathbf{r}_2 &= \mathbf{R}_1(\vartheta_0, \varphi_0) r_{\text{II}} \cdot \begin{pmatrix} \sin(\vartheta_1) \cos(\varphi_1) \\ \sin(\vartheta_1) \sin(\varphi_1) \\ \cos(\vartheta_1) \end{pmatrix} \\ \mathbf{r}_3 &= \mathbf{R}_2(\vartheta_0, \varphi_0, \vartheta_1, \varphi_1) r_{\text{III}} \cdot \begin{pmatrix} \sin(\vartheta_{\text{II}}) \cos(\varphi) \\ \sin(\vartheta_{\text{II}}) \sin(\varphi) \\ \cos(\vartheta_{\text{II}}) \end{pmatrix}. \end{aligned} \quad (\text{A.12})$$

Usual spherical coordinates are used to describe the positions of the three particles. The coordinates  $\mathbf{r}_2$  and  $\mathbf{r}_3$  are then rotated by the rotational matrices  $\mathbf{R}_1(\vartheta_0, \varphi_0)$  and  $\mathbf{R}_2(\vartheta_0, \varphi_0, \vartheta_1, \varphi_1)$ . The first matrix rotates the  $z$ -axis for  $\mathbf{r}_2$  into the direction of  $\mathbf{r}_1$ . The polar angle  $\vartheta_1$  of the second position then is the pair angle between the first two positions. The second matrix rotates the  $z$ -axis for  $\mathbf{r}_3$  into the direction of  $\mathbf{r}_1$ , and the  $x$ -axis is oriented along the projection of the pair distance  $\mathbf{r}_{12} = \mathbf{r}_2 - \mathbf{r}_1$  into the plane perpendicular to  $\mathbf{r}_1$  after the rotation. The polar angle  $\vartheta_{\text{II}}$  of the third position then is the pair angle between the first and the third position and azimuth angle is the bond angle. Due to the assumed invariance of the Hamiltonian under rotation, the relevant coordinates for describing the three particle density are  $Q = (r_1, r_{\text{II}}, r_{\text{III}}, \vartheta_1, \vartheta_{\text{II}}, \varphi)$ , whereas the coordinates  $B = (\vartheta_0, \varphi_0, \varphi_1)$  are irrelevant. Focusing on the *intra-shell* configuration, the three radial coordinates are fixed by the radius of the shell  $R_s$ . Again, the explicit form of the rotational matrices is not of interest since only their determinants are important. However the determinant of any rotational matrix equals unity.



The Jacobi matrix of the coordinate transformation from generalized coordinates  $(Q, B)$  to three Cartesian positions has the form

$$\mathcal{J}\Phi_{\text{TCF}}^{\text{sphere}}(r_{\text{I}}, \vartheta_0, \varphi_0, r_{\text{II}}, \vartheta_1, \varphi_1, r_{\text{III}}, \vartheta_{\text{II}}, \varphi) = \begin{pmatrix} \frac{\partial x_1}{\partial r_1} & \frac{\partial x_1}{\partial \vartheta_0} & \frac{\partial x_1}{\partial \varphi_0} & \frac{\partial x_1}{\partial r_{\text{II}}} & \frac{\partial x_1}{\partial \vartheta_1} & \frac{\partial x_1}{\partial \varphi_1} & \frac{\partial x_1}{\partial r_{\text{III}}} & \frac{\partial x_1}{\partial \vartheta_{\text{II}}} & \frac{\partial x_1}{\partial \varphi} \\ \frac{\partial y_1}{\partial r_1} & \ddots & & & & & & & \vdots \\ \frac{\partial z_1}{\partial r_1} & & \ddots & & & & & & \vdots \\ \frac{\partial x_2}{\partial r_1} & & & \ddots & & & & & \vdots \\ \frac{\partial y_2}{\partial r_1} & & & & \ddots & & & & \vdots \\ \frac{\partial z_2}{\partial r_1} & & & & & \ddots & & & \vdots \\ \frac{\partial x_3}{\partial r_1} & & & & & & \ddots & & \vdots \\ \frac{\partial y_3}{\partial r_1} & & & & & & & \ddots & \vdots \\ \frac{\partial z_3}{\partial r_1} & \dots & \dots & \dots & \dots & \dots & \dots & \dots & \frac{\partial z_3}{\partial \varphi} \end{pmatrix}. \quad (\text{A.13})$$

In an analogous way as in the sections above for the center-two-particle and the triple-correlation function in flat systems, this matrix is decomposed into nine different  $3 \times 3$  blocks. Since  $\mathbf{r}_1$  ( $\mathbf{r}_2$ ) depends only on the first three (six) coordinates, the three blocks above the diagonal are all equal zero. The simplified Jacobi matrix reads

$$\mathcal{J}\Phi_{\text{TCF}}^{\text{sphere}} = \begin{pmatrix} \mathcal{J}_1\Phi(r_{\text{I}}, \vartheta_0, \varphi_0) & \mathbf{0} & \mathbf{0} \\ \mathbf{C} & \mathbf{R}_1(\vartheta_0, \varphi_0) \mathcal{J}_2\Phi(r_{\text{II}}, \vartheta_1, \varphi_1) & \mathbf{0} \\ \mathbf{D} & \mathbf{E} & \mathbf{R}_2(\vartheta_0, \varphi_0, \vartheta_1, \varphi_1) \mathcal{J}_3\Phi(r_{\text{III}}, \vartheta_{\text{II}}, \varphi) \end{pmatrix}, \quad (\text{A.14})$$

where  $\mathcal{J}_1$ ,  $\mathcal{J}_2$  and  $\mathcal{J}_3$  are the Jacobi matrices of the transformations from spherical coordinates to Cartesian coordinates of the three positions excluding the rotations by  $\mathbf{R}_1$  and  $\mathbf{R}_2$ .

The Jacobi determinant can now be expressed as the sum of nine products of the determinants of  $3 \times 3$  matrices. Eight of these summands vanish due to the zeros in the upper half and only the product of the diagonal determinants remains,

$$\left| \mathcal{J}\Phi_{\text{TCF}}^{\text{sphere}} \right| = |\mathcal{J}_1\Phi(r_{\text{I}}, \vartheta_0, \varphi_0)| \cdot |\mathbf{R}_1(\vartheta_0, \varphi_0)| \cdot |\mathcal{J}_2\Phi(r_{\text{II}}, \vartheta_1, \varphi_1)| \cdot |\mathbf{R}_2(\vartheta_0, \varphi_0, \vartheta_1, \varphi_1)| \cdot |\mathcal{J}_3\Phi(r_{\text{III}}, \vartheta_{\text{II}}, \varphi)| \quad (\text{A.15})$$

$$= r_{\text{I}}^2 \sin \vartheta_0 \cdot r_{\text{II}}^2 \sin \vartheta_1 \cdot r_{\text{III}}^2 \sin \vartheta_{\text{II}}. \quad (\text{A.16})$$

As above, the well-known results  $|\mathcal{J}\Phi(r, \vartheta, \varphi)| = r^2 \sin \vartheta$  and  $|\mathbf{R}| = 1$  were used for the Jacobi determinant of spherical coordinates and for the determinants of the rotational matrices, respectively.

Note that the first position  $\mathbf{r}_1$  could also be expressed in Cartesian coordinates. In that case, it is readily verified that the first determinant of the product in Eq. (A.15) vanishes and the Jacobi determinant is given by

$$\left| \mathcal{J}\Phi_{\text{TCF}}^{\text{sphere}*}(x_1, y_1, z_1, r_{\text{II}}, \vartheta_1, \varphi_1, r_{\text{III}}, \vartheta_{\text{II}}, \varphi) \right| = r_{\text{II}}^2 \sin \vartheta_1 \cdot r_{\text{III}}^2 \sin \vartheta_{\text{II}}. \quad (\text{A.17})$$

As the spatial factor  $V_3(\vartheta_1, \vartheta_{\text{II}}, \varphi)$  involves the  $\mathbf{r}_1$  integration of  $\left| \mathcal{J}\Phi_{\text{TCF}}^{\text{sphere}} \right|$  over a sphere with radius  $R_s$ , both Eq. (A.16) and Eq. (A.17) yield the same result. It is though appropriate to describe the first position by spherical coordinates because of the symmetry of a spherical shell.

## A.2 Representations of the Entropy in the Canonical Ensemble

There are two definitions of the *entropy*  $S$ . On the one hand, there is the thermodynamic definition as the temperature derivative of the free energy. On the other hand, in statistical mechanics, the entropy is defined via the probabilities of the microstates. The latter definition agrees with SHANNON's understanding of the entropy [166] in units of  $k_{\text{B}}$  and this definition is used in order to introduce a reduced entropy  $S^{(n)}$  for the  $n$ -particle distribution. In order to justify this approach, the equivalence of the two definitions is shown in this section.

In the *canonical ensemble*, the partition function of  $N$  identical particles in 3D at temperature  $T$  given by

$$Z = \frac{1}{(2\pi\hbar)^{3N} N!} \int d^{3N} \mathbf{P} \int d^{3N} \mathbf{R} e^{-\frac{\mathcal{H}(\mathbf{P}, \mathbf{R})}{k_{\text{B}} T}}, \quad (\text{A.18})$$

where  $\mathcal{H}$  is the Hamiltonian of the system. The Hamiltonian is a function of the momenta  $\mathbf{P} = (\mathbf{p}_1, \dots, \mathbf{p}_N)$  and the positions  $\mathbf{R} = (\mathbf{r}_1, \dots, \mathbf{r}_N)$  of all particles. The entropy  $S$  can be written as temperature derivative of the partition function as,

$$S = - \left( \frac{\partial F}{\partial T} \right)_{V, N} = k_{\text{B}} \left[ \frac{\partial}{\partial T} (T \log Z) \right]_{V, N} \quad (\text{A.19})$$

$$\begin{aligned} &= k_{\text{B}} T \frac{1}{k_{\text{B}} T^2} \frac{1}{Z} \frac{1}{(2\pi\hbar)^{3N} N!} \int d^{3N} \mathbf{P} \int d^{3N} \mathbf{R} \mathcal{H}(\mathbf{P}, \mathbf{R}) e^{-\frac{\mathcal{H}(\mathbf{P}, \mathbf{R})}{k_{\text{B}} T}} + k_{\text{B}} \log(Z) \\ &= \frac{1}{T} \frac{1}{Z} \frac{1}{(2\pi\hbar)^{3N} N!} \int d^{3N} \mathbf{P} \int d^{3N} \mathbf{R} \mathcal{H}(\mathbf{P}, \mathbf{R}) e^{-\frac{\mathcal{H}(\mathbf{P}, \mathbf{R})}{k_{\text{B}} T}} + k_{\text{B}} \log(Z). \end{aligned} \quad (\text{A.20})$$

This expression is compared with the *information entropy* in units of  $k_B$  of the probability distribution  $\mathcal{P}_i$  of the microstates  $i$ ,

$$S = -k_B \sum_i \mathcal{P}_i \log(\mathcal{P}_i) \quad (\text{A.21})$$

$$\begin{aligned} &= -k_B \frac{1}{N!} \int d^{3N} \mathbf{P} \int d^{3N} \mathbf{R} \mathcal{P}_N(\mathbf{P}, \mathbf{R}) \log \{ \mathcal{P}_N(\mathbf{P}, \mathbf{R}) \} \\ &= -k_B \frac{1}{(2\pi\hbar)^{3N} N!} \int d^{3N} \mathbf{P} \int d^{3N} \mathbf{R} \frac{1}{Z} e^{-\frac{\mathcal{H}(\mathbf{P}, \mathbf{R})}{k_B T}} \log \left\{ \frac{1}{Z} e^{-\frac{\mathcal{H}(\mathbf{P}, \mathbf{R})}{k_B T}} \right\} \end{aligned} \quad (\text{A.22})$$

$$\begin{aligned} &= k_B \frac{1}{(2\pi\hbar)^{3N} N!} \int d^{3N} \mathbf{P} \int d^{3N} \mathbf{R} \frac{1}{Z} e^{-\frac{\mathcal{H}(\mathbf{P}, \mathbf{R})}{k_B T}} \frac{\mathcal{H}(\mathbf{P}, \mathbf{R})}{k_B T} \\ &\quad + \log(Z) \underbrace{\frac{1}{Z} k_B \frac{1}{(2\pi\hbar)^{3N} N!} \int d^{3N} \mathbf{P} \int d^{3N} \mathbf{R} e^{-\frac{\mathcal{H}(\mathbf{P}, \mathbf{R})}{k_B T}}}_{=Z} \\ &= \frac{1}{T} \frac{1}{Z} \frac{1}{(2\pi\hbar)^{3N} N!} \int d^{3N} \mathbf{P} \int d^{3N} \mathbf{R} \mathcal{H}(\mathbf{P}, \mathbf{R}) e^{-\frac{\mathcal{H}(\mathbf{P}, \mathbf{R})}{k_B T}} + k_B \log(Z), \end{aligned} \quad (\text{A.23})$$

and it is found that both the thermodynamic expression, Eq. (A.19), and the statistical definition, Eq. (A.21), of the entropy are equivalent. In the two steps between Eqs. (A.21) and (A.22), the discrete probability  $\mathcal{P}_i$  of a  $N$ -particle microstate was expressed as

$$\mathcal{P}_i = \mathcal{P}(\mathbf{P}_i, \mathbf{R}_i) = \frac{1}{Z} e^{-\frac{\mathcal{H}(\mathbf{P}_i, \mathbf{R}_i)}{k_B T}}, \quad (\text{A.24})$$

which was then converted to a continuous probability distribution  $\mathcal{P}_N(\mathbf{P}, \mathbf{R})$  via the division by the phase-space volume  $(2\pi\hbar)^{3N}$  of the  $N$ -particle microstate,

$$\mathcal{P}_N(\mathbf{P}, \mathbf{R}) = \frac{1}{(2\pi\hbar)^{3N}} \frac{1}{Z} e^{-\frac{\mathcal{H}(\mathbf{P}, \mathbf{R})}{k_B T}}. \quad (\text{A.25})$$

The discrete probability  $\mathcal{P}_i$  of a microstate  $i$  can then be interpreted as the integral of the continuous probability distribution  $\mathcal{P}_N(\mathbf{P}, \mathbf{R})$  over the  $6N$  dimensional phase-space box centered around  $(\mathbf{P}_i, \mathbf{R}_i)$  which has the volume  $(2\pi\hbar)^{3N}$ . The multiple counting of identical microstates as permutations of the particle coordinates is compensated by the *Gibbs factor*  $1/N!$ .

### A.3 Splitting the Entropy into Momentum and Spatial Contributions

Throughout the derivation of reduced entropies  $S^{(n)}$  from the full  $N$ -particle distribution, there is always considered the spatial contribution only. This approach is justified if the momentum part of the Hamiltonian is given by the sum of the squared momenta of all individual particles. For this case, the phase-space probability distribution can be factorized into a spatial and a momentum contribution where the latter one has a closed analytic form.

Using the factorization of  $\mathcal{P}_N(\mathbf{P}, \mathbf{R})$ , Eq. (4.18), the expression for the entropy  $S$  is as well split as follows,

$$\begin{aligned}
S &= -\frac{k_B}{N!} \int d^{3N} \mathbf{P} \int d^{3N} \mathbf{R} \mathcal{P}_N(\mathbf{P}, \mathbf{R}) \log \left\{ (2\pi\hbar)^{3N} \mathcal{P}_N(\mathbf{P}, \mathbf{R}) \right\} \\
&= -\frac{k_B}{N!} \int d^{3N} \mathbf{P} \int d^{3N} \mathbf{R} f_N(\mathbf{P}) \cdot \rho_N(\mathbf{R}) \log \left\{ (2\pi\hbar)^{3N} f_N(\mathbf{P}) \cdot \rho_N(\mathbf{R}) \right\} \\
&= -\frac{k_B}{N!} \frac{1}{(2\pi m k_B T)^{3N/2}} \frac{1}{Z_R} \int d^{3N} \mathbf{P} \int d^{3N} \mathbf{R} e^{-\beta \mathcal{H}_P(\mathbf{P})} \cdot e^{-\beta \mathcal{H}_R(\mathbf{R})} \\
&\quad \times \log \left\{ \frac{(2\pi\hbar)^{3N}}{(2\pi m k_B T)^{3N/2}} \frac{1}{Z_R} e^{-\beta \mathcal{H}_P(\mathbf{P})} \cdot e^{-\beta \mathcal{H}_R(\mathbf{R})} \right\}. \tag{A.26}
\end{aligned}$$

Splitting the logarithm and using the thermal de Broglie wavelength  $\lambda_{\text{DB}} = \left( \frac{2\pi\hbar^2}{m k_B T} \right)^{1/2}$ , the entropy  $S$  can be expressed by

$$\begin{aligned}
S &= k_B \log \left\{ \frac{Z_R}{\lambda_{\text{DB}}^{3N}} \right\} \\
&\quad - \frac{k_B}{N! Z_R} \left( \frac{\lambda_{\text{DB}}}{2\pi\hbar} \right)^{3N} \int d^{3N} \mathbf{P} \int d^{3N} \mathbf{R} e^{-\beta \mathcal{H}_P(\mathbf{P})} \cdot e^{-\beta \mathcal{H}_R(\mathbf{R})} \log \left\{ e^{-\beta \mathcal{H}_P(\mathbf{P})} \right\} \\
&\quad - \frac{k_B}{N! Z_R} \left( \frac{\lambda_{\text{DB}}}{2\pi\hbar} \right)^{3N} \int d^{3N} \mathbf{P} \int d^{3N} \mathbf{R} e^{-\beta \mathcal{H}_P(\mathbf{P})} \cdot e^{-\beta \mathcal{H}_R(\mathbf{R})} \log \left\{ e^{-\beta \mathcal{H}_R(\mathbf{R})} \right\} \\
&= k_B \log \left\{ \frac{Z_R}{\lambda_{\text{DB}}^{3N}} \right\} \\
&\quad - \frac{k_B}{N! Z_R} \left( \frac{\lambda_{\text{DB}}}{2\pi\hbar} \right)^{3N} \underbrace{\left( \int d^{3N} \mathbf{R} e^{-\beta \mathcal{H}_R(\mathbf{R})} \right)}_{=N! Z_R} \int d^{3N} \mathbf{P} (-\beta \mathcal{H}_P(\mathbf{P})) \cdot e^{-\beta \mathcal{H}_P(\mathbf{P})} \\
&\quad - \frac{k_B}{N! Z_R} \left( \frac{\lambda_{\text{DB}}}{2\pi\hbar} \right)^{3N} \underbrace{\left( \int d^{3N} \mathbf{P} e^{-\beta \mathcal{H}_P(\mathbf{P})} \right)}_{=\left(\frac{2\pi\hbar}{\lambda_{\text{DB}}}\right)^{3N}} \int d^{3N} \mathbf{R} (-\beta \mathcal{H}_R(\mathbf{R})) \cdot e^{-\beta \mathcal{H}_R(\mathbf{R})} \\
&= k_B \log \left\{ \frac{Z_R}{\lambda_{\text{DB}}^{3N}} \right\} - k_B \left( \frac{\lambda_{\text{DB}}}{2\pi\hbar} \right)^{3N} \int d^{3N} \mathbf{P} (-\beta \mathcal{H}_P(\mathbf{P})) \cdot e^{-\beta \mathcal{H}_P(\mathbf{P})} \\
&\quad - \frac{k_B}{N! Z_R} \int d^{3N} \mathbf{R} (-\beta \mathcal{H}_R(\mathbf{R})) \cdot e^{-\beta \mathcal{H}_R(\mathbf{R})}. \tag{A.27}
\end{aligned}$$

The second summand is solved analytically in an auxiliary calculation as

$$\begin{aligned}
I_2 &= k_B \left( \frac{\lambda_{\text{DB}}}{2\pi\hbar} \right)^{3N} \int d^{3N} \mathbf{P} (-\beta \mathcal{H}_P(\mathbf{P})) \cdot e^{-\beta \mathcal{H}_P(\mathbf{P})} \\
&= k_B \left( \frac{\lambda_{\text{DB}}}{2\pi\hbar} \right)^{3N} \int d^3 \mathbf{p}_1 \dots \int d^3 \mathbf{p}_N \frac{-\beta}{2m} \sum_{i=1}^N \sum_{\alpha=1}^3 p_{i,\alpha}^2 \cdot \prod_{j=1}^N \prod_{\beta=1}^3 e^{-\beta \frac{p_{j,\beta}^2}{2m}} \\
&= k_B \left( \frac{\lambda_{\text{DB}}}{2\pi\hbar} \right)^{3N} \frac{-\beta}{2m} \sum_{i=1}^N \sum_{\alpha=1}^3 \int_{-\infty}^{\infty} dp_{i,\alpha} p_{i,\alpha}^2 \cdot e^{-\beta \frac{p_{i,\alpha}^2}{2m}} \cdot \int d^{3N-1} \mathbf{P}^* \prod_{j=1}^N \prod_{\beta=1}^3 e^{-\beta \frac{p_{j,\beta}^2}{2m}}. \quad (\text{A.28})
\end{aligned}$$

The Latin indices  $i$  and  $j$  count the particles, while the Greek indices  $\alpha$  and  $\beta$  correspond to the spatial direction. The \*-symbols at the momentum vector  $\mathbf{P}^*$  and the product symbol  $\prod^*$  mean that they contain all momenta except for the  $\alpha$ -th component of the  $i$ -th particle. The multi-dimensional momentum integral in Eq. (A.28) is factorized into a product of one-dimensional integrals which are solved analytically in the following,

$$\begin{aligned}
I_2 &= k_B \left( \frac{\lambda_{\text{DB}}}{2\pi\hbar} \right)^{3N} \frac{-\beta}{2m} \cdot 3N \int_{-\infty}^{\infty} dp p^2 \cdot e^{-\beta \frac{p^2}{2m}} \cdot \left[ \int_{-\infty}^{\infty} dp e^{-\beta \frac{p^2}{2m}} \right]^{3N-1} \\
&= k_B \left( \frac{\lambda_{\text{DB}}}{2\pi\hbar} \right)^{3N} \frac{-\beta}{2m} \cdot 3N \cdot \sqrt{2\pi} \cdot \sqrt{mk_B T}^3 \cdot \sqrt{2\pi mk_B T}^{3N-1} \\
&= -k_B \left( \frac{\lambda_{\text{DB}}}{2\pi\hbar} \right)^{3N} \frac{3N}{2} \frac{1}{\sqrt{2\pi mk_B T}^2} \cdot \sqrt{2\pi mk_B T}^{3N+2} \\
&= -k_B \left( \frac{\lambda_{\text{DB}}}{2\pi\hbar} \right)^{3N} \frac{3N}{2} \left( \frac{2\pi\hbar}{\lambda_{\text{DB}}} \right)^{3N} \\
&= -\frac{3}{2} N k_B. \quad (\text{A.29})
\end{aligned}$$

Throughout the simplification of  $I_2$ , the Gaussian integrals

$$\int_{-\infty}^{\infty} e^{-\frac{1}{2} \frac{x^2}{\sigma^2}} dx = \sqrt{2\pi} \sigma \quad \text{and} \quad \int_{-\infty}^{\infty} x^2 \cdot e^{-\frac{1}{2} \frac{x^2}{\sigma^2}} dx = \sqrt{2\pi} \sigma^3, \quad (\text{A.30})$$

were used, where the width of the Gaussian is  $\sigma = \sqrt{m/\beta} = \sqrt{mk_B T}$ . The expression from Eq. (A.29) is now entered for the second summand in Eq. (A.27) and the final result for the entropy is

$$\begin{aligned}
S &= k_B \log \left\{ \frac{Z_R}{\lambda_{\text{DB}}^{3N}} \right\} + k_B \frac{3N}{2} - \frac{k_B}{N! Z_R} \int d^{3N} \mathbf{R} (-\beta \mathcal{H}_R(\mathbf{R})) \cdot e^{-\beta \mathcal{H}_R(\mathbf{R})} \\
&= k_B \cdot \frac{3N}{2} - 3N k_B \log \lambda_{\text{DB}} - \frac{k_B}{N! Z_R} \int d^{3N} \mathbf{R} \log \left\{ \frac{1}{Z_R} e^{-\beta \mathcal{H}_R(\mathbf{R})} \right\} \cdot e^{-\beta \mathcal{H}_R(\mathbf{R})} \quad (\text{A.31})
\end{aligned}$$

$$= 3N k_B \left( \frac{1}{2} - \log \lambda_{\text{DB}} \right) - \frac{k_B}{N! Z_R} \int d^{3N} \mathbf{R} \log \left\{ \frac{1}{Z_R} e^{-\beta \mathcal{H}_R(\mathbf{R})} \right\} \cdot e^{-\beta \mathcal{H}_R(\mathbf{R})}. \quad (\text{A.32})$$

Here, two dimension afflicted arguments occur under the logarithms for the momentum part (second summand) and for the spatial part (third summand). This problem can be solved by introducing an *arbitrary length scale*  $\Delta l$  in both logarithms in Eq. (A.31).

$$\begin{aligned}
S &= k_B \cdot \frac{3N}{2} - 3Nk_B \log \left( \frac{\lambda_{\text{DB}}}{\Delta l} \right) - \frac{k_B}{N!Z_R} \int d^{3N} \mathbf{R} \log \left\{ \frac{\Delta l^{3N}}{Z_R} e^{-\beta \mathcal{H}_R(\mathbf{R})} \right\} \cdot e^{-\beta \mathcal{H}_R(\mathbf{R})} \\
&\quad + 3Nk_B \log \Delta l - \underbrace{\frac{k_B}{N!Z_R} \int d^{3N} \mathbf{R} e^{-\beta \mathcal{H}_R(\mathbf{R})} \cdot \log \Delta l^{3N}}_{=N!Z_R} \\
&= k_B \cdot \frac{3N}{2} - 3Nk_B \log \left( \frac{\lambda_{\text{DB}}}{\Delta l} \right) - \frac{k_B}{N!Z_R} \int d^{3N} \mathbf{R} \log \left\{ \frac{\Delta l^{3N}}{Z_R} e^{-\beta \mathcal{H}_R(\mathbf{R})} \right\} \cdot e^{-\beta \mathcal{H}_R(\mathbf{R})} \\
&\quad + 3Nk_B \log \Delta l - 3Nk_B \log \Delta l \\
&= k_B \cdot \frac{3N}{2} - 3Nk_B \log \left( \frac{\lambda_{\text{DB}}}{\Delta l} \right) - \frac{k_B}{N!Z_R} \int d^{3N} \mathbf{R} \log \left\{ \frac{\Delta l^{3N}}{Z_R} e^{-\beta \mathcal{H}_R(\mathbf{R})} \right\} \cdot e^{-\beta \mathcal{H}_R(\mathbf{R})} \\
&= k_B \cdot \frac{3N}{2} \underbrace{- 3Nk_B \log \left( \frac{\lambda_{\text{DB}}}{\Delta l} \right)}_{:=S_P} \underbrace{- \frac{k_B}{N!} \int d^{3N} \mathbf{R} \log \{ \Delta l^{3N} \cdot \rho_N(\mathbf{R}) \} \cdot \rho_N(\mathbf{R})}_{:=S_R}, \quad (\text{A.33})
\end{aligned}$$

where each of the two logarithms has a dimensionless argument. Splitting of the entropy into a momentum part  $S_P$  and a spatial part  $S_R$  is unambiguous except for the offset due to the ambiguous definition of the length scale  $\Delta l$ . However, the length scale  $\Delta l$  does not affect the physically relevant total entropy. Since the offset is constant, both temperature dependencies of  $S_P$  and  $S_R$  are not affected by the choice of  $\Delta l$ . In fact, the temperature dependencies of  $S_P$  and  $S_R$  are usually of higher interest than the absolute values of the entropies.

Note that the derivation is analogous for 2D systems. The result is the same except for the replacement  $3N \mapsto 2N$  in Eq. (A.33).

## A.4 Calculation of the Reduced Entropy from Sampled Histograms

The spatial  $n$ -particle probability density  $\tilde{\rho}_n(Q)$  in the relevant generalized coordinates  $Q = \{q_1, \dots, q_\alpha\}$  with the dimension  $\alpha$  is sampled in computer simulations or from experimental data. When sampling a histogram with bin widths  $\Delta q_1, \dots, \Delta q_\alpha$ , the result is an  $\alpha$ -dimensional array of counts  $h[i_{q_1}, \dots, i_{q_\alpha}]$ . From the normalization of spatial the  $N$ -particle distribution function

$$1 = \frac{1}{N!} \int d^{3N} \mathbf{R} \rho(\mathbf{R}) \quad (\text{A.34})$$

and the definition in Eq. (4.22), the normalization of the  $n$ -particle spatial probability distribution follows as

$$\begin{aligned}
1 &= \frac{(N-n)!}{N!} \int d^3\mathbf{r}_1 \dots \int d^3\mathbf{r}_n \rho_n(\mathbf{r}_1, \dots, \mathbf{r}_n) \\
&= \frac{(N-n)!}{N!} \int dq_1 \dots \int dq_\alpha \underbrace{\tilde{\rho}_n(q_1, \dots, q_\alpha)}_{=\tilde{\rho}_n(Q)}. \tag{A.35}
\end{aligned}$$

Examples: Considering the one-particle density and the pair-density as two examples, these are normalized by,

$$\int d^3\mathbf{r}_1 \rho_1(\mathbf{r}_1) = N, \tag{A.36}$$

$$\int d^3\mathbf{r}_1 \int d^3\mathbf{r}_2 \rho_2(\mathbf{r}_1, \mathbf{r}_2) = N \cdot (N-1), \tag{A.37}$$

as the number of particles and to the number of particle pairs, respectively.

The normalization, Eq. (A.35), has to be fulfilled also for the normalized histogram counts  $\tilde{h}[i_{q_1}, \dots, i_{q_\alpha}]$ , where the integral over  $q_1, \dots, q_\alpha$  is split up into the  $\alpha$ -dimensional sum over small integrals. The small integral over the volume, that corresponds to a histogram box, can be identified as the histogram counts  $\tilde{h}$ . Hence, the normalization of these histogram counts is given by

$$1 = \frac{(N-n)!}{N!} \int dq_1 \dots \int dq_\alpha \tilde{\rho}_n(q_1, \dots, q_\alpha) \tag{A.38}$$

$$\Leftrightarrow 1 = \frac{(N-n)!}{N!} \sum_{i_{q_1}=1}^{N_{q_1}^{\text{bin}}} \dots \sum_{i_{q_\alpha}=1}^{N_{q_\alpha}^{\text{bin}}} \underbrace{\left( \int_{i_{q_1}\Delta_{q_1}}^{(i_{q_1}+1)\Delta_{q_1}} dq_1 \dots \int_{i_{q_\alpha}\Delta_{q_\alpha}}^{(i_{q_\alpha}+1)\Delta_{q_\alpha}} dq_\alpha \tilde{\rho}_n(q_1, \dots, q_\alpha) \right)}_{=\tilde{h}[i_{q_1}, \dots, i_{q_\alpha}]}$$

$$\Leftrightarrow 1 = \frac{(N-n)}{N!} \sum_{i_{q_1}=1}^{N_{q_1}^{\text{bin}}} \dots \sum_{i_{q_\alpha}=1}^{N_{q_\alpha}^{\text{bin}}} \tilde{h}[i_{q_1}, \dots, i_{q_\alpha}]. \tag{A.39}$$

The normalization factor  $\frac{N!}{(N-n)!}$  is the number of  $n$ -particle pairs. In order to calculate the information entropy  $S^{(n)}$  from the sampled histogram, the integral in Eq. (4.50) is decomposed

the analogous way as in Eq. (A.38),

$$\begin{aligned}
S^{(n)} &= -k_B \frac{(N-n)!}{N!} \int d^\alpha Q \tilde{\rho}_n(Q) \log \left\{ \Delta l^{3n} \frac{\tilde{\rho}_n(Q)}{V_n(Q)} \right\} \\
&= -k_B \frac{(N-n)!}{N!} \sum_{i_{q_1}=1}^{N_{q_1}^{\text{bin}}} \cdots \sum_{i_{q_\alpha}=1}^{N_{q_\alpha}^{\text{bin}}} \\
&\quad \left( \int_{i_{q_1} \Delta_{q_1}}^{(i_{q_1}+1)\Delta_{q_1}} dq_1 \cdots \int_{i_{q_\alpha} \Delta_{q_\alpha}}^{(i_{q_\alpha}+1)\Delta_{q_\alpha}} dq_\alpha \tilde{\rho}_n(Q) \log \left\{ \Delta l^{3n} \frac{\tilde{\rho}_n(Q)}{V_n(Q)} \right\} \right) \\
&\approx -k_B \frac{(N-n)!}{N!} \sum_{i_{q_1}=1}^{N_{q_1}^{\text{bin}}} \cdots \sum_{i_{q_\alpha}=1}^{N_{q_\alpha}^{\text{bin}}} \left( \int_{i_{q_1} \Delta_{q_1}}^{(i_{q_1}+1)\Delta_{q_1}} dq_1 \cdots \int_{i_{q_\alpha} \Delta_{q_\alpha}}^{(i_{q_\alpha}+1)\Delta_{q_\alpha}} dq_\alpha \right. \\
&\quad \left. \tilde{\rho}_n(Q) \log \left\{ \Delta l^{3n} \frac{\tilde{\rho}_n[i_{q_1}, \dots, i_{q_\alpha}]}{V_n[i_{q_1}, \dots, i_{q_\alpha}]} \right\} \right). \tag{A.40}
\end{aligned}$$

In the last step, there were introduced the average  $n$ -particle density of a histogram box

$$\tilde{\rho}_n[i_{q_1}, \dots, i_{q_\alpha}] = \frac{1}{\Delta_{q_1} \cdots \Delta_{q_\alpha}} \underbrace{\int_{i_{q_1} \Delta_{q_1}}^{(i_{q_1}+1)\Delta_{q_1}} dq_1 \cdots \int_{i_{q_\alpha} \Delta_{q_\alpha}}^{(i_{q_\alpha}+1)\Delta_{q_\alpha}} dq_\alpha \tilde{\rho}_n(Q)}_{=\tilde{h}[i_{q_1}, \dots, i_{q_\alpha}]} \tag{A.41}$$

and the average geometric factor of a histogram box

$$\begin{aligned}
V_n[i_{q_1}, \dots, i_{q_\alpha}] &= \frac{1}{\Delta_{q_1} \cdots \Delta_{q_\alpha}} \int_{i_{q_1} \Delta_{q_1}}^{(i_{q_1}+1)\Delta_{q_1}} dq_1 \cdots \int_{i_{q_\alpha} \Delta_{q_\alpha}}^{(i_{q_\alpha}+1)\Delta_{q_\alpha}} dq_\alpha V_n(Q) \\
&= \frac{1}{\Delta_{q_1} \cdots \Delta_{q_\alpha}} \\
&\quad \cdot \underbrace{\int_{i_{q_1} \Delta_{q_1}}^{(i_{q_1}+1)\Delta_{q_1}} dq_1 \cdots \int_{i_{q_\alpha} \Delta_{q_\alpha}}^{(i_{q_\alpha}+1)\Delta_{q_\alpha}} dq_\alpha \int db_1 \cdots \int db_\beta |\mathcal{J}\Phi(Q, B)|}_{=\tilde{u}[i_{q_1}, \dots, i_{q_\alpha}]}, \tag{A.42}
\end{aligned}$$

as an approximation. In Eq. (A.40), the ratio of the averages  $\tilde{\rho}_n[i_{q_1}, \dots, i_{q_\alpha}]/V_n[i_{q_1}, \dots, i_{q_\alpha}]$  is replaced by  $\tilde{h}[i_{q_1}, \dots, i_{q_\alpha}]/\tilde{u}[i_{q_1}, \dots, i_{q_\alpha}]$  since the common factor  $\Delta_{q_1} \cdots \Delta_{q_\alpha}$  cancels. The



reduced entropy  $S^{(n)}$ , Eq. (A.40), can therefore be rewritten as

$$\begin{aligned}
S^{(n)} &\approx -k_B \frac{(N-n)!}{N!} \sum_{i_{q_1}=1}^{N_{q_1}^{\text{bin}}} \cdots \sum_{i_{q_\alpha}=1}^{N_{q_\alpha}^{\text{bin}}} \\
&\quad \left( \int_{i_{q_1} \Delta_{q_1}}^{(i_{q_1}+1)\Delta_{q_1}} dq_1 \cdots \int_{i_{q_\alpha} \Delta_{q_\alpha}}^{(i_{q_\alpha}+1)\Delta_{q_\alpha}} dq_\alpha \tilde{\rho}_n(Q) \log \left\{ \Delta l^{3n} \frac{\tilde{h}[i_{q_1}, \dots, i_{q_\alpha}]}{\tilde{u}[i_{q_1}, \dots, i_{q_\alpha}]} \right\} \right) \\
&= -k_B \frac{(N-n)!}{N!} \sum_{i_{q_1}=1}^{N_{q_1}^{\text{bin}}} \cdots \sum_{i_{q_\alpha}=1}^{N_{q_\alpha}^{\text{bin}}} \log \left\{ \Delta l^{3n} \frac{\tilde{h}[i_{q_1}, \dots, i_{q_\alpha}]}{\tilde{u}[i_{q_1}, \dots, i_{q_\alpha}]} \right\} \\
&\quad \cdot \underbrace{\left( \int_{i_{q_1} \Delta_{q_1}}^{(i_{q_1}+1)\Delta_{q_1}} dq_1 \cdots \int_{i_{q_\alpha} \Delta_{q_\alpha}}^{(i_{q_\alpha}+1)\Delta_{q_\alpha}} dq_\alpha \tilde{\rho}_n(Q) \right)}_{=\tilde{h}[i_{q_1}, \dots, i_{q_\alpha}]} \\
&= -k_B \frac{(N-n)!}{N!} \sum_{i_{q_1}=1}^{N_{q_1}^{\text{bin}}} \cdots \sum_{i_{q_\alpha}=1}^{N_{q_\alpha}^{\text{bin}}} \tilde{h}[i_{q_1}, \dots, i_{q_\alpha}] \cdot \log \left\{ \Delta l^{3n} \frac{\tilde{h}[i_{q_1}, \dots, i_{q_\alpha}]}{\tilde{u}[i_{q_1}, \dots, i_{q_\alpha}]} \right\}. \tag{A.43}
\end{aligned}$$

In Eq. (A.40), the ratio  $\tilde{\rho}_n(Q)/V_n(Q)$  was approximated by the ratio of the individual averages of  $\tilde{\rho}_n(Q)$  and  $V_n(Q)$  for each histogram box. Since the ratio  $\tilde{\rho}_n/V_n$  represents the spatial  $n$ -particle density with the dimension ‘‘one over volume to the power of  $n$ ’’, the approximation requires the resolution of the  $Q$  to be sufficient to resolve the variations of that density. For such a sufficient resolution, the  $n$ -particle density can be treated as constant over each single histogram bin. The result becomes exact in the limit of infinitesimal bin sizes. However, the total number of bins is limited due to computational and memory capacities. Moreover, decreasing the bin sizes increases the number of configurations which have to be sampled in order to obtain sufficient statistics. The quality of the approximation that the spatial density is constant over a histogram bin is again dependent on the choice of the generalized coordinates  $Q$ .

#### A.4.1 Example: Entropy of a Discrete Multi-Dimensional Probability Distribution

This section points out a few important properties of the entropy  $S$  of a multi-dimensional probability distribution. The goal is to make up a concrete understanding of the entropy  $S$  and its statements about the underlying probability distribution  $\mathcal{P}$ . Certain very simple discrete probability distributions serve as examples for this purpose. A well-written introduction to the concept of information entropy is given by SHANNON in his work published in 1948 [166].

In the three examples (a), (b), and (c) considered here, both random variables  $x$  and  $y$  can take values from  $\{1, 2, 3\}$ . The probabilities  $\mathcal{P}(x, y)$  are given by the matrices which are shown in Tab. A.1. The single-variable probability distributions follow from the full probability

(a) product	(b) non-product	(c) non-product
-------------	-----------------	-----------------

		$\mathcal{P}(x)$		
		1/2	1/4	1/4
$\mathcal{P}(y)$	$\mathcal{P}(x, y)$	$x = 1$	$x = 2$	$x = 3$
	$y = 1$	1/4	1/8	1/8
	$y = 2$	1/8	1/16	1/16
	$y = 3$	1/8	1/16	1/16

		$\mathcal{P}(x)$		
		1/2	1/4	1/4
$\mathcal{P}(y)$	$\mathcal{P}(x, y)$	$x = 1$	$x = 2$	$x = 3$
	$y = 1$	1/2	0	0
	$y = 2$	0	1/4	0
	$y = 3$	0	0	1/4

		$\mathcal{P}(x)$		
		1/2	1/4	1/4
$\mathcal{P}(y)$	$\mathcal{P}(x, y)$	$x = 1$	$x = 2$	$x = 3$
	$y = 1$	1/4	1/8	1/8
	$y = 2$	1/8	1/8	0
	$y = 3$	1/8	0	1/8

**Table A.1:** Three examples for a two-dimensional discrete probability distribution. The white matrix shows the joint probability for both random variables  $x$  and  $y$ . In the upper gray row, the probability of the variable  $x$  is obtained by the summation over all values of  $y$ . The probability of the variable  $y$  is obtained by summation over all values of  $x$  in the gray left column, analogously. All three examples are symmetric in the two variables.

distribution  $\mathcal{P}(x, y)$  by summation,

$$\mathcal{P}(x) = \sum_y \mathcal{P}(x, y), \quad \text{and} \quad \mathcal{P}(y) = \sum_x \mathcal{P}(x, y). \quad (\text{A.44})$$

In each of the three examples, can now calculate the information entropy  $S^{xy}$  for the joint probability  $\mathcal{P}(x, y)$  and the information entropies  $S^x$  and  $S^y$  for the single-variable probability distributions  $\mathcal{P}(x)$  and  $\mathcal{P}(y)$ , respectively. For practical reasons, the *binary logarithm*  $\text{lb } x = \log_2 x$  is applied which results in rational values for powers of 2 as its argument.

Example (a)-(c)

$$S^x = S^y = -\frac{1}{2} \cdot \text{lb } \frac{1}{2} + 2 \cdot \frac{1}{4} \cdot \text{lb } \frac{1}{4} = \frac{1}{2} \cdot 1 + \frac{1}{2} \cdot 2 = 1.5 \quad (\text{A.45})$$

Example (a):

$$\begin{aligned} S_a^{xy} &= -\frac{1}{4} \cdot \text{lb } \frac{1}{4} - 4 \cdot \frac{1}{8} \cdot \text{lb } \frac{1}{8} - 4 \cdot \frac{1}{16} \cdot \text{lb } \frac{1}{16} = \frac{1}{4} \cdot 2 + \frac{1}{2} \cdot 3 + \frac{1}{4} \cdot 4 \\ &= 3 \end{aligned} \quad (\text{A.46})$$

Example (b):

$$\begin{aligned} S_b^{xy} &= -\frac{1}{2} \cdot \text{lb } \frac{1}{2} + 2 \cdot \frac{1}{4} \cdot \text{lb } \frac{1}{4} = \frac{1}{2} \cdot 1 + \frac{1}{2} \cdot 2 \\ &= 1.5 \end{aligned} \quad (\text{A.47})$$

Example (c):

$$\begin{aligned} S_c^{xy} &= -\frac{1}{4} \cdot \text{lb} \frac{1}{4} - 6 \cdot \frac{1}{8} \cdot \text{lb} \frac{1}{8} = \frac{1}{4} \cdot 2 + \frac{3}{4} \cdot 3 \\ &= 2.75 \end{aligned} \tag{A.48}$$

Since the single random variables  $x$  and  $y$  have the same probability distributions  $\mathcal{P}(x)$  and  $\mathcal{P}(y)$  in all three examples (a)-(c), the single-variable entropies are  $S^x = S^y = 1.5$  in all these examples. In example (a), both random variables  $x$  and  $y$  are statistically independent, i.e. their joint probability is given by the product of the single probabilities. Hence, measuring the variable  $x$  provides no information about variable  $y$ . In other words, the uncertainty about the latter remains the same regardless of the first measurement. For this reason, the joint entropy is  $S_a^{xy} = S^x + S^y = 3$ .

In example (b), however, the knowledge of the variable  $x$  includes the certain knowledge of variable  $y$ , since only pairs with  $x = y$  are possible in this example. When  $x$  is known, there is no further uncertainty about  $y$  and the measurement of the latter variable provides no addition information. Hence, the joint entropy is equal the single-variable entropy  $S_b^{xy} = S^x = S^y = 1.5$ .

In the last example (c), both variables are not statistically independent but, in contrast to example (b), some uncertainty about the variable  $y$  remains when  $x$  is known. This uncertainty is however smaller than it was without the knowledge about  $x$ . As a consequence, the joint entropy  $S_c^{xy} = 2.75$  is below  $S_a^{xy} = 3$  in the fully uncorrelated example but above  $S_b^{xy} = 1.5$  in the fully correlated example.

Interestingly, the calculation of  $S^x$  is sufficient for both the fully uncorrelated probability distribution as in example (a) and in the fully correlated probability distribution as in example (b). In the former case the joint entropy is obtained as  $S^{xy} = 2 \cdot S^x$  and in the latter case is directly given by  $S^{xy} = S^x$ . Only a partially correlated joint probability distribution as sketched in example (b) does not allow for a determination of the joint entry  $S^{xy}$  from the single-variable entropy  $S^x$ .

The correlation of both random variables is connected to the *conditional probability*  $\mathcal{P}_x(y)$  or vice versa  $\mathcal{P}_y(x)$ . The condition probability  $\mathcal{P}_x(y)$  describes the probability distribution of the random variable  $y$  when the value of the random variable  $x$  is known,

$$\mathcal{P}_x(y) = \frac{\mathcal{P}(x, y)}{\sum_y \mathcal{P}(x, y)} = \frac{\mathcal{P}(x, y)}{\mathcal{P}(x)} \quad \Leftrightarrow \quad \mathcal{P}(x, y) = \mathcal{P}(x) \cdot \mathcal{P}_x(y) . \tag{A.49}$$

and the *conditional entropy*  $S_x^y$  is given by

$$S_x^y = - \sum_x \mathcal{P}(x) \sum_y \mathcal{P}_x(y) \text{lb} \mathcal{P}_x(y) = - \sum_{x,y} \mathcal{P}(x, y) \text{lb} \mathcal{P}_x(y) . \tag{A.50}$$

		(a) product			(b) non-product			(c) non-product					
$\mathcal{P}(y)$	$\mathcal{P}(x)$	1/2	1/4	1/4	$\mathcal{P}(x)$	1/2	1/4	1/4	$\mathcal{P}(x)$	1/2	1/4	1/4	
	$\mathcal{P}(x,y)$	x = 1	x = 2	x = 3	$\mathcal{P}(x,y)$	x = 1	x = 2	x = 3	$\mathcal{P}(x,y)$	x = 1	x = 2	x = 3	
1/2	y = 1	1/4	1/2	1/8	1/2	1/8	1/2	1/8	1/2	1/4	1/2	1/4	1/4
	1/4	y = 2	1/8	1/4	1/16	1/4	1/16	1/4	1/16	1/4	1/8	1/4	1/8
		y = 3	1/8	1/4	1/16	1/4	1/16	1/4	1/16	1/4	1/8	1/4	1/8
		1/2	1/4	1/4	1/2	1/4	1/4	1/2	1/4	1/2	1/4	1/4	
		$\mathcal{P}_y(x)$	$\mathcal{P}_y(x)$	$\mathcal{P}_y(x)$	$\mathcal{P}_y(x)$	$\mathcal{P}_y(x)$	$\mathcal{P}_y(x)$	$\mathcal{P}_y(x)$	$\mathcal{P}_y(x)$	$\mathcal{P}_y(x)$	$\mathcal{P}_y(x)$	$\mathcal{P}_y(x)$	$\mathcal{P}_y(x)$
		$\mathcal{P}_x(y)$	$\mathcal{P}_x(y)$	$\mathcal{P}_x(y)$	$\mathcal{P}_x(y)$	$\mathcal{P}_x(y)$	$\mathcal{P}_x(y)$	$\mathcal{P}_x(y)$	$\mathcal{P}_x(y)$	$\mathcal{P}_x(y)$	$\mathcal{P}_x(y)$	$\mathcal{P}_x(y)$	$\mathcal{P}_x(y)$

**Table A.2:** The three examples for a two-dimensional discrete probability distribution from Tab. A.1 including the conditional probabilities  $\mathcal{P}_x(y)$  and  $\mathcal{P}_y(x)$ .

The conditional entropy  $S_x^y$  is connected to the full entropy  $S^{xy}$  and the single-variable entropy  $S^x$  as follows,

$$\begin{aligned}
 S^{xy} &= - \sum_{x,y} \mathcal{P}(x,y) \text{lb} \mathcal{P}(x,y) = - \sum_{x,y} \mathcal{P}(x,y) \text{lb} \{ \mathcal{P}(x) \cdot \mathcal{P}_x(y) \} \\
 &= - \sum_x \mathcal{P}(x) \text{lb} \mathcal{P}(x) - \sum_{x,y} \mathcal{P}(x,y) \text{lb} \mathcal{P}_x(y) \\
 &= S^x + S_x^y .
 \end{aligned} \tag{A.51}$$

The entropy  $S^{xy}$  of the joint distribution  $\mathcal{P}(x,y)$  is hence expressed as sum of the entropy  $S^x$  of the first random variable and the conditional entropy  $S_x^y$  of the second random variable with knowledge of the first. Analogously, one can calculate the entropy of the second random variable  $S^y$  and add the entropy of the first random variable with knowledge of the second random variable  $S_y^x$ .

The conditional probabilities for the three examples above are added in Tab. A.2. For example (a) where both random variables are independent,  $\mathcal{P}(x,y) = \mathcal{P}(x) \cdot \mathcal{P}(y)$ , the conditional probability is identical with the single probability,  $\mathcal{P}_y(x) = \mathcal{P}(x)$  independently of the value of  $y$ . Moreover, the second conditional entropy is  $\mathcal{P}_x(y) = \mathcal{P}(y)$  independently of the value of  $x$ . Hence, the conditional entropy  $S_x^y$  for the second random variable  $y$  with knowledge of  $x$  is the same as the entropy  $S^y$  without that knowledge. The knowledge about one random variable does not reduce the uncertainty about the other random variable, here, due to their statistical independence.

For the second example (b) where both random variables are totally correlated, the conditional probabilities contain no uncertainty about the second random variable when one of the random variables is already known. Hence, the conditional entropies  $S_x^y$  and  $S_y^x$  are exactly zero in this case. The knowledge about one random variable leaves no uncertainty about the other random variable at all, here, due to their total correlation.

Finally, for the third example (c), both random variables are partially correlated. The knowledge about the first random variable reduces the uncertainty about the second random variable, but it does not remove the uncertainty about it completely. The conditional probabilities  $\mathcal{P}_x(y)$  and  $\mathcal{P}_y(x)$  in Tab. A.2 differ from the overall probabilities of a single random variable  $\mathcal{P}(y)$  and  $\mathcal{P}(x)$ . Hence, the conditional entropies  $S_x^y$  and  $S_y^x$  are smaller than the unconditional single-variable entropies  $S^y$  and  $S^x$  but it is yet finite.

These simple examples illustrated the relations between the entropy  $S^{xy}$  of a joint probability distribution  $\mathcal{P}(x, y)$ , the entropies  $S^x$  and  $S^y$  of the single-variable probability distributions  $\mathcal{P}(x)$  and  $\mathcal{P}(y)$ , and the conditional entropies  $S_x^y$  and  $S_y^x$  of the conditional probability distributions  $\mathcal{P}_x(y)$  and  $\mathcal{P}_y(x)$  where one random variable is known. The examples revealed the impact of statistical independence and correlations between different random variables on the entropy.

The concept of a conditional entropy can be extended to probability distributions with more than two random variables and with continuous probability distributions of these variables. The introduction of the reduced entropies  $S^{(2)}$  and  $S^{(3)}$  for the spatial distribution functions of particle pairs and triples, respectively, can be understood as such a generalization.



## Appendix B

# Analytical Model of the Laser Heating Process: Calculations and Tables

During the derivation of the analytic model for the heating power in the laser manipulation setup, several steps require solving integrals and the simplification of expression. These calculations are given in this section. Furthermore the predictions of the model are compared to the results of Langevin molecular dynamics (LMD) simulations in Sec. B.3.

### B.1 Simplification of the Spatial Factor $\Sigma$

In Eq. (6.9), the spatial factor  $\Sigma$  was introduced in order to describe the dependence of the passing distance of the spot from the particle position to the transferred momentum. Re-substituting the time scale

$$\tau = \frac{1}{\sqrt{\frac{v_x^2}{\sigma_x^2} + \frac{v_y^2}{\sigma_y^2}}} \quad (\text{B.1})$$

from Eq. (6.7), this factor can be simplified to

$$\Sigma = \frac{1}{\sqrt{2\pi}} \frac{1}{\sigma_x \sigma_y} \exp \left\{ -\frac{1}{2} \left[ \frac{\Delta y_0^2}{\sigma_y^2} - \tau^2 \frac{\Delta y_0^2 v_y^2}{\sigma_y^4} \right] \right\} \quad (\text{B.2})$$

$$= \frac{1}{\sqrt{2\pi}} \frac{1}{\sigma_x \sigma_y} \exp \left\{ -\frac{1}{2} \frac{\Delta y_0^2 v_x^2 \tau^2}{\sigma_y^2 \sigma_x^2} \right\}. \quad (\text{B.3})$$

In this compact form without any sum within the exponential function, the spatial factor  $\Sigma$  can easily be integrated over  $\Delta y_0$ , for example. The dependences of this parameter on the passing parameter  $\Delta y_0$ , on the spot velocity  $v_x$  and also on the time scale  $\tau$  is described by a Gaussian shape.

## B.2 Effective Time Scale $\tau_{\text{eff}}$ for the Acceleration by a Moving Laser Spot

Since the spot velocity changes dynamically for the elaborated laser heating method B, an effective time scale  $\tau_{\text{eff}}$  is introduced by averaging  $\tau$  over all possible spot velocities  $v_x \in [v_x^{\min}, v_x^{\max}]$  and  $v_y \in [v_y^{\min}, v_y^{\max}]$ . The integral in the expression for the effective time scale,

$$\begin{aligned}
\tau_{\text{eff}} &= \frac{1}{\underbrace{v_x^{\max} - v_x^{\min}}_{:=\Delta v_x}} \frac{1}{\underbrace{v_y^{\max} - v_y^{\min}}_{:=\Delta v_y}} \int_{v_y^{\min}}^{v_y^{\max}} dv_y \int_{v_x^{\min}}^{v_x^{\max}} dv_x \tau \\
&= \frac{1}{\Delta v_x \Delta v_y} \int_{v_y^{\min}}^{v_y^{\max}} dv_y \int_{v_x^{\min}}^{v_x^{\max}} dv_x \frac{1}{\sqrt{\frac{v_x^2}{\sigma_x^2} + \frac{v_y^2}{\sigma_y^2}}} \\
&= \frac{1}{\Delta v_x \Delta v_y} \cdot \left[ \sigma_x v_y^{\max} \ln \left\{ \frac{\sigma_y v_x^{\max} + \sqrt{\sigma_y^2 v_x^{\max 2} + \sigma_x^2 v_y^{\max 2}}}{\sigma_y v_x^{\min} + \sqrt{\sigma_y^2 v_x^{\min 2} + \sigma_x^2 v_y^{\max 2}}} \right\} \right. \\
&\quad + \sigma_y v_x^{\max} \ln \left\{ \frac{\sigma_x v_y^{\max} + \sqrt{\sigma_y^2 v_x^{\max 2} + \sigma_x^2 v_y^{\max 2}}}{\sigma_x v_y^{\min} + \sqrt{\sigma_y^2 v_x^{\max 2} + \sigma_x^2 v_y^{\min 2}}} \right\} \\
&\quad + \sigma_x v_y^{\min} \ln \left\{ \frac{\sigma_y v_x^{\min} + \sqrt{\sigma_y^2 v_x^{\min 2} + \sigma_x^2 v_y^{\min 2}}}{\sigma_y v_x^{\max} + \sqrt{\sigma_y^2 v_x^{\max 2} + \sigma_x^2 v_y^{\min 2}}} \right\} \\
&\quad \left. + \sigma_y v_x^{\min} \ln \left\{ \frac{\sigma_x v_y^{\min} + \sqrt{\sigma_y^2 v_x^{\min 2} + \sigma_x^2 v_y^{\min 2}}}{\sigma_x v_y^{\max} + \sqrt{\sigma_y^2 v_x^{\min 2} + \sigma_x^2 v_y^{\max 2}}} \right\} \right], \quad (\text{B.4})
\end{aligned}$$

was solved using MATHEMATICA. The velocity of the spot is given by the product of the size of the scanned rectangle and the frequency of the triangular driver signal of the scanner mirrors,

$$v_x = 4Xf_x \quad \text{and} \quad v_y = 4Yf_y. \quad (\text{B.5})$$

Therefore, the effective time scale  $\tau_{\text{eff}}$  decreases linearly with the edge length  $2X$  of the scanned rectangle provided that the aspect ratio  $X : Y$  is conserved.

## B.3 Comparison of the Model for the Laser Heating Process and Simulation Results

The kinetic temperature estimated by the analytic formula, Eq. (6.27) in section 6.1.3, is compared with the LMD simulations. In these LMD simulations were performed for  $N = 25$  particles, a screening parameter  $\kappa = 1$  and different friction coefficients  $\gamma$ . The kinetic temperature was determined by a Maxwellian fit to the velocity distribution.



$\gamma$	formula	simulation	deviation
	$\sigma_x = 0.20, \sigma_y = 0.04$		
0.67	25.341 $39.46 \times 10^{-3}$	24.963 $40.06 \times 10^{-3}$	$\Gamma$ -1.49% $T$
1.00	35.601 $28.09 \times 10^{-3}$	35.605 $28.09 \times 10^{-3}$	$\Gamma$ 0.0107% $T$
1.33	44.722 $22.36 \times 10^{-3}$	45.774 $21.85 \times 10^{-3}$	$\Gamma$ 2.35% $T$
1.66	52.885 $18.91 \times 10^{-3}$	55.161 $18.13 \times 10^{-3}$	$\Gamma$ 4.31% $T$
2.00	60.443 $16.54 \times 10^{-3}$	63.404 $15.77 \times 10^{-3}$	$\Gamma$ 4.90% $T$
2.33	67.071 $14.91 \times 10^{-3}$	70.767 $14.13 \times 10^{-3}$	$\Gamma$ 5.51% $T$
2.66	73.099 $13.68 \times 10^{-3}$	78.528 $12.73 \times 10^{-3}$	$\Gamma$ 7.43% $T$
	$\sigma_x = 0.30, \sigma_y = 0.06$		
0.67	35.747 $27.97 \times 10^{-3}$	37.067 $26.98 \times 10^{-3}$	$\Gamma$ 3.69% $T$
1.00	49.037 $20.39 \times 10^{-3}$	51.353 $19.47 \times 10^{-3}$	$\Gamma$ 4.72% $T$
1.33	60.337 $16.57 \times 10^{-3}$	63.753 $15.69 \times 10^{-3}$	$\Gamma$ 5.66% $T$
1.66	70.064 $14.27 \times 10^{-3}$	73.442 $13.62 \times 10^{-3}$	$\Gamma$ 4.82% $T$
2.00	78.763 $12.70 \times 10^{-3}$	82.922 $12.06 \times 10^{-3}$	$\Gamma$ 5.28% $T$
2.33	86.160 $11.61 \times 10^{-3}$	90.573 $11.04 \times 10^{-3}$	$\Gamma$ 5.12% $T$
2.66	92.706 $10.79 \times 10^{-3}$	97.455 $10.26 \times 10^{-3}$	$\Gamma$ 5.12% $T$

Table B.1: Kinetic dust temperature from analytic approximation formula and LMD simulation (part 1)

$\gamma$	formula	simulation	deviation	$\gamma$	formula	simulation	deviation
	$\sigma_x = 0.40, \sigma_y = 0.08$				$\sigma_x = 0.50, \sigma_y = 0.10$		
0.67	44.983 $22.23 \times 10^{-3}$	49.767 $20.09 \times 10^{-3}$	$\Gamma$ 10.6%	0.67	53.235 $18.78 \times 10^{-3}$	62.160 $16.09 \times 10^{-3}$	$\Gamma$ 16.8%
1.00	60.443 $16.54 \times 10^{-3}$	66.235 $15.10 \times 10^{-3}$	$\Gamma$ 9.58%	1.00	70.246 $14.24 \times 10^{-3}$	81.021 $12.34 \times 10^{-3}$	$\Gamma$ 15.3%
1.33	73.099 $13.68 \times 10^{-3}$	79.633 $12.56 \times 10^{-3}$	$\Gamma$ 8.94%	1.33	83.723 $11.94 \times 10^{-3}$	94.788 $10.55 \times 10^{-3}$	$\Gamma$ 13.2%
1.66	83.650 $11.95 \times 10^{-3}$	90.445 $11.06 \times 10^{-3}$	$\Gamma$ 8.12%	1.66	94.664 $10.56 \times 10^{-3}$	105.74 $9.457 \times 10^{-3}$	$\Gamma$ 11.7%
2.00	92.831 $10.77 \times 10^{-3}$	100.21 $9.979 \times 10^{-3}$	$\Gamma$ 7.95%	2.00	103.97 $9.618 \times 10^{-3}$	114.87 $8.705 \times 10^{-3}$	$\Gamma$ 10.5%
2.33	100.45 $9.955 \times 10^{-3}$	107.91 $9.267 \times 10^{-3}$	$\Gamma$ 7.42%	2.33	111.56 $8.964 \times 10^{-3}$	122.22 $8.182 \times 10^{-3}$	$\Gamma$ 9.55%
2.66	107.07 $9.340 \times 10^{-3}$	115.00 $8.695 \times 10^{-3}$	$\Gamma$ 7.41%	2.66	118.04 $8.472 \times 10^{-3}$	128.60 $7.776 \times 10^{-3}$	$\Gamma$ 8.95%

Table B.2: Kinetic dust temperature from analytic approximation formula and LMD simulation (part 2)

$\gamma$	formula	simulation	deviation
	$\sigma_x = 0.60, \sigma_y = 0.12$		
0.67	60.653 $16.49 \times 10^{-3}$	74.979 $13.34 \times 10^{-3}$	$\Gamma$ 23.6% $T$
1.00	78.763 $12.70 \times 10^{-3}$	94.269 $10.61 \times 10^{-3}$	$\Gamma$ 19.7% $T$
1.33	92.706 $10.79 \times 10^{-3}$	107.78 $9.278 \times 10^{-3}$	$\Gamma$ 16.3% $T$
1.66	103.77 $9.636 \times 10^{-3}$	118.49 $8.440 \times 10^{-3}$	$\Gamma$ 14.2% $T$
2.00	113.02 $8.848 \times 10^{-3}$	127.09 $7.868 \times 10^{-3}$	$\Gamma$ 12.5% $T$
2.33	120.44 $8.303 \times 10^{-3}$	134.75 $7.421 \times 10^{-3}$	$\Gamma$ 11.9% $T$
2.66	126.69 $7.893 \times 10^{-3}$	140.19 $7.133 \times 10^{-3}$	$\Gamma$ 10.7% $T$
	$\sigma_x = 0.70, \sigma_y = 0.14$		
0.67	67.358 $14.85 \times 10^{-3}$	87.615 $11.41 \times 10^{-3}$	$\Gamma$ 30.1% $T$
1.00	86.230 $11.60 \times 10^{-3}$	106.45 $9.394 \times 10^{-3}$	$\Gamma$ 23.5% $T$
1.33	100.40 $9.960 \times 10^{-3}$	120.78 $8.280 \times 10^{-3}$	$\Gamma$ 20.3% $T$
1.66	111.43 $8.974 \times 10^{-3}$	130.63 $7.655 \times 10^{-3}$	$\Gamma$ 17.2% $T$
2.00	120.50 $8.298 \times 10^{-3}$	138.13 $7.239 \times 10^{-3}$	$\Gamma$ 14.6% $T$
2.33	127.69 $7.831 \times 10^{-3}$	143.87 $6.951 \times 10^{-3}$	$\Gamma$ 12.7% $T$
2.66	133.69 $7.480 \times 10^{-3}$	149.27 $6.699 \times 10^{-3}$	$\Gamma$ 11.7% $T$

Table B.3: Kinetic dust temperature from analytic approximation formula and LMD simulation (part 3)

## B.4 Correction Factor for the Finite Overlap of the Laser Spots

In order to calculate the average overlap, the laser force from Eq. (6.4) is recapped, but with explicit distances,  $\Delta x = x_d - x_+$  for the laser in  $+x$ -direction etc.

$$f_+(x_+, y_+, x_d, y_d) = +F_L \frac{1}{2\pi} \frac{1}{\sigma_x \sigma_y} \exp \left\{ -\frac{1}{2} \left( \left( \frac{x_d - x_+}{\sigma_x} \right)^2 + \left( \frac{y_d - y_+}{\sigma_y} \right)^2 \right) \right\}, \quad (\text{B.6})$$

$$f_-(x_-, y_-, x_d, y_d) = -F_L \frac{1}{2\pi} \frac{1}{\sigma_x \sigma_y} \exp \left\{ -\frac{1}{2} \left( \left( \frac{x_d - x_-}{\sigma_x} \right)^2 + \left( \frac{y_d - y_-}{\sigma_y} \right)^2 \right) \right\}. \quad (\text{B.7})$$

The overlap is calculated as the convolution of the two forces over all particle coordinates  $x_d, y_d$  as

$$\begin{aligned} O_f(x_+, y_+, x_-, y_-) &= f_+ \otimes f_-(x_+, y_+, x_-, y_-) \\ &= \int_{-X}^X dx_d \int_{-Y}^Y dy_d f_+(x_+, y_+, x_d, y_d) \cdot f_-(x_-, y_-, x_d, y_d) \\ &\geq \int_{-\infty}^{\infty} dx_d \int_{-\infty}^{\infty} dy_d f_+(x_+, y_+, x_d, y_d) \cdot f_-(x_-, y_-, x_d, y_d) \\ &= -F_L^2 \frac{1}{4\pi^2} \frac{1}{\sigma_x^2 \sigma_y^2} \int_{-\infty}^{\infty} dx_d \int_{-\infty}^{\infty} dy_d \\ &\quad \exp \left\{ -\frac{1}{2} \left( \left( \frac{x_d - x_+}{\sigma_x} \right)^2 + \left( \frac{y_d - y_+}{\sigma_y} \right)^2 \right) \right\} \\ &\quad \cdot \exp \left\{ -\frac{1}{2} \left( \left( \frac{x_d - x_-}{\sigma_x} \right)^2 + \left( \frac{y_d - y_-}{\sigma_y} \right)^2 \right) \right\} \\ &= -F_L^2 \frac{1}{4\pi \sigma_x \sigma_y} \exp \left\{ -\frac{1}{2} \frac{(x_+ - x_-)^2}{2\sigma_x^2} \right\} \cdot \exp \left\{ -\frac{1}{2} \frac{(y_+ - y_-)^2}{2\sigma_y^2} \right\}, \quad (\text{B.8}) \end{aligned}$$

and is a function of the positions of both laser spots. The average overlap is obtained by averaging the coordinates of both laser spots over the whole levitation plane,

$$\begin{aligned}
\langle f_+ \otimes f_- \rangle &= \frac{1}{(2X)^2(2Y)^2} \int_{-X}^X dx_- \int_{-Y}^Y dy_- \int_{-X}^X dx_+ \int_{-Y}^Y dy_+ O_f(x_+, y_+, x_-, y_-) \\
&= \frac{-F_L^2}{16X^2Y^2} \frac{1}{4\pi\sigma_x\sigma_y} \cdot \int_{-X}^X dx_- \int_{-Y}^Y dy_- \int_{-X}^X dx_+ \int_{-Y}^Y dy_+ \\
&\quad \exp\left\{-\frac{1}{2} \frac{(x_+ - x_-)^2}{2\sigma_x^2}\right\} \cdot \exp\left\{-\frac{1}{2} \frac{(y_+ - y_-)^2}{2\sigma_y^2}\right\} \\
&= \frac{-F_L^2}{4\pi} \frac{1}{X^2Y^2} \left[ \left( \underbrace{e^{-\frac{X^2}{\sigma_x^2}}}_{\ll 1} - 1 \right) \cdot \sigma_x + \underbrace{\sqrt{\pi}X \cdot \operatorname{erf}\left(\frac{X}{\sigma_x}\right)}_{\approx 1} \right] \\
&\quad \times \left[ \left( \underbrace{e^{-\frac{Y^2}{\sigma_y^2}}}_{\ll 1} - 1 \right) \cdot \sigma_y + \underbrace{\sqrt{\pi}Y \cdot \operatorname{erf}\left(\frac{Y}{\sigma_y}\right)}_{\approx 1} \right] \tag{B.9}
\end{aligned}$$

$$\approx -F_L^2 \cdot \frac{X - \frac{\sigma_x}{\sqrt{\pi}}}{2X^2} \cdot \frac{Y - \frac{\sigma_y}{\sqrt{\pi}}}{2Y^2}. \tag{B.10}$$

In order to estimate the influence of this overlap, the total squared force of a single laser spot,

$$\begin{aligned}
|f_{\pm}^2| &= \int_{-X}^X dx_{\pm} \int_{-Y}^Y dy_{\pm} |f_{\pm}(x_{\pm}, y_{\pm}, x_d, y_d)|^2 \\
&\approx \int_{-\infty}^{\infty} dx_{\pm} \int_{-\infty}^{\infty} dy_{\pm} |f_{\pm}(x_{\pm}, y_{\pm}, x_d, y_d)|^2 \\
&= \frac{F_L^2}{2\pi\sigma_x\sigma_y}, \tag{B.11}
\end{aligned}$$

is calculated as well, and the overlap from Eq. (B.10) is related to this value. The resulting correction factor is

$$\epsilon_O = \frac{\langle f_- \otimes f_+ \rangle}{2|f_{\pm}^2|} = -\frac{\pi}{2} \left( X - \frac{\sigma_x}{\sqrt{\pi}} \right) \cdot \left( Y - \frac{\sigma_y}{\sqrt{\pi}} \right) \cdot \frac{\sigma_x\sigma_y}{X^2Y^2}. \tag{B.12}$$

## B.5 Acceleration with Friction

Throughout the derivation of the analytic approximation of the heating power, Eq. (6.27), an instantaneous acceleration event without friction was considered. This acceleration event was followed by the subsequent deceleration by the neutral gas friction. In order to validate this approach, the equation of motion for the particle acceleration by a Gaussian force pulse is

solved at this point including the friction term, i.e.,

$$m \cdot \frac{d}{dt}v(t) = -m\gamma \cdot v(t) + \frac{F_L}{\sqrt{2\pi\tau}} \exp\left\{-\frac{1}{2} \frac{t^2}{\tau^2}\right\}. \quad (\text{B.13})$$

The general solution of the equation is

$$v(t) = c_1 \cdot e^{-\gamma t} - \frac{F_L}{2m} \cdot \exp\left\{-\gamma t + \frac{\gamma^2 \tau^2}{2}\right\} \cdot \operatorname{erf}\left\{\frac{-t + \gamma \tau^2}{\sqrt{2}\tau}\right\}, \quad (\text{B.14})$$

where  $c_1$  is an integration constant. This constant is determined by the condition that the particle is at rest at the beginning. This condition leads to

$$\begin{aligned} 0 &= \lim_{t \rightarrow -\infty} v(t) \\ \Leftrightarrow 0 &= \lim_{t \rightarrow -\infty} c_1 \cdot e^{-\gamma t} - \frac{F_L}{2m} \cdot e^{\frac{\gamma^2 \tau^2}{2}} \cdot e^{-\gamma t} \\ \Leftrightarrow c_1 &= \frac{F_L}{2m} \cdot e^{\frac{\gamma^2 \tau^2}{2}}, \end{aligned} \quad (\text{B.15})$$

and hence, the velocity of the particle is

$$v(t) = \frac{F_L}{2m} \cdot e^{\frac{\gamma^2 \tau^2}{2}} \cdot e^{-\gamma t} \cdot \left[1 - \operatorname{erf}\left\{\frac{-t + \gamma \tau^2}{\sqrt{2}\tau}\right\}\right]. \quad (\text{B.16})$$

This solution converges to the well-known case of instantaneous acceleration with subsequent damping for  $\tau \rightarrow 0$ ,

$$v_{\text{inst}}(t) = \frac{F_L}{m} \cdot e^{-\gamma t} \cdot \Theta(t), \quad (\text{B.17})$$

with the Heaviside Unit Step function  $\Theta(t)$ . The total energy lost by friction can easily be calculated for the instantaneous case

$$\Delta E = \int_{-\infty}^{\infty} dt m\gamma \cdot v_{\text{inst}}^2(t) = \frac{\gamma F_L^2}{m} \cdot \left[-\frac{1}{2\gamma} \cdot e^{-\gamma t}\right]_0^{\infty} = \frac{F_L^2}{2m} = \frac{m}{2} \cdot v_0^2, \quad (\text{B.18})$$

where  $v_0 = F_L/m$  is the particle's velocity right after the instantaneous acceleration event.

# Appendix C

## Used Abbreviations and Symbols

Several abbreviations and symbols are used in this thesis. While many of them are commonly used in the plasma community, some are less known. Therefore, an overview of used abbreviations is provided in Tab. C.1 and the used symbols are listed in Tab. C.2.

abbreviation	meaning
C2P	center-two-particle
bcc	base centered cubic (lattice)
fcc	face centered cubic (lattice)
ISP	inverse stereographic projection
MC	Monte Carlo (simulations)
MD	molecular dynamics (simulations)
LMD	Langevin molecular dynamics (simulations)
PDF	pair distribution function
RNG	random number generator
SP	stereographic projection
rf	radio frequency
TCF	triple-correlation function

**Table C.1:** List of abbreviations which are used in this thesis.

symbol	meaning
$m_d$	mass of one dust particle
$Q_d$	charge of one dust particle
$r_d$	radius of one dust particle
$d_d = 2r_d$	diameter of one dust particle
$\omega_0$	trap frequency of the harmonic confinement
$\Phi_Y$	Yukawa or Debye-Hückel interaction potential
$\kappa = \lambda_D^{-1}$	screening parameter as inverse Debye length
$\lambda_D$	combined Debye screening length of both electrons and ions
$\lambda_{DB}$	thermal de Broglie wavelength
$\Gamma$	Coulomb coupling parameter: ratio of typical interaction energy and thermal energy
$\gamma$	friction frequency of the dust grains describing the friction by the neutral gas
$\lambda = m_d \gamma$	damping parameter due to the friction by the neutral gas
$F_L$	heating power of a manipulation laser
$d_{nn}$	distance of nearest neighbors
$n_e$	electron density
$n_i$	ion density
$\sigma_{\parallel}, \sigma_{\perp}$	spot width in beam direction / in perpendicular direction
$T_e$	electron temperature
$T_i$	ion temperature
$\vartheta$	angular pair distance with respect to the trap center in spherical clusters
$\varphi$	bond angle

**Table C.2:** Symbols which are used in this thesis.



# Bibliography

- [1] O. Arp, D. Block, A. Piel, and A. Melzer. *Dust Coulomb balls: Three-dimensional plasma crystals*. Phys. Rev. Lett. **93**, 165004 (2004).
- [2] A. Melzer, B. Buttenschön, T. Miksch, M. Passvogel, D. Block, O. Arp, and A. Piel. *Finite dust clusters in dusty plasmas*. Plasma Phys. Controlled Fusion **52**, 124028 (2010).
- [3] J. P. Schiffer. *Melting of Crystalline Confined Plasmas*. Phys. Rev. Lett. **88**, 205003 (2002).
- [4] M. Wolter and A. Melzer. *Laser heating of particles in dusty plasmas*. Phys. Rev. E **71**, 036414 (2005).
- [5] V. Nosenko, J. Goree, and A. Piel. *Laser method of heating monolayer dusty plasmas*. Phys. Plasmas **13**, 032106 (2006).
- [6] H. Thomsen, P. Ludwig, M. Bonitz, J. Schablinski, D. Block, A. Schella, and A. Melzer. *Controlling strongly correlated dust clusters with lasers*. J. Phys. D: Appl. Phys. **47**, 383001 (2014).
- [7] L.D. Landau and E. Lifschitz, *Course of Theoretical Physics VI, Fluid Mechanics* (Pergamon Press, Oxford, 1987), 2nd ed.
- [8] M. Eckert, *The Dawn of Fluid Dynamics: A Discipline between Science and Technology* (Wiley-VCH Verlag GmbH & Co. KGaA, Weinheim, 2005), 1st ed., ISBN 978-3527 4051 38.
- [9] J. P. Hansen and I. R. McDonald, *Theory of Simple Liquids* (Academic Press, Burlington, 2006), 3rd ed., ISBN 978-0123 7053 58.
- [10] A. Piel, *Plasma Physics: An Introduction to Laboratory, Space, and Fusion Plasmas* (Springer, Heidelberg; New York, 2010), ISBN 978-3642 1049 09.
- [11] M. Bonitz, N. Horing, and P. Ludwig (eds.), *Introduction to complex plasmas* (Springer, Heidelberg; New York, 2010), ISBN 978-3642 1059 13.
- [12] D. M. Ceperley and B. J. Alder. *Ground State of the Electron Gas by a Stochastic Method*. Phys. Rev. Lett. **45**, 566 (1980).
- [13] C. Kittel, *Introduction to Solid State Physics* (John Wiley & Sons, Hoboken, NJ, 2004), 8th ed., ISBN 978-0471 4152 68.

- [14] M. Ziegler, J. Kröger, R. Berndt, A. Filinov, and M. Bonitz. *Scanning tunneling microscopy and kinetic Monte Carlo investigation of cesium superlattices on Ag(111)*. Phys. Rev. B **78**, 245427 (2008).
- [15] C. I. Blaga, J. Xu, A. D. DiChiara, E. Sistrunk, K. Zhang, P. Agostini, T. A. Miller, L. F. DiMauro, and C. D. Lin. *Imaging ultrafast molecular dynamics with laser-induced electron diffraction*. Nature **483**, 194 (2012).
- [16] A. Melzer, T. Trottenberg, and A. Piel. *Experimental determination of the charge on dust particles forming Coulomb lattices*. Phys. Lett. A **191**, 301 (1994).
- [17] A. Melzer, A. Homann, and A. Piel. *Experimental investigation of the melting transition of the plasma crystal*. Phys. Rev. E **53**, 2757 (1996).
- [18] O. Arp, D. Block, M. Bonitz, H. Fehske, V. Golubnychiy, S. Kosse, P. Ludwig, A. Melzer, and A. Piel. *3D Coulomb balls: experiment and simulation*. J. Phys.: Conf. Ser. **11**, 234 (2005).
- [19] O. Arp, D. Block, M. Klindworth, and A. Piel. *Confinement of Coulomb balls*. Phys. Plasmas **12**, 122102 (2005).
- [20] M. Kroll, J. Schablinski, D. Block, and A. Piel. *On the influence of wakefields on three-dimensional particle arrangements*. Phys. Plasmas **17**, 013702 (2010).
- [21] F. Greiner, J. Carstensen, N. Köhler, I. Pilch, H. Ketelsen, S. Knist, and A. Piel. *Imaging Mie ellipsometry: dynamics of nanodust clouds in an argon-acetylene plasma*. Plasma Sources Sci. Technol. **21**, 065005 (2012).
- [22] A. Bogaerts, E. Neyts, R. Gijbels, and J. van der Mullen. *Gas discharge plasmas and their applications*. Spectrochim. Acta, Part B **57**, 609 (2002).
- [23] H. Thomas, G. E. Morfill, V. Demmel, J. Goree, B. Feuerbacher, and D. Möhlmann. *Plasma crystal: Coulomb crystallization in a dusty plasma*. Phys. Rev. Lett. **73**, 652 (1994).
- [24] G. E. Morfill, H. M. Thomas, U. Konopka, H. Rothermel, M. Zuzic, A. Ivlev, and J. Goree. *Condensed plasmas under microgravity*. Phys. Rev. Lett. **83**, 1598 (1999).
- [25] D. J. Wineland, J. C. Bergquist, W. M. Itano, J. J. Bollinger, and C. H. Manney. *Atomic-ion Coulomb clusters in an ion trap*. Phys. Rev. Lett. **59**, 2935 (1987).
- [26] M. Bonitz, P. Ludwig, H. Baumgartner, C. Henning, A. Filinov, D. Block, O. Arp, A. Piel, S. Käding, Y. Ivanov, et al. *Classical and quantum Coulomb crystals*. Phys. Plasmas **15**, 055704 (2008).
- [27] V. E. Fortov. *Extreme states of matter on Earth and in space*. Phys. Usp. **52**, 615 (2009).
- [28] T. Ott, M. Stanley, and M. Bonitz. *Non-invasive determination of the parameters of strongly coupled 2D Yukawa liquids*. Phys. Plasmas **18**, 063701 (2011).

- [29] O. Vaulina, S. Khrapak, and G. Morfill. *Universal scaling in complex (dusty) plasmas*. Phys. Rev. E **66**, 016404 (2002).
- [30] P. Hartmann, G. J. Kalman, Z. Donkó, and K. Kutasi. *Equilibrium properties and phase diagram of two-dimensional Yukawa systems*. Phys. Rev. E **72**, 026409 (2005).
- [31] M. Bonitz, J. Lopez, K. Becker, and H. Thomsen (eds.), *Complex Plasmas: Scientific Challenges and Technological Opportunities* (Springer, New York, 2014), ISBN 978-3319 0543 60.
- [32] G. J. Kalman, P. Hartmann, Z. Donkó, and M. Rosenberg. *Two-dimensional Yukawa liquids: Correlation and dynamics*. Phys. Rev. Lett. **92**, 065001 (2004).
- [33] P. Hartmann, G. J. Kalman, and Z. Donkó. *Two-dimensional Yukawa liquids: structure and collective excitations*. J. Phys. A: Math. Gen. **39**, 4485 (2006).
- [34] T. Ott, M. Bonitz, L. G. Stanton, and M. S. Murillo. *Coupling strength in Coulomb and Yukawa one-component plasmas*. Phys. Plasmas **21**, 113704 (2014).
- [35] T. Ott and M. Bonitz. *First-Principle Results for the Radial Pair Distribution Function in Strongly Coupled One-Component Plasmas*. Contrib. Plasma Phys. **55**, 243 (2015).
- [36] V. Nosenko, J. Goree, Z. W. Ma, and A. Piel. *Observation of Shear-Wave Mach Cones in a 2D Dusty-Plasma Crystal*. Phys. Rev. Lett. **88**, 135001 (2002).
- [37] S. Hamaguchi, R. T. Farouki, and D. H. E. Dubin. *Triple point of Yukawa systems*. Phys. Rev. E **56**, 4671 (1997).
- [38] S. A. Khrapak and G. E. Morfill. *fcc-bcc-fluid triple point for model pair interactions with variable softness*. Europhys. Lett. **100**, 66004 (2012).
- [39] H. Kählert, J. Carstensen, M. Bonitz, H. Löwen, F. Greiner, and A. Piel. *Magnetizing a complex plasma without a magnetic field*. Phys. Rev. Lett. **109**, 155003 (2012).
- [40] J. Schablinski, D. Block, A. Piel, A. Melzer, H. Thomsen, H. Kählert, and M. Bonitz. *Laser heating of finite two-dimensional dust clusters: A. Experiments*. Phys. Plasmas **19**, 013705 (2012).
- [41] Y.-J. Lai and L. I. *Packings and defects of strongly coupled two-dimensional Coulomb clusters: Numerical simulation*. Phys. Rev. E **60**, 4743 (1999).
- [42] W. Juan, Z. Huang, J. Hsu, Y. Lai, and L. I. *Observation of dust Coulomb clusters in a plasma trap*. Phys. Rev. E **58**, R6947 (1998).
- [43] V. M. Bedanov and F. Peeters. *Ordering and phase transitions of charged particles in a classical finite two-dimensional system*. Phys. Rev. B **49**, 2667 (1994).
- [44] V. A. Schweigert and F. Peeters. *Spectral properties of classical two-dimensional clusters*. Phys. Rev. B **51**, 7700 (1995).

- [45] M. Klindworth, A. Melzer, A. Piel, and V. A. Schweigert. *Laser-excited intershell rotation of finite Coulomb clusters in a dusty plasma*. Phys. Rev. B **61**, 8404 (2000).
- [46] A. Melzer. *Mode spectra of thermally excited two-dimensional dust Coulomb clusters*. Phys. Rev. E **67**, 016411 (2003).
- [47] Y. Ivanov and A. Melzer. *Melting dynamics of finite clusters in dusty plasmas*. Phys. Plasmas **12**, 072110 (2005).
- [48] Y. Feng, J. Goree, and B. Liu. *Accurate particle position measurement from images*. Rev. Sci. Instrum. **78**, 053704 (2007).
- [49] H. Thomsen, H. Kählert, M. Bonitz, J. Schablinski, D. Block, A. Piel, and A. Melzer. *Laser heating of finite two-dimensional dust clusters: B. Simulations*. Phys. Plasmas **19**, 023701 (2012).
- [50] J. Schablinski, D. Block, J. Carstensen, F. Greiner, and A. Piel. *Sheared and unsheared rotation of driven dust clusters*. Phys. Plasmas **21**, 073701 (2014).
- [51] M. Schwabe, S. K. Zhdanov, H. M. Thomas, A. V. Ivlev, M. Rubin-Zuzic, G. E. Morfill, V. I. Molotkov, A. M. Lipaev, V. E. Fortov, and T. Reiter. *Nonlinear waves externally excited in a complex plasma under microgravity conditions*. New J. Phys. **10**, 033037 (2008).
- [52] M. D. Kilgore, J. E. Daugherty, R. K. Porteous, and D. B. Graves. *Ion drag on an isolated particulate in a low-pressure discharge*. J. Appl. Phys. **73**, 7195 (1993).
- [53] G. M. Jellum, J. E. Daugherty, and D. B. Graves. *Particle thermophoresis in low pressure glow discharges*. J. Appl. Phys. **69**, 6923 (1991).
- [54] H. Rothermel, T. Hagl, G. E. Morfill, M. H. Thoma, and H. M. Thomas. *Gravity compensation in complex plasmas by application of a temperature gradient*. Phys. Rev. Lett. **89**, 175001 (2002).
- [55] O. Arp, D. Block, and A. Piel, *Structure and trapping of three-dimensional dust clouds in a capacitively coupled rf-discharge*, in *AIP Conference Proceedings* (AIP Publishing, 2005), vol. 799, pp. 20–28.
- [56] A. Schella, T. Miksch, A. Melzer, J. Schablinski, D. Block, A. Piel, H. Thomsen, P. Ludwig, and M. Bonitz. *Melting scenarios for three-dimensional dusty plasma clusters*. Phys. Rev. E **84**, 056402 (2011).
- [57] P. Ludwig, S. Kosse, and M. Bonitz. *Structure of spherical three-dimensional Coulomb crystals*. Phys. Rev. E **71**, 046403 (2005).
- [58] H. Totsuji, C. Totsuji, T. Ogawa, and K. Tsuruta. *Ordering of dust particles in dusty plasmas under microgravity*. Phys. Rev. E **71**, 045401(R) (2005).
- [59] C. Henning, P. Ludwig, A. Filinov, A. Piel, and M. Bonitz. *Ground state of a confined Yukawa plasma including correlation effects*. Phys. Rev. E **76**, 036404 (2007).

- [60] A. Melzer, S. Käding, D. Block, and A. Piel. *Energy landscape in 3D finite dust clusters derived from shell transitions*. J. Phys. Condens. Matter **20**, 404204 (2008).
- [61] C. Killer, A. Schella, T. Miksch, and A. Melzer. *Vertically elongated three-dimensional Yukawa clusters in dusty plasmas*. Phys. Rev. B **84**, 054104 (2011).
- [62] D. Block, J. Carstensen, P. Ludwig, W. Miloch, F. Greiner, A. Piel, M. Bonitz, and A. Melzer. *Wake Formation and Wake Field Effects in Complex Plasmas*. Contrib. Plasma Phys. **52**, 804 (2012).
- [63] A. Piel, O. Arp, D. Block, I. Pilch, T. Trottenberg, S. Käding, A. Melzer, H. Baumgartner, C. Henning, and M. Bonitz. *Complex plasmas: forces and dynamical behaviour*. Plasma Phys. Controlled Fusion **50**, 124003 (2008).
- [64] V. A. Schweigert, I. V. Schweigert, A. Melzer, A. Homann, and A. Piel. *Plasma crystal melting: A nonequilibrium phase transition*. Phys. Rev. Lett. **80**, 5345 (1998).
- [65] I. V. Schweigert, V. A. Schweigert, A. Melzer, and A. Piel. *Melting of dust plasma crystals with defects*. Phys. Rev. E **62**, 1238 (2000).
- [66] T. Trottenberg, A. Melzer, and A. Piel. *Measurement of the electric charge on particulates forming Coulomb crystals in the sheath of a radiofrequency plasma*. Plasma Sources Sci. Technol. **4**, 450 (1995).
- [67] B. M. Annaratone, T. Antonova, D. D. Goldbeck, H. M. Thomas, and G. E. Morfill. *Complex-plasma manipulation by radiofrequency biasing*. Plasma Phys. Controlled Fusion **46**, B495 (2004).
- [68] T. Antonova, B. Annaratone, D. Goldbeck, V. Yaroshenko, H. Thomas, and G. Morfill. *Measurement of the interaction force among particles in three-dimensional plasma clusters*. Phys. Rev. Lett. **96**, 115001 (2006).
- [69] E. Thomas, J. D. Williams, and J. Silver. *Application of stereoscopic particle image velocimetry to studies of transport in a dusty (complex) plasma*. Phys. Plasmas **11**, L37 (2004).
- [70] S. Käding and A. Melzer. *Three-dimensional stereoscopy of Yukawa (Coulomb) balls in dusty plasmas*. Phys. Plasmas **13**, 090701 (2006).
- [71] D. Block, M. Kroll, O. Arp, A. Piel, S. Käding, Y. Ivanov, A. Melzer, C. Henning, H. Baumgartner, and M. Bonitz, *Structure And Dynamics Of Finite Dust Clouds*, in *AIP Conference Proceedings* (AIP Publishing, 2008), vol. 1041, pp. 69–72.
- [72] M. Himpel, C. Killer, B. Buttenschön, and A. Melzer. *Three-dimensional single particle tracking in dense dust clouds by stereoscopy of fluorescent particles*. Phys. Plasmas **19**, 123704 (2012).
- [73] S. Käding, A. Melzer, O. Arp, D. Block, and A. Piel, *Stereoscopic investigations of 3D Coulomb balls*, in *AIP Conf. Proc.* (AIP Publishing, 2005), vol. 799, pp. 335–338.

- [74] G. Pan and H. Meng. *Digital holography of particle fields: reconstruction by use of complex amplitude*. Appl. Opt. **42**, 827 (2003).
- [75] Y. Pu and H. Meng. *Four-dimensional dynamic flow measurement by holographic particle image velocimetry*. Appl. Opt. **44**, 7697 (2005).
- [76] M. Kroll, S. Harms, D. Block, and A. Piel. *Digital in-line holography of dusty plasmas*. Phys. Plasmas **15**, 063703 (2008).
- [77] M. Kroll, L. Muhlfeld, and D. Block. *Stereoscopic digital holography*. IEEE Trans. Plasma Sci. **38**, 897 (2010).
- [78] J. Schablinski, M. Kroll, and D. Block. *Particle tracking velocimetry of dusty plasmas using stereoscopic in-line holography*. IEEE Trans. Plasma Sci. **41**, 779 (2013).
- [79] D. Block, O. Arp, A. Piel, and A. Melzer, *Coulomb balls in Experiment and Simulation*, in *AIP Conference Proceedings* (AIP Publishing, 2005), vol. 799, pp. 454–457.
- [80] D. Block, M. Kroll, O. Arp, A. Piel, S. Käding, Y. Ivanov, A. Melzer, C. Henning, H. Baumgartner, P. Ludwig, et al. *Structural and dynamical properties of Yukawa balls*. Plasma Phys. Controlled Fusion **49**, B109 (2007).
- [81] V. Golubnychiy, H. Baumgartner, M. Bonitz, A. Filinov, and H. Fehske. *Screened Coulomb balls—structural properties and melting behaviour*. J. Phys. A: Math. Gen. **39**, 4527 (2006).
- [82] M. Bonitz, D. Block, O. Arp, V. Golubnychiy, H. Baumgartner, P. Ludwig, A. Piel, and A. Filinov. *Structural properties of screened Coulomb balls*. Phys. Rev. Lett. **96**, 075001 (2006).
- [83] S. W. S. Apolinario, B. Partoens, and F. M. Peeters. *Structural and dynamical aspects of small three-dimensional spherical Coulomb clusters*. New J. Phys. **9**, 283 (2007).
- [84] H. Kählert, P. Ludwig, H. Baumgartner, M. Bonitz, D. Block, S. Käding, A. Melzer, and A. Piel. *Probability of metastable configurations in spherical three-dimensional Yukawa crystals*. Phys. Rev. E **78**, 036408 (2008).
- [85] D. Block, S. Käding, A. Melzer, A. Piel, H. Baumgartner, and M. Bonitz. *Experiments on metastable states of three-dimensional trapped particle clusters*. Phys. Plasmas **15**, 040701 (2008).
- [86] H. Baumgartner, D. Block, and M. Bonitz. *Structure and phase transitions of Yukawa balls*. Contrib. Plasma Phys. **49**, 281 (2009).
- [87] J. Wrighton, J. W. Dufty, H. Kählert, and M. Bonitz. *Theoretical description of Coulomb balls: Fluid phase*. Phys. Rev. E **80**, 066405 (2009).
- [88] S. W. S. Apolinario and F. M. Peeters. *Melting transitions in isotropically confined three-dimensional small Coulomb clusters*. Phys. Rev. E **76**, 031107 (2007).

- [89] S. W. S. Apolinario, J. A. Aguiar, and F. M. Peeters. *Angular melting scenarios in binary dusty-plasma Coulomb balls: Magic versus normal clusters*. Phys. Rev. E **90**, 063113 (2014).
- [90] J. H. Chu and L. I. *Direct observation of Coulomb crystals and liquids in strongly coupled rf dusty plasmas*. Phys. Rev. Lett. **72**, 4009 (1994).
- [91] H. M. Thomas and G. E. Morfill. *Solid/liquid/gaseous phase transitions in plasma crystals*. J. Vac. Sci. Technol., A **14**, 501 (1996).
- [92] A. Homann, A. Melzer, S. Peters, and A. Piel. *Determination of the dust screening length by laser-excited lattice waves*. Phys. Rev. E **56**, 7138 (1997).
- [93] K. Takahashi, T. Oishi, K.-i. Shimomai, Y. Hayashi, and S. Nishino. *Analyses of attractive forces between particles in Coulomb crystal of dusty plasmas by optical manipulations*. Phys. Rev. E **58**, 7805 (1998).
- [94] A. Piel and A. Melzer. *Dynamical processes in complex plasmas*. Plasma Phys. Controlled Fusion **44**, R1 (2002).
- [95] A. Homann, A. Melzer, S. Peters, R. Madani, and A. Piel. *Laser-excited dust lattice waves in plasma crystals*. Phys. Lett. A **242**, 173 (1998).
- [96] A. Homann, A. Melzer, and A. Piel. *Measuring the charge on single particles by laser-excited resonances in plasma crystals*. Phys. Rev. E **59**, R3835 (1999).
- [97] A. Melzer, S. Nunomura, D. Samsonov, Z. W. Ma, and J. Goree. *Laser-excited Mach cones in a dusty plasma crystal*. Phys. Rev. E **62**, 4162 (2000).
- [98] D. R. Nelson and B. I. Halperin. *Dislocation-mediated melting in two dimensions*. Phys. Rev. B **19**, 2457 (1979).
- [99] L.D. Landau and E. Lifschitz, *Course of Theoretical Physics V, Statistical Physics, Part 1* (Pergamon Press, Oxford, 1980), 3rd ed.
- [100] J. Thomson. *XXIV. On the structure of the atom: an investigation of the stability and periods of oscillation of a number of corpuscles arranged at equal intervals around the circumference of a circle; with application of the results to the theory of atomic structure*. Philos. Mag. **7**, 237 (1904).
- [101] E. L. Altschuler, T. J. Williams, E. R. Ratner, R. Tipton, R. Stong, F. Dowla, and F. Wooten. *Possible Global Minimum Lattice Configurations for Thomson's Problem of Charges on a Sphere*. Phys. Rev. Lett. **78**, 2681 (1997).
- [102] S. W. S. Apolinario, B. Partoens, and F. M. Peeters. *Multiple rings in a 3D anisotropic Wigner crystal: Structural and dynamical properties*. Phys. Rev. B **77**, 035321 (2008).
- [103] F. Calvo and E. Yurtsever. *Non-monotonic size effects on the structure and thermodynamics of Coulomb clusters in three-dimensional harmonic traps*. Eur. Phys. J. D **44**, 81 (2007).

- [104] J. Wrighton, H. Kählert, T. Ott, P. Ludwig, H. Thomsen, J. Dufty, and M. Bonitz. *Charge Correlations in a Harmonic Trap*. *Contrib. Plasma Phys.* **52**, 45 (2012).
- [105] D. D. Frantz. *Magic number behavior for heat capacities of medium-sized classical Lennard-Jones clusters*. *J. Chem. Phys.* **115**, 6136 (2001).
- [106] R. D. Eppers and J. Kaelberer. *Thermodynamic properties of small aggregates of rare-gas atoms*. *Phys. Rev. A* **11**, 1068 (1975).
- [107] R. S. Berry, T. L. Beck, H. L. Davis, and J. Jellinek. *Solid-Liquid Phase Behavior in Microclusters*. *Adv. Chem. Phys.* **70**, part 2, 75 (1988).
- [108] J. Böning, A. Filinov, P. Ludwig, H. Baumgartner, M. Bonitz, and Y. Lozovik. *Melting of Trapped Few-Particle Systems*. *Phys. Rev. Lett.* **100**, 113401 (2008).
- [109] P. Debye and E. Hückel. *The theory of electrolytes. I. lowering of freezing point and related phenomena*. *Phys. Z.* **24**, 185 (1923).
- [110] H. Yukawa. *On the Interaction of Elementary Particles. I*. *J. Phys. Soc. Jpn.* 3rd Series **17**, 48 (1935).
- [111] J.-P. Joost, P. Ludwig, H. Kählert, C. Arran, and M. Bonitz. *Screened Coulomb potential in a flowing magnetized plasma*. *Plasma Phys. Controlled Fusion* **57**, 025004 (2015).
- [112] Z. A. Moldabekov, P. Ludwig, J.-P. Joost, M. Bonitz, and T. S. Ramazanov. *Dynamical Screening and Wake Effects in Classical, Quantum, and Ultrarelativistic Plasmas*. *Contrib. Plasma Phys.* **55**, 186 (2015).
- [113] A. Melzer, M. Klindworth, and A. Piel. *Normal Modes of 2D Finite Clusters in Complex Plasmas*. *Phys. Rev. Lett.* **87**, 115002 (2001).
- [114] P. P. Ewald. *Die Berechnung optischer und elektrostatischer Gitterpotentiale*. *Annalen der Physik* **369**, 253 (1921).
- [115] N. Metropolis, A. W. Rosenbluth, M. N. Rosenbluth, A. H. Teller, and E. Teller. *Equation of State Calculations by Fast Computing Machines*. *J. Chem. Phys.* **21**, 1087 (1953).
- [116] M. Matsumoto and T. Nishimura. *Mersenne Twister: A 623-dimensionally Equidistributed Uniform Pseudo-random Number Generator*. *ACM Trans. Model. Comput. Simul.* **8**, 3 (1998).
- [117] D. P. Landau and K. Binder, *A Guide to Monte-Carlo Simulations in Statistical Physics* (Springer, 2009), 1st ed., ISBN 978-0521 7684 81.
- [118] K. Hukushima and K. Nemoto. *Exchange Monte Carlo method and application to spin glass simulations*. *J. Phys. Soc. Japan* **65**, 1604 (1996).
- [119] R. H. Swendsen and J.-S. Wang. *Replica Monte Carlo simulation of spin-glasses*. *Phys. Rev. Lett.* **57**, 2607 (1986).



- [120] A. Filinov and M. Bonitz, *Classical and Quantum Monte Carlo*, in *Introduction to Computational Methods in Many Body Physics* (Rinton Press, Paramus, NJ, 2006), ISBN 978-1589 4900 93.
- [121] P. Langevin. *On the theory of Brownian motion*. C. R. Acad. Sci. (Paris) **146**, 530 (1908).
- [122] R. Mannella. *Quasisymplectic integrators for stochastic differential equations*. Phys. Rev. E **69**, 041107 (2004).
- [123] F. Aurenhammer. *Voronoi diagrams —A survey of a fundamental geometric data structure*. ACM Comput. Surv. **23**, 345 (1991).
- [124] C. S. Kaplan, *Voronoi diagrams and ornamental design*, in *The first annual symposium of the International Society for the Arts, Mathematics, and Architecture* (ISAMA, Spain, 1999), pp. 277–283.
- [125] A. Zippelius, B. I. Halperin, and D. R. Nelson. *Dynamics of two-dimensional melting*. Phys. Rev. B **22**, 2514 (1980).
- [126] K. J. Strandburg. *Two-dimensional melting*. Rev. Mod. Phys. **60**, 161 (1988).
- [127] D. G. Grier and C. A. Murray. *The microscopic dynamics of freezing in supercooled colloidal fluids*. J. Chem. Phys. **100**, 9088 (1994).
- [128] M. Eisenberg and R. Guy. *A proof of the hairy ball theorem*. Amer. Math. Monthly **86**, 571 (1979).
- [129] J.-P. Hansen and I. R. McDonald, in *Theory of Simple Liquids* (Academic Press, Burlington, 2006), pp. 11 – 45, 3rd ed., ISBN 978-0123 7053 58.
- [130] P. Ludwig, H. Thomsen, K. Balzer, A. Filinov, and M. Bonitz. *Tuning correlations in multi-component plasmas*. Plasma Phys. Controlled Fusion **52**, 124013 (2010).
- [131] A. Melzer, A. Schella, T. Miksch, J. Schablinski, D. Block, A. Piel, H. Thomsen, H. Kählert, and M. Bonitz. *Phase Transitions of Finite Dust Clusters in Dusty Plasmas*. Contrib. Plasma Phys. **52**, 795 (2012).
- [132] P. Rehmus, C. C. Roothaan, and R. Stephen Berry. *Visualization of electron correlation in ground states of He and H<sup>-</sup>*. Chem. Phys. Lett. **58**, 321 (1978).
- [133] P. Rehmus and R. Berry. *Visualization of electron correlation in a series of helium S states*. Chem. Phys. **38**, 257 (1979).
- [134] K. Tsuruta and S. Ichimaru. *Binding energy, microstructure, and shell model of Coulomb clusters*. Phys. Rev. A **48**, 1339 (1993).
- [135] R. E. Nettleton and M. S. Green. *Expression in terms of molecular distribution functions for the entropy density in an infinite system*. J. Chem. Phys. **29**, 1365 (1958).

- [136] H. J. Raveché. *Entropy and Molecular Correlation Functions in Open Systems. I. Derivation*. J. Chem. Phys. **55**, 2242 (1971).
- [137] R. D. Mountain and H. J. Raveché. *Entropy and Molecular Correlation Functions in Open Systems. II Two- and Three-Body Correlations*. J. Chem. Phys. **55**, 2250 (1971).
- [138] J. Mittal, J. R. Errington, and T. M. Truskett. *Quantitative link between single-particle dynamics and static structure of supercooled liquids*. J. Phys. Chem. B **110**, 18147 (2006).
- [139] T. Kawasaki, T. Araki, and H. Tanaka. *Correlation between dynamic heterogeneity and medium-range order in two-dimensional glass-forming liquids*. Phys. Rev. Lett. **99**, 215701 (2007).
- [140] S. Käding, D. Block, A. Melzer, A. Piel, H. Kählert, P. Ludwig, and M. Bonitz. *Shell transitions between metastable states of Yukawa balls*. Phys. Plasmas **15**, 073710 (2008).
- [141] S. Smale. *Mathematical problems for the next century*. Math. Intell. **20**, 7 (1998).
- [142] H. Baumgartner, D. Asmus, V. Golubnychiy, P. Ludwig, H. Kählert, and M. Bonitz. *Ground states of finite spherical Yukawa crystals*. New J. Phys. **10**, 093019 (2008).
- [143] H. Thomsen and M. Bonitz. *Resolving structural transitions in spherical dust clusters*. Phys. Rev. E **91**, 043104 (2015).
- [144] D. J. Wales and S. Ulker. *Structure and dynamics of spherical crystals characterized for the Thomson problem*. Phys. Rev. B **74**, 212101 (2006).
- [145] V. Nosenko and J. Goree. *Shear flows and shear viscosity in a two-dimensional Yukawa system (dusty plasma)*. Phys. Rev. Lett. **93**, 155004 (2004).
- [146] Y. Feng, J. Goree, and B. Liu. *Evolution of Shear-Induced Melting in a Dusty Plasma*. Phys. Rev. Lett. **104**, 165003 (2010).
- [147] V. Nosenko, S. Zhdanov, A. V. Ivlev, G. Morfill, J. Goree, and A. Piel. *Heat transport in a two-dimensional complex (dusty) plasma at melting conditions*. Phys. Rev. Lett. **100**, 025003 (2008).
- [148] J. Goree, B. Liu, and Y. Feng. *Diagnostics for transport phenomena in strongly coupled dusty plasmas*. Plasma Phys. Controlled Fusion **55**, 124004 (2013).
- [149] A. Melzer, A. Schella, J. Schablinski, D. Block, and A. Piel. *Instantaneous normal mode analysis of melting of finite dust clusters*. Phys. Rev. Lett. **108**, 225001 (2012).
- [150] H. Thomsen, *Excitation and Melting of Yukawa Balls*, Diplomarbeit, Christian-Albrechts-Universität zu Kiel (2011).
- [151] V. Nosenko, A. V. Ivlev, and G. E. Morfill. *Laser-induced rocket force on a microparticle in a complex (dusty) plasma*. Phys. Plasmas **17**, 123705 (2010).

- [152] A. Melzer. *Laser manipulation of particles in dusty plasmas*. Plasma Sources Sci. Technol. **10**, 303 (2001).
- [153] A. Ashkin. *History of optical trapping and manipulation of small-neutral particle, atoms, and molecules*. IEEE J. Sel. Top. Quantum Electron. **6**, 841 (2000).
- [154] B. Liu, J. Goree, V. Nosenko, and L. Boufendi. *Radiation pressure and gas drag forces on a melamine-formaldehyde microsphere in a dusty plasma*. Phys. Plasmas **10**, 9 (2003).
- [155] G. Kudelis, H. Thomsen, and M. Bonitz. *Heat transport in confined strongly coupled two-dimensional dust clusters*. Phys. Plasmas **20**, 073701 (2013).
- [156] S. Nunomura, D. Samsonov, S. Zhdanov, and G. Morfill. *Heat transfer in a two-dimensional crystalline complex (dusty) plasma*. Phys. Rev. Lett. **95**, 025003 (2005).
- [157] V. E. Fortov, O. S. Vaulina, O. F. Petrov, M. N. Vasiliev, A. V. Gavrikov, I. A. Shakova, N. A. Vorona, Y. V. Khrustalyov, A. A. Manohin, and A. V. Chernyshev. *Experimental study of the heat transport processes in dusty plasma fluid*. Phys. Rev. E **75**, 026403 (2007).
- [158] M. S. Green. *Markoff Random Processes and the Statistical Mechanics of Time-Dependent Phenomena. II. Irreversible Processes in Fluids*. J. Chem. Phys. **22**, 398 (1954).
- [159] R. Kubo. *Statistical-mechanical theory of irreversible processes. I. General theory and simple applications to magnetic and conduction problems*. J. Phys. Soc. Japan **12**, 570 (1957).
- [160] R. Kubo, M. Yokota, and S. Nakajima. *Statistical-mechanical theory of irreversible processes. II. Response to thermal disturbance*. J. Phys. Soc. Japan **12**, 1203 (1957).
- [161] A. Kundu, A. Dhar, and O. Narayan. *The Green-Kubo formula for heat conduction in open systems*. J. Stat. Mech: Theory Exp. **2009**, L03001 (2009).
- [162] Q. Spreiter and M. Walter. *Classical Molecular Dynamics Simulation with the Velocity Verlet Algorithm at Strong External Magnetic Fields*. J. Comput. Phys. **152**, 102 (1999).
- [163] T. Ott and M. Bonitz. *Diffusion in a strongly coupled magnetized plasma*. Phys. Rev. Lett. **107**, 135003 (2011).
- [164] T. Ott, *Transport and waves in strongly coupled Coulomb and Yukawa one-component plasmas*, Dissertation zur Erlangung des Doktorgrads, Mathematisch-Naturwissenschaftliche Fakultät der Christian-Albrechts-Universität zu Kiel, Kiel (2012).
- [165] T. Ott, H. Löwen, and M. Bonitz. *Magnetic field blocks two-dimensional crystallization in strongly coupled plasmas*. Phys. Rev. Lett. **111**, 065001 (2013).
- [166] C. E. Shannon. *A Mathematical Theory of Communication*. Bell System Technical Journal **27**, 379 (1948).



# Danksagung

An allererster Stelle möchte ich meinem Betreuer Prof. Dr. Michael Bonitz dafür danken, dass er es mir ermöglicht hat, in seiner Arbeitsgruppe diese Dissertation anzufertigen. Ich bin seit Ende 2009 in seiner Arbeitsgruppe, und er stand mir stets mit wertvollen Anregungen und Kommentaren, sowie mit fachlichen Diskussionen zur Seite. Die vorliegenden Ergebnisse sind auch seiner hervorragenden Betreuung geschuldet.

Bei ihm und bei allen derzeitigen sowie ehemaligen Kollegen in der Arbeitsgruppe möchte ich mich ganz herzlich für den ausgesprochen freundlichen Umgang miteinander bedanken. Neben den fachlichen Diskussionen haben auch zahlreiche gemeinsame Unternehmungen stets für eine angenehme Atmosphäre und viel Spaß gesorgt. Für den fachlichen Austausch über physikalische und auch programmiertechnische Fragestellungen, ebenso wie für das Korrekturlesen dieser Arbeit danke ich Jan Willem Abraham, Dr. Karsten Balzer, Dr. Sebastian Bauch, Dr. Jens Böning, Tobias Dornheim, Dr. habil. Alexei Filinov, Kenji Fujioka, Simon Groth, Sebastian Hermanns, Christopher Hinz, Dr. David Hochstuhl, Jan-Philip Joost, Dr. Hanno Kählert, Kay Kobusch, Dr. Patrick Ludwig, Dr. Torben Ott, Dr. Lasse Rosenthal, Niclas Schlünzen, Ingmar Schnell, Mawussey Segnon und Tim Schoof.

Außerdem möchte ich den Kollegen Dr. habil. Dietmar Block, Prof. Dr. Alexander Piel und Jan Schablinski aus der Experimentalphysik in Kiel, sowie Prof. Dr. André Melzer und Dr. André Schella aus Greifswald meinen Dank aussprechen für zahlreiche interessante Diskussionen und die konstruktive Zusammenarbeit zwischen Experiment und Theorie.

Der Deutschen Forschungsgesellschaft danke ich für die Finanzierung meiner Doktorandenstelle im Rahmen des Sonderforschungsbereichs Transregio 24 "Grundlagen komplexer Plasmen".

Ein abschließender Dank gebührt meinen Eltern und auch meinen Geschwistern für ihre stetige Unterstützung.



# Selbstständigkeitserklärung

Hiermit versichere ich, dass die vorliegende Dissertation – abgesehen von der Beratung durch meinen Betreuer Prof. Dr. Michael Bonitz und der angegebenen Fachliteratur – nach Inhalt und Form meine eigene Arbeit ist.

Ich versichere weiter, dass die vorliegende Arbeit weder ganz noch zum Teil schon einer anderen Stelle im Rahmen eines Prüfungsverfahrens vorgelegen hat. Sie ist in dieser Form weder veröffentlicht worden noch zur Veröffentlichung eingereicht. Die im Rahmen der Arbeit entstandenen Publikationen in wissenschaftlichen Fachzeitschriften sind auf den Seiten 88 und 120 vermerkt. Weiterhin versichere ich, dass ich die Arbeit unter Einhaltung der Regeln guter wissenschaftlicher Praxis der Deutschen Forschungsgemeinschaft angefertigt habe.

Kiel, den